THE UNIVERSITY OF
SYDNEY

THE UNIVERSITY OF SYDNEY

Advanced functional coatings for biomedical applications: patterning cells onto biomaterials

Andrew Michael Telford

The University of Sydney

School of Chemistry

and

CSIRO Future Manufacturing National Research Flagship

November 2011

Submitted in accordance with the requirements for the degree of
Doctor of Philosophy

Declaration

This Thesis is presented at the School of Chemistry, University of Sydney, as part of the requirements for the degree of Doctor of Philosophy in Science. All of the experimental work reported within this Thesis has been carried out by the author in the School of Chemistry, University of Sydney, Sydney NSW, and in CSIRO Material Science and Engineering, Clayton VIC, during March 2008 to July 2011. No part of this Thesis has been submitted for any other degree to this, or any other institution. When collaboration has been necessary, the collaborators have been named and the extent of the collaboration made clear. Results from other authors are referenced in the usual manner throughout the text.

_____ _____

Andrew M. Telford Date

Abstract

The aim of this work was to develop engineered coatings for protein and cell patterning on a surface. Cell patterning is important for biomedical applications such as single-cell studies, cell microcolonies arrays for high throughput drug screening, and the growth of geometrically controlled cell co-cultures for tissue engineering.

In this work, the patterning of cells relied on the controlled positioning of protein domains on a surface, on which the cells could adhere. This was done by dewetting a protein-repellent polymer film from a protein-adsorptive one. Dewetting is the process by which an unstable thin liquid film (such as a polymer over its glass transition temperature) spontaneously breaks up, resulting in the formation of holes. The duration of dewetting controls the dimensions of the holes, from tens of nanometers to tens of microns. By tuning the thickness of the films and the molecular weight of the polymers it is possible to vary the type of pattern that is obtained. The result of the dewetting was a chemically and topographically patterned coating. Proteins in contact with such surface could only adsorb inside the dewetted holes, where the adsorptive polymer was exposed.

The first system investigated was dewetted poly(*N*-vinylpyrrolidone) (PNVP) on polystyrene (PS). PNVP was found to cross-link upon annealing, as well as dewetting from PS. Insoluble cross-linked PNVP films were characterized by neutron reflectometry, infrared spectroscopy and ellipsometry, and found to be stable in water for many days, resistant to harsh solvents, and excellent in repelling proteins. The hole growth observed during concurrent dewetting and cross-linking was fully characterized by time elapsed optical microscopy, and a model was developed to predict it. The pattern obtained by dewetting PNVP could be controlled by selecting

the appropriate annealing temperature, in order to tune the ratio between the rates of dewetting and cross-linking.

The PNVP/PS architecture was improved by substituting the PNVP film with a functional polymer brush, in order to achieve a more versatile system. A polymer was designed so as to be able to dewet from PS, as well as bear initiators for the grafting of a polymer brush. This macroinitiator was synthesised by reversible addition-fragmentation chain transfer polymerization (RAFT). A protein-repellent poly(poly(ethylene glycol)methyl ether methacrylate) (poly(PEGMA)) brush was grafted from the dewettable macroinitiator film using activators generated by electron transfer atom transfer radical polymerization (AGET ATRP). This type of polymerization allows growing brushes of controlled thickness, with "living" ends that may easily be post-functionalised with simple chemical reactions, to interact selectively with different biological molecules or cells. The grafting process was investigated by ellipsometry, size exclusion chromatography and X-ray photoelectron spectroscopy. The functional patterned coatings developed were able to effectively immobilise extracellular matrix proteins and cells in selected areas of the surface, as shown by fluorescence microscopy and atomic force microscopy. The cells could spread on the surface, showing good viability.

The patterned coatings here described could be prepared on non-flat and large objects, offering a simple and cheap alternative to other patterning techniques, such as photolithography and micro-contact printing, and opening exciting prospects in biomedical applications.

Acknowledgments

This Thesis represents an important milestone in my life. This is the result of long studies in Italy, and of the hard decision to move to Australia. But this achievement is not just mine: this belongs to all the people that have taught me and supported me in many years.

First and above all, my family. To support a son or a brother in the decision of moving to the other side of the world for a few years, to be able to see him only once a year, having always positive, selfless and soothing words for him, is not something that anyone can do. I'm always told how proud of me my family is; the truth is I am much more proud of them. My greatest wish is to be able to be one day as strong a guide for my sons as my parents were for me.

Often, family does not end where blood bonds do. My friends in Siena are part of what made me who I am. Davide, Ciccio, Orso, Sotto, Gigi, Ruggie, Checca know me and accept me better than anybody. The list of friends is far longer than this, and cannot exclude the people who have been in my life in my years in Florence.

Sooner or later everyone feels the need of a family for himself. My companion and best friend in my adventure in Australia has slowly but steadily managed to charm me and keep me in this beautiful country. Irene, I am very excited about what the future holds for us.

Thanks to all the beautiful people who have made me feel so welcome when I felt alone, so far away from home. My closest friends in Sydney are also my most esteemed colleagues, from which I constantly learn about chemistry and life.

A special acknowledgment must go to my supervisors. Chiara and Laurence, you have taught me so much, and it is because of you that I now

feel much closer to be an open-minded and independent scientist. I would also like to thank Michael James for all his help and support.

I am finally grateful to the University of Sydney and CSIRO Future Manufacturing National Research Flagship for funding.

Ringraziamenti

Questa Tesi rappresenta una tappa importante della mia vita. E' il risultato di lunghi studi in Italia, e della dura decisione di trasferirmi in Australia. Questo raggiungimento non è però solo mio: appartiene a tutte le persone che mi hanno insegnato e sostenuto per molti anni.

Prima di tutti la mia famiglia. Sostenere un figlio o un fratello nella decisione di trasferirsi dall'altra parte del mondo, essere in grado di vederlo solo una volta all'anno, avere sempre parole positive, confortanti e mai egoiste, è qualcosa che non tutti sono in grado di fare. La mia famigla mi dice sempre quanto sia orgogliosa di me; la verità è che sono molto più orgoglioso di loro di quanto loro lo siano di me. Il mio desiderio più grande è di essere in grado un giorno di essere una guida per i miei figli forte come lo sono stati i miei genitori per me.

Spesso la famiglia non finisce dove finiscono i legami di sangue. I miei amici a Siena sono parte di quello che mi ha reso chi sono. Davide, Ciccio, Orso, Sotto, Gigi, Ruggie, Checca mi conoscono e accettano come nessun altro. La lista di amici è molto più lunga di questa, e non può escludere le persone che sono state parte della mia vita nei miei anni a Firenze.

Prima o poi tutti sentono il bisogno di una famiglia tutta loro. La mia migliore amica e compagnia nella mia avventura in Australia è riuscita

lentamente ma con determinazione ad incantarmi e a tenermi in questo paese meraviglioso. Irene, sono molto entusiasta di cosa ci riserva il futuro.

Grazie a tutte le persone meravigliose che mi hanno fatto sentire così benvenuto quando mi sono sentito solo, così lontano da casa. I miei amici più cari a Sydney sono anche i miei colleghi più stimati, da cui imparo continuamente di chimica e di vita.

Un ringraziamento speciale va ai miei supervisori. Chiara e Laurence, mi avete insegnato moltissimo, ed è grazie a voi che mi sento adesso così vicino a diventare uno scienziato indipendente e di ampie vedute. Vorrei ringraziare anche Michael James per tutto il suo aiuto e supporto.

Sono grato infine all'Università di Sydney e a CSIRO Future Manufacturing National Research Flagship per il sostegno economico.

Publications arising from this work

1. **Telford, A. M.**; Meagher, L.; Neto, C., Polymer Functional Coatings for Proteins and Cells Patterning via Thin Film Dewetting and Polymer Grafting. *IN PREPARATION*.

2. **Telford, A. M.**; Thickett, S. C.; James, M.; Neto, C., Competition between Dewetting and Cross-Linking in Poly(N-vinylpyrrolidone)/Polystyrene Bilayer Films. *Langmuir* 2011. *Just accepted manuscript (DOI 10.1021/la2029577).*

3. **Telford, A. M.**; James, M.; Meagher, L.; Neto, C., Thermally Cross-Linked PNVP Films As Antifouling Coatings for Biomedical Applications. *ACS Applied Materials & Interfaces* 2010, 2 (8), 2399-2408.

Presentations arising from this work

1. **2011:** "Advanced functional coatings for biomedical applications: control over cell interaction with artificial surfaces" (poster), Andrew M. Telford, Laurence Meagher, Chiara Neto. *Australian Nanotechnology Network Early Career Research Symposium*, Sydney NSW (Australia). Poster prize winner.

2. **2011:** "Development of Polymer Coatings for Proteins and Cells Patterning via Thin Film Dewetting and Polymer Grafting" (oral), Andrew M. Telford, Laurence Meagher, Chiara Neto. *Australian Colloids and Interfaces Symposium*, Hobart TAS (Australia).

3. **2011:** "Understanding the Thermodynamics of Dewetting and Cross-

linking in Poly(N-vinyl pyrrolidone)/Polystyrene Thin Bi-layer Films" (poster), Andrew M. Telford, Stuart Thickett, Michael James, Laurence Meagher, Chiara Neto. *Australian Colloids and Interfaces Symposium*, Hobart TAS (Australia).

4. **2010:** "New biocompatible polymer coatings for medical applications" (Poster); Andrew M. Telford, Chiara Neto, Laurence Meagher, Michael James. *International Conference on Nanoscience and Nanotechnology*, Sydney NSW (Australia).

5. **2009:** "Conformal Nanometric Surface Patterning Using Polymer Film Dewetting" (Oral), Andrew M. Telford, Chiara Neto, Laurence Meagher. *NanoBioTech meeting*, Montreux (Switzerland).

6. **2009** "Conformal nanometric surface patterning using polymer film dewetting" (poster), Andrew M. Telford, Chiara Neto, Laurence Meagher. *Australian Colloid and Interfaces Symposium*, Adelaide SA (Australia).

7. **2008** "Micro- and nano- patterns of proteins as cell culture substrates" (oral and poster), Andrew M. Telford, Chiara Neto. Sydney *University Tissue Engineering Network meeting*, Sydney NSW (Australia).

Table of contents

CHAPTER 1

Introduction

1.1 Preamble

The interaction of a synthetic surface with biological media is a very complex process. The material surface is interfaced with an extremely complex mixture of salts, proteins and cells. Proteins can adsorb onto the surface and change their structural configuration, depending on the structure and the chemistry of the surface and on the properties of the protein. They hence present different chemical cues to the surrounding cells, which react accordingly. The understanding and control of the interaction of a synthetic surface with biological media is crucial in modern biology and medicine, where artificial devices are commonly employed.

A very important example is the case of medical implants. When these or similar medical devices are interfaced with a living tissue, they generally trigger an inflammatory reaction usually referred to as the foreign body reaction (FBR).[1] This defence mechanism encompasses many different types of processes, the most common of which being the isolation of the foreign body in a fibrous capsule. The very first step of such response is the coverage of the unknown surface with proteins that allow it to be detected by macrophages and other cells, and direct their attachment. This complex layer is referred to as provisional matrix, and in Anderson *et al.*'s words, "may be viewed as a naturally derived, biodegradable sustained release system in which bioactive agents are released to control subsequent phases of wound healing."[1] The foreign body is eventually walled out by a thick layer of cells and proteins. This affects dramatically the performance of the *in vivo* device, that cannot be integrated or interact with the living body anymore, and may suffer from mechanical failure, e.g. due to pH effects inside the fibrous capsule. As well as the host cells, also bacteria can adhere on the foreign surface, forming an impenetrable biofilm that acts as a stronghold from which future bacterial infections can spread.[2, 3] Modern *in*

vivo devices have to be designed so to avoid non-specific protein adsorption, which can play a role in both the FBR and bacterial infections.

The understanding and control of the interaction of synthetic surfaces with cells in a biological medium is also extremely important in *in vitro* tissue engineering. Again, the support surface used to grow the tissue can trigger a specific response in the seeded cells. It is crucial that the synthetic substrate can guide the complex process of cells assembling in a functional tissue and suppress any unwanted cell response.

The interaction between a cell and a surface is always mediated by proteins, which can be already present in the biological media, or can be secreted by the cell itself or surrounding cells.[4] This is a very important piece of information: to control protein adsorption on a surface is the first step towards controlling the way that cells will interact with it. The protein-surface interaction can be tailored for different purposes. A common strategy to control the FBR is to design surfaces that prevent any non-specific protein adsorption. Such surfaces are commonly referred to as antifouling or bio-inert. In principle, antifouling materials can have an impact on the FBR by preventing the formation of the protein provisional matrix that directs the first stages of the process. Antifouling materials prevent protein adsorption as a result of their intrinsic surface properties, such as wettability, surface charge, swelling ability and compressibility. Such coatings do not require any chemical or topological heterogeneity to perform their task. A detailed description of antifouling surfaces, including protein-surface interactions, is presented in Section 1.4.

In many applications, such as catheters, surgical tools and biosensors, completely avoiding the interaction of the device with the host proteins and cells is enough. Other applications require instead a controlled protein and cell adsorption on a substrate. For example, implants that require integration with the host cannot be inert to it. The device has to interact with the host

tissue, and promote the same type of wound healing process that would occur in any other damaged tissues. The microenvironment presented on the surface has to promote the natural cascade of events that brings from the wound to the healed tissue.

Tissue engineering is another very pertinent example of creating surfaces that must interact controllably with biological media. The adhesion of multiple types of cells has to be allowed on the substrate, yet avoiding uncontrolled proliferation or, at the other extreme, cell death. The substrate has to control cell behaviour, guiding the adhesion and interaction of the cells towards the assembly of the final tissue.

Control over protein adsorption and cell adhesion is also very important in fundamental biological studies, where the biochemical mechanisms of single cells or colonies of controlled size are of interest. Such studies are important to understand fully the basic mechanisms of cell-surface interactions, in order to successfully design the next generation of medical implants. The substrate used has to induce the localized adhesion of a specific number of cells, often in large arrays for high throughput analyses. More details on the interaction of polymer coatings with cells can be found in Section 1.6.

Organic polymer coatings have been extensively used in biomedical applications, because of ease of preparation, tuneable mechanical properties, and the possibility of easy modification and functionalisation to optimise their properties and potentially improve, for example, biocompatibility. Polymer coatings have a number of advantages when compared to bulk polymeric devices or materials. They allow the tailoring of the properties (e.g. biocompatibility) of any surface, bypassing the need to redesign instruments, implants, tools, which have already been optimized to meet a specific need, such as hardness, sharpness and flexibility. Polymer coatings are routinely used in devices such as stents, cardiac assist devices,

electrosurgical tools, catheters, needles and epidural probes, medical electronics (e.g. biosensors), where there is a need to reduce friction, impart chemical or thermal resistance, control infections and reduce the defensive reaction of the biological host. Polymer coatings also find application as tissue engineering substrates.

1.2 Aim of this work

The aim of this work was to design functional polymer coatings for biomedical applications. Two types of systems were investigated. The first was a very robust and easy to prepare coating with excellent antifouling properties, suitable for applications in which protein adsorption is undesirable, such as catheters, contact lenses and intravenous devices. The second was a coating consisting of a chemical and topographical micropattern. This coating was designed for applications where controlled, localized cell adhesion was required, as in fundamental biological studies or in tissue engineering. The pattern was obtained by the combination of polymer thin film dewetting and selective polymer brush grafting by surface-initiated reversible-deactivation radical polymerization.

The underlying idea behind all this work was to develop low cost and easy to implement alternatives to the fabrication techniques currently available, and to investigate the capabilities of the newly designed coatings in selected biomedical applications.

1.3 Outline of this Thesis

The first Chapter of this Thesis provides background information on the research undertaken. The basics of the interaction of proteins with polymer coatings are presented, with special emphasis on polymer brushes. Common techniques used to produce polymer brushes are introduced, with focus on the surface-initiated method used herein. Patterned surfaces and their ability to induce specific responses in cells are then described. Finally, common techniques to produce patterned surfaces are summarised, and the dewetting method used to create a pattern used in this work is described.

Summarised in Chapter 2 are the main techniques and methodologies common to all the experimental work in this Thesis.

Presented in Chapter 3 is the investigation on the cross-linking mechanism that spontaneously occurs in poly(*N*-vinylpyrrolidone) (PNVP) films upon thermal annealing. Cross-linked PNVP films are extremely robust and have excellent protein-repellent behaviour, so they are promising candidates in a range of biotechnological applications. In Chapter 4, the investigation on the competition between cross-linking and dewetting in these PNVP films is presented. The hole growth during dewetting was described with a newly developed model, which also allowed to extrapolate the cross-linking rate coefficient for PNVP.

Presented in Chapter 5 is research on a micropatterned coating, produced by spontaneous polymer thin film dewetting and grafting of a highly protein-repellent poly(poly(ethylene glycol) methyl ether methacrylate) (poly(PEGMA)) brush in selected locations. The chemically and topographically patterned coating obtained showed excellent protein adsorption contrast. The studies on controlled adhesion of fibroblasts on the developed patterns are reported in Chapter 6. The shape and spreading of

the cells on the adhesive domains of the pattern was investigated to determine the cell viability.

Finally, summarised in Chapter 7 are the general conclusions from the whole Thesis.

1.4 Interaction of polymer coatings with proteins

A protein approaching a surface experiences a number of repulsive and attractive forces, which will ultimately determine the interaction between the two. This Section focuses on the interaction of proteins with a grafted polymer brush, based on the extensive literature on the topic. The general conclusions are valid for any similar polymer coating which can swell with water, such as hydrophilic cross-linked polymers. The investigation of a thermally cross-linked poly(*N*-vinylpyrrolidone) film able to trap water and strongly repel protein molecules is reported in Chapter 3. In Chapter 5, a poly(poly(ethylene glycol) methyl ether methacrylate) brush was grafted from a substrate to reduce protein adsorption in selected locations.

1.4.1 Polymer brushes

The term "polymer brush" refers to a set of polymer chains end-tethered to a surface with high graft density, i.e. high number of chains per surface unit, such that the surface-attached chains become crowded and are stretched away from the surface.[5, 6] The dense packing of the chains in a brush gives it its unique properties. Examples are ultralow friction of surfaces coated in polymer brushes,[7] autophobic dewetting, i.e. inability of a polymer melt to wet a polymer brush of the same chemical composition,[8, 9]

and low fouling properties of polymer brushes (discussed in detail in Section 1.4.2).

An isolated polymer chain tethered on a surface will have a conformation very similar to the one of an isolated chain in solution, assuming no interactions between the chain segments of the grafted polymer and its substrate. This is a simplistic generalization useful to describe the difference between chains in brushes with different steric hindrance, as discussed below. The grafted chain conformation will differ slightly from the one in solution because of the tethered end. Furthermore, if attractive interactions with the substrate are present, the chain is likely to completely collapse on the surface, while it is likely to moderately extend away from the surface if the interactions are repulsive. An unperturbed coil has a characteristic dimension defined by the Flory radius, R_F (Equation 1.1):[10]

$$R_F = R_g \alpha \tag{1.1}$$

where α is the intramolecular expansion factor and R_g is the radius of gyration,[10] defined in Equation (1.2). α is unity for an ideal solvent (or theta-solvent), which has neither repulsive nor attractive interactions with the polymer. α is greater than one for good solvents (the polymer segments repel each other and the polymer swells) and smaller than one for poor solvents (the polymer segments attract each other and the polymer shrinks).

$$R_g = \frac{(l\sqrt{N})}{\sqrt{6}} \tag{1.2}$$

In Equation (1.2), l is the repeating unit length and N is the degree of polymerization (i.e. the number of monomers in the polymer chain).

A layer of isolated end-tethered polymer chains not interacting with their substrate will hence have thickness equal to the Flory radius of the polymer chain. Each chain is described as having a "mushroom" conformation. In a polymer brush, many polymer chains are immobilized in a small area, and they inevitably influence each other. More precisely, the distance between grafting points is smaller than the Flory radius of each chain, and excluded volume comes into play. The steric repulsion between adjacent chains forces them to stretch away from the surface to minimize their energy. Therefore, in a polymer brush the chains will have a perturbed conformation.[10, 11] The equilibrium conformation of a chain in a brush, for a given grafting density, will be the result of the balance between steric hindrance from neighbouring chains (excluded volume) and the spring restoring force of the chain, which minimizes the entropic cost associated with stretching out (Figure 1.1).[11]

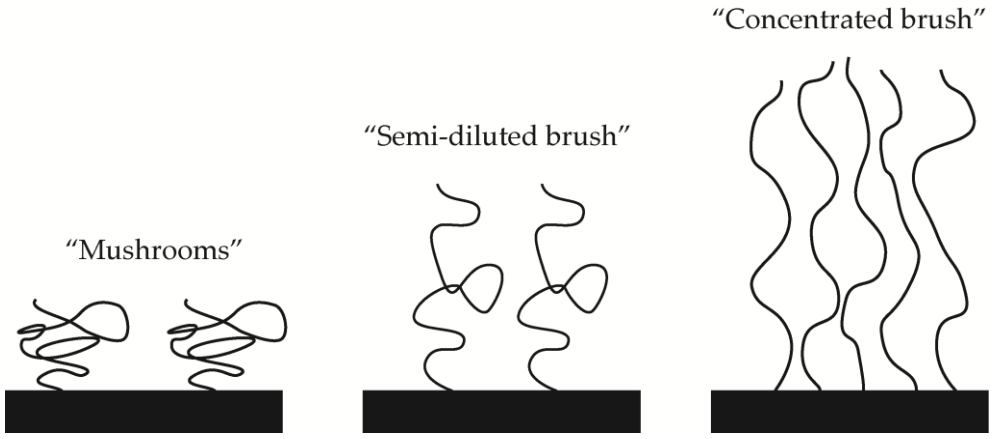

Figure 1.1 Possible configurations of polymer chains in an end-tethered layer at different grafting densities (i.e. degrees of stretching). At low grafting densities, the chains lie on the substrate in a "mushroom" shape. When the chains start to overlap, they extend away from the substrate, and the brush thickness is described by Alexander's scaling law ("semi-dilute brush").[12] When the grafting density becomes very high, the polymer chains stretch much further, and the scaling law describing the brush thickness changes accordingly ("concentrated brush").

Now, only the case of a brush swollen in a good solvent will be considered, since it is the system most used in biological applications. According to the Alexander model,[12] the thickness of such a brush will scale linearly with the polymer length (Equation 1.3):

$$L \propto N\sigma^{1/3} \tag{1.3}$$

where σ is the grafting density defined as surface coverage fraction, and N is the degree of polymerization of the polymer (number of monomers per chain). This relationship is valid over an extended range of grafting densities, provided that N > 50.[13] The scaling law is different for dry brushes, as a polymer is considered to be a θ-solvent for itself. The brush chains are therefore less extended, and the scaling law is defined by Equation 1.4:

$$L \propto N\sigma^{1/2} \tag{1.4}$$

More recently, a distinction has been made between the "semi-dilute brush" regime, where the Alexander scaling law (Equation 1.3) is valid, and the "concentrated brush" regime, where the brush length scaling would change to σ^n, with n > 1/3 and equal to 1 for the theoretical limit of σ = 1.[14, 15] This behaviour has been observed experimentally.[16-18] The regime cross-over occurs over a wide range of grafting densities, and depends strongly on the system.[19] A concentrated brush has higher resistance to compression than a semi-dilute one.[14-16] Also, a semi-dilute brush has a density profile that is poorly described by the step-like function assumed by the Alexander model, and is rather parabolic,[11] while the stretching away from the substrate of a concentrated brush is so great that its density profile approaches Alexander's step-like behaviour.[14]

There are two main strategies which have been used to prepare polymer brushes, namely the "grafting-to" and the "grafting-from" techniques. They will be described in Section 1.5.

1.4.2 Interaction of proteins with hydrophilic polymer brushes

Currie *et al.*[20] have published an extensive review on the modelling of interactions between spherical particles and polymer brushes. They describe three types of adsorption (Figure 1.2): a particle can diffuse through the brush and adhere to the grafting substrate (primary adsorption), can adhere at the brush-solvent interface (secondary adsorption), or diffuse within the brush and adhere to the grafted chains without reaching the grafting substrate (tertiary adsorption).

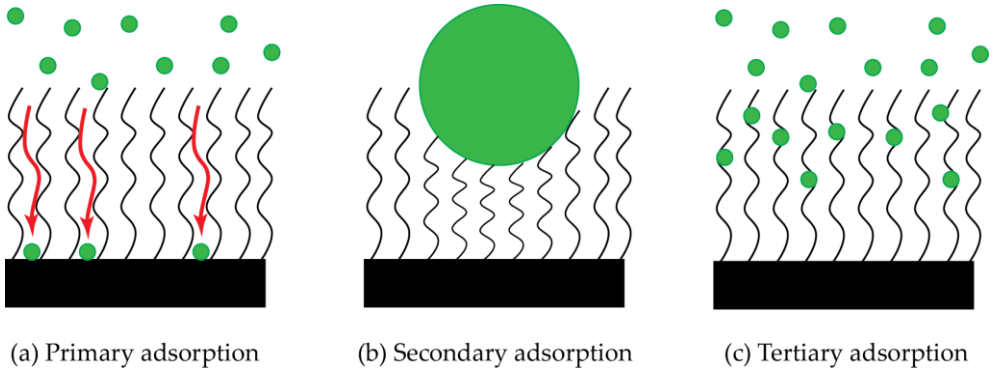

Figure 1.2 Modalities of protein adsorption on a polymer brush, as described by Currie et al.[20] Proteins can (a) penetrate into the brush and adhere on the substrate, (b) adhere on top of the brush or (c) partly penetrate into the brush and adsorb onto it.

The predominant type of particle adsorption on the surface is dictated by the size of the particle relatively to the inter-chain distance, in combination with the interaction between the particle and the polymer chain segments. A small particle can diffuse within a loosely packed brush and

reach the substrate. A larger particle cannot diffuse through a densely packed brush, and will hence adsorb to the outermost of the polymer brush (provided the net interaction is attractive). It may strongly adsorb only if it can compress the brush enough to overcome the repulsive steric interactions between polymer chains and effectively interact with the coated substrate. These two scenarios were previously modelled by Halperin.[21] Tertiary adsorption comes into play when the particles are small relative to the inter-chain distance, i.e. are able to diffuse into the brush to some extent, and have an affinity to the grafted chains themselves. Tsujii and co-workers[22] reviewed Halperin's work and others, and highlighted the importance of (I) grafting density and (II) molecular weight of the brush in effective particle repulsion. High grafting density prevents primary adsorption by steric repulsion, and combined with high MWs, it provides a brush with very low compressibility, which can prevent secondary adsorption.[23]

The model described above of rigid particles interacting with a brush is a very important starting point to begin to understand the interaction between proteins and polymer brush layers, and ultimately to design antifouling coatings. In the following, a more comprehensive scenario is depicted, which includes considerations on the role of water, ubiquitous solvent in biological environments.

A hydrophilic brush that can swell in water will have strong protein-repellent properties. This can be explained from a thermodynamic point view. A swollen brush is more favourable energetically because it has higher entropy; such brush is less confined and the chains are freer to move than in a collapsed configuration. In order to adsorb on a polymer brush layer, large protein molecules would have to compress the chains, which would reduce the entropy and thus be unfavourable. Again, a high grafting density is desirable both to exclude the protein molecules and to reduce the compressibility of the brush (because of higher steric repulsion between the

chains). A more complete picture is given when the adsorbed water is taken into account. Swollen hydrophilic brushes tightly bind water molecules, to the point that the adsorbed water often behaves differently from the bulk water; such water may freeze well below 0 °C, or not freeze at all, because of very strong hydrogen bonds with the grafted chains. The effect is greater the stronger the water-polymer interaction, as seen when comparing neutral hydrophilic brushes to charged (e.g. zwitterionic) brushes, where electrostatic interactions help confine more "non-freezable" water.[24-26] The compression of a brush in a secondary adsorption scenario would displace the water in the brush, similarly to squeezing a damp sponge, which is enthalpically unfavorable.[27] A similar conclusion can be given for primary and tertiary adsorption, where small proteins able to penetrate the brush would displace the water molecules and may increase the enthalpy. It is important to notice in this description that the displacement of water molecules from the brush to the bulk solution increases their entropy, and stabilizes the system. The antifouling properties of a coating hence arise from the delicate balance of enthalpy and entropy of the entire system. An outstanding consequence of this is that counter intuitively, too high grafting density may produce poorer antifouling properties in a brush.[28]

Finally, the behaviour of the protein itself adds to the complexity of the picture. The first step in irreversible protein adsorption is the dehydration of the protein and of the upmost layer of the surface: the gained entropy reduces the energetic barrier of the protein-surface interaction and brings the two in close proximity. The protein undergoes a partial irreversible denaturation when it loses the water. The presence of adsorbed water in and above the brush creates an environment in which the protein can retain its stable configuration. A protein in its stable state is likely to adsorb only reversibly on a surface and hence be easily detachable by small shear force.[28-30]

The force of the interaction of bovine serum albumin (BSA) with a polymer brush in water has recently been investigated by Inoue *et al.*[31] The work shows how the protein strongly adsorbed on a hydrophobic material, but not on a hydrophilic swollen brush. Chemically different brushes would repel proteins with slightly different efficiency, but this effect became almost undetectable when the brushes were thicker than a critical value. This confirms the importance of the brush thickness in reducing protein adsorption.

The considerations made so far assume an ideal brush composed of monodisperse chains. It is generally believed that good control over the MW distribution in polymer antifouling brushes is advantageous. Controlled polymerization gives a brush with high packing, i.e. high size exclusion capability, which is more effective in repelling biomolecules. Recently though, de Vos *et al.*[32] published a very interesting computer simulation on the interaction of proteins with mono- and polydisperse brushes. They analysed a comprehensive set of scenarios, with small and large particles which could interact or not with the brush itself. They described a monodisperse brush as having a constant local grafting density throughout its thickness (N.B. not brush density, which has a parabolic profile, but density of chains per area unit at any given distance from the substrate), while a polydisperse brush as having a local grafting density that decreases with the distance from the grafted substrate. In a polydisperse brush the inner layer is very dense because of the presence of short chains, while the outer layer is less dense, and is composed mainly of ends from the longer chains (Figure 1.3). Because of this configuration, small proteins can better penetrate the more loosely packed top layer of the polydisperse brush, while they cannot penetrate the monodisperse brush at all, which is densely packed even at the interface. The polydisperse brush though can outperform the monodisperse one when it comes to large particles such as very large

proteins or bacteria, which interact with the polymer by secondary adsorption. In this case, the repulsion on the particle is higher. This difference arises from the fact that the polydisperse brush can be compressed more than a monodisperse brush, thus giving a greater entropy loss. According to the model, this would overcome the enthalpic effect of lower steric repulsion between chains in a polydisperse brush. The model does not take into consideration any solvent (e.g. water) that may permeate the brush, so it is not the best representation of an antifouling surface. It gives though a new perspective to the use of grafted polymers in biological applications, indicating that having high MW polydispersities might not always be deleterious.

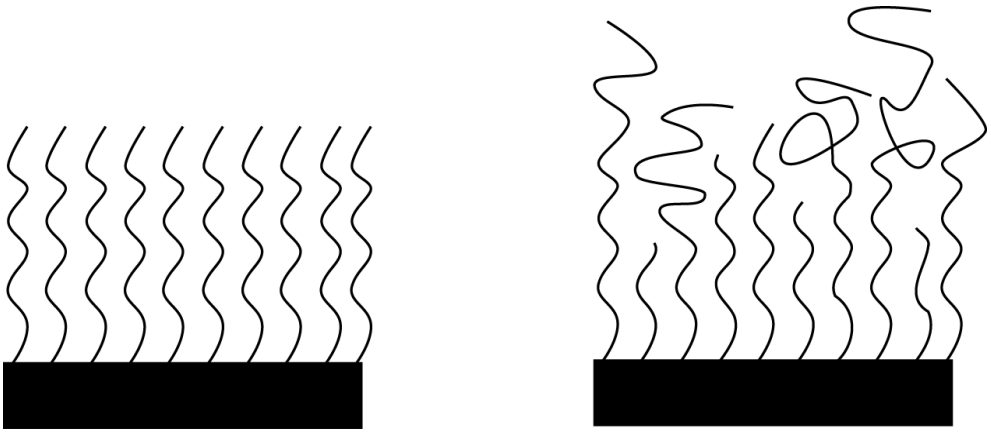

Figure 1.3 Schematic representations of (a) a monodisperse and (b) a polydisperse brush.

1.5 Grafting of polymer brushes

In Section 1.4, two main methods to prepare polymer brushes were mentioned. The attachment of fully grown polymer chains to a surface, i.e.

"grafting-to", and the growth of polymer chains from the surface, i.e. "grafting-from", will be described in this Section.

1.5.1 Attaching polymers onto surfaces: Grafting-to

The "grafting-to" strategy consists of two simple steps. In the first step polymer chains of the desired molecular weight (MW), bearing an anchoring group, are synthesized. This group may interact with the surface *via* non-covalent interactions, in which case it physisorbs on the surface, or form covalent bonds with the surface, in which case it chemisorbs. The second step consists of the deposition of the polymer monolayer on the selected surface from solution, and reactive attachment to it.

In physisorption, the anchoring group is chosen for its high affinity to the selected surface.[33] The solvent is chosen so to be a good solvent for the polymer chain, but a bad solvent for the anchoring group. In this scenario, the anchoring group spontaneously adsorbs on the surface, and a brush is formed. Physisorption relies on weak van der Waals or electrostatic interactions, and is therefore reversible. Examples are the case of Pluronics (triblock copolymers of polyethylene glycol and polypropylene glycol PEO-PPO-PEO) on hydrophobic surfaces, where the PPO section acts as the anchoring section,[34] and the case of polylysine-polyethylene glycol brushes, where the positively charged lysine backbone interacts strongly with negatively charged oxide surfaces.[35]

In chemisorption, the anchoring group is chosen for its ability to form a chemical bond with the surface. The most studied chemistries are the gold-thiol[36] and the silane-silicon oxide ones.[37] Chemisorbed layers are much more stable than physisorbed layers, allowing the use of different solvents and temperatures.

The grafting-to technique allows grafting of polymers with very well controlled MWs and polydispersities, because they can be synthesized in solution prior to adsorption. The technique though has also a number of intrinsic limitations, well described by Ruhe and Knoll.[38] First of all, the choice of functional polymers available is restricted by the need to have a highly reactive anchoring group. This reactivity is necessary to force the formation of a polymer layer on the surface. The anchoring group though can interact or form bonds (depending on its nature) with functional groups on the polymer chain, rather than the surface. For example, a chlorosilane functionality would readily react with any amine, hydroxyl or carboxylic acid moieties. Furthermore, the polymer's functional groups can interact with the surface, effectively competing with the anchoring group and forming layers on the surface that do not necessarily have the desired brush conformation. Finally, the grafting densities obtainable with the grafting-to technique are fairly low.[10, 39] This is because the polymer chains will tend to deposit on the surface in their most stable conformation, i.e. maintaining their unperturbed radius of gyration as much as possible. The consequence of this is that the surface will be rapidly covered in mushroom-like structures, which will prevent more polymer chains coming into contact with the surface. Additional chains from solution would have to diffuse through a high concentrated layer of polymer, which is a highly unfavourable process. In general, the higher the MW of the polymer, the lower will the grafting density achievable be because of the greater steric hindrance from polymer chains already grafted onto the surface. Because the anchored polymer chains do not need to stretch into the solvent to avoid each other, the layer thicknesses obtained by grafting-to are also limited.

A variety of techniques have been developed in the last decade to successfully increase the grafting densities obtainable with the grafting-to technique, including "cloud point" grafting, where a relatively poor solvent

is used to reduce the volume occupied by the molecules in solutions, allowing for higher grafting densities. Simply changing to a good solvent after the grafting process changes the conformation from collapsed to extended.[40-42]

1.5.2 Polymerizing chains from the substrate: Grafting-from

The "grafting-from" technique is also referred to as "surface-initiated polymerization". The surface is modified with a monolayer bearing a polymerization initiator. As in the grafting-to case, the monolayer can be immobilized *via* physical interaction or chemical bonds. The latter is widely preferred due to its stability. Because the initiator molecule is much smaller than a polymer chain, the grafting densities achievable are much higher than in the grafting-to approach. Once the initiator is immobilized on the surface, a polymerization is carried out, growing polymer chains from the initiating sites. The diffusion of the monomer to the initiator is not hindered in this system, and densely packed polymer chains can be grown from the surface. In good solvent conditions, the grafted chains will stretch out from the surface, making the growing ends readily available for more monomer to be added.

The high grafting densities achievable by grafting-from result in unique properties in the resulting brush, which are described by a concentrated regime (see Section 1.4.1). The close packing of tethered chains produces a polymer layer that is highly resistant to compression, which is very important in, for example, nanoparticle dispersability.[20] The limited free volume between chains can also be used for their size exclusion properties towards solutes, in chromatography[22, 43] and in biomedical applications. This latter field was discussed in Section 1.4.2.

The surface-initiated polymerization can be performed by different methods, but the general preference is towards reversible-deactivation polymerization techniques. Uncontrolled polymerizations, such as free radical polymerization, can achieve high grafting densities and brush thicknesses, but the resulting brush is highly polydisperse, and its mechanical and physicochemical properties are strongly influenced by the longer chains, which may form a semi-dilute outer fringe and mask the underlying densely packed brush.[22]

In this Thesis, a reversible-deactivation polymerization approach was taken because it allows high control of the molecular weight distribution of the polymer chains, and the retention of an active ("living") site at the chain end. This living end can be used to extend the polymer backbone with new monomer, to elongate the homopolymer chain or to create block copolymers, to functionalize it or to perform branching reactions. These features are the main distinctions between a reversible-deactivation radical polymerization and a free radical polymerization. In a free radical process, the radical lifetime is very short, and ends by a radical-radical combination (termination). In a reversible-deactivation radical polymerization, the radical species reversibly react with certain additives. If this equilibrium is much faster than termination, the radical effective lifetime (i.e. non terminated radicals) can be extended to the duration of the experiment.

In the following, two types of reversible-deactivation polymerization will be discussed: reversible addition-fragmentation chain transfer polymerization (RAFT) and atom transfer radical polymerization (ATRP). RAFT and ATRP have been widely investigated in the preparation of brushes of controlled MW.[22, 44, 45] The main advantage of a reversible-deactivation technique is that theoretically all the chains grow at the same time, giving dense, well defined brushes. Additionally, each chain bears a "living" end that can be post-functionalized, i.e. react further at a second

stage by adding different functional groups. The main limitation of grafting-from is the somewhat limited control on the polymer MW compared to grafting-to. The example of surface-initiated ATRP will be considered here, but similar conclusions can be applied to all reversible-deactivation radical polymerizations.

1.5.3 Reversible addition-fragmentation chain transfer (RAFT)

RAFT was developed by Moad and co-workers[46, 47] at the Commonwealth Scientific and Industrial Research Organization (CSIRO). Zard and co-workers, in collaboration with Rhodia,[48] independently developed a technique which they christened macromolecular design *via* the interchange of xanthates (MADIX). This reaction is mechanistically identical to RAFT, but differs in the type of chain transfer agent used (xanthates instead of non-oxygenated thiocarbonyl-thio derivatives). Shown in Figure 1.4 are a RAFT chain transfer agent and a xanthate. The leaving group R allows the formation of a radical species on the sulphur, and determines the kinetics of initiation, while the Z group determines the stability of such a radical.

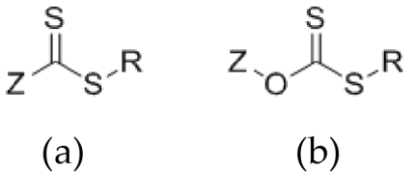

Figure 1.4 Structures of (a) a generic RAFT agent and (b) a xanthate.

Summarised in Figure 1.5 is the mechanism of RAFT polymerization. In the initiation step (I), the monomer is forced to form a radical (thermal or chemical initiation), which reacts with other monomers to form a short

macroradical. A conventional free radical polymerization would proceed this way until two macroradicals couple and no further growth is possible.

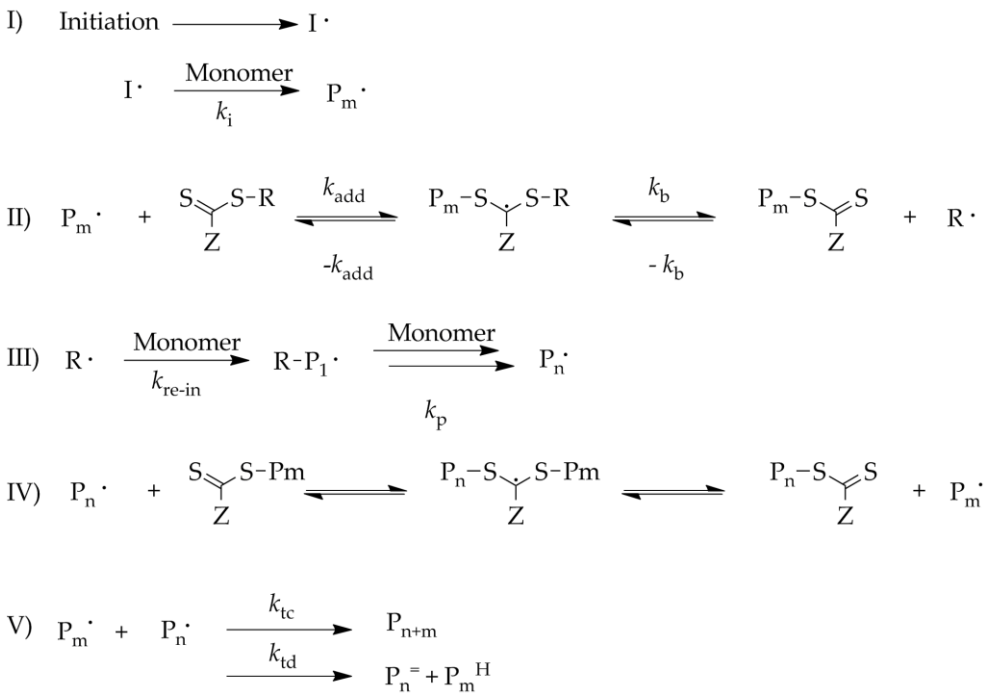

Figure 1.5 Reversible addition-fragmentation chain transfer (RAFT) polymerization mechanism. (I) A radical initiator starts the growth of macroradicals.(II) All the macroradicals are captured by a RAFT agent to form metastable radical species, which eventually fragments to release the R group. (III) The radical R group can initiate the growth of more macroradicals. (IV) A new addition-fragmentation equilibrium is established, among free and RAFT capped oligomers. (V) Eventually, the concentration of polymer chains is high enough to promote termination.

In RAFT, the more reactive di-thiocarbonate (instead of the monomer) combines with the macroradical, to form a more stable radical species (II). The RAFT agent has here the crucial role of being reactive enough to quickly catch and stabilize all the oligomeric radicals, but to eventually fragment to release the R group. The now free R group can then act as an initiator (III), and add monomers to form yet more macroradicals. The addition and asymmetric fragmentation equilibria between radical oligomers and RAFT

capped oligomers repeat themselves over and over (IV) until all the monomer is consumed, and the chains can only react among themselves in the termination stage (V). In brief, all the macroradical chains are able to add only a few units at a time, before forming a "dormant" species with a RAFT agent. This oscillating equilibrium leads to the formation of chains of very similar molecular weight.

RAFT was used in this work to produce a polymer of controlled MW bearing ATRP initiators on each monomer. Control over the MW of this macroinitiator was needed because of the influence of the polymer MW on the pattern obtained upon dewetting. The work is described in detail in Chapter 5.

1.5.4 Atom transfer radical polymerization (ATRP)

ATRP was developed independently by Matyjaszewski and co-workers[49] and Sawamoto and co-workers.[50] A recent review on ATRP techniques has been published by Ayres.[51] As in RAFT, a high degree of control over the polymerization kinetics is achieved in ATRP by introducing a species that can quickly and reversibly react with the growing oligomeric chains. In ATRP, such species is a metal complex bearing a halide ligand. Again, the choice of this species is very critical: it has to be very reactive in the initiation step, but allow reversible fragmentation for chain propagation. Presented in Figure 1.6 is the mechanism of ATRP. The initiator species has a labile halide that can easily detach *via* homolytic bond cleavage. The metal complex extracts the halide from the initiator in a redox process which oxidizes the metal, and leaves the initiator with a radical on which a few monomers can add. The halide on the metal complex then quickly reacts with the growing oligomer and stops monomer addition.

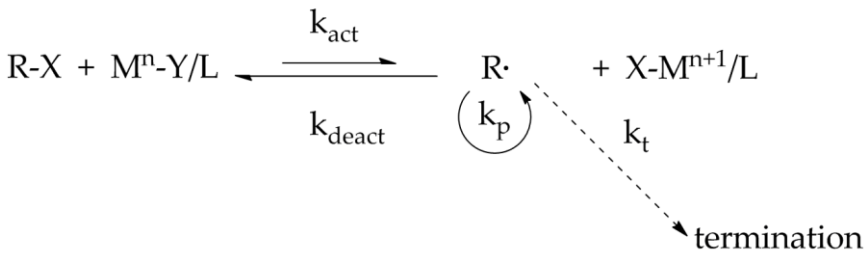

Figure 1.6 Atom transfer radical polymerization (ATRP) mechanism. The carbon-halogen bond in the halogen-containing initiator (R-X) is cleaved by the metal catalyst coordinated to the appropriate ligand (L). The resulting radical species can add a few monomers before being re-capped by the halogen (X). The equilibrium continuously un-caps and re-caps the growing chain adding only a few monomers at each cycle. Eventually the polymer concentration becomes high enough to promote termination.

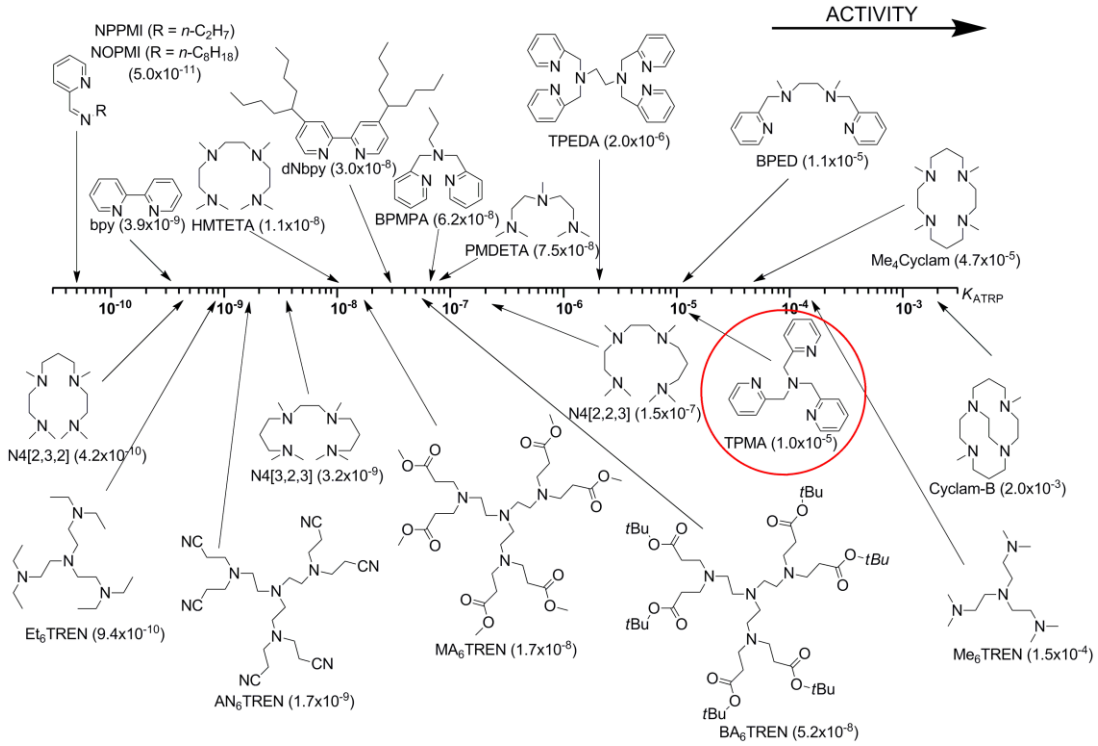

Figure 1.7 Common ligands for copper in atom transfer radical polymerization ATRP, adapted from reference 52. The ligand used in this work, tris-(pyridyl methyl) amine, is circled in red.

In brief, the halide quickly "un-caps" and "re-caps" the growing chain, allowing all the radicals to add only a few monomers at a time. The catalyst complex continuously switches between its activator (reduced) and deactivator (oxidized) form.

The polymerization equilibrium constant, K_{atrp}, is given by the ratio between the rates of activation and deactivation of the catalyst (K_{act}/K_{deact}). A small K_{atrp} gives a very slow polymerization, a large K_{atrp} gives a concentration of radicals which is too high, facilitating termination and resulting in poor control over the polymer molecular weight. Fine tuning of the K_{atrp} is possible by choosing the appropriate ligand for the catalyst.

Presented in Figure 1.7 is a selection of ligands for copper, and their respective K_{atrp} values. Copper is one of the most commonly used catalysts in ATRP, because it is inexpensive and allows for the polymerization of a wide range of monomers in a wide range of solvents.[53, 54] In this Thesis, tris(pyridyl methyl)amine (TPMA) was used because of its high ATRP activity and low susceptibility to side reactions and displacement from the copper ion.

1.5.5 Low catalyst concentration ATRP

One of the main drawbacks of ATRP is the instability of the copper catalyst. The control of the process is obtained by a careful balance between activation and deactivation. The concentrations of the activator and deactivator forms of the catalyst are therefore critical. Copper (I) is susceptible to oxidation during storage, as well as in solution during polymerization, especially in aqueous solutions, which can be difficult to completely deoxygenize. Matyjaszewski and co-workers have solved this problem in their technique named activators generated by electron transfer (AGET).[55] The idea is to utilize only the stable oxidized form of the catalyst

in the experimental set up, and to eventually reduce a portion of the oxidized form *in situ*, using a reducing agent. The process then proceeds following the conventional ATRP mechanism. Careful choice of the amount of reducing agent used in the reaction allows obtaining the desired activator/deactivator ratio, as well as scavenging any oxygen left in solution after deoxygenating. The electron transfer process does not interfere with any other aspect of the polymerization. Presented in Figure 1.8 is the mechanism of AGET ATRP.

In this Thesis, AGET ATRP was used to graft a protein-repellent polymer brush from a substrate. The system was used because of its robustness and ease of use.

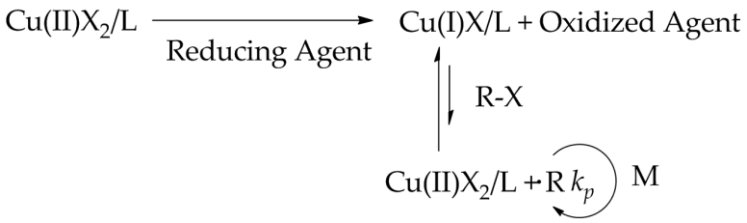

Figure 1.8 Mechanism of activators generated by electron transfer atom transfer radical polymerization (AGET ATRP). Only the deactivator species is added to the reaction mixture. The deactivator is then partly reduced in situ to give the optimal activator/deactivator ratio. The process then proceeds as conventional ATRP.

A second major issue in ATRP is that when a termination event occurs, two molecules of the oxidized metal catalyst accumulate in the system. As the deactivator accumulates, the polymerization equilibrium is shifted to the left, proceeding to the point where the reaction stops completely. In order for the reaction to proceed to completion, a large amount of catalyst (e.g. catalyst to initiator ratio = 1:1) has to be used. The metal must be removed from the reaction mixture containing the product,

which is difficult and expensive. This limitation was overcome after Matyjaszewski and co-workers, who were working with a copper bromide complex, discovered that the ATRP polymerization rate does not depend on the absolute catalyst concentration, but rather on the ratio of the concentrations of activator and deactivator species.[56] Therefore, if the deactivator is constantly regenerated into the activator, the initial catalyst concentration can be very low. One of the main techniques developed on this basis is named activators regenerated by electron transfer (ARGET).[56, 57]

The regeneration mechanism used in ARGET ATRP is shown in Figure 1.9. The choice of the compound used for regeneration is critical, because it will directly affect the ratio between the catalyst activator and deactivator species. Continuous reduction allows for polymerizations to be conducted in the presence of limited amounts of oxygen, i.e. without deoxygenating the mixture. In a sealed vessel, the reducing agent will first consume all the oxygen present, and then reduce the catalyst. After consumption of the oxygen in the sample, which appears as an induction period, the polymerization will proceed.[58]

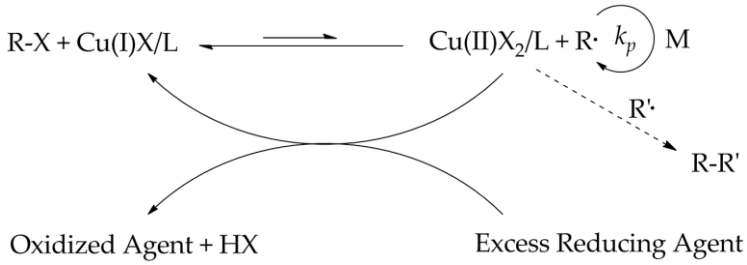

Figure 1.9 Activators regenerated by electron transfer atom transfer radical polymerization (ARGET ATRP) mechanism. Similar to AGET ATRP, the deactivator is the only species added to the reaction mix. A reducing agent is used to reduce the deactivator to the activator specie, and continuously reduce any excess deactivator species formed.

ARGET ATRP was at first employed in the present work to attempt the preparation of a polymer brush by grafting-from. The reaction could not be properly controlled, so the choice of polymerization method was shifted to AGET ATRP. Details on the attempts to use ARGET ATRP are reported in Chapter 5.

1.5.6 Surface-initiated atom transfer radical polymerization (SI-ATRP)

Surface-initiated graft polymerizations are processes confined to a small surface area. In SI-ATRP, the concentration of initiator and capping (deactivator) species are much lower than what would be used in a solution polymerization. Once all the initiators present on the surface have reacted with an activator, a minute amount of deactivators is formed. The polymerization can only be controlled if such species can quickly re-cap the growing polymer chains in the ATRP equilibrium. However, in this scenario, it is likely that a number of the deactivating species will diffuse away from the surface. The likelihood of a deactivating species encountering the surface again is greatly reduced compared to a homogeneous ATRP reaction in solution, and this strongly affects control of the polymerization from the surface. Matyjaszewski and co-workers improved the control in SI-ATRP of styrene and methylacrylate by adding a certain amount of deactivator in the reaction mixture, to ensure a reasonable concentration of this species at the surface.[59] Fukuda and co-workers[60] were able to obtain control in surface-initiated ATRP of methylmethacrylate by adding an excess of free initiator in the reaction mixture. This technique has two main advantages: it improves the control over the MW, because many deactivators are formed in solution, and it provides a large amount of free chains in solution. The formation of these free polymer chains in solution can give important information about

the chains grafted on the surface, assuming that the solution and the surface polymerizations progress in the same way.

The validity of this assumption has been highly debated, particularly because of the experimental difficulty of analysing the MWs of the surface-initiated grafted chains. A few groups have reported controlled SI-ATRP on colloidal particles.[61-63] The grafted chains were cleaved from the particles and analysed by size exclusion chromatography, and showed low polydispersity and MWs close to those obtained in homogeneous solution polymerizations under the same conditions. It should be noted though, that in the studies of Pyun *et al.*[62] and von Werme *et al.*,[63] the MWs of the grafted chains were observed to be higher than those obtained in solution at low degrees of polymerization (N). The two sets of data converged for higher values of N. Ohno *et al.*[61] did not report data for low N, and did not observe differences between the MWs of chains prepared in solution and on surfaces. The difference in MW between grafted and free polymer can be explained by low initiation efficiencies in the early stages of the polymerization, due to overcrowding of the initiators present on the surface. The effect becomes less significant for higher values of N, because the effective surface area of the grafted colloid increases, reducing the radical density on the surface. This is consistent with computer simulations recently reported by Turgman-Cohen and Genzer,[64] which predict higher polydispersities in surface-initiated "controlled" radical polymerization for higher grafting densities. This being said, the dynamics of surface confined polymerizations are far from being fully understood. A number of different groups[65-67] have focused their attention on grafting from porous materials. They reported that the MW of grafted chains was lower than those obtained for free chains formed in solution, and explained the results by claiming that the confinement of the growing chains within the pores limited their growth rate, but did not affect the polydispersity of the grafted chains. This is in contradiction with the

scenario described above, since the convex shape of the grafting surface should produce higher crowding of initiating sites compared to flat surfaces. This, according to Turgman-Cohen and Genzer's model, should produce high MW, polydisperse polymer chains. The assumption that free and grafted chains behave in a similar way must therefore be taken with caution, and might be valid only in some systems. All things being considered, the presence of solution initiators during surface-initiated polymerizations is a powerful stratagem for both enhancing level of control over MW and polydispersity in surface-initiated polymerizations, as well as providing some insights into the properties of the grafted chains.

As well as providing a certain degree of control over the grafting reaction, surface-initiated ATRP produces "living" chains, which can be easily extended or post-functionalized *via* their living end. ATRP produces polymers with a halide end cap, typically a chlorine or bromine atom. The halide cap can be modified to add a terminal functional group on the polymer chains. A very common choice is the use of an azide salt to obtain an azide functionalized end group. This can then be used for alkyne-azide "click" reactions.[68] Other strategies include the reaction of the bromine cap with a thiol terminal functional group,[69, 70] the radical addition of an allyl-terminal functionality[71] and the transformation of the halide end group to a thiol group using thiourea; the thiol end can then be used in thiol-ene click couplings.[72]

The main advantage of the grafting-from technique is its applicability to any type of substrate. As long as initiators are present on the surface at a sufficient surface concentration, a polymer brush can be grown. In Chapter 5, the combination of grafting and patterning by dewetting will be described. The patterned polymer coating utilised was engineered so to bear the initiator moieties that are required to graft a polymer brush from the surface. The grafted polymer was used to post-modify the dewetted pattern in order

to reduce the non-specific adsorption of protein molecules in the areas surrounding the protein-adsorptive domains. This provided surfaces that contained localised domains on which cell-adhesive proteins could be selectively adsorbed.

1.6 Interaction of polymer coatings with cells

In Section 1.1, the concept of controlled protein adsorption on a surface in order to control cell response was introduced. As mentioned, the microenvironment presented on a surface can direct cellular response. Recent reviews on cell behaviour on micro- and nanopatterned surfaces were published by Tay *et al.*,[73] Choi *et al.*,[74] and Tanaka.[75]

A significant proportion of surfaces that actively interact with cells possess patterns that can provide a heterogeneous set of cues. Often extra cellular matrix (ECM) proteins, which are component of the biological environment with which cells interact in a living organism (or a substitute which provides similar cues to the cells), are immobilized on a surface in patterns with different geometries and length scales. A detailed introduction to patterning techniques can be found in Section 1.7.

Cues provided on patterns with different length scales can influence cells differently. A pattern with dimensions much smaller than the size of the cell under study, typically with features of hundreds of nanometers to several microns, can interact with a variety of receptors within a single cell. For example, Chen *et al.*[76] observed that patterns of ordered pillars of different sizes had a different effect on the behaviour of a single cell, which would either adhere and spread, or die. Detailed reviews on similar experiments were published by Flemming *et al.*[77] and Lehnert *et al.*[78]

Tensegrity theory explains the response of a cell to its microenvironment using cell mechanotransduction.[79-82] In brief, one of the ways in which cells interact with their environment is *via* proteins called integrins. These receptors are expressed by the cell as membrane proteins that can act as probes when the cell comes in contact with a surface. If ECM proteins that have exposed cell-binding domains are present on the surface, the integrins will bind to them, and create tension in the cell actin framework (actin is a structural protein often found in cells). Such mechanical input is transduced in chemical inputs within the cell, which ultimately determine its behaviour. A cell often has a rounded shape when suspended in a medium. If the cell adheres on a surface it tends to spread, creating focal adhesion points where clusters of integrins and other proteins attach to the surface. These focal adhesion points are used as "tactile" peripherals to sense the properties of the surface, such as elasticity and chemical cues.[83, 84] Once this information has been acquired, the cell can pull itself from the focal point, to spread further or migrate.[85] The process is bidirectional: the cell often creates tension on an adhesion point to modify the ECM to suit its needs.[83] By controlling the localization of ECMs on a surface *via* patterning, it is therefore possible to control the position of possible focal adhesion points, and subsequently induce a specific cell response.

The response of a cell to the interaction with a surface is a very complex and largely unknown process, and varies from no adhesion whatsoever (which often means cell death, if the particular cell type needs to adhere to exploit its functions; e.g. tissue cells like fibroblasts) to normal proliferation, to over proliferation and formation of an uncontrolled mass.[86] Many examples can be found in the recent literature. Arnold *et al.*[87] demonstrated control over the spreading of osteoblasts, i.e. cells that produce bone tissue, on patterns of nanoparticles deposited on a surface,

having a gradient of interparticle distance. They demonstrated that the cell spreading was greater where the distance between the cell-adhesive particles was larger. Dalby *et al.*[88] worked with mesenchymal stem cells (MSCs), which are multipotent cells that can differentiate in bone, cartilage muscle, connective tissue and fat cells. They introduced MSCs in bone marrow as being able to often react to metal implants by producing soft tissue rather than bone, which leads to mechanical failure of the implant-bone joint. They investigated the effect of nanoscale topographical features on the differentiation of MSCs. They were able to obtain bone formation (mineralization) on an array of randomly displaced square pits, while reduced cell adhesion was observed on the same square pits but arranged in a hexagonal packing. This effect demonstrates the level of complexity of the cell-substrate interaction, and how nanopatterns have the potential to solve such puzzles. Mendoça *et al.*[89] also worked towards a better integration of metal implants with bone tissue. They reported that the introduction of a nanoscale roughness on an otherwise flat titanium surface increased the differentiation of MSCs in bone tissue. They also investigated the introduction of different chemical cues, and observed that alumina impurities combined with nano-roughness gave the highest production of bone tissue on the metal surface. More examples of nanopatterned surfaces for cell response control include nanowire arrays,[90] nanodot arrays[91] and films of phase separated block copolymers.[92] A recent review on the effect of nanopatterns on cell attachment was published by Shekaran and Garcia.[93]

In a different manner to a nanoscale pattern, a microscale pattern can immobilize whole cells in each domain. The patterns can be used as an analytical tool for single-cell studies, or for colony size dependent studies, depending on the area of the pattern domains. In this sense, microwells are more effective than patches, as they can trap the cells as a result of their three-dimensional shape,[94] but both two-dimensional and three-dimensional

patterns are widely employed. Mei *et al.*[95] used a robotic stage to print micrometric patches of different monomers on a surface, which were eventually polymerized by exposure to UV radiation. These massive arrays were then used to investigate the effect of each monomer type on cell adhesion and proliferation with very high throughput. In a similar fashion, Ceriotti *et al.*[96] printed patches of different proteins with different surface coverage to investigate the effect of protein type and density on cell behaviour. They reported, for example, that fibronectin promoted neural stem cell spreading, laminin allowed adhesion but only small degrees of spreading, and the use of albumin resulted in no adhesion. Studies like this are very important for optimizing cell culture conditions. High throughput testing and analysis are possible thanks to the miniaturization accessible with microarrays.

Micro-patterned surfaces can also be used to grow cell co-cultures with controlled homotypic (same type) and heterotypic (different type) cell interactions.[97] The behaviour of a cell is strongly influenced by the signals that it receives from the substrate as well as the signals it receives from neighbouring cells. A significant example of patterned cell co-cultures was reported by Hannachi *et al.*[98] They were able to produce sheets of patterned cell co-cultures, which could be detached from the culture substrate by the use of thermoresponsive polymer graft layers. Below the lower critical solution temperature (LCST), a thermoresponsive polymer is soluble in a solvent. Increasing the temperature to above the LCST results in desolvation of the polymer, which becomes insoluble. In the work of Hannachi *et al.*,[98] poly(*N*-isopropyl acrylamide) brushes were in a collapsed, hydrophobic state above the LCST, so that the proteins which mediate cell attachment could adsorb, resulting in cell attachment. Rehydration of the polymer layer and subsequent swelling below the LCST resulted in release of the cells. Using a pattern of two polymers with different LCSTs allowed the authors to

selectively pattern two types of cells, and eventually detach the entire cell sheet. The authors emphasised the fact that the cells were harvested along with the ECM proteins they secreted during the seeding stage. This is important in order to maintain the viability of the harvested sheet. The cell sheets can be stacked to create three-dimensional constructs for tissue replacement, as in the example reported by Sekine *et al.*[99] The authors employed three-dimensional constructs of endothelial cells and cardiomyocites to replace damaged cardiac tissue. Endothelial cells constitute the internal layer of all the blood vessels, while cardiomyocites constitute part of the cardiac muscle wall. The authors not only observed vascularisation of the grafted tissue, but also that these newly formed blood vessels bridged to connect with capillaries of the host heart. The degree of vascularisation of the graft could be controlled by changing the density of endothelial cells in the co-culture cell sheets.

Otsuka *et al.*[100] reported the use of arrays of plasma etched holes in a poly(ethylene glycol) background to grow co-cultures of hepatocytes and endothelial cells. Hepatocytes are a major component of the liver and are widely used to screen compounds for toxicity in the pharmaceutical industry. The authors were able to grow three-dimensional spheroids that behaved like miniaturize artificial livers. They suggested that the array of spheroids could be used as a biosensor to detect biologically active threats, or that the free spheroids could potentially be seeded on a three-dimensional scaffold to engineer a full scale liver.

The work described so far was possible only through the control of the homotypic and heterotypic interaction achievable in patterned cell co-cultures. Cell-cell interactions seem to be a fundamental parameter in the control of cell behaviour. Tang *et al.*[101] investigated the influence of cell-cell contact on stem cell differentiation, using patterns of holes with different degrees of contact. They observed an enhanced differentiation with

increased cell-cell contact, as well as a linear relationship between differentiation and coordination number per cell, i.e. the number of partners a cell is in contact with at any given time. This study helped the understanding of the dynamics that take place in a topographically controlled co-culture, where the cell-cell contact could be finely tailored.

A separate approach to tissue engineering involves the use of three-dimensional scaffolds to mimic the extra cellular matrix found *in vivo*.[102, 103] Three-dimensional scaffolds are commonly prepared by stereolithography,[104] electrospinning,[105] and cross-linking to form hydrogels,[106] and their mechanical and chemical properties can be tailored to induce cell growth to produce implantable tissue replacements. Although three-dimensional scaffolds may mimic the architecture of extra cellular matrices in ways that two-dimensional patterns my never do, they have a few intrinsic limitations. The spreading of cells in an intricate scaffold cannot be readily controlled, while this is easily achievable on two-dimensional patterns with cell-adhesive geometries of defined shape and size. Spreading, as already explained, directly influences cell behaviour. Furthermore, the degree of homotypic and heterotypic contact between two different types of cells in a co-culture can be finely controlled in a two-dimensional pattern, while it is challenging to achieve in a three-dimensional scaffold. Cell-cell contact also strongly influences cell behaviour. Finally, three-dimensional scaffolds are not designed for applications such as single-cell studies and high throughput essays.

1.7 Patterning of surfaces

As discussed in Section 1.6, patterned surfaces are often used as substrates for controlled cell response. A surface bearing a chemical and/or

topographical pattern offers a set of signals to cells, which can induce a specific response.

A number of techniques have been used to pattern surfaces for biomedical applications.[107, 108] The most widely applied technique for patterning biological molecules and cells is micro-contact printing (μ-CP), developed by Whitesides and co-workers.[109, 110] The technique employs an elastomeric mould (usually made of poly(dimethylsiloxane), PDMS) to stamp patterned self-assembled monolayers (SAMs) on a surface. Typically, the mould is wetted with a solution of thiol-terminal molecules; the stamp is then put in contact with a flat gold substrate, where the thiols bind covalently in a pattern dictated by the shape of the mould (Figure 1.10).

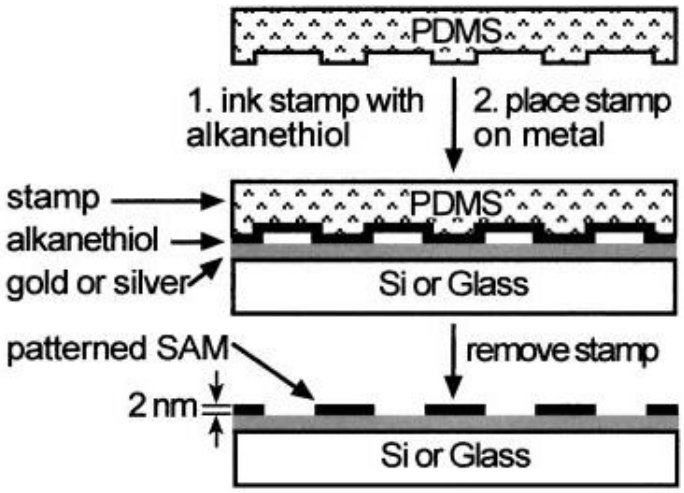

Figure 1.10 Schematic of patterning of thiol self-assembled monolayers by micro-contact printing. Adapted from reference 111. A PDMS stamp was used to print a pattern of thiol-terminated molecules on a gold-coated glass surface.

This technique meets the needs of the biology community in a number of ways: it has a lateral resolution of up to 30 nm, which is small enough for any cell application, it can be used to pattern large areas (up to 50 cm^2), and it uses non toxic reagents and mild conditions. A review from

Whitesides and co-workers describes in detail the numerous applications that this technique has in biological studies.[111] A downside of μ-CP is that although the process itself is based on very inexpensive materials, it still suffers from high costs arising from the fabrication of the PDMS moulds. These stamps are usually prepared by curing the PDMS precursors on a master etched by electron beam or ion beam lithography, techniques that require expensive equipment and highly skilled personnel. It is also very difficult to pattern non-flat surfaces using μ-CP.[112]

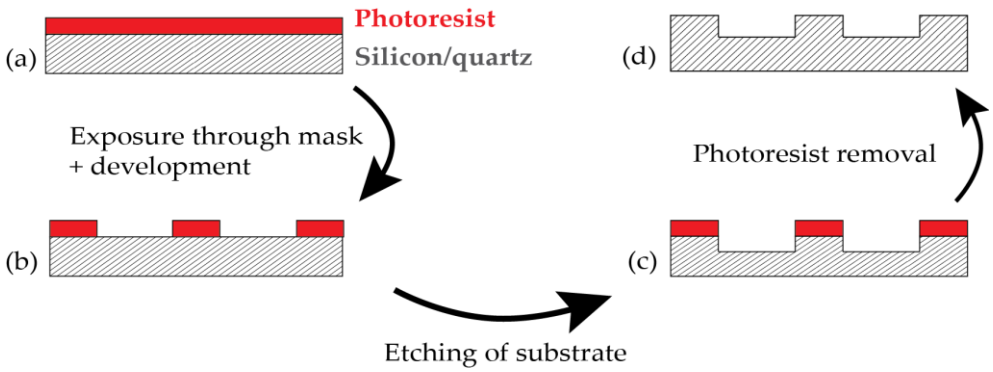

Figure 1.11 Schematic of patterning by photolithography. (a) The substrate to be patterned is coated with a UV sensitive polymer film (photoresist). (b) The photoresist is exposed to UV light through a patterned mask. The photoresist can either be cured by the UV or degraded by the UV. Upon washing, uncured or degraded polymers are eliminated. (c) An etching solution is used to selectively etch the substrate where no photoresist is present. (d) After the etching, the photoresist is removed with an appropriate solvent, and the substrate is left with a topographical pattern.

A second very popular patterning technique is photolithography. A layer of UV reactive material (the photoresist) is cast on the desired flat substrate, and then irradiated with UV light through a mask. A "positive" photoresist will be cured in the areas where the UV light is not blocked by the mask. After the exposure, the photoresist is developed, i.e. the un-cured material is washed away, leaving a pattern replicated from the one on the

mask. A "negative" photoresist will not be cured but degraded in the areas where the UV light is not blocked by the mask. The degraded material is washed away, leaving a pattern which is complementary to the one on the mask. At this point the substrate can be selectively etched through the pattern (Figure 1.11). Modern equipment can achieve 65 nm resolution patterns on one hundred wafers in one hour (wafer diameter 300 mm). Again, this technique suffers from high costs involved in both the manufacturing of the mask and the extremely expensive equipment used. Conformal patterning is also not achievable by photolithography.[112]

In this Thesis, a novel patterning approach was developed, based on self-assembly of polymer thin films to produce coatings for the control of cellular responses. Such coatings could easily be applied on non-flat surfaces.

1.7.1 Thermodynamics of liquids: wetting and dewetting

In most studies on the thermodynamics of wetting and dewetting films, polymers are used. In synthetic oil-derived polymers a common form is a glass state. The transition between a low viscosity (liquid-like) and a high viscosity (solid-like) form happens in a small temperature range. A glass transition temperature (T_g) is defined to identify the mean transition point from solid to liquid melt. Polymers above their T_g behave like liquids, and if the chains are long enough to entangle in a melt, viscoelastic, non-Newtonian behaviour is often observed. The entanglement of polymer chains is possible only if the chain length is above a critical value; one may think of it like the minimum length necessary to form a loop rather than a semi-stiff rod. The molecular weight of a polymer chain that can entangle is referred to as entanglement molecular weight or entanglement length, *Ne.*

Polymer melts are the candidate of choice for dewetting experiments because their viscosity, and hence the timescale of the dewetting process, can be easily controlled by tuning the annealing temperature. Polymers can be easily spin coated as thin films, and are non-volatile. Finally, polymers such as atactic polystyrene are heavily used because they are readily available, inert and do not crystallise.

It is common experience to observe different wetting phenomena in everyday life. Water will cover clean glass to form a film, but it will retract from the bottom of a Teflon pan, and form droplets. The behaviour of a liquid on a solid surface can be predicted by the spreading parameter S, which measures the difference in surface energy per unit area between the dry and wet substrate. The spreading parameter can be related to the surface tensions at the three interfaces (solid/liquid, liquid/vapour, solid/vapour) by Equation 1.5:

$$S = \gamma_{SV} - (\gamma_{SL} + \gamma) \tag{1.5}$$

where the surface tension at the liquid/vapour interface has no subscript.[113]

The sign of the spreading parameter describes the wetting regime. A positive value of S indicates that the liquid spreads completely. The film will spread and continue thinning until its thickness reaches a critical value. At this point the film will stop spreading and form a flat "pancake-like" film, which coexists with the dry substrate. A negative value of S indicates partial wetting or non-wetting, where the dry substrate coexists with large droplets of the liquid.

The wetting properties of a surface are macroscopically defined by the contact angle of a droplet of a given liquid, usually water, placed on it. Described in Figure 1.12 is the contact angle of a liquid in three different

wetting regimes. A liquid that completely wets the surface has a contact angle of zero. If the liquid cannot wet the surface at all, the contact angle is 180°. In real systems, the most common state is that of partial wetting, with contact angle 0° < θ < 180°. Surfaces on which the contact angle of water is θ > 90° are called hydrophobic, and those with θ < 90° are hydrophilic.

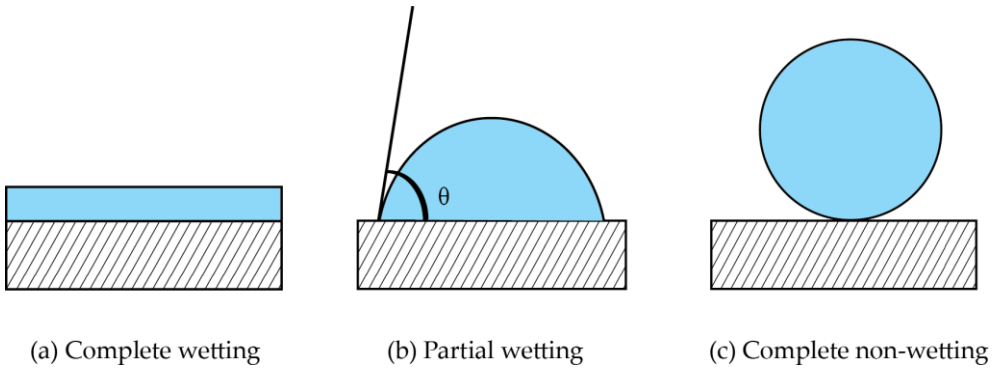

Figure 1.12 Schematic of three situations of wetting of a liquid on a solid surface. (a) In complete wetting, the liquid spreads to cover the surface, and the contact angle is zero. (b) In partial wetting, the liquid collects in droplets with contact angle between zero and 180°. (c) In complete non-wetting, the liquid does not spread at all and has a contact angle of 180°.

The equilibrium contact angle of a liquid on a solid can be determined using Young's equation, as described below:

$$cos\,\theta = \frac{(\gamma_{SV} - \gamma_{SL})}{\gamma} \tag{1.6}$$

Equation (1.6) can be rewritten in light of Equation (1.5):

$$S = \gamma(cos\,\theta - 1) \tag{1.7}$$

The interaction of a liquid with a solid surface, and the resulting macroscopic effects, i.e. wetting, arise from the combination of long and

short range forces, mainly steric repulsion, van der Waals and electrostatic interactions.[10] In this discussion the liquid and solid are considered neutral, so electrostatic interactions are neglected to simplify the description of the system. This approximation is not valid when the liquid can charge the solid/liquid interface, such as in the case of water.

Steric repulsion is a short range force, which arises from the superimposition of electronic shells. In the case of two planar surfaces it varies as $1/r^8$. Van der Waals forces arise from induced dipole-dipole interactions, and are instead long range forces. They decay as $1/r^2$, and affect significantly the stability of liquid films with thicknesses up to approximately 100 nm.[114]

The effective interfacial potential, $\phi(h)$, describes wettability in terms of both short and long range forces, effectively predicting the liquid macroscopic behaviour based on the forces that act on the microscopic scale. The potential describes the free energy per unit area necessary to bring two surfaces from infinity to a certain distance h apart. This means that the potential describes liquid films of thickness h, sandwiched between the solid surface and the vapour phase. The second derivative of the interfacial potential ($\phi(h)''$) indicates wether a liquid film is stable or not on a solid surface. When $\phi(h)'' > 0$, the film is stable and wets the surface, while when $\phi(h)'' < 0$, the film is unstable and dewets from the surface.

In Figure 1.13 the interfacial potential is plotted as a function of the film thickness, i.e. the separation between solid and vapour interfaces for a polystyrene (PS) thin film onto a silicon wafer.[114-116] Curve (a) shows the potential profile for a PS film on a silicon wafer with no silicon oxide layer. The minimum interfacial potential is achieved at infinite thickness, hence no dewetting occurs. In case (b), the silicon wafer is coated with a 1.7 nm thick silicon oxide layer, while in case (c) the silicon wafer is coated with a 190 nm thick silicon oxide layer. The presence of the silica affects dramatically the

stability of the liquid film on the substrate. In cases (b) and (c), the liquid film is unstable on the solid surface because the minimum potential is reached when the separation between the vapour and the solid is a finite value h^*. This means that films of thickness greater than h^* will spontaneously thin down to this critical value. In practical scenarios, where the starting point is a flat liquid film of finite thickness h, the film will dewet from the solid surface. The liquid will do this by nucleating holes in random positions, according to a Poisson distribution, that will grow in time and eventually coalesce. The resulting network of liquid cylinders will then break down into isolated droplets with equilibrium contact angle θ, leaving on the solid surface only a very thin residual film of thickness h^*.[113]

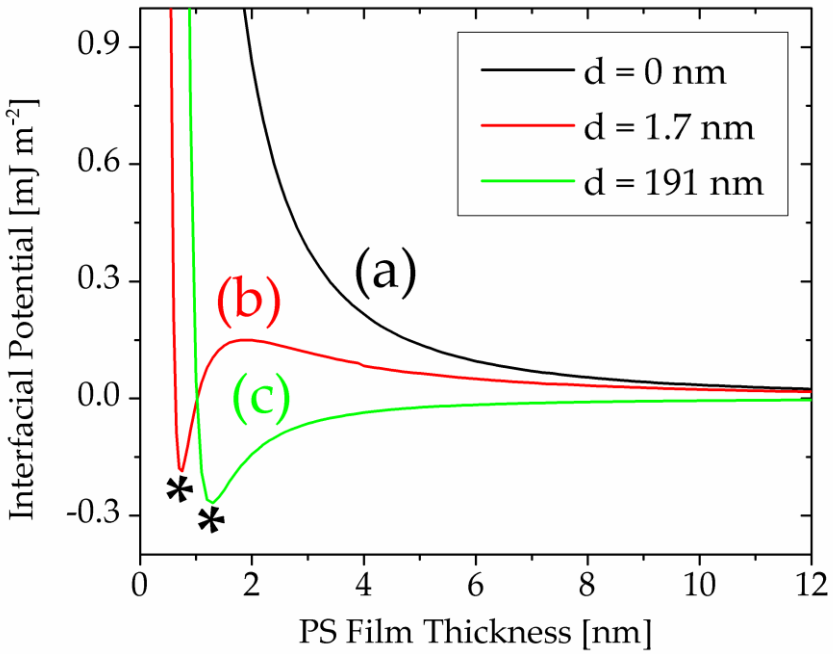

Figure 1.13 Calculated interfacial potential for a polystyrene film deposited on silicon substrates with silicon oxide layers of different thicknesses, which alter the film stability. Curve (a) represents the case of a stable film, curve (b) represents the case of a metastable film and curve (c) represents the case of an unstable film. The equilibrium film thickness, h, is indicated with stars for curves (b) and (c). The legend reports the thickness of the SiOx layer for each system.*

The main difference observable between curves (b) and (c) is that in the first case, a potential barrier must be overcome in order for dewetting to occur. This barrier can only be overcome if holes are nucleated, e.g. around a film defect or a dust particle. In the second case instead, the dewetting proceeds spontaneously. The hole formation here is induced by perturbations in the film thickness, with a characteristic wavelength, which are amplified and lead to disruption of the liquid film. This dewetting type is termed spinodal.[117]

The brief description that follows explains in more detail the experimental dewetting process, which can be separated in three stages: nucleation, hole growth and hole coalescence. It should be stressed that at any moment the dewetting of a metastable or unstable thin polymer film can be stopped, and the produced pattern of holes fixed by simply reducing the temperature of the film below the T_g of the polymer.

1.7.2 Stage one: nucleation

As described above, hole formation in a dewetting liquid film can occur by heterogeneous nucleation or spinodal dewetting (Figure 1.14). Heterogeneous nucleation is caused by local chemical or physical heterogeneities in the liquid film. Typically, this can be a dust particle or a strain point within the film.

Where the interfacial potential is negative, capillary waves arise on the surface of the film in a wide range of wavelengths. Among all wavelengths, some modes are selected whose amplitude grows exponentially with time as $\exp(t/\tau)$, where τ is the characteristic growth time of the mode in consideration. This produces a pattern that is characterized by a spinodal wavelength λ. The growth time τ varies with the fifth exponent of the liquid film thickness, so it becomes longer and longer as the

film gets thicker. In practice, in polymer films thicker than about 4 nm spinodal dewetting is so slow that heterogeneous nucleation comes into play, and dominates the developing dewetting pattern.

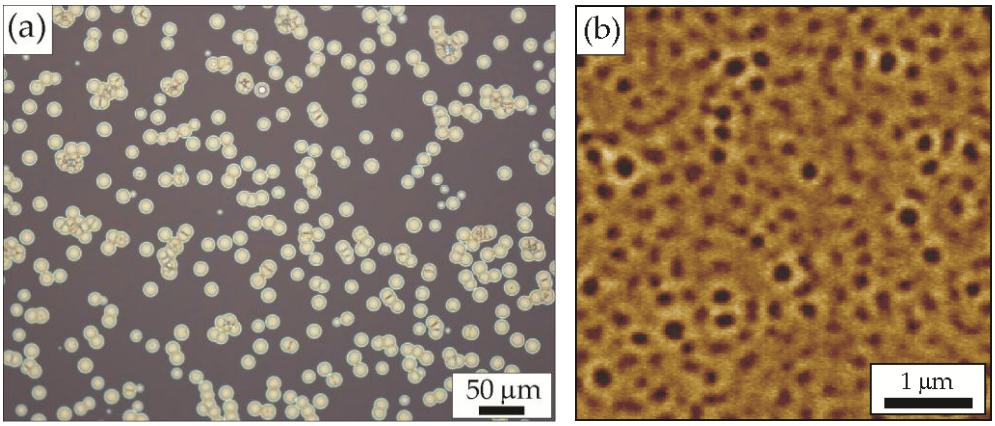

Figure 1.14 Examples of different types of dewetting. (a) Optical micrograph of a poly(methyl methacrylate) film of thickness 36 nm dewetting by heterogeneous nucleation on a polystyrene film and (b) atomic force microscopy image of a polystyrene film of thickness < 10 nm dewetting by spinodal mechanism on silicon. Figure 1.14(b) was adapted from reference 115.

1.7.3 Stage two: hole growth

Once holes have been nucleated in a liquid film, the three phase contact line between solid, liquid and air moves so to increase the dry solid area. The holes therefore grow with time until their dewetting fronts meet, and coalescence of holes occurs. Brochard-Wyart *et al.*[118] characterised the growth of a dewetting hole in a polymer melt, defining three distinct regimes. The dewetting region grows exponentially in the first regime, and a homogenous thickening of the liquid film around it is observed. In the second regime, when the hole radius becomes bigger than a critical value, the liquid starts to accumulate in a rim around the hole. Here, energy is dissipated by friction within the liquid (viscous dissipation) as well as at the

liquid/solid interface (slip). When viscous friction within the liquid film is predominant, the rim is hemispherical, and the dewetting velocity is constant. When instead slippage is involved, the liquid film behaves as a solid sliding on the substrate, and the rim is asymmetrical, stretched towards the "wet" side. The most common scenario is given by the superimposition of viscous flow and slip, such as the velocity is initially proportional to $t^{-1/3}$ (t = time), and eventually switches to a linear growth (Figure 1.15).[114, 119]

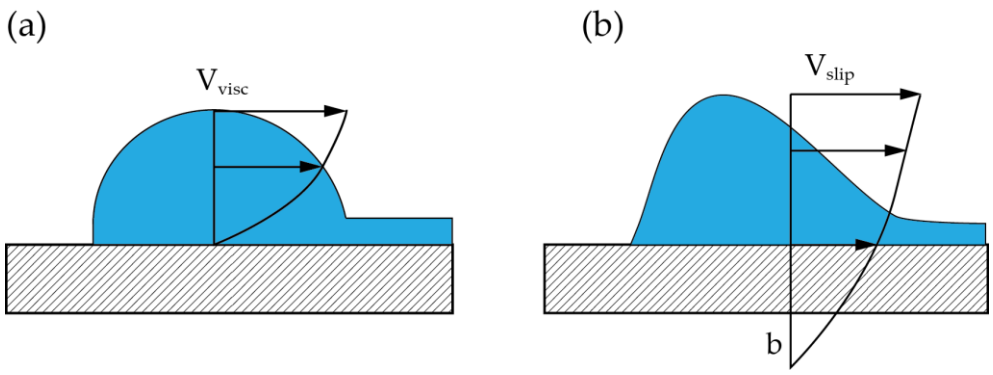

Figure 1.15 Cross-sectional profile of a rim in a dewetting thin liquid film over a solid surface, in the two extreme cases of (a) full viscous flow and (b) full slip. In case of viscous flow the rim is symmetric, while if slip occurs, the rim is asymmetric and its profile decades exponentially towards the "wet" side.

The critical radius at which the rim is born is defined as:

$$R_c = (hb)^{1/2} \tag{1.8}$$

where h is the film thickness and b is the slip length.

When enough material is accumulated in the rim, at long dewetting times, the surface tension rounds the rim. If the height of the rim is much larger than the slip length, viscous flow dominates and slip is negligible.

The dewetting kinetics and the rim shape in polymer melts are strongly influenced by slippage, which in turn depends on both the solid substrate and the dewetting melt. Jacobs and co-workers have extensively studied the dewetting of polystyrene melts on different substrates.[120-122] They investigated the dewetting dynamics and morphology of polystyrene melts of low molecular weight on silicon wafers coated with either a monolayer of octadecyltrichlorosilane (OTS) or with dodecyltrichlorosilane (DTS), while keeping all other properties of the substrate and the liquid fixed. This way they were able to investigate the influence of only the liquid/substrate interactions on the slip. They showed that for small slip lengths the rim is symmetrical, while it becomes more and more asymmetrical the bigger the slip length becomes.

The entanglement of the polymer chains in a melt also affects its slip length. According to de Gennes' model,[113] the slip length in a polymer melt dewetting on a non adsorbing solid substrate is:

$$b = a\,N^3/N_e^2 \tag{1.9}$$

where a is the repeating unit length, N is the degree of polymerization (number of monomers per chain) and N_e is the entanglement length. The slip length increases drastically above the entanglement length of the polymer. Again Jacobs and co-workers have proven this experimentally, by characterising the shape of the rim for polymer melts of different molecular weights.[123, 124]

For high molecular weight melts (i.e. above the entanglement length), the transition from the intermediate regime of hole growth, where slip dominates, to the final regime, where viscous flow dominates, depends on the ability of the polymer chains to slide on each other. The reptation time is the time necessary for a polymer chain to "slither" within a polymer melt.

Reiter and co-workers found that the characteristic transition time from slippage to viscous flow in high molecular weight polymer melts in fact coincides with the reptation time under the same conditions.[125]

1.7.4 Stage three: formation of isolated droplets

When a hole grows enough to meet its neighbours, it cannot grow any further. The rims of the holes overlap to form ribbons. The film is now reduced to a network of ribbons, which decay to form droplets because of the Rayleigh-Plateau instability.[113] The droplets are hemispherical, with Young's equilibrium contact angle. This is an equilibrium configuration of the system, which can no longer evolve, although the true final equilibrium configuration for the system would require all droplets to coalesce into one. Summarised in Figure 1.16 are the three stages of dewetting.

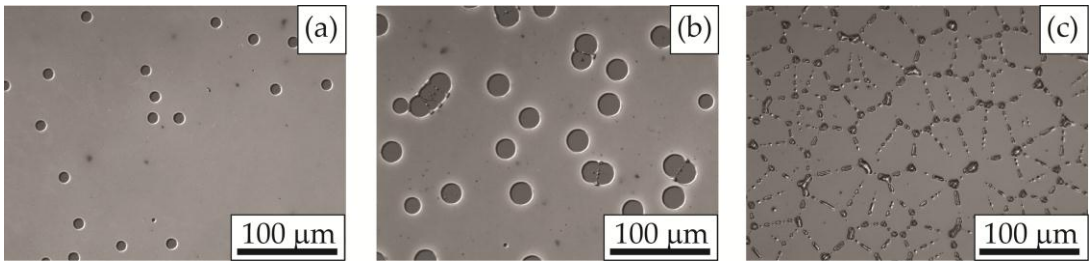

Figure 1.16 Optical micrographs of the three stages of dewetting: (a) nucleation, (b) hole growth and (c) hole coalescence and formation of droplets.

1.7.5 Dewetting in stressed polymer films

As described above, metastable polymer thin films nucleate holes because of localized alterations of the effective interfacial potential. One of the possible causes of such alterations is the presence of stresses generated during the preparation of the film. In many solvent-assisted film preparation

techniques, such as spin-coating, the polymer chains may be deposited in a non-equilibrium state, i.e. with an entanglement density lower than the equilibrated melt. In such films, the polymer chains are stretched and stress facilitates greatly the nucleation process.[126, 127] The stress increases with the molecular weight of the polymer.[128] It was demonstrated that these stresses spontaneously relax with the aging of the film, on the timescale of the reptation time of the polymer chains. This means that polymer chains can slowly move to minimize the stresses, even below their T_g. The reduction of stress is greater the higher the temperature of aging.[127] This has major consequences in the dewetting of spin-cast polymer films. The number of holes nucleated upon annealing depends on the stress within the film, hence it increases with increasing molecular weight of the polymer and with decreasing aging time of the film.

1.7.6 Patterning by dewetting

As mentioned above, dewetting by nucleation leads to many holes located at random positions all over the substrate. However, a certain degree of control can be exercised over a dewetting system. In a polymer thin film dewetting by heterogeneous nucleation holes form all within a very short interval, typically 100 s, and grow at the same rate. This leads to holes with controlled and uniform size, which can be varied by simply varying the annealing time.

A second aspect of control on the random pattern is related to the hole density on the surface. A film with high internal stress (i.e. with high molecular weight, well above the entanglement length, prepared by non-equilibrium techniques such as spin-coating), will nucleate a high number of holes to relieve stress by polymer chain re-entanglement. A smaller density of holes can be achieved by letting the film age (i.e. anneal it below its T_g), to

reduce the internal stress without nucleation occurring, and eventually dewetting the film. As discussed in the previous Section, the nucleation probability, and hence the hole density, decreases with aging of the non-equilibrated polymer film.

For many applications, this kind of control over the pattern is sufficient. In others, an ordered organization of the pattern is required. External factors can be introduced to locally modify the interfacial potential of the system, and force the dewetting to occur in ordered manner. A brief discussion of this follows, and includes patterning induced by physically/chemically heterogeneous substrates and patterning induced by topographical structures above the film. For a more comprehensive description see the review by Xue and Han.[129]

1.7.7 Patterning induced by physically and chemically heterogeneous substrates

Physical and chemical heterogeneities on the substrate introduce local changes in the interfacial potential energy barrier. Lowering the interfacial potential favours the nucleation of holes in specific locations. If the heterogeneity is ordered, then the film will dewet in an ordered pattern (Figure 1.17). One of the first examples of this was reported by Higgins and Jones in 2000.[130] They imprinted a pattern of parallel grooves in a polymer film by spin-coating it on a glass slide which was pre-rubbed with a lens tissue. The polymer film was then detached and deposited on a flat substrate. Upon annealing the film dewetted in parallel ribbons. This work opened a vast investigation in the field. Kargupta and Sharma described in detail the theory of dewetting on chemically and physically striped substrates.[131] They showed that, on a substrate containing many potentially destabilizing sites (i.e. stripes), only the ones separated by a characteristic

length scale of the order of the spinodal wavelength, were effective in causing the film rupture. Nucleation on the remaining sites would result in an increase of the overall surface energy.

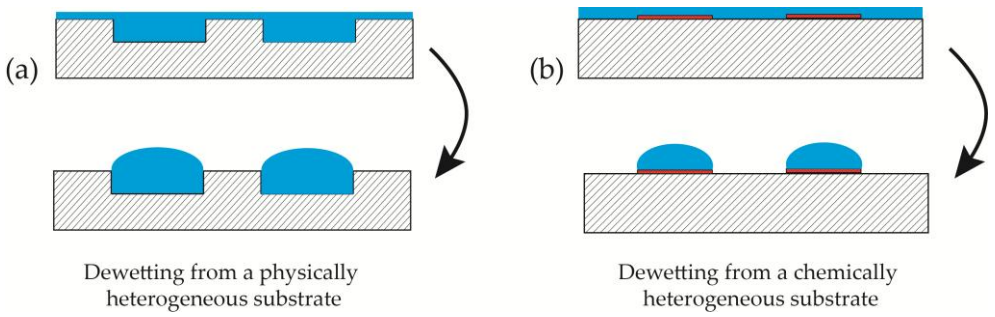

Figure 1.17 Dewetting of a liquid film on (a) a topographically and (b) a chemically heterogeneous substrates. The film is initially flat, in a metastable state. The heterogeneity on the substrate nucleates features in the liquid film, which eventually accumulates (a) in the substrate holes or (b) on affine chemical areas.

Geoghegan *et al.*[132] investigated the dewetting of polystyrene on corrugated silicon/silica substrates. They showed how the polystyrene collected within the grooves upon dewetting. If a chemical heterogeneity was also introduced (e.g. one facet of the ridges was coated in gold), then the polystyrene not only dewetted from the corrugation's tips, but accumulated on the gold covered side, towards which polystyrene had more affinity.

Similar studies have been published by many groups, presenting a wide variety of pattern geometries.[133-139] A study that stands out in particular is the one by Park and Cheng,[140] where the patterning technique was used to fabricate three-dimensional scaffolds. A series of polymers, including the ones used for transistors and LEDs, was spin coated on a flat surface, then transferred on a striped mould and dewetted to form stripes. The stripes could then be detached from the mould and imprinted on a new flat support. By repeating the last step, they could stack layers of stripes with

different orientations to produce a three-dimensional architecture. The ability to transfer polymer stripes from a mould to a flat substrate (a sort of dewetting/contact printing combination technique) has been extensively exploited to produce a variety of patterns with potential for up-scaling.[141-143]

1.7.8 Patterning induced by topographical structures above the film

As seen in the previous Section, an ordered pattern can be obtained by dewetting a polymer film on a pre-patterned substrate. A second way to obtain similar patterns is to force a topographical structure on the surface of the film, which is supported on a flat substrate. This can be achieved by using a mould. The literature is rich in interesting works where a mould is mechanically forced on the polymer film, which then dewets in an ordered pattern mirroring the one of the mould.[144-149] The mould locally alters the film thickness, and offers vertical surfaces on which the polymer melt can "climb" by capillary forces (Figure 1.18).

Chou *et al.*[150] presented an interesting process to develop a pattern in a polymer film using a mould which does not need to come in contact with the film. The process is called lithographically induced self-construction (LISC) and is described as follows: a thin polymer film is cast on a flat substrate, then a mask with protruding patterns is placed at a specific distance above the polymer film. During a heat-and-cool cycle, the polymer film self-constructs into mesas under the mask protrusions. The mesas have lateral dimension identical to that of the mask protrusion, height equal to the distance between the mask and the substrate, and steep side walls. The phenomenon derives from the presence of a temperature gradient between the film and the mould, which amplifies the spontaneous capillary waves in the film. Eventually the lateral disjoining pressure in the film becomes bigger than the Laplace pressure generated by the curvature of the film, and a

patterned dewetting occurs. The protrusions on the mould influence the temperature gradient and drive the pattern formation. A similar phenomenon was observed by Schaffer *et al.*,[151] in a set up involving an electric field applied between the substrate holding the polymer film and the protruded mask. In this case, the formation of mesas was mainly due to electrostatic interaction between the polymer melt and the patterned capacitor plate.

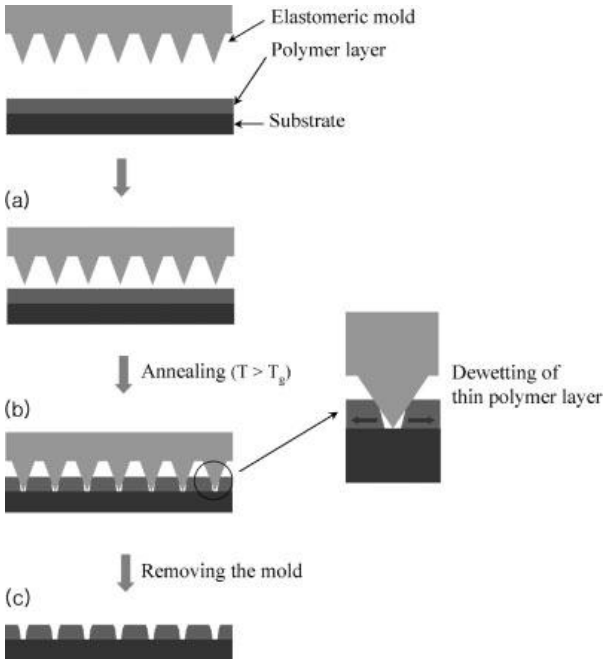

Figure 1.18 Schematic of patterning by dewetting using a mould. Adapted from reference 144. (a) The mould is brought in contact with the polymer film, (b) the film is annealed above its T_g, and dewets where the asperities of the mould induce the nucleation. (c) Upon removal of the mould and cooling down below the T_g of the polymer, a pattern is obtained in the polymer film.

1.7.9 Advantages of patterning by dewetting

Dewetting is a powerful tool to obtain patterns.[152, 153] Although patterning by dewetting cannot achieve the lateral resolution and variety of

shapes obtainable by techniques such as photolithography, it presents a number of advantages, which make it suitable for device fabrication. First of all, the dewetting technique is very inexpensive, because it does not involve expensive machinery or components, particularly when no pre-pattern is involved, and the process is completely self-guided. A second advantage is the simplicity of the method. Only a few pieces of equipment are needed for film preparation and film annealing, along with some care in preparing dust free samples. Because of its simplicity, this patterning process is very easily up-scalable. Surfaces of any size can be patterned, provided that a uniform coating can be prepared. In this work, it was found that spin-coating uniform films onto substrates 100 mm in diameter was much more challenging than onto 10 mm ones, yet dip coating is expected to make up-scaling more accessible. The whole film will dewet in the same way if annealed in a uniformly heated environment. This is expected to be reasonably easy for large scale coatings, as modern ovens can achieve high heat uniformity. Patterning by dewetting is very flexible, because the size of the patterns can be tuned from a few hundred nanometers to a few hundred microns by simply varying the annealing time. Finally, one of the greatest advantages of patterning by dewetting over other techniques is that it can be used on non-flat surfaces. This technique is truly conformal, because any shape with smooth topographical features can be coated with a film and annealed, in no different way than a flat surface (sharp edges though may represent a challenge, as they may induce dewetting). This is an easy task when using techniques such as dip-coating, where the surface is immersed in a polymer solution and slowly extracted to produce a dry film.

In this Thesis, patterning by dewetting was employed to produce a heterogeneous surface starting from a polymer thin film bilayer. In such a system, the top polymer is chosen so to form a metastable film on the bottom film, which is stable on the underlying silicon wafer. Upon annealing, the

top polymer dewets exposing the underlying bottom polymer, which remains unchanged. The result is a topographical and chemical pattern which presents the functionalities of both the polymers used. In Chapter 5, this approach was used in combination with grafting of a polymer brush to pattern proteins and cells on a surface.

1.8 References

1. Anderson, J. M.; Rodriguez, A.; Chang, D. T., Foreign body reaction to biomaterials. *Seminars in Immunology* **2008**, *20* (2), 86-100.
2. Lewis, K.; Klibanov, A. M., Surpassing nature: rational design of sterile-surface materials. *Trends in Biotechnology* **2005**, *23* (7), 343-348.
3. Costerton, J. W.; Cheng, K. J.; Geesey, G. G.; Ladd, T. I.; Nickel, J. C.; Dasgupta, M.; Marrie, T. J., Bacterial biofilms in nature and disease. *Annual Review of Microbiology* **1987**, *41* (1), 435-464.
4. Wilson, C. J.; Clegg, R. E.; Leavesley, D. I.; Pearcy, M. J., Mediation of biomaterial-cell interactions by adsorbed proteins: A review. *Tissue Engineering* **2005**, *11* (1-2), 1-18.
5. Advincula, R. C.; Brittain, W. J.; Caster, K. C.; Ruhe, J., *Polymer brushes: Synthesis, characterization, applications*. Wiley-VCH Verleg GmbH & Co. KGaA: Weinheim, **2004**.
6. Zhao, B.; Brittain, W. J., Polymer brushes: surface-immobilized macromolecules. *Progress in Polymer Science* **2000**, *25* (5), 677-710.
7. Klein, J.; Kamiyama, Y.; Yoshizawa, H.; Israelachvili, J. N.; Fredrickson, G. H.; Pincus, P.; Fetters, L. J., Lubrication forces between surfaces bearing polymer brushes. *Macromolecules* **1993**, *26* (21), 5552-5560.
8. Reiter, G.; Khanna, R., Real-time determination of the slippage length in autophobic polymer dewetting. *Physical Review Letters* **2000**, *85* (13), 2753-2756.
9. Reiter, G.; Auroy, P.; Auvray, L., Instabilities of thin polymer films on layers of chemically identical grafted molecules. *Macromolecules* **1996**, *29* (6), 2150-2157.
10. Israelachvili, J., *Intermolecular and Surface Forces*. 2nd ed.; Academic Press: London, **1991**.
11. Milner, S. T., Polymer brushes. *Science* **1991**, *251* (4996), 905-914.
12. Alexander, S., Adsorption of chain molecules with a polar head - A scaling description. *Journal De Physique* **1977**, *38* (8), 983-987.

13. Binder, K., *Monte Carlo and molecular dynamics simulations in polymer science*. Oxford University Press: New York, **1995**.
14. Lai, P. Y.; Halperin, A., Polymer brush at high coverage. *Macromolecules* **1991**, *24* (17), 4981-4982.
15. Shim, D. F. K.; Cates, M. E., Finite extensibility and density saturation effects in the polymer brush. *Journal De Physique* **1989**, *50* (24), 3535-3551.
16. Yamamoto, S.; Ejaz, M.; Tsujii, Y.; Fukuda, T., Surface interaction forces of well-defined, high-density polymer brushes studied by atomic force microscopy. 2. Effect of graft density. *Macromolecules* **2000**, *33* (15), 5608-5612.
17. Wu, T.; Efimenko, K.; Vlcek, P.; Subr, V.; Genzer, J., Formation and properties of anchored polymers with a gradual variation of grafting densities on flat substrates. *Macromolecules* **2003**, *36* (7), 2448-2453.
18. Moh, L. C. H.; Losego, M. D.; Braun, P. V., Solvent quality effects on scaling behavior of poly(methyl methacrylate) brushes in the moderate- and high-density regimes. *Langmuir* **2011**, *27* (7), 3698-3702.
19. Brittain, W. J.; Minko, S., A structural definition of polymer brushes. *Journal of Polymer Science, Part A: Polymer Chemistry* **2007**, *45* (16), 3505-3512.
20. Currie, E. P. K.; Norde, W.; Cohen Stuart, M. A., Tethered polymer chains: surface chemistry and their impact on colloidal and surface properties. *Advances in Colloid and Interface Science* **2003**, *100-102*, 205-265.
21. Halperin, A., Polymer brushes that resist adsorption of model proteins: Design parameters. *Langmuir* **1999**, *15* (7), 2525-2533.
22. Tsujii, Y.; Ohno, K.; Yamamoto, S.; Goto, A.; Fukuda, T., Structure and properties of high-density polymer brushes prepared by surface-initiated living radical polymerization. *Advanced Polymer Science* **2006**, *197*, 1-45.
23. Zhao, T. L.; Chen, H.; Zheng, J.; Yu, Q.; Wu, Z. Q.; Yuan, L., Inhibition of protein adsorption and cell adhesion on PNIPAAm-grafted polyurethane surface: Effect of graft molecular weight. *Colloids and Surfaces B-Biointerfaces* **2011**, *85* (1), 26-31.
24. Tanaka, M.; Mochizuki, A.; Ishii, N.; Motomura, T.; Hatakeyama, T., Study of blood compatibility with poly(2-methoxyethyl acrylate). Relationship between water structure and platelet compatibility in poly(2-methoxyethylacrylate-co-2-hydroxyethylmethacrylate). *Biomacromolecules* **2002**, *3* (1), 36-41.
25. Morisaku, T.; Watanabe, J.; Konno, T.; Takai, M.; Ishihara, K., Hydration of phosphorylcholine groups attached to highly swollen polymer hydrogels studied by thermal analysis. *Polymer* **2008**, *49* (21), 4652-4657.
26. Cheng, G.; Zhang, Z.; Chen, S.; Bryers, J. D.; Jiang, S., Inhibition of bacterial adhesion and biofilm formation on zwitterionic surfaces. *Biomaterials* **2007**, *28* (29), 4192-4199.

27. Kim, J.; Qian, W.; Al-Saigh, Z. Y., Measurements of water sorption enthalpy on polymer surfaces and its effect on protein adsorption. *Surface Science* **2011**, *605* (3-4), 419-423.
28. Chen, S.; Li, L.; Zhao, C.; Zheng, J., Surface hydration: Principles and applications toward low-fouling/nonfouling biomaterials. *Polymer* **2010**, *51* (23), 5283-5293.
29. Chen, H.; Yuan, L.; Song, W.; Wu, Z. K.; Li, D., Biocompatible polymer materials: Role of protein-surface interactions. *Progress in Polymer Science* **2008**, *33* (11), 1059-1087.
30. Rosenhahn, A.; Schilp, S.; Kreuzer, H. J.; Grunze, M., The role of "inert" surface chemistry in marine biofouling prevention. *Physical Chemistry Chemical Physics* **2010**, *12* (17), 4275-4286.
31. Inoue, Y.; Nakanishi, T.; Ishihara, K., Adhesion force of proteins against hydrophilic polymer brush surfaces. *Reactive & Functional Polymers* **2011**, *71* (3), 350-355.
32. de Vos, W. M.; Leermakers, F. A. M.; de Keizer, A.; Kleijn, I. M.; Stuart, M. A. C., Interaction of particles with a polydisperse brush: A self-consistent-field analysis. *Macromolecules* **2009**, *42* (15), 5881-5891.
33. Balazs, A. C.; Singh, C.; Zhulina, E.; Chern, S.-S.; Lyatskaya, Y.; Pickett, G., Theory of polymer chains tethered at interfaces. *Progress in Surface Science* **1997**, *55* (3), 181-269.
34. Brandani, P.; Stroeve, P., Kinetics and equilibria of adsorption of PEO-PPO-PEO triblock copolymers on a hydrophilic self-assembled monolayer on gold. *Macromolecules* **2004**, *37* (17), 6640-6643.
35. Huang, N. P.; Michel, R.; Voros, J.; Textor, M.; Hofer, R.; Rossi, A.; Elbert, D. L.; Hubbell, J. A.; Spencer, N. D., Poly(L-lysine)-g-poly(ethylene glycol) layers on metal oxide surfaces: Surface-analytical characterization and resistance to serum and fibrinogen adsorption. *Langmuir* **2001**, *17* (2), 489-498.
36. Schreiber, F., Structure and growth of self-assembling monolayers. *Progress in Surface Science* **2000**, *65* (5-8), 151-257.
37. Wasserman, S. R.; Tao, Y. T.; Whitesides, G. M., Structure and reactivity of alkylsiloxane monolayers formed by reaction of alkyltrichlorosilanes on silicon substrates. *Langmuir* **1989**, *5* (4), 1074-1087.
38. Ruhe, J.; Knoll, N., Functional polymer brushes (Reprinted from Supramolecular Polymers, pg 565-613, 2000). *Journal of Macromolecular Science: Polymer Reviews* **2002**, *C42* (1), 91-138.
39. Mansky, P.; Liu, Y.; Huang, E.; Russell, T. P.; Hawker, C., Controlling polymer-surface interactions with random copolymer brushes. *Science* **1997**, *275* (5305), 1458-1460.
40. Huang, H. Q.; Penn, L. S., Dense tethered layers by the "grafting-to" approach. *Macromolecules* **2005**, *38* (11), 4837-4843.

41. Minko, S.; Patil, S.; Datsyuk, V.; Simon, F.; Eichhorn, K. J.; Motornov, M.; Usov, D.; Tokarev, I.; Stamm, M., Synthesis of adaptive polymer brushes via "grafting to" approach from melt. *Langmuir* **2002**, *18* (1), 289-296.
42. Taylor, W.; Jones, R. A. L., Producing high-density high-molecular-weight polymer brushes by a "grafting to" method from a concentrated homopolymer solution. *Langmuir* **2010**, *26* (17), 13954-13958.
43. Wang, H. S.; Jiang, P.; Zhang, M.; Dong, X. C., Synthesis of a novel restricted access chiral stationary phase based on atom transfer radical polymerization and click chemistry for the analysis of chiral drugs in biological matrices. *Journal of Chromatography A* **2011**, *1218* (9), 1310-1313.
44. Barbey, R.; Lavanant, L.; Paripovic, D.; Schuwer, N.; Sugnaux, C.; Tugulu, S.; Klok, H. A., Polymer brushes via surface-initiated controlled radical polymerization: Synthesis, characterization, properties, and applications. *Chemical Reviews* **2009**, *109* (11), 5437-5527.
45. Edmondson, S.; Osborne, V. L.; Huck, W. T. S., Polymer brushes via surface-initiated polymerizations. *Chemical Society Reviews* **2004**, *33* (1), 14-22.
46. Chiefari, J.; Chong, Y. K.; Ercole, F.; Krstina, J.; Jeffery, J.; Le, T. P. T.; Mayadunne, R. T. A.; Meijs, G. F.; Moad, C. L.; Moad, G.; Rizzardo, E.; Thang, S. H., Living free-radical polymerization by reversible addition-fragmentation chain transfer: The RAFT process. *Macromolecules* **1998**, *31* (16), 5559-5562.
47. Le, T. P. T.; Moad, G.; Rizzardo, E.; Thang, S. H. Polymerization with living characteristics. Pat. Num. WO 98/01478, **1998**.
48. Corpart, P.; Charmot, D.; Biadatti, T.; Zard, S.; Michelet, D. Method for block copolymer synthesis by controlled radical polymerization. Pat. Num. WO 98/9858974, **1998**.
49. Wang, J. S.; Matyjaszewski, K., Controlled living radical polymerization - Atom-transfer radical polymerization in the presence of transition-metal complexes. *Journal of the American Chemical Society* **1995**, *117* (20), 5614-5615.
50. Kato, M.; Kamigaito, M.; Sawamoto, M.; Higashimura, T., Polymerization of methyl-methacrylate with the carbon-tetrachloride dichlorotris(triphenylphosphine)ruthenium(II) methylaluminum bis(2,6-di-tert-butylphenoxide) initiating system - Possibility of living radical polymerization. *Macromolecules* **1995**, *28* (5), 1721-1723.
51. Ayres, N., Atom transfer radical polymerization: A robust and versatile route for polymer synthesis. *Polymer Reviews (Philadelphia, PA, United States)* **2011**, *51* (2), 138-162.
52. Tang, W.; Matyjaszewski, K., Effect of ligand structure on activation rate constants in ATRP. *Macromolecules* **2006**, *39* (15), 4953-4959.
53. Braunecker, W. A.; Matyjaszewski, K., Controlled/living radical polymerization: Features, developments, and perspectives. *Progress in Polymer Science* **2007**, *32* (1), 93-146.

54. Matyjaszewski, K.; Xia, J. H., Atom transfer radical polymerization. *Chemical Reviews* **2001**, *101* (9), 2921-2990.
55. Jakubowski, W.; Matyjaszewski, K., Activator generated by electron transfer for atom transfer radical polymerization. *Macromolecules* **2005**, *38* (10), 4139-4146.
56. Jakubowski, W.; Min, K.; Matyjaszewski, K., Activators regenerated by electron transfer for atom transfer radical polymerization of styrene. *Macromolecules* **2006**, *39* (1), 39-45.
57. Jakubowski, W.; Matyjaszewski, K., Activators regenerated by electron transfer for atom-transfer radical polymerization of (meth)acrylates and related block copolymers. *Angewandte Chemie-International Edition* **2006**, *45* (27), 4482-4486.
58. Matyjaszewski, K.; Dong, H. C.; Jakubowski, W.; Pietrasik, J.; Kusumo, A., Grafting from surfaces for "Everyone": ARGET ATRP in the presence of air. *Langmuir* **2007**, *23* (8), 4528-4531.
59. Matyjaszewski, K.; Miller, P. J.; Shukla, N.; Immaraporn, B.; Gelman, A.; Luokala, B. B.; Siclovan, T. M.; Kickelbick, G.; Vallant, T.; Hoffmann, H.; Pakula, T., Polymers at interfaces: Using atom transfer radical polymerization in the controlled growth of homopolymers and block copolymers from silicon surfaces in the absence of untethered sacrificial initiator. *Macromolecules* **1999**, *32* (26), 8716-8724.
60. Ejaz, M.; Yamamoto, S.; Ohno, K.; Tsujii, Y.; Fukuda, T., Controlled graft polymerization of methyl methacrylate on silicon substrate by the combined use of the Langmuir-Blodgett and atom transfer radical polymerization techniques. *Macromolecules* **1998**, *31* (17), 5934-5936.
61. Ohno, K.; Akashi, T.; Huang, Y.; Tsujii, Y., Surface-initiated living radical polymerization from narrowly size-distributed silica nanoparticles of diameters less than 100 nm. *Macromolecules* **2010**, *43* (21), 8805-8812.
62. Pyun, J.; Jia, S. J.; Kowalewski, T.; Patterson, G. D.; Matyjaszewski, K., Synthesis and characterization of organic/inorganic hybrid nanoparticles: Kinetics of surface-initiated atom transfer radical polymerization and morphology of hybrid nanoparticle ultrathin films. *Macromolecules* **2003**, *36* (14), 5094-5104.
63. von Werne, T.; Patten, T. E., Preparation of structurally well-defined polymer-nanoparticle hybrids with controlled/living radical polymerizations. *Journal of the American Chemical Society* **1999**, *121* (32), 7409-7410.
64. Turgman-Cohen, S.; Genzer, J., Computer simulation of controlled radical polymerization effect of chain confinement due to initiator grafting density and solvent quality in "grafting from" method. *Macromolecules* **2010**, *43* (22), 9567-9577.
65. Pasetto, P.; Blas, H.; Audouin, F.; Boissiere, C.; Sanchez, C.; Save, M.; Charleux, B., Mechanistic insight into surface-initiated polymerization of

methyl methacrylate and styrene via ATRP from ordered mesoporous silica particles. *Macromolecules* **2009**, *42* (16), 5983-5995.
66. Kruk, M.; Dufour, B.; Celer, E. B.; Kowalewski, T.; Jaroniec, M.; Matyjaszewski, K., Grafting monodisperse polymer chains from concave surfaces of ordered mesoporous silicas. *Macromolecules* **2008**, *41* (22), 8584-8591.
67. Gorman, C. B.; Petrie, R. J.; Genzer, J., Effect of substrate geometry on polymer molecular weight and polydispersity during surface-initiated polymerization. *Macromolecules* **2008**, *41* (13), 4856-4865.
68. Lutz, J. F., 1,3-dipolar cycloadditions of azides and alkynes: A universal ligation tool in polymer and materials science. *Angewandte Chemie-International Edition* **2007**, *46* (7), 1018-1025.
69. Rosen, B. M.; Lligadas, G.; Hahn, C.; Percec, V., Synthesis of dendrimers through divergent iterative thio-bromo "click" chemistry. *Journal of Polymer Science, Part A: Polymer Chemistry* **2009**, *47* (15), 3931-3939.
70. Rosen, B. M.; Lligadas, G.; Hahn, C.; Percec, V., Synthesis of dendritic macromolecules through divergent iterative thio-bromo "click" chemistry and SET-LRP. *Journal of Polymer Science, Part A: Polymer Chemistry* **2009**, *47* (15), 3940-3948.
71. Coessens, V.; Pyun, J.; Miller, P. J.; Gaynor, S. G.; Matyjaszewski, K., Functionalization of polymers prepared by ATRP using radical addition reactions. *Macromolecular Rapid Communications* **2000**, *21* (2), 103-109.
72. Uygun, M.; Tasdelen, M. A.; Yagci, Y., Influence of type of initiation on thiol-ene "click" chemistry. *Macromolecular Chemistry and Physics* **2010**, *211* (1), 103-110.
73. Tay, C. Y.; Irvine, S. A.; Boey, F. Y. C.; Tan, L. P.; Venkatraman, S., Micro-/nano-engineered cellular responses for soft tissue engineering and biomedical applications. *Small* **2011**, *7* (10), 1361-1378.
74. Choi, C. K.; Breckenridge, M. T.; Chen, C. S., Engineered materials and the cellular microenvironment: a strengthening interface between cell biology and bioengineering. *Trends in Cell Biology* **2010**, *20* (12), 705-714.
75. Tanaka, M., Design of novel 2D and 3D biointerfaces using self-organization to control cell behavior. *Biochimica Et Biophysica Acta-General Subjects* **2011**, *1810* (3), 251-258.
76. Chen, C. S.; Mrksich, M.; Huang, S.; Whitesides, G. M.; Ingber, D. E., Geometric control of cell life and death. *Science* **1997**, *276* (5317), 1425-1428.
77. Flemming, R. G.; Murphy, C. J.; Abrams, G. A.; Goodman, S. L.; Nealey, P. F., Effects of synthetic micro- and nano-structured surfaces on cell behavior. *Biomaterials* **1999**, *20* (6), 573-588.
78. Lehnert, D.; Wehrle-Haller, B.; David, C.; Weiland, U.; Ballestrem, C.; Imhof, B. A.; Bastmeyer, M., Cell behaviour on micropatterned substrata: limits of extracellular matrix geometry for spreading and adhesion. *Journal of Cell Science* **2004**, *117* (1), 41-52.

79. Ingber, D. E., Cellular mechanotransduction: putting all the pieces together again. *Faseb Journal* **2006**, *20* (7), 811-827.
80. Mammoto, T.; Ingber, D. E., Mechanical control of tissue and organ development. *Development* **2010**, *137* (9), 1407-1420.
81. Giancotti, F. G.; Ruoslahti, E., Transduction - Integrin signaling. *Science* **1999**, *285* (5430), 1028-1032.
82. Chen, C. S., Mechanotransduction - a field pulling together? *Journal of Cell Science* **2008**, *121* (20), 3285-3292.
83. Geiger, B.; Bershadsky, A.; Pankov, R.; Yamada, K. M., Transmembrane extracellular matrix-cytoskeleton crosstalk. *Nature Reviews Molecular Cell Biology* **2001**, *2* (11), 793-805.
84. Pozos-Vazquez, C.; Boudou, T.; Dulong, V.; Nicolas, C.; Picart, C.; Glinel, K., Variation of polyelectrolyte film stiffness by photo-cross-linking: A new way to control cell adhesion. *Langmuir* **2009**, *25* (6), 3556-3563.
85. Ananthakrishnan, R.; Ehrlicher, A., The forces behind cell movement. *International Journal of Biological Sciences* **2007**, *3* (5), 303-317.
86. Mitra, A. K.; Agrawal, D. K., In stent restenosis: bane of the stent era. *Journal of Clinical Pathology* **2006**, *59* (3), 232-239.
87. Arnold, M.; Hirschfeld-Warneken, V. C.; Lohmuller, T.; Heil, P.; Blummel, J.; Cavalcanti-Adam, E. A.; Lopez-Garcia, M.; Walther, P.; Kessler, H.; Geiger, B.; Spatz, J. P., Induction of cell polarization and migration by a gradient of nanoscale variations in adhesive ligand spacing. *Nano Letters* **2008**, *8* (7), 2063-2069.
88. Dalby, M. J.; Gadegaard, N.; Tare, R.; Andar, A.; Riehle, M. O.; Herzyk, P.; Wilkinson, C. D. W.; Oreffo, R. O. C., The control of human mesenchymal cell differentiation using nanoscale symmetry and disorder. *Nature Materials* **2007**, *6* (12), 997-1003.
89. Mendonça, G.; Mendonça, D. B. S.; Simões, L. G. P.; Araújo, A. L.; Leite, E. R.; Duarte, W. R.; Aragão, F. J. L.; Cooper, L. F., The effects of implant surface nanoscale features on osteoblast-specific gene expression. *Biomaterials* **2009**, *30* (25), 4053-4062.
90. Qi, S.; Yi, C.; Ji, S.; Fong, C.-C.; Yang, M., Cell adhesion and spreading behavior on vertically aligned silicon nanowire arrays. *ACS Applied Materials & Interfaces* **2009**, *1* (1), 30-34.
91. Hung, Y.-C.; Pan, H.-A.; Tai, S.-M.; Huang, G. S., A nanodevice for rapid modulation of proliferation, apoptosis, invasive ability, and cytoskeletal reorganization in cultured cells. *Lab on a Chip* **2010**, *10* (9), 1189-1198.
92. Seo, J.-H.; Matsuno, R.; Takai, M.; Ishihara, K., Cell adhesion on phase-separated surface of block copolymer composed of poly(2-methacryloyloxyethyl phosphorylcholine) and poly(dimethylsiloxane). *Biomaterials* **2009**, *30* (29), 5330-5340.

93. Shekaran, A.; Garcia, A. J., Nanoscale engineering of extracellular matrix-mimetic bioadhesive surfaces and implants for tissue engineering. *Biochimica et Biophysica Acta (BBA) - General Subjects* **2011**, *1810* (3), 350-360.
94. Charnley, M.; Textor, M.; Khademhosseini, A.; Lutolf, M. P., Integration column: microwell arrays for mammalian cell culture. *Integrative Biology* **2009**, *1* (11-12), 625-634.
95. Mei, Y.; Gerecht, S.; Taylor, M.; Urquhart, A. J.; Bogatyrev, S. R.; Cho, S.-W.; C. Davies, M.; Alexander, M. R.; Langer, R. S.; Anderson, D. G., Mapping the interactions among biomaterials, adsorbed proteins, and human embryonic stem cells. *Advanced Materials* **2009**, *21* (27), 2781-2786.
96. Ceriotti, L.; Buzanska, L.; Rauscher, H.; Mannelli, I.; Sirghi, L.; Gilliland, D.; Hasiwa, M.; Bretagnol, F.; Zychowicz, M.; Ruiz, A.; Bremer, S.; Coecke, S.; Colpo, P.; Rossi, F., Fabrication and characterization of protein arrays for stem cell patterning. *Soft Matter* **2009**, *5* (7), 1406-1416.
97. Kaji, H.; Camci-Unal, G.; Langer, R.; Khademhosseini, A., Engineering systems for the generation of patterned co-cultures for controlling cell-cell interactions. *Biochimica et Biophysica Acta (BBA) - General Subjects* **2011**, *1810* (3), 239-250.
98. Hannachi, I. E.; Yamato, M.; Okano, T., Cell sheet technology and cell patterning for biofabrication. *Biofabrication* **2009**, *1* (2), 022002.
99. Sekine, H.; Shimizu, T.; Hobo, K.; Sekiya, S.; Yang, J.; Yamato, M.; Kurosawa, H.; Kobayashi, E.; Okano, T., Endothelial cell coculture within tissue-engineered cardiomyocyte sheets enhances neovascularization and improves cardiac function of ischemic hearts. *Circulation* **2008**, *118* (14), S145-S152.
100. Otsuka, H., Nanofabrication of nonfouling surfaces for micropatterning of cell and microtissue. *Molecules* **2010**, *15* (8), 5525-5546.
101. Tang, J.; Peng, R.; Ding, J., The regulation of stem cell differentiation by cell-cell contact on micropatterned material surfaces. *Biomaterials* **2010**, *31* (9), 2470-2476.
102. Lutolf, M. P.; Hubbell, J. A., Synthetic biomaterials as instructive extracellular microenvironments for morphogenesis in tissue engineering. *Nature Biotechnology* **2005**, *23* (1), 47-55.
103. Place, E. S.; George, J. H.; Williams, C. K.; Stevens, M. M., Synthetic polymer scaffolds for tissue engineering. *Chemical Society Reviews* **2009**, *38* (4), 1139-1151.
104. Melchels, F. P. W.; Feijen, J.; Grijpma, D. W., A review on stereolithography and its applications in biomedical engineering. *Biomaterials* **2010**, *31* (24), 6121-6130.
105. Sill, T. J.; von Recum, H. A., Electrospinning: Applications in drug delivery and tissue engineering. *Biomaterials* **2008**, *29* (13), 1989-2006.
106. Zhu, J., Bioactive modification of poly(ethylene glycol) hydrogels for tissue engineering. *Biomaterials* **2010**, *31* (17), 4639-4656.

107. Quist, A. P.; Oscarsson, S., Micropatterned surfaces: techniques and applications in cell biology. *Expert Opinion on Drug Discovery* **2010**, *5* (6), 569-581.
108. Nie, Z. H.; Kumacheva, E., Patterning surfaces with functional polymers. *Nature Materials* **2008**, *7* (4), 277-290.
109. Xia, Y. N.; Whitesides, G. M., Soft lithography. *Annual Review of Materials Science* **1998**, *28*, 153-184.
110. Love, J. C.; Estroff, L. A.; Kriebel, J. K.; Nuzzo, R. G.; Whitesides, G. M., Self-assembled monolayers of thiolates on metals as a form of nanotechnology. *Chemical Reviews* **2005**, *105* (4), 1103-1169.
111. Whitesides, G. M.; Ostuni, E.; Takayama, S.; Jiang, X. Y.; Ingber, D. E., Soft lithography in biology and biochemistry. *Annual Review of Biomedical Engineering* **2001**, *3*, 335-373.
112. Gates, B. D.; Xu, Q. B.; Stewart, M.; Ryan, D.; Willson, C. G.; Whitesides, G. M., New approaches to nanofabrication: Molding, printing, and other techniques. *Chemical Reviews* **2005**, *105* (4), 1171-1196.
113. de Gennes, P.-G.; Brochard-Wyart, F.; Quere, D., *Capillarity and wetting phenomena*. Springer Science and Business Media Inc.: New York, **2004**.
114. Seemann, R.; Herminghaus, S.; Neto, C.; Schlagowski, S.; Podzimek, D.; Konrad, R.; Mantz, H.; Jacobs, K., Dynamics and structure formation in thin polymer melt films. *Journal of Physics: Condensed Matter* **2005**, *17*, S267 - S290.
115. Seemann, R.; Herminghaus, S.; Jacobs, K., Dewetting patterns and molecular forces: A reconciliation. *Physical Review Letters* **2001**, *86* (24), 5534.
116. Seemann, R.; Herminghaus, S.; Jacobs, K., Gaining control of pattern formation of dewetting liquid films. *Journal of Physics-Condensed Matter* **2001**, *13* (21), 4925-4938.
117. Mitlin, V. S., Dewetting of Solid Surface: Analogy with Spinodal Decomposition. *Journal of Colloid and Interface Science* **1993**, *156* (2), 491-497.
118. Brochard-Wyart, F.; Debregeas, G.; Fondecave, R.; Martin, P., Dewetting of supported viscoelastic polymer films: Birth of rims. *Macromolecules* **1997**, *30* (4), 1211-1213.
119. Jacobs, K.; Seemann, R.; Schatz, G.; Herminghaus, S., Growth of holes in liquid films with partial slippage. *Langmuir* **1998**, *14* (18), 4961-4963.
120. Fetzer, R.; Jacobs, K., Slippage of newtonian liquids: Influence on the dynamics of dewetting thin films. *Langmuir* **2007**, *23* (23), 11617-11622.
121. Fetzer, R.; Jacobs, K.; Munch, A.; Wagner, B.; Witelski, T. P., New slip regimes and the shape of dewetting thin liquid films. *Physical Review Letters* **2005**, *95* (12), 127801.
122. Fetzer, R.; Rauscher, M.; Munch, A.; Wagner, B. A.; Jacobs, K., Slip-controlled thin-film dynamics. *Europhysics Letters* **2006**, *75* (4), 638-644.

123. Baumchen, O.; Fetzer, R.; Jacobs, K., Reduced interfacial entanglement density affects the boundary conditions of polymer flow. *Physical Review Letters* **2009**, *103* (24), 247801.
124. Seemann, R.; Herminghaus, S.; Jacobs, K., Shape of a liquid front upon dewetting. *Physical Review Letters* **2001**, *87* (19), 196101.
125. Gabriele, S.; Sclavons, S.; Reiter, G.; Damman, P., Disentanglement time of polymers determines the onset of rim instabilities in dewetting. *Physical Review Letters* **2006**, *96* (15).
126. Yang, M. H.; Hou, S. Y.; Chang, Y. L.; Yang, A. C. M., Molecular recoiling in polymer thin film dewetting. *Physical Review Letters* **2006**, *96* (6).
127. Reiter, G.; Hamieh, M.; Damman, P.; Sclavons, S.; Gabriele, S.; Vilmin, T.; Raphael, E., Residual stresses in thin polymer films cause rupture and dominate early stages of dewetting. *Nature Materials* **2005**, *4* (10), 754-758.
128. Damman, P.; Gabriele, S.; Coppee, S.; Desprez, S.; Villers, D.; Vilmin, T.; Raphael, E.; Hamieh, M.; Al Akhrass, S.; Reiter, G., Relaxation of residual stress and reentanglement of polymers in spin-coated films. *Physical Review Letters* **2007**, *99* (3).
129. Xue, L.; Han, Y., Pattern formation by dewetting of polymer thin film. *Progress in Polymer Science* **2011**, *36* (2), 269-293.
130. Higgins, A. M.; Jones, R. A. L., Anisotropic spinodal dewetting as a route to self-assembly of patterned surfaces. *Nature* **2000**, *404*, 476-478.
131. Kargupta, K.; Sharma, A., Dewetting of thin films on periodic physically and chemically patterned surfaces. *Langmuir* **2002**, *18* (5), 1893-1903.
132. Geoghegan, M.; Wang, C.; Rehse, N.; Magerle, R.; Krausch, G., Thin polymer films on chemically patterned, corrugated substrates. *Journal of Physics-Condensed Matter* **2005**, *17* (9), S389-S402.
133. Yoon, B.; Acharya, H.; Lee, G.; Kim, H. C.; Huh, J.; Park, C., Nanopatterning of thin polymer films by controlled dewetting on a topographic pre-pattern. *Soft Matter* **2008**, *4* (7), 1467-1472.
134. Mukherjee, R.; Bandyopadhyay, D.; Sharma, A., Control of morphology in pattern directed dewetting of thin polymer films. *Soft Matter* **2008**, 2086-2097.
135. Xing, R. B.; Luo, C. X.; Wang, Z.; Han, Y. C., Dewetting of polymethyl methacrylate on the patterned elastomer substrate by solvent vapor treatment. *Polymer* **2007**, *48* (12), 3574-3583.
136. Benor, A.; Hoppe, A.; Wagner, V.; Knipp, D., Microcontact printing and selective surface dewetting for large area electronic applications. *Thin Solid Films* **2007**, *515* (19), 7679-7682.
137. Zhang, Z.; Wang, Z.; Xing, R.; Han, Y., Patterning thin polymer films by surface-directed dewetting and pattern transfer. *Polymer* **2003**, *44* (13), 3737-3743.

138. Xia, Y.; Qin, D.; Yin, Y., Surface patterning and its application in wetting/dewetting studies. *Current Opinion in Colloid & Interface Science* **2001**, *6*, 54 - 64.
139. Lu, G.; Li, W.; Yao, J. M.; Zhang, G.; Yang, B.; Shen, J. C., Fabricating ordered two-dimensional arrays of polymer rings with submicrometer-sized features on patterned self-assembled monolayers by dewetting. *Advanced Materials* **2002**, *14* (15), 1049-1053.
140. Park, H.; Cheng, X., Thermoplastic polymer patterning without residual layer by advanced nanoimprinting schemes. *Nanotechnology* **2009**, *20* (24), 245308.
141. Kim, M. J.; Song, S.; Lee, H. H., A two-step dewetting method for large-scale patterning. *Journal of Micromechanics and Microengineering* **2006**, *16* (8), 1700-1704.
142. Wang, X.; Tvingstedt, K.; Inganas, O., Single- and bilayer submicron arrays of fluorescent polymer on conducting polymer surface with surface energy controlled dewetting. *Nanotechnology* **2005**, *16* (4), 437-443.
143. Luan, S. F.; Cheng, Z. Y.; Xing, R. B.; Wang, Z.; Yu, X. H.; Han, Y. C., Patterning organic luminescent materials by solvent-assisted dewetting and polymer-bonding lithography. *Journal of Applied Physics* **2005**, *97* (8), 086102.
144. Kim, Y. S.; Lee, H. H., Selective dewetting for general purpose patterning. *Advanced Materials* **2003**, *15* (4), 332-334.
145. Luo, C. X.; Xing, R. B.; Han, Y. C., Ordered pattern formation from dewetting of polymer thin film with surface disturbance by capillary force lithography. *Surface Science* **2004**, *552* (1-3), 139-148.
146. Zhang, H. L.; Bucknall, D. G.; Dupuis, A., Uniform nanoscopic polystyrene patterns produced from a microscopic mold. *Nano Letters* **2004**, *4* (8), 1513-1519.
147. Yoon, B. K.; Huh, J.; Kim, H. C.; Hong, J. M.; Park, C., Ordered patterns of microimprinted bilayer polymer films with controlled dewetting and layer inversion. *Macromolecules* **2006**, *39* (3), 901-903.
148. Park, M.; Hyun, D. C.; Kim, J.; Kim, Y. S.; Jeong, U., Dewetting-induced formation of periodic dot arrays of polymer/Au composites by capillary force lithography. *Chemistry of Materials* **2010**, *22* (14), 4166-4174.
149. Suh, K. Y.; Lee, H. H., Capillary force lithography: Large-area patterning, self-organization, and anisotropic dewetting. *Advanced Functional Materials* **2002**, *12* (6-7), 405-413.
150. Chou, S. Y.; Zhuang, L.; Guo, L. J., Lithographically induced self-construction of polymer microstructures for resistless patterning. *Applied Physics Letters* **1999**, *75* (7), 1004-1006.
151. Schaffer, E.; Thurn-Albrecht, T.; Russell, T. P.; Steiner, U., Electrically induced structure formation and pattern transfer. *Nature* **2000**, *403* (6772), 874-877.

152. Neto, C., A novel approach to the micropatterning of proteins using dewetting of polymer bilayers. *Physical Chemistry Chemical Physics* **2007**, *9* (1), 149-155.
153. Ramanathan, M.; Darling, S. B., Mesoscale morphologies in polymer thin films. *Progress in Polymer Science* **2011**, *36* (6), 793-812.

CHAPTER 2

Methods

2.1 Sample preparation

Sample preparation was performed in clean conditions, i.e. all the procedures were carried out in a class-100 laminar flow cabinet. Tweezers and all glassware were thoroughly cleaned with distilled ethanol, using Kimberly-Clark Kimwipe® tissues, and blown dry with pure nitrogen.

The substrates used to support the polymer films were silicon wafers with a native oxide layer (MMRC Pty Ltd, Malvern VIC Australia), typically 1.5 x 1.5 cm^2. The surfaces had to be thoroughly cleaned to remove chemical and particulate contaminants. In order to remove organic and large particulate contaminants, the silicon substrates were sonicated in distilled ethanol and then in distilled acetone. After blowing dry with pure nitrogen, they were cleaned with a custom built CO_2 snow jet to remove any residual small particles,[1] and treated further using a plasma cleaner (Harrick Plasma, Itacha NY, model PDC-002) to remove small traces of remaining organic contaminants.

Polymer films were cast on the silicon substrates by spin-coating (instrument: Laurell Technologies Co., PA, model WS400B-6NPP-LITE). During the spin-coating procedure, a drop of polymer solution in a volatile solvent is deposited on the substrate, which is then spun at a selected speed. The drop of polymer solution spreads on the sample due to centrifugal forces, while the solvent quickly evaporates leaving a smooth thin polymer film on the substrate. The thickness of the prepared film is directly proportional to the polymer solution concentration and the polymer molecular weight, and inversely proportional to the rotation speed.

Given the small thickness, the polymer films prepared in this work were easilly scratched by sharp tweezers.

2.2 Protein adsorption tests on polymer films

Protein adsorption tests were performed on the coatings developed in Chapters 3 and 5, to establish their protein adsorption/repulsion properties. The protein solutions were all prepared in phosphate buffer saline (PBS). The buffer was prepared by mixing $NaH_2PO_4 \cdot 7H_2O$ (10 mM), KCl (3 mM) and NaCl (140 mM) in Milli-Q® water and adjusting the pH to 7.4 using 1 M NaOH solution. The buffer solution was filtered using 0.45 μm cellulose acetate filters to eliminate potential bacterial contamination that could interact with the proteins. In Chapter 3, a quartz crystal microbalance was used to accurately determine the amount of adsorbed protein on cross-linked poly(*N*-vinylpyrrolidone), polystyrene and gold films. In Chapter 5, the presence of adsorbed proteins on patterned surfaces was determined by fluorescence optical microscopy and atomic force microscopy. Refer to the relevant chapters for details on the protein adsorption tests.

2.3 Atomic force microscopy (AFM)

The atomic force microscope is a type of scanning probe microscope that can be used to image the topography and surface properties of surfaces with high resolution, i.e. down to atomic resolution.[2] A sharp tip (in the order of 20 nm), positioned at the end of a spring cantilever, is scanned over the sample surface (Figure 2.1). In the simplest set up, namely contact mode, a sharp tip mounted on a flexible cantilever scans the surface of the sample in a raster fashion. The sample is mounted on a piezoelectric actuator, which adjusts its position so to maintain a constant distance (or force) between the probe and the surface. The XYZ movement of the piezoelectric is translated in a three-dimensional map of the sample's surface. The deflection of the

cantilever due to interaction with the sample is monitored through a laser reflected off the back surface of the cantilever and onto a photodiode. If the cantilever deflects by a larger or smaller amount than the nominated setpoint, the position of the laser reflected onto the photodiode will vary. A feedback loop adjusts the piezoelectric element height to restore the cantilever deflection to the nominated setpoint.[3, 4]

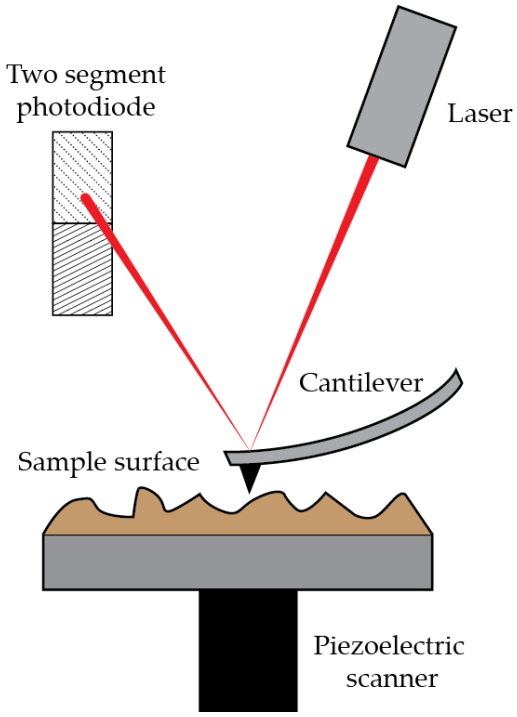

Figure 2.1 Schematic of the mechanism of the light lever in an atomic force microscope. The spring cantilever probes the surface, while the piezoelectric that holds the sample moves in a raster on the XY plane, and adjusts the Z distance thanks to the feedback loop and guided by the laser position on the photodiode reflected by the cantilever. The feedback loop works to keep the tip-surface distance (or force) constant.

State of the art AFMs can provide much more information than a simple topography image. In intermittent mode (defined Tapping Mode™ by Digital Instruments©), the cantilever oscillates at a given frequency and amplitude, "tapping" the surface lightly.[5, 6] This technique is widely used to

image soft samples such as polymer films or biological specimens. Tapping Mode™ AFM can provide additional information over contact mode: the amplitude of the cantilever oscillation can vary depending on the hardness of the surface, providing a map of its mechanical properties. This imaging mode can be used to identify biological matter on a hard surface, or different domains in topographically flat, phase-separated block-copolymer films.[7] In this Thesis, Tapping Mode™ AFM was used extensively to image flat poly(*N*-vinylpyrrolidone) films, and to determine their surface roughness (Chapter 3). The same technique was used to image micropatterned polymer films prepared by dewetting and grafted with PEG-like brushes (Chapter 5). The imaging was useful to determine the presence of proteins adsorbed in the dewetted holes on the surface. In this work, the instrument used was an Asylum Research (San Francisco CA) model MFP-3D-SA.

2.4 Ellipsometry

Ellipsometry is an optical technique that allows the characterization of the thickness and dielectric properties of thin films.[8] Shown in Figure 2.2 is a schematic of a typical set up. A beam is emitted from a light source (a monochromatic laser or a polychromatic source in the UV, visible or infrared) and linearly polarized before interacting with the sample. The light, with known linear polarization, penetrates the film, reflects from the underlying substrate and escapes the sample carrying information in the form of amplitude and phase changes in the polarized light. Because of these changes, the light is now elliptically polarized, hence the name of the technique. The second polarizer, called analyser, allows a certain amount of light to pass depending on its orientation relative to the elliptical electric field of the reflected beam. The light is finally captured by a detector. The

instrument records the complex reflectance ratio ρ, which is the ratio between the Fresnel reflection coefficients for the *p*- and *s*- polarized light (electric fields parallel and perpendicular to the plane of incidence, respectively), and is a function of the relative amplitude change Ψ and the phase shift Δ (Equation 2.1).[9]

$$\rho = tan(\Psi)\, e^{i\Delta} \tag{2.1}$$

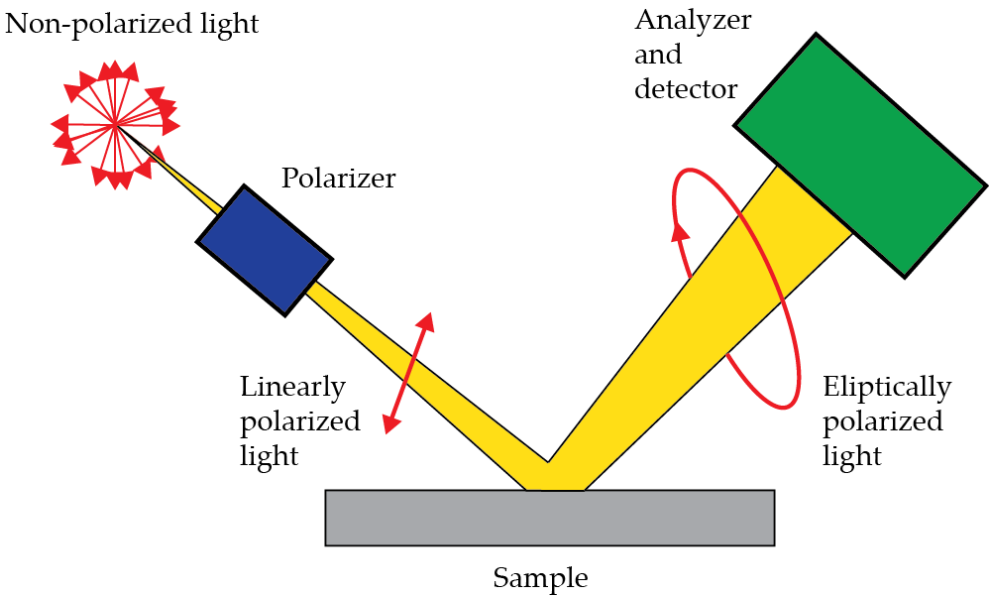

Figure 2.2 Schematic diagram of a reflection ellipsometer. The light source, in this work a multi-wavelength source in the UV-visible range, is linearly polarized before interacting with the sample. Once the light is reflected by the sample, it carries information in the form of amplitude and phase offsets, which cause the polarization of the light to change to elliptical. These parameters can be fitted with an appropriate model to extrapolate the film thickness and optical constants. Monolayered and multilayered films can be easily modelled.

In a second step, a model must be compiled in order to generate theoretical Ψ and Δ values based on the known composition of the sample (i.e. number and composition of layers, roughness and estimated refractive

indices), using Fresnel's equation. The model is then used to fit to the experimental data in an iterative minimum square deviation algorithm. The fitting provides accurate values for the layer thicknesses and refractive indices.

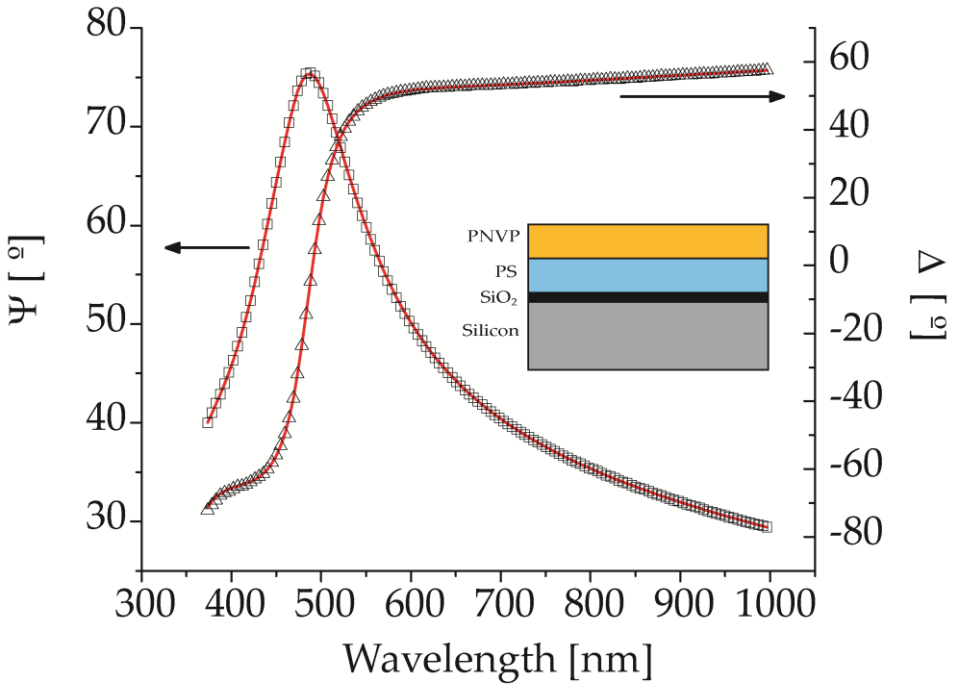

Figure 2.3 Experimental Ψ and Δ data acquired for wavelengths in the range 370-1000 nm for a PNVP/PS bilayer on a silicon wafer, at an angle of incidence of 75°. The thickness of the silicon base layer was assumed to be 1 mm, which is very large compared to the studied layers. The thickness of silica (1 nm) was determined in a previous step, as well as the thickness (56.65 nm) and refractive index (1.562) of the PS layer, using the Cauchy formula. The PNVP film refractive index was also modelled with the Cauchy dispersion formula. The fitting parameters in the overall model were the PNVP film thickness and Cauchy coefficients. The model scenario is shown in the inset.

Shown in Figure 2.3 are experimental curves of Ψ and Δ at different wavelength for a multilayer obtained by sequential spin-coating of poly(*N*-vinylpyrrolidone) (PNVP) on top of polystyrene (PS), on a silicon wafer

coated with a thin layer of silicon oxide. The study on dewetting and cross-linking of PNVP on polystyrene is discussed in Chapter 4. Also shown in Figure 2.3 is the fitting of the experimental data. The Cauchy dispersion equation was used to model the refractive index of the PNVP layer (Equation 2.2):

$$n(\lambda) = A_n + \frac{B_n}{\lambda} + \frac{C_n}{\lambda^4} + \ldots \quad (2.2)$$

The contributions of the 4th term and above in the equation are irrelevant for most applications. The overall model fitting parameters were the PNVP thickness and the Cauchy refractive index coefficients A_n, B_n and C_n. The results are summarised in Table 2.1, along with the minimum square error (MSE).

Table 2.1 Fitted thickness and Cauchy coefficients obtained from the modelling of the optical data for a PNVP film on a PS film. The experimental data is reported in Figure 2.3.

MSE = 5.87	
PNVP thickness	44.845 ± 0.026
An	1.5030 ± 0.0007
Bn	0.00248 ± 0.00033
Cn	0.00027 ± 0.00004

In this work, a J.A. Woollam Co. Inc. model M-2000 V was used to determine the thickness of the prepared polymer films on silicon, using an angle of incidence of 75° in a wavelength range of 370 – 1000 nm. In preliminary experiments, the angle of incidence was scanned in the range 60° - 80°, to identify the optimal value that produced the best data quality. The data were processed and fitted using the software WVASE32® provided with the instrument. Details on the fitting procedures for the polymer films

prepared in this work are reported in the Methods sections in each relevant chapter (Sections 3.2, 4.2 and 5.2).

2.5 Neutron and X-ray reflectometry

Reflectometry is a technique that uses radiation of different wavelengths to investigate the internal structure of thin films on a substrate. The types of radiation used in this Thesis were X-rays and neutrons.

X-rays interact with the electron clouds in matter. They are very weakly penetrating, as electron clouds occupy much of the volume of matter. X-rays interacting with matter may scatter, with higher atomic numbers scattering by a greater amount. The scattering is related to the refractive index of a given material n, via the scattering length density (SLD) (Equation 2.3 and 2.4). SLD is a parameter that describes the scattering cross section of a given material towards a given radiation (Equation 2.5).

$$n = 1 - (\delta + i\beta) \tag{2.3}$$

$$\delta = \frac{\lambda^2}{2\pi} SLD \tag{2.4}$$

$$SLD = r_e N_a \rho \frac{\sum_i Z_i}{\sum_i M_i} \tag{2.5}$$

In Equation 2.3, δ is the deviation of the refractive index from 1 and β is the absorption index. In Equation 2.4, λ is the radiation wavelength. In Equation 2.5, r_e is Bohr's radius, N_a is Avogadro's number, ρ is the mass density, and Z_i and M_i are the atomic number and the molar mass of the i^{th} atom.

Neutrons on the other hand are extremely penetrating, as they interact only with nuclei. Nuclei are about 1/5th of the total atom size, hence the cross section of a material to neutrons, described by the *SLD*, is much smaller than for X-rays. The *SLD* for neutrons is reported in Equation 2.6.

$$SLD = N_a \rho \frac{\sum_i b_i}{\sum_i M_i} \tag{2.6}$$

where b_i is the neutron scattering length of the i^{th} atom.

As neutrons interact only with the nuclei, they can give much better contrast than X-rays. The downside to this technique is that because they are scarcely scattered, a very long acquisition time is required to obtain a reasonably intense signal.

Neutron reflectometry (NR) and X-ray reflectometry (XRR) were used in this Thesis to investigate the structure and composition of polymer thin films on flat silicon wafers. In standard NR or XRR experimental set ups, samples are irradiated by a collimated beam at a given angle, θ. The radiation is reflected and collected by the detector, positioned at the same angle as the radiation source, in a mirror configuration. The intensity of the reflected radiation is called reflectivity, R, and is plotted against the momentum transfer vector, Q, a parameter that contains the radiation angle of incidence, θ and its wavelength, λ (Equation 2.7).

$$Q = 4\pi \sin\frac{\theta}{\lambda} \tag{2.7}$$

Reflectivity is related to Q as described in Equation 2.8.

$$R(Q) = \frac{16\pi^2(\Delta SLD)^2}{Q^4} \tag{2.8}$$

In the instruments accessible at the Australian Nuclear Science and Technology Organization (ANSTO) facilities located at Lucas Heights, Sydney NSW, Q is varied by varying the incidence angle in XRR. In NR instead, Q is varied by varying the radiation wavelength, using a time of flight detector combined with a set of choppers, which separate neutrons of different speed (i.e. wavelength). The radiation is completely reflected for low angles of incidence. Once a critical angle, θ_c, is overcome, the radiation penetrates the sample, and the reflectivity decays as Q^4 (Equation 2.8).

Shown in Figure 2.4 are X-ray and neutron reflectivity profiles for a multilayer of poly(methyl methacrylate) (PMMA) over deuterated polystyrene (d-PS), supported on a silicon wafer. This example is representative of the structures investigated in this Thesis. The NR and XRR data are fitted with a model where the variables are the thickness, the *SLD* and the roughness of the layers. The data modelling includes *SLD* profiles versus sample depth, to easily visualise the *SLD* contrast between the layers (insets in Figure 2.4). The profiles show Kiessing fringes, which arise by the constructive and destructive interaction of waves scattered by the different layers. The distance between the fringes is inversely proportional to the film thickness. In XRR the *SLD* contrast between the two polymer films is very low, as indicated by the *SLD* profile against sample depth (inset in XRR graph, Figure 2.4). The curve can only be fitted with a 20 nm thick monolayer. By using neutron reflectivity, the contrast between the polymer layers makes it easier to measure the thickness of the d-PS film. However, the PMMA film has very little contrast with air and it is not detected, and all that is possible to measure is a 10 nm thick d-PS film. This could be solved by substituting air with D_2O, a strategy often used in neutron reflectometry experiments.[10]

XRR is often used as a preliminary investigation to obtain accurate values of the film thickness and roughness. As roughness dampens the

Kiessing fringes and hides much of the information in the data, only relatively flat samples can then be studied by NR.

The technical specifications of the instruments used at ANSTO are reported in the following. X-ray reflectivity profiles were measured on a Panalytical Ltd X'Pert Pro Reflectometer using Cu Kα X-ray radiation (λ = 1.54056 Å). The X-ray beam was focused using a Göbel mirror and collimated with 0.2 mm pre- and post-sample slits.

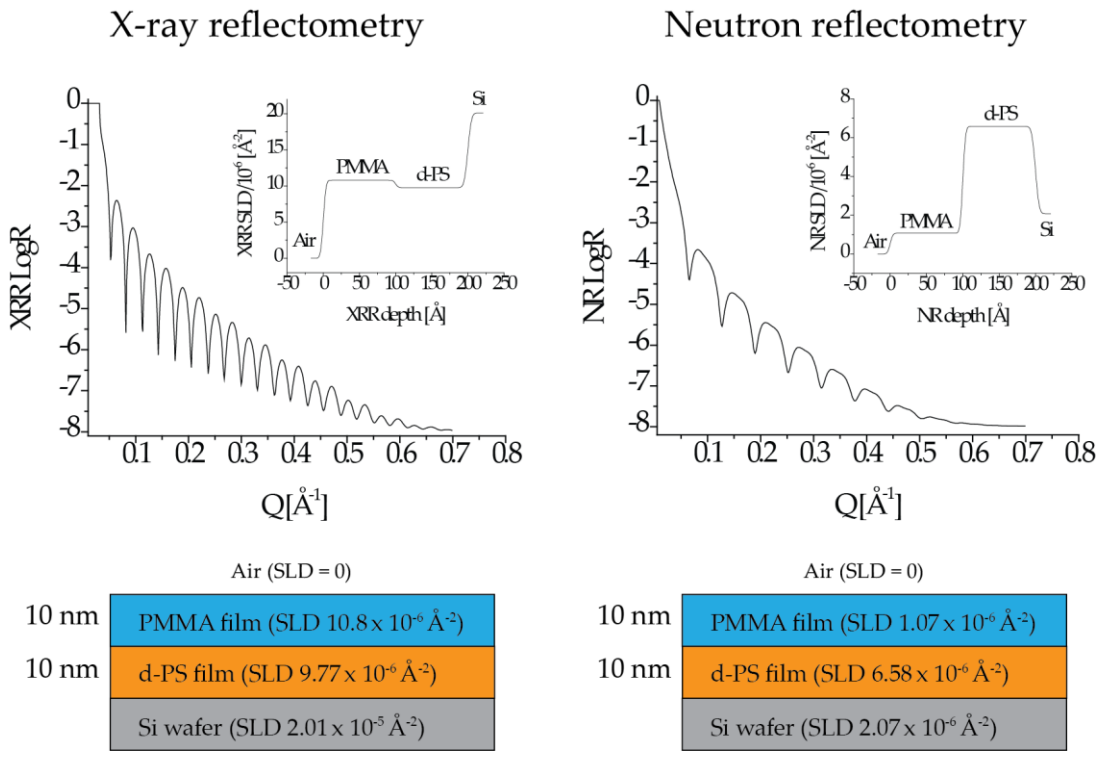

Figure 2.4 Example of X-ray and neutron reflectivity curves showing Kiessing fringes for a multilayer of poly(methyl methacrylate) (PMMA) over deuterated polystyrene (d-PS), supported on a silicon wafer. The substitution of hydrogen with deuterium, as in PS here, is often used to enhance the contrast between components, because deuterium has a much higher SLD than hydrogen. The film thicknesses and the scattering length densities (SLD) are indicated in the schematic. Picture adapted from data kindly provided by Prof. Michael James, ANSTO Lucas Heights NSW.

Neutron reflectivity data were measured using the Platypus time-of-flight neutron reflectometer and a cold neutron spectrum (3.0 Å ≤ λ ≤ 18.0 Å) at the OPAL 20 MW research reactor at ANSTO, Lucas Heights.[10] 23 Hz neutron pulses were generated using a disc chopper system (EADS Astrium GmbH) in the medium resolution mode ($\Delta\lambda/\lambda$ = 4%), and recorded on a two-dimensional helium-3 neutron detector (Denex GmbH).

Structural parameters were refined using the MOTOFIT reflectivity analysis software with reflectivity data as a function of the momentum transfer vector, Q.[11] In the fitting routines, the Levenberg-Marquardt method was selected to minimize χ^2 values by varying the films thickness, roughness and scattering length density (*SLD*).

2.6 Thermogravimetric analysis (TGA) and differential scanning calorimetry (DSC)

TGA and DSC were used in this Thesis to determine the thermal properties of the polymers used. In TGA, the mass change of the polymer sample is monitored while the temperature is changed according to a pre-defined program. In a basic experiment the temperature was ramped over a certain range, to identify the mass loss due to impurities such as water, and the temperature at which degradation occurred. In the work presented in Chapter 3, TGA was used to ascertain that poly(*N*-vinylpyrrolidone) was stable at the temperatures used for cross-linking, in air and in nitrogen atmospheres.

DSC is used to monitor the heat flow in and out of a sample. For example, to identify phase transitions of endothermic nature, such as glass transitions or meltings, and of exothermic nature, such as crystallizations.

For polymers, DSC curves can be quite complex, and provide much information about the polymer structure, impurities and molecular weight polydispersity. In Chapter 3, DSC was used to identify the glass transition temperature of poly(*N*-vinylpyrrolidone), and in Chapter 5 it was used to determine the thermal transitions of the synthetised macroinitiator polymer. The instruments used in this work were a Hi Res TGA 2950 (TA Instruments, New Castle, DE) and a DSC 2920 (TA Instruments, New Castle, DE).

2.7 Size exclusion chromatography (SEC)

SEC is a member of a vast family of physical methods used to separate and analyse complex mixtures.[12] SEC separates macromolecules such as polymers depending on their hydrodynamic volume in the chosen solvent. This volume can be related to the polymer molecular weight, given an appropriate calibration curve.[13, 14]

In the general experimental set up, an eluent is pumped at a constant flow through a column packed with porous beads, with which the polymer does not interact. This makes SEC different to other chromatographic techniques such as high performance liquid chromatography (HPLC). The eluent carries the analyte through the column and to the detector; the different components of the sample are separated solely because of their size difference. Small molecules can penetrate in all the pores of the column packing, and hence spend a longer time in the column, while larger molecules cannot penetrate most of the pores, and elute more quickly. The data collected by the detector are plots of signal intensity against elution time. In the common case of a differential refractive index detector (DRI), the signal arises from the difference in refractive index between a cell filled with pure eluent and one containing the analyte solution eluted from the column.

These data plots show peaks for each component of the separated mixture. The peaks always exhibit a Gaussian shape, due to the unavoidable distribution of elution times for a given analyte size. In the case of polymers, the broadening of a chromatographic peak is mainly due to their molecular weight distribution. Once the SEC system is calibrated by eluting polymers of known molecular weight, the analyte molecular weight can be determined from its elution time, and its molecular weight distribution can be determined from the width of the peak. It is important to notice that the relationship between hydrodynamic volume and mass is not the same for all the polymers, so in theory calibration curves should be built using standards of the same polymer that is being analysed. Often this is not possible due to unavailability of such standards, so in the case of DRI only approximate molecular weight can be measured, using the same standard (generally polystyrene) for the characterization of many different polymers. It is possible to improve the accuracy of the molecular weight values determined using polystyrene standards by employing appropriate Mark-Houwink-Sakurada parameters for the polymer analysed in the software calculation routine. An even more accurate molecular weight may be obtained using the combination of multiple detectors.[15] Details on the instruments and conditions used in the work reported in this Thesis can be found in Section 5.2.4.

2.8 Nuclear magnetic resonance spectroscopy (NMR)

NMR spectroscopy is widely used to characterize organic compounds such as polymers.[16] It is able to discriminate nuclei based on their chemical environment, and can therefore give precious information on the chemical structure of a molecule. In brief, any given nucleus with an odd number of

protons and/or neutrons has an intrinsic magnetic moment and angular momentum, which ultimately gives it non-zero spin. Both the magnitude and orientation of this momentum are quantised. For example, the most commonly used nucleus in NMR is ^1_1H, which has spin = ±1/2. These two states are degenerate, i.e. have the same energy. If such nuclei are placed in a magnetic field, they interact differently with it, and become separated in two states with different energy.

An electromagnetic radiation of the correct frequency, typically a radio frequency radiation, can induce a transition of the low energy nuclei to the high energy state. Such transition can be recorded by the instrument. In this scenario, the data would consist of a single peak, because all the nuclei would give the same transition. In a real molecule though, the electrons surrounding the resonating nuclei can shield them from the magnetic field in different ways, effectively reducing the energy gap between spin states, and hence the resonating frequency, of each nucleus. The offset from the unshielded frequency is called chemical shift, and is characteristic for a given chemical functionality. To avoid solvent interference in ^1_1H NMR, polymer samples are dissolved in a deuterated solvent, as deuterium has a zero spin. In this work, samples of the synthesised polymers were routinely analysed by NMR to confirm the reaction chemistry.

2.9 Quartz crystal microbalance (QCM)

A QCM measures the mass adsorbed on a quartz crystal acoustic resonator. Quartz is a piezoelectric material, and can hence vibrate if an alternate voltage is applied to it. The frequency of the resonator changes proportionally to the adsorbed mass, according to the Sauerbrey equation[17] (Equation 2.9):

$$\Delta m = \Delta f \sqrt{(p_q \mu_q)}/2f_0 \tag{2.9}$$

where Δm is the adsorbed mass (g cm^{-2}), Δf is the frequency shift, p_q is the density of quartz (2.648 g cm^{-3}), μ_q is the shear modulus of quartz for the specific type of crystal used, and f_0 is the fundamental resonant frequency of the crystal. The equation is theoretically valid only for rigid thin films that behave as solids, with masses much smaller than that of the crystal, evenly distributed on the surface, and where no viscoelastic dissipation occurs upon vibration. In the case of proteins adsorbed from a solution onto the crystal surface this is often not the case, yet the equation gives fairly accurate values of adsorbed mass.[17] It should also be noted that often hydration water in the sample, which can move with the crystal, is included in the measured adsorbed mass.

In this work, the crystals used were AT-cut gold coated crystals, with a shear modulus, μ_0 = 2.947x10^{11} g cm^{-1} s^{-1} and a fundamental resonant frequency, f_0 = 5 MHz. The third overtone of this frequency was used for the calculations because of the reduced noise and baseline drift.

2.10 Fourier transform infrared spectroscopy (FTIR)

Infrared spectroscopy utilizes infrared (IR) radiation to gain information on the identity and structure of molecules. IR radiation has wavelengths typically in the range 0.8 – 1000 μm. The radiation energy is conventionally expressed in wavenumbers (cm^{-1}), so the range would be 14000 – 25 cm^{-1}. Molecules can absorb IR radiation to undergo rotational-vibrational transitions. As energy absorption due to bond vibrations and

rotations of a molecule, or of functional groups within large and complex molecules, have distinct frequencies that depend on the bond strength and the mass of the atoms involved, they can be identified readily in an IR spectrum.

In the present study, a Bruker Vertex 80v FTIR spectrophotometer with a Hyperion 3000 FPA microscope system was employed to acquire data on polymer thin films. The microscope piece allowed focusing of the IR radiation on the thin film, so to maximize its absorption signal. The data were analysed using the OPUS® software provided by the manufacturer. Each spectrum was corrected for CO_2 and H_2O absorption, which are ubiquitous in IR experiments in air.

2.11 X-ray photoelectron spectroscopy (XPS)

X-ray photoelectron spectroscopy (XPS) is a quantitative spectroscopic technique that uses X-rays to obtain information on the composition of a material.[18] In an ultra-high vacuum chamber, used to avoid scattering interference of photoelectrons from air molecules, the sample is bombarded with high energy, typically monochromatic X-rays (~10^3 eV). The energy involved allows the extraction of electrons from the inner, core valence shells of an atom. The photoelectrons ejected are collected by a detector, which records their kinetic energy and number. The kinetic energy of a photoelectron depends on its binding energy. Every chemical element has a unique electronic structure; hence they emit photoelectrons with specific kinetic energies, which are tabulated.

In molecules, the electron binding energies of an atom are strongly influenced by the surrounding chemical species, so the kinetic energies of such photoelectrons carry information on the nature of the functional group

they arise from. The number of photoelectrons emitted, normalized against a reference, is related to the concentration of each chemical species in the sample. X-rays can penetrate the sample to a depth of a few microns, but only the photoelectrons from the top 1-10 nm can escape into the vacuum. Electrons from deeper within the material are both elastically and in-elastically scattered and do not escape the surface of the material.

XPS is widely used to characterize polymers. The carbon photoelectron peak contains signals from carbon based species such as alcohols, esters, ethers, and carboxylic acids. The complex peak can be deconvoluted into a number of components using appropriate software, so that the functional groups in the polymer can be identified by photoelectrons with distinct binding energies. In this work, XPS was used to investigate the chemical changes arising during cross-linking of PNVP in Chapter 3, and the chemical compositional changes associated with the growth of poly(PEGMA) brushes, synthesised using surface initiated reversible-deactivation radical polymerisation reactions, in Chapter 5.

In polymer thin film characterisation, XPS offers the possibility to map a certain area of a sample by analysing for specific elements. The detector can be set to record data only for a specific element, and the sample surface can be probed in a raster to produce an image that corresponds to a chemical map. The image will show a contrast based on the amount of the targeted element in each pixel. This technique was employed in this work to characterize the chemical patterns obtained upon dewetting of polymer thin bilayer films (Chapter 5). Details on the instruments and acquisition setting used in this work can be found in the experimental details of the relevant chapters (Chapters 3 and 5).

2.12 References

1. Sherman, R., Carbon dioxide snow cleaning. *Particulate Science and Technology: An International Journal* **2007**, *25* (1), 37 - 57.
2. Binnig, G.; Quate, C. F.; Gerber, C., Atomic force microscopy. *Physical Review Letters* **1986**, *56* (9), 930-933.
3. Giessibl, F. J., Advances in atomic force microscopy. *Reviews of Modern Physics* **2003**, *75* (3), 949-983.
4. Alessandrini, A.; Facci, P., AFM: a versatile tool in biophysics. *Measurement Science & Technology* **2005**, *16* (6), R65-R92.
5. Martin, Y.; Williams, C. C.; Wickramasinghe, H. K., Atomic force microscope mapping and profiling on a sub 100-A scale. *Journal of Applied Physics* **1987**, *61* (10), 4723-4729.
6. Zhong, Q.; Inniss, D.; Kjoller, K.; Elings, V. B., Fractured polymer silica fiber surface studied by tapping mode atomic-force microscopy. *Surface Science* **1993**, *290* (1-2), L688-L692.
7. Garcia, R.; Perez, R., Dynamic atomic force microscopy methods. *Surface Science Reports* **2002**, *47* (6-8), 197-301.
8. Neal, W. E. J.; Fane, R. W., Ellipsometry and its applications to surface examination. *Journal of Physics E-Scientific Instruments* **1973**, *6* (5), 409-416.
9. Fujiwara, H., *Spectroscopic ellipsometry: principles and applications.* John Wiley & Sons Ltd: Chichester, **2007**.
10. James, M.; Nelson, A.; Holt, S. A.; Saerbeck, T.; Hamilton, W. A.; Klose, F., The multipurpose time-of-flight neutron reflectometer "Platypus" at Australia's OPAL reactor. *Nuclear Instruments and Methods in Physics Research Section A: Accelerators, Spectrometers, Detectors and Associated Equipment* **2011**, *632* (1), 112-123.
11. Nelson, A., Co-refinement of multiple-contrast neutron/X-ray reflectivity data using MOTOFIT. *Journal of Applied Crystallography* **2006**, *39*, 273-276.
12. Moore, J. C., Gel permeation chromatography. I. New method for molecular weight distribution of high polymers. *Journal of Polymer Science Part A-General Papers* **1964**, *2* (2PA), 835-843.
13. Wang, Y.; Teraoka, I.; Hansen, F. Y.; Peters, G. n. H.; Hassager, O., A theoretical study of the separation principle in size exclusion chromatography. *Macromolecules* **2010**, *43* (3), 1651-1659.
14. Grubisic, Z.; Rempp, P.; Benoit, H., A universal calibration for gel permeation chromatography. *Journal of Polymer Science Part B-Polymer Letters* **1967**, *5* (9PB), 753-759.
15. Holding, S. R.; Meehan, E., *Molecular weight characterization of synthetic polymers*. Rapra Technology Ltd: GBR, **1995**.

16. Bovey, F. A.; Mirau, P. A., *NMR of polymers*. Academic Press: San Diego, **1996**.
17. Sauerbrey, G., Verwendung von schwingquarzen zur wagung dunner schichten und zur mikrowagung. *Zeitschrift Fur Physik* **1959**, *155* (2), 206-222.
18. Briggs, D.; Grant, J. T., *Surface analysis by Auger and x-ray photoelectron spectroscopy*. IM Publications LLP: Chichester, **2003**.

CHAPTER 3

Thermally cross-linked poly(*N*-vinylpyrrolidone) films as bio-inert coatings

3.1 Introduction

Surgical implantation procedures such as artificial cochlea implantation[1] and stent implantation[2] have become more and more widespread in medicine and are now routinely performed. *In vivo* biosensing to continuously monitor the concentration of analytes in the blood stream, such as glucose in diabetic patients, is also common.[3-5] The performance of biomaterials and biosensing devices however can be hampered by biofouling, i.e. the non-specific adsorption of proteins and biomolecules from solution,[6] as introduced in Chapter 1. Briefly, when a foreign material comes in contact with a tissue, it is rapidly coated by proteins in the first instance, and then platelets and immune cells. In some cases a fibrous capsule can develop which can severely limit the ability of the device to function properly. This is collectively known as foreign body reaction (FBR). Non-specific protein adsorption on the surfaces of biomedical devices can also allow attachment of bacteria, and the formation of a biofilm which can be very difficult to treat with antibiotics.[7-10] Once injected in the blood stream, drug delivery particles or magnetic particles for medical imaging are quickly covered with plasma proteins before they can perform their function.[11, 12] *In vivo* devices such as biomedical implants inserted in the human body may provoke a dramatic cascade of events that eventually causes surface-induced thrombosis.[13] The accumulation of proteins on the surface of contact lenses can also lead to infections.[14] An effective strategy to overcome the non-specific adsorption of proteins is to use a bio-inert coating, which limits the interaction of the foreign body with the host.

Hydrophilic polymers, such as poly (ethylene glycol)s,[15, 16] poly (*N*-vinylpyrrolidone),[17] and polymers containing zwitterionic functionalities,[18] are widely used as antifouling coatings for medical devices, since their

properties can be finely tailored and surfaces can relatively easily be coated with them.[19-21] The general mechanism of antifouling of polymer coatings has been described in Chapter 1 for polymer brushes. As stated earlier, similar mechanisms come into play for any hydrophilic polymer coating that has the ability to swell in water, or adsorb a tightly bound layer of water at the interface. This is the case of poly (*N*-vinylpyrrolidone) (PNVP, top of Figure 3.13). PNVP is well known for its antifouling properties, widely used and readily available.[22-25] PNVP is non-toxic, water-soluble and completely biocompatible in humans.[26, 27] It is used as a binder in many pharmaceutical tablets,[28] in dental care and wound care products,[29, 30] in cosmetics,[31] in contact lenses,[32] and as a plasma expander.[33] In its bulk cross-linked form (as a hydrogel) it is used in drug delivery systems.[34, 35] However, because of its solubility in water, PNVP coatings are only useful for contact with body fluids after treatment or modification to make the polymer insoluble. PNVP brushes have been used as antifouling coatings.[17, 25] The grafting technique, although effective, requires a number of synthetic chemical steps.

As noted above, PNVP coatings are also commonly prepared in the form of hydrogels. A hydrogel is a loosely cross-linked polymer swollen with a large volume of water (i.e. contains a high water volume fraction). PNVP hydrogels can be prepared by using either an electron beam,[36] redox reactions,[37] or UV-activated molecules[38] as cross-linking mechanisms. In the case of radiation-induced cross-linking it is believed that the water in the hydrogel is necessary to allow chain mobility and produce an effective cross-linking[39, 40] so homopolymeric PNVP thin films have rarely been investigated.[41] The generation of radicals in PNVP by thermal annealing has been previously proposed,[42] but thermally-induced cross-linking has never been characterised in thin films, nor have such films been employed in biomedical applications.

In the work described in this Chapter, for the first time a method is introduced to prepare cross-linked PNVP antifouling coatings on surfaces of any geometry and size by simple and cost effective techniques such as spin- or dip-coating and thermal annealing, without the use of cross-linking agents or high energy radiation. Under specific annealing conditions, PNVP films spontaneously cross-link, becoming insoluble in water and many other solvents, whilst maintaining the antifouling properties of unmodified PNVP. The degree and the rate of the process can be tuned by controlling the temperature. This work has been recently published.[43]

3.2 Materials and Methods

3.2.1 Surface preparation

The silicon wafers used as substrates and their cleaning procedure were described in Section 2.1.

PNVP films were prepared by spin coating a 10 mg mL^{-1} filtered ethanol solution of PNVP (29000 g mol^{-1}, 95%, Sigma-Aldrich) at 3000 rpm for 1 minute. Polystyrene (PS) films were prepared in a similar manner from a 10 mg mL^{-1} toluene solution of PS (96000 g mol^{-1}, *PDI* 1.04, PSS Germany) at 4000 rpm for 1 minute. The average thickness of the PNVP films obtained was 40 ± 1 nm, as determined by spectroscopic ellipsometry (J.A. Woollam Co.). Annealing of PNVP films was performed on a hot plate with fine temperature control (ATV Technologie GmbH Muenchen, model TR-124) in air. Non-cross-linked PNVP was eliminated by rinsing the films with 150 mL of Milli-Q® water. After rinsing, the films were blown dry with a pure nitrogen stream and dried on a hot plate at 100 °C for 30 minutes to remove residual water. Ellipsometry was described in Section 2.4.

3.2.2 Bulk polymer characterization

The PNVP in powder form was characterized by thermogravimetric analysis in air and in nitrogen and by differential scanning calorimetry. The techniques and equipment were described in Section 2.6. The measurements were carried out by Dr. Hank deBruyn at the University of Sydney.

3.2.3 Thin Film characterization

The thickness of the PNVP/PS films was characterized by ellipsometry (see Section 2.4). The thickness of the SiO_2 layer (1 nm) on top of the silicon wafer was determined on the bare silicon wafer first, using the relevant model provided with the software. The system was treated as a monolayer. Then the PNVP film was spin-cast onto the silicon wafer. The system was modelled as a bilayer, where the SiO_2 thickness was fixed, and the polymer film was modelled using the Cauchy equation. The polymer thickness, and the constants A and B for the Cauchy equation, were measured. The constant C for the Cauchy equation was fixed to zero. The constant A, which is by far the largest contribution to the refractive index value, was about 1.50.

PNVP films were characterized using X-ray and neutron reflectometry at the Australian Nuclear Scientific and Technology Organization (ANSTO) Lucas Heights facility in Sydney, under the direction of Prof. Michael James. Four films were characterized after different annealing and washing procedures. Reflectivity data were collected over the angular range $0.05° \leq \lambda \leq 5.00°$, with a step size of 0.01° and counting times of 10 s per step.

Neutron reflectivity data was obtained from these polymer films using the Platypus time-of-flight neutron reflectometer. Reflected beam spectra were collected for each of the as-prepared and modified PNVP films

at 0.5° for 2 hours (0.5 mm slits) and 2.0° for 6 hours (2 mm slits) respectively. Neutron reflectivity data were also collected for one film at 4.0° for 8 hours (4.0 mm slits). Direct beam measurements were collected under the same collimation conditions for 1 hour each.

Structural parameters for these PNVP films were refined using the MOTOFIT reflectivity analysis software. One or two layer models were used, and single-layer models were chosen when no significant improvement in the fitting quality was observed upon the introduction of an additional layer. Due to the lack of X-ray scattering contrast between silicon (SLD = 2.01×10^{-5} Å^{-2}) and the native silicon oxide layer (SLD = 1.89×10^{-5} Å^{-2}), the silicon oxide layer was omitted from structure refinements using X-ray reflectivity data. In the case of models refined using neutron reflectivity data, an additional ~10 Å layer was included adjacent to the silicon (SLD = 2.07×10^{-6} Å^{-2}), representing the native oxide layer (SLD = 3.47×10^{-6} Å^{-2}). More details on neutron and X-ray reflectivity can be found in Section 2.5.

Investigations of the chemical composition of untreated and annealed films were carried out by transmission Fourier transform infrared spectroscopy (Section 2.10), at the vibrational spectroscopy unit at the University of Sydney.

Further information about the elemental make-up of the as-prepared and annealed (but not rinsed) PNVP thin films was obtained from X-ray photoelectron spectroscopy (XPS) data. The XPS analysis and data fitting were performed by Dr. Bill Gong at the surface analysis facility at the University of New South Wales. In the work described in this Chapter, the data was collected using an Escalab 220i-XL spectrometer (VG, UK) with monochromatic Al $K\alpha$ exciting radiation (energy 1486.6 eV). Typical operating conditions were: power 120 W (10 kV, 12 mA) and spot size 1 mm^2. Survey spectra were collected with a step width of 1 eV and high resolution spectra with a step width of 0.1 eV.

The wetting properties of the PNVP films were investigated by measuring the static contact angle of 5-10 μL sessile droplets of Milli-Q® water with a KSV CAM200 Contact Angle System (KSV Instruments Ltd., Helsinki, Finland).

Due to the fact that cross-linked PNVP was insoluble in water, the percentage of cross-linked film could be related to the residual film thickness after rinsing with Milli-Q® water. The cross-linking dependence on annealing time and temperature was investigated using spectroscopic ellipsometry (Section 2.4). The films were annealed at different temperatures and for different times (160 °C, 170 °C, 180 °C, 200 °C for 30 minutes, 1 hour, and 3 hours) and the thickness of the films was measured. The films were then rinsed with Milli-Q® water, dried as described above, and the thickness re-measured. Two samples were analysed for each annealing time and temperature. Ellipsometry was also used to investigate the stability of PNVP films annealed at 200 °C for 3 hours, after soaking in water for extended periods. Film thickness was measured after annealing and again after soaking in water for specified periods of time and drying.

The topography and surface roughness of the PNVP films were investigated using atomic force microscopy in Tapping Mode™.

3.2.4 Protein adsorption

A quartz crystal microbalance with dissipation (QCM-D) was used to investigate the adsorption of two proteins, fibrinogen (FGN, Sigma -Aldrich) and immunoglobulin G (IgG, Sigma-Aldrich), on PNVP films, PS films, and gold. The PS and the PNVP films were prepared by spin coating onto these sensors as described above. The PNVP film was annealed at 200 °C for 3 hours to obtain complete cross-linking.

Before each measurement, the QCM crystals were all initially equilibrated in phosphate buffer saline (PBS, prepared as described in Section 2.2). Protein adsorption experiments were then carried out in parallel using a 1 mg mL^{-1} FGN solution in PBS on one set of crystals, and a 1 mg mL^{-1} IgG solution in PBS on another set. The protein solutions were passed over the sensor at a flow rate of 100 μL min^{-1} for 20 minutes, the flow stopped, and the surfaces left in contact with the protein solution for about 1 hour. Finally the surfaces were rinsed with PBS. The whole analysis was performed under temperature control at 37 ± 1 °C.

3.3 Results

3.3.1 Thermogravimetric analysis (TGA)

The TGA was performed by Dr. Hank deBruyn at the University of Sydney. The PNVP powder used to prepare all the samples was characterized by TGA to determine the mass loss under the annealing conditions used in the preparation of the coatings, as well as to ensure that no significant decomposition of the polymer was taking place. The powder was quickly heated (in less than 2 minutes) to 200 °C and left at this temperature for 3 hours, both in air and in nitrogen. The TGA profiles in Figure 3.1 present a small decrease in mass (about 8-9%) in the first minutes of the annealing, both in air and in nitrogen. This initial mass loss was due to a small quantity of water retained by PNVP (up to 5% according to the manufacturer product description, given that PNVP is a hydrophilic polymer), as well as impurities such as unreacted monomer. After the first few minutes in a nitrogen atmosphere, the mass of the PNVP sample remained constant for the rest of the measurement time (3 hours), while in

air the sample mass increased by about 0.1%, which could be interpreted as a sign of mild oxidation. Apart from this, the polymer did not decompose nor gain substantial mass after three hours thermal annealing at 200 °C both in air and in nitrogen.

Previous studies have revealed that thermal treatment of PNVP in an oxygen atmosphere gave rise to volatile degraded products at lower temperatures than in an inert atmosphere, with degradation of the polymer occurring above 250 °C, which is considerably higher than the 200 °C used in this study. At these elevated temperatures, as high as 400 °C, the presence of an oxygen atmosphere has been shown to lead to the formation of peroxide residues, which decompose and give rise to the formation of active radicals.[42] The mechanism of photooxidation of PNVP films under UV light irradiation has also been investigated before and leads primarily to the formation of insoluble fractions.[41]

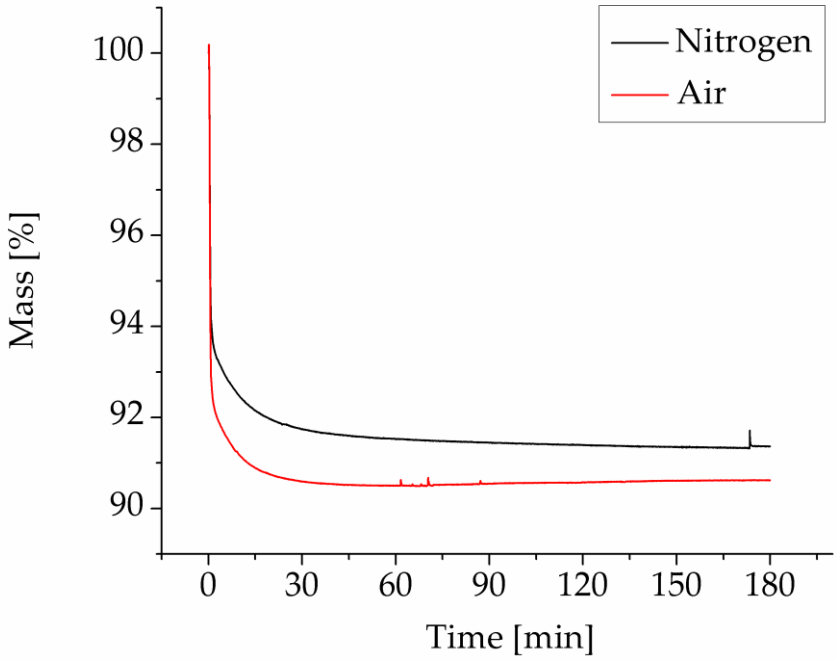

Figure 3.1 Termogravimetric analysis profile of the PNVP employed. The polymer in its powder form was heated to 200 °C for 3 hours in air and in nitrogen.

3.3.2 Differential scanning calorimetry (DSC)

The DSC analysis was performed by Dr. Hank deBruyn at the University of Sydney. The PNVP powder was characterized by DSC to identify its glass transition temperature (T_g). The sample was heated from 110 °C to 197 °C over 18 minutes (Figure 3.2). The DSC data show a single sharp transition in the heat flow profile. The mid-point of the transition corresponds to the T_g of the polymer, at about 160 °C. This is slightly lower than the T_g of 175 °C reported in the literature,[44, 45] yet comparable.

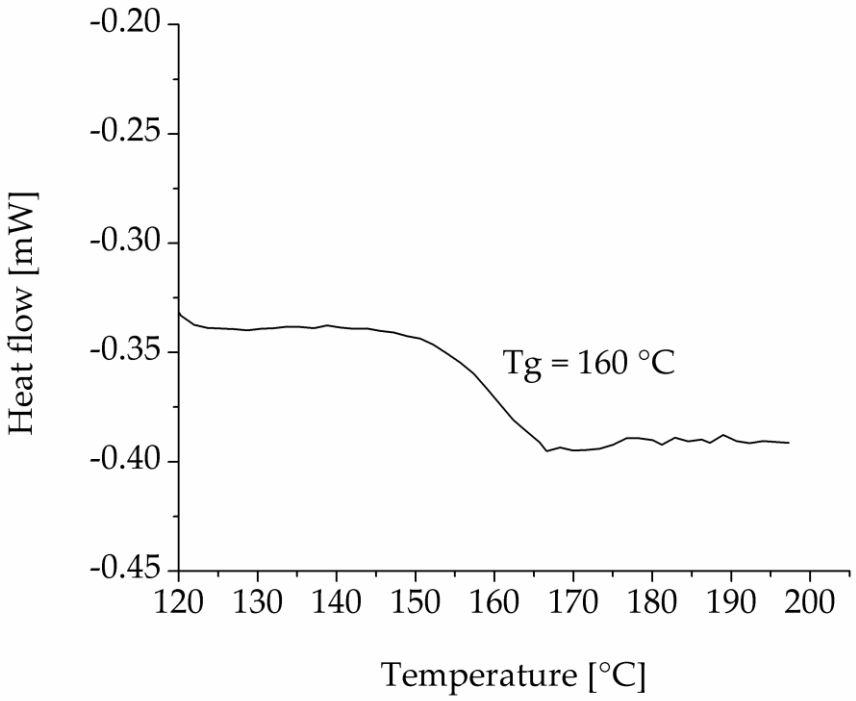

Figure 3.2 Differential scanning calorimetry profile of PNVP. The polymer in its powder form was heated from 110 °C to 197 °C in 18 minutes. The glass transition temperature is indicated.

3.3.3 Atomic force microscopy

Shown if Figure 3.3 are Tapping Mode™ AFM topography images of an as-prepared PNVP film (a) and a PNVP film that was annealed for 3

hours at 200 °C (b). The morphology of the films remained featureless, and did not change significantly upon thermal annealing. Root mean square (RMS) roughness values, before (203 ± 1 pm) and after (252 ± 8 pm) annealing indicate that these thin films were very smooth, and with roughness similar to that of the underlying silicon substrate (typically below 200 pm).

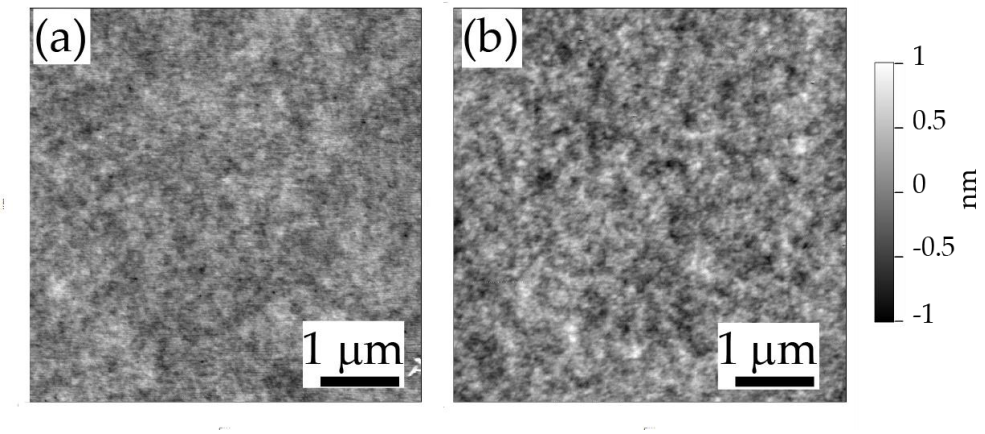

Figure 3.3 Tapping Mode™ AFM topography images for (a) an untreated PNVP film and (b) an annealed PNVP film (200 °C for 3 hours).

3.3.4 X-ray photoelectron spectroscopy (XPS)

The XPS analysis and data fitting were performed by Dr. Bill Gong at the surface analysis facility at the University of New South Wales. XPS data were collected on an untreated film and on a film annealed at 200 °C for 3 hours, prior to rinsing with water. Presented in Figure 3.4 are survey XPS spectra of the untreated and treated films (a) as well as high resolution C 1s (b), N 1s (c) and O 1s (d) spectra. In the Figure the data for the untreated film was offset up the y-axis by 20000 counts s^{-1} in part (a), and by 2000 in parts (b)-(d) to highlight differences before and after the treatment. The C 1s spectra (Figure 3.4(b)) were fitted with 5 different components: component C1 was due to the presence of aliphatic hydrocarbon (C-C, C-H), component

C2 was due to secondary shifted aliphatic carbon, component C3 was due to the presence of C-N/C-O groups, component C4 was due to the presence of C=O/O-C-O/N-C=O groups, and component C5 was due to the presence of O-C=O groups such as carboxylic acids and esters.

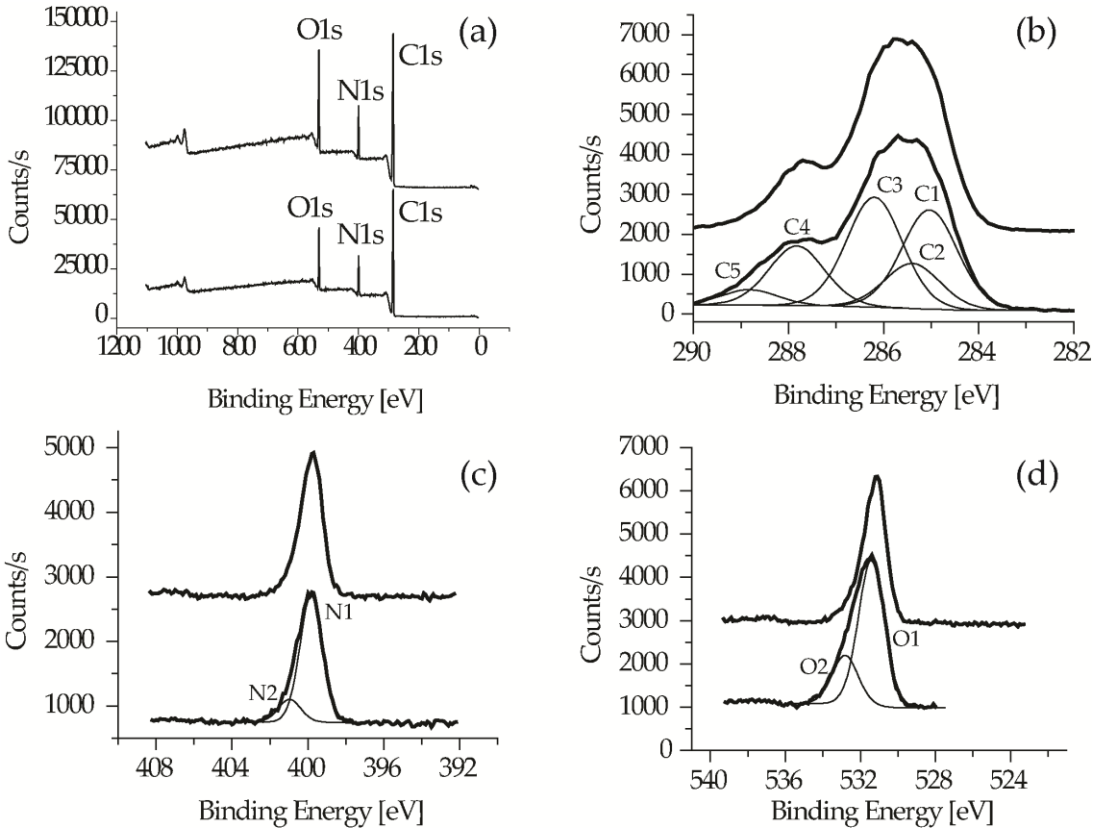

Figure 3.4 X-ray photoelectron spectroscopy data collected on an untreated PNVP film (upper curves, offset for clarity), and on a PNVP film annealed at 200 °C for three hours (lower curves, including fits). (a) Survey spectra and high resolution spectra for (b) C 1s,(c) N 1s , and (d) O 1s.

The presence of component C5 in the untreated film indicates that the polymer as-received was already slightly oxidized. This peak was more intense in the annealed sample data, suggesting that the polymer underwent some degree of oxidation as a result of the thermal treatment. The N 1s spectra obtained before and after annealing did not show any remarkable

differences, except for the appearance of component N2 in the spectrum, likely due to a mild oxidation on the pyrrolidone ring (Figure 3.4(c)). Analysis of the O 1s spectrum for the annealed film (Figure 3.4(d)) suggested an increase in component O2, which was due to the presence of oxygen bound to carbon with a higher oxidation state (O=C-O), supporting the possibility of slight oxidation of the polymer.

Table 3.1 XPS elemental composition data for an untreated PNVP film and a thermally modified PNVP film following annealing at 200 °C for 3 hours.

As-prepared film			
Label	Peak binding energy [eV]	Atomic content [%]	Total atomic content [%]
C1	285.0	15.1	C1s = 77.0 %
C2	285.3	18.7	
C3	286.1	28.5	
C4	287.8	13.7	
C5	289.0	0.9	
N1	399.9	10.0	N1s = 11.7 %
N2	401.0	1.7	
O1	531.3	9.7	O1s = 11.3 %
O2	532.5	1.7	
After Annealing 200 °C, 3 hours			
Label	Peak binding energy [eV]	Atomic content [%]	Total atomic content [%]
C1	285.0	21.9	C1s = 72.8 %
C2	285.4	10.0	
C3	286.2	24.3	
C4	287.8	13.2	
C5	288.8	3.4	
N1	399.9	9.6	N1s = 11.4 %
N2	401.1	1.7	
O1	531.5	11.9	O1s = 15.8 %
O2	532.9	4.0	

Summarised in Table 3.1 are the carbon, nitrogen and oxygen content in the two samples. The carbon content is slightly higher than what expected

for the theoretical C:N:O atomic ration of 6:1:1, and this is explained by the presence of unavoidable contamination of the polymer with hydrocarbons. The oxygen atomic content in the polymer increased by about 30% upon annealing, the carbon content decreased by 5% and the nitrogen content was essentially unchanged. These data were used to obtain the hydrogen content in the two types of film (untreated and annealed), when used in combination with the neutron reflectivity data (see below). No repeated experiment was performed in this study, but the fit deviation on a typical XPS analysis, evaluated by Monte Carlo simulations, lies between 1% and 5%.[46]

3.3.5 X-ray and neutron reflectometry

X-ray and neutron reflectometry analysis were carried out under the direction of Prof. Michael James at the Australian Nuclear Scientific and Technology Organization (ANSTO) Lucas Heights facility in Sydney. All the data fitting was performed by Prof. James.

The degree of cross-linking of PNVP films induced by thermal annealing was characterized by X-ray and neutron reflectometry, by investigating films after increasing annealing times (5 minutes, *Film 1*; 30 minutes and 60 minutes, *Film 2*; and 180 minutes, *Film 3*).

Shown in Figure 3.5(A) are X-ray reflectivity profiles for a PNVP coating (*Film 1*) in the as-prepared state (trace (a)), after annealing for 5 minutes at 200 °C (trace (b)), and after rinsing with 30 mL Milli-Q® water (trace (c)). Shown in Figure 3.5(B) are neutron reflectivity data for the same untreated PNVP film (*film 1*) (trace (a)), after annealing for 5 minutes at 200 °C (trace (b)) and after rinsing with 30 mL of Milli-Q® water (trace (c)).

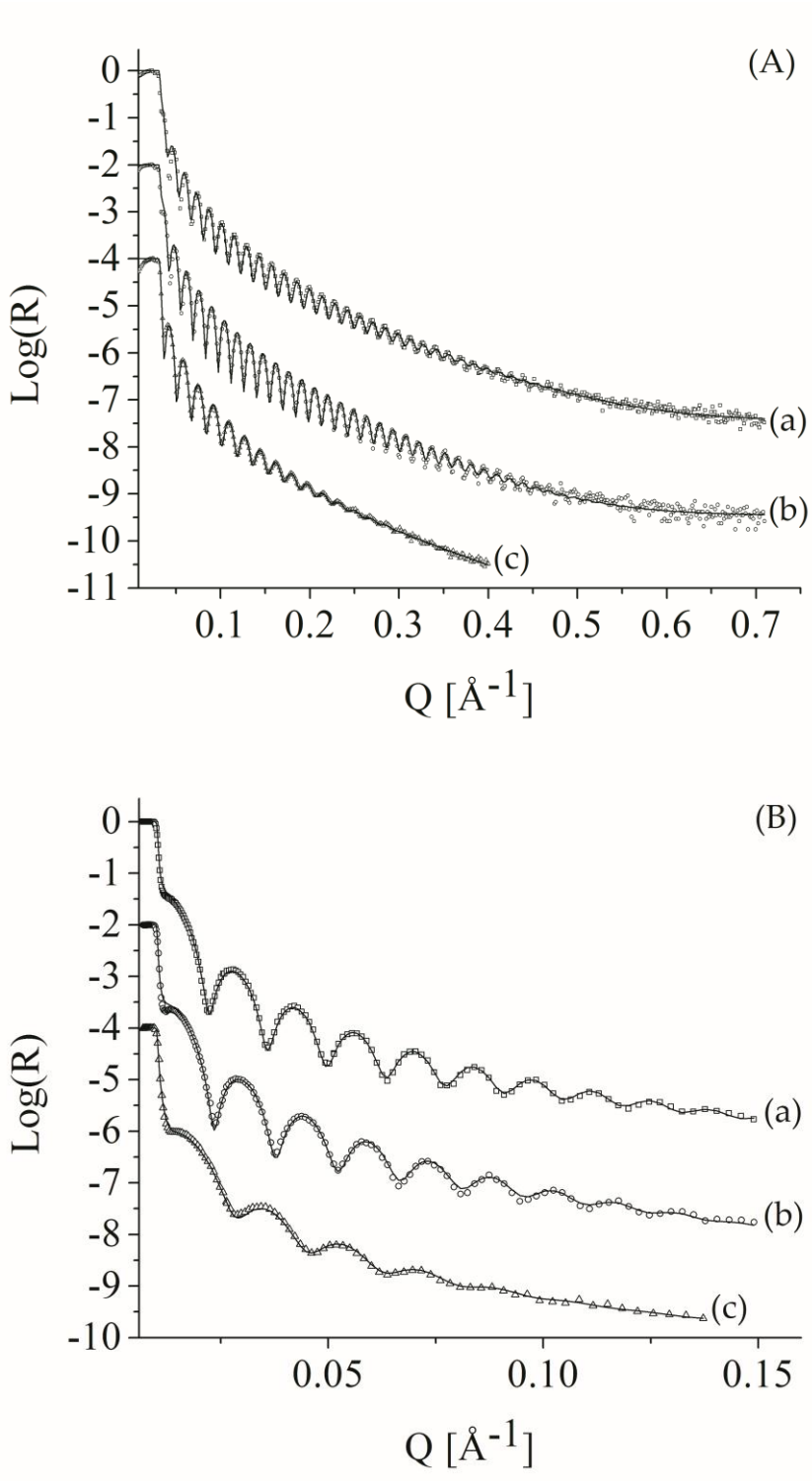

Figure 3.5 (A) X-ray reflectivity and (B) neutron reflectivity data for (trace (a)) an untreated PNVP film, (trace (b)) after annealing for 5 minutes at 200 °C, and (trace (c)) after rinsing with 30 mL Milli-Q water and drying. The data have been offset by a factor of 0.01 for traces (b) and 0.0001 for traces (c) for clarity. Observed data (points) and calculated data (solid lines) are reported.

Refined structural parameters for these films are given in Table 3.2. The structure of the untreated film was refined using a single layer model for both the X-ray and neutron reflectivity data, indicating a film of ~44 nm in thickness and a surface roughness of less than 1 nm. Based on the monomer composition C_6H_9NO and the observed *SLD* values, the mass density of this film was found to be 0.79 g cm^{-3}.

Following the annealing of *Film 1* at 200 °C for 5 minutes, X-ray reflectivity data were fitted by a single layer model (Figure 3.5(A), trace (b)). Comparison between these data and that for the as-prepared film (trace (a)) shows more pronounced Kiessig fringes with wider spacing, indicating a slightly thinner (43 nm), denser film after annealing. An adequate fit to the neutron reflectivity data was not possible using a single layer model. A two layer model was then used to fit these data (Figure 3.5(B), trace (b)), indicating a 9.9 nm less dense upper layer (*SLD* of 0.89×10^{6} $Å^{-2}$) and a 33.4 nm more dense lower layer (*SLD* of 1.02×10^{6} $Å^{-2}$) (Table 3.2).

The uppermost surface of the film was found to be relatively smooth (0.8 nm), although the interfacial region between the two layers was found to be quite diffuse (5.8 nm) indicating a gradient in composition.

Rinsing with a small amount of water (30 mL) produced a further reduction in film thickness and a substantial increase in surface roughness, which was evident in the damping of fringes at high *Q*. Both X-ray (Figure 3.5(A), trace (c)) and neutron (Figure 3.5(B), trace (c)) reflectivity profiles required a two layer model in order to produce an adequate fit. The refined structural data (Table 3.2) indicate a partial removal of the upper non-cross-linked polymer layer, a diffuse interfacial layer and a denser lower layer adjacent to the silicon wafer.

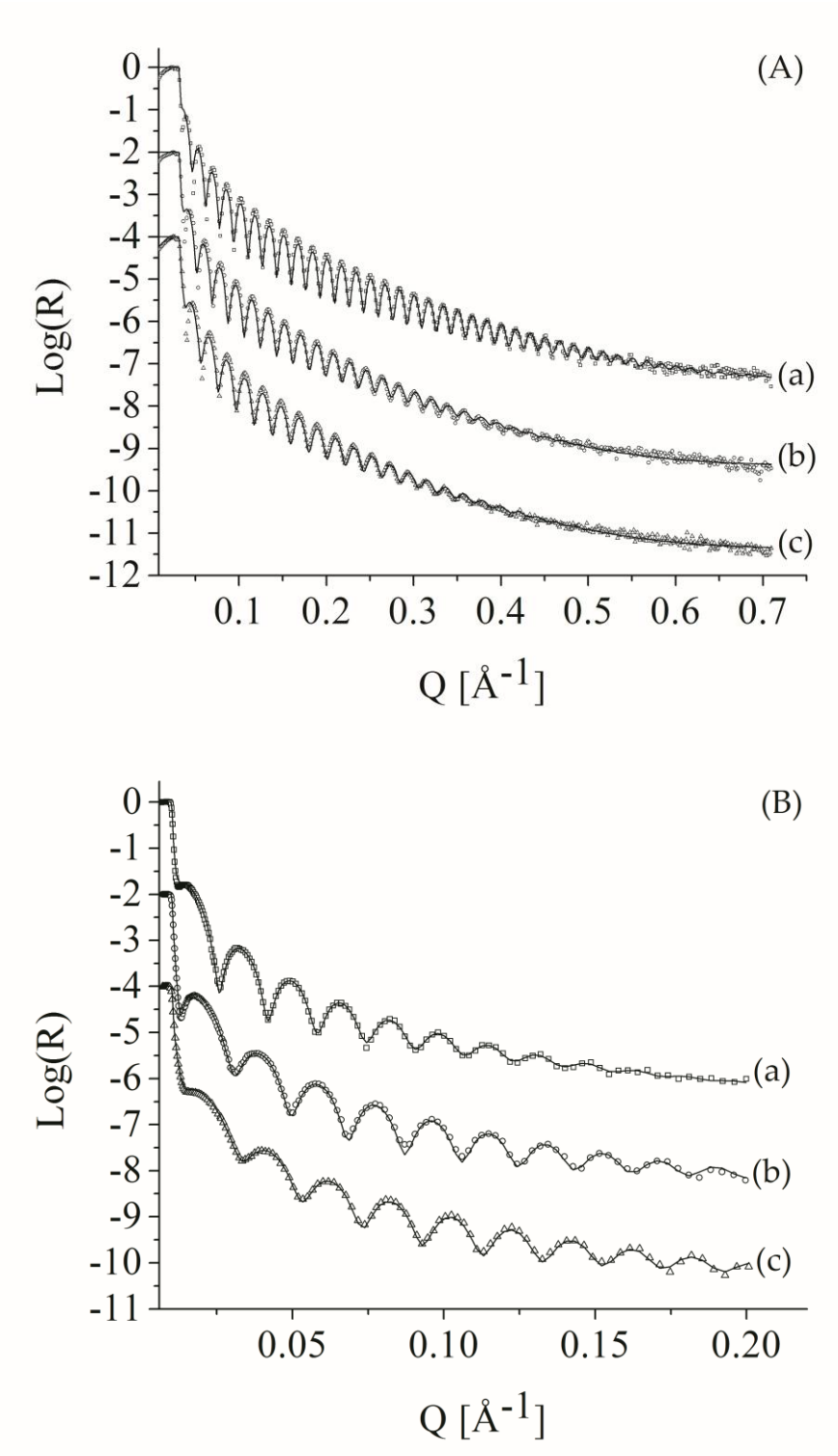

Figure 3.6 (A) X-ray reflectivity and (B) neutron reflectivity data for (trace (a)) an untreated PNVP coating (Film 2), (trace (b)) after annealing the sample for 30 minutes at 200 °C, and (trace (c)) 60 minutes at 200 °C. Data have been offset be a factor of 0.01 for traces (b) and 0.0001 for traces (c) for clarity. Observed data (points) and calculated data (solid lines) are reported.

Presented in Figure 3.6(A) are observed (points) and calculated (solid lines) X-ray reflectivity profiles for a PNVP coating (*Film 2*) in the as-prepared state (trace a), after annealing for 30 minutes at 200 °C (trace b), and after subsequent annealing for 60 minutes at 200 °C (trace c). Prior to measurement, the annealed surfaces were rinsed with Milli-Q® water and then dried. Analogous neutron reflectivity data after each stage of processing are shown in Figure 3.6(B). Refined structural parameters for *Film 2* based on single layer models are given in Table 3.2.

The PNVP film was found to decrease in thickness from 37.7 nm in the as-prepared state, to 33.3 nm, and 29.9 nm upon subsequent annealing for 30 and 60 minutes, respectively (a decrease in thickness of about 11% after 30 minutes, and of about 21 % after 60 minutes). Annealing of this film also led to a small increase in surface roughness (from 0.4 nm to 0.6 nm) as indicated by the damping of the Kiessig fringes for datasets (b) and (c) in Figure 3.6(A). Based on these X-ray reflectivity data, relatively little change was observed for the scattering length density upon annealing.

The neutron reflectivity data for these films indicate a slightly different picture. Refinement of the neutron data for the as-prepared film (trace (a)) in Figure 3.6(B) gave essentially the same model as used for the X-ray measurements on the as-prepared film of Figure 3.5(B): a smooth uniform film with a mass density of 0.81 g cm^{-3}.

Refinement of the neutron reflectivity data (traces (b) and (c)) for the annealed samples revealed significantly increased *SLD* values: 1.48×10^{6} $Å^{-2}$ (after 30 minutes) and 1.65×10^{6} $Å^{-2}$ (after 60 minutes). The combination of little variation in X-ray *SLD* and increases in the neutron *SLD* suggest that the mass density of the annealed films remained relatively constant, while the hydrogen content decreased compared to the as-prepared film.

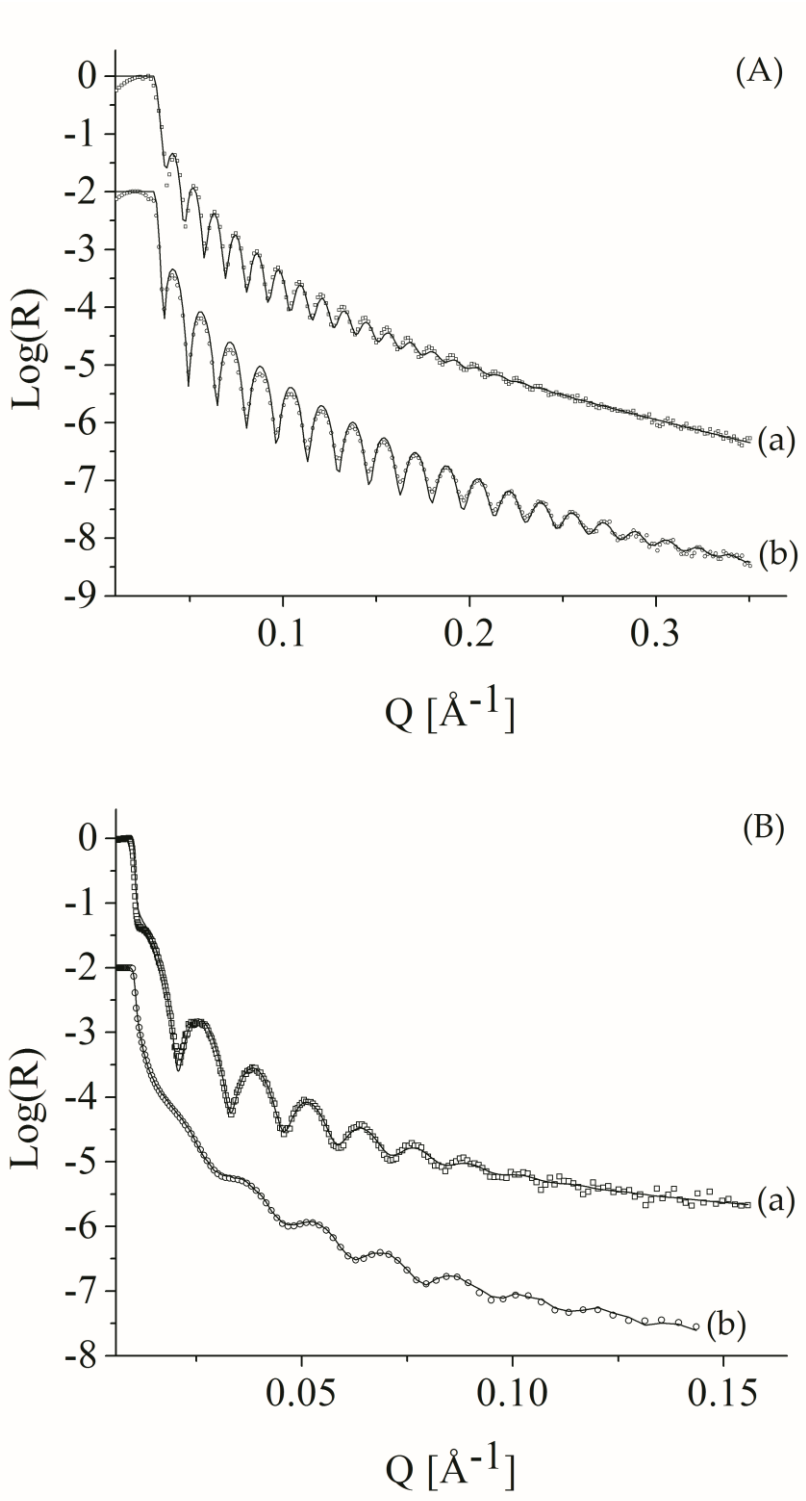

Figure 3.7 (A) X-ray reflectivity and (B) neutron reflectivity data for (trace (a)) an untreated PNVP coating (Film 3) and (trace (b)) after annealing the sample for 180 minutes at 200 °C and rinsing. Data have been offset be a factor of 0.01 for traces (b) for clarity. Observed (points) and calculated (solid lines) data are reported.

Presented in Figure 3.7(A) and Figure 3.7(B) are X-ray and neutron reflectivity profiles, respectively, for an as-prepared coating (*Film 3*) (trace (a)), and the film after annealing at 200 °C for 3 hours and rinsing (trace (b)) with the refined structural parameters reported in Table 3.2. These refinements reveal that the film thickness decreased from 50.6 nm for the as-prepared film, to 37 nm for the annealed film. This densification was reflected in an increase in scattering length density: from 7.62 to 10.35×10^{6} $Å^{-2}$ for X-rays, and from 0.94 to 1.98×10^{6} $Å^{-2}$ for neutrons. In the case of the neutron reflectivity data (Figure 3.7B, trace (b)) the Kiessig fringes showed much weaker oscillations for the annealed film compared to the as-prepared film (Figure 3.7(B), trace (a)); this is an indication of the poor scattering length density contrast between the annealed film and the silicon substrate, as the mass density, and hence the *SLD* of the film, increased greatly upon annealing.

In summary, analysis of these reflectivity data on films annealed for increasing amounts of time indicate a gradual cross-linking, starting from the bottom of the film (side closer to the heating source), and then extending with time to the rest of the film. Thermal annealing led to a slight increase in mass density of these films, with a consequent increase in X-ray scattering length density. The scattering length density of the non-cross-linked portion of these films was the same as the un-treated polymer, indicating that cross-linking was indeed the main phenomenon occurring, and no other degradation or chemical modification were observed.

In addition, the residual non-cross-linked polymer that was present after short annealing times retained a high degree of solubility in water. The combined neutron and X-ray reflectivity data for the annealed samples suggest that at intermediate annealing times (30 and 60 minutes) the mass density of the annealed films remained relatively constant, while the hydrogen content decreased compared to the as-prepared film.

Table 3.2 Refined structural parameters from X-ray and neutron reflectivity data for as-prepared PNVP films, and for films annealed at 200 °C for 5, 30, 60 and 180 minutes, with estimated standard deviations on the last significant figure in parentheses.

	Film 1			Film 2			Film 3	
Annealing Temperat.	As-Prep.	200 °C	200 °C	As-Prep.	200 °C	200 °C	As-Prep.	200 °C
Annealing Time [min]	-	5	5	-	30	60	-	180
Rinsed with water	-	-	30 mL	-	150 mL	-	-	150 mL
X-rays								
Film Thickness [nm]	44.1 (1)	43.0 (1)	U: 1.8(3)[a] L: 4.3(1)	37.7 (1)	33.3 (1)	29.9 (1)	50.6 (3)	37.0 (2)
SLD [×10^6 Å^{-2}]	7.21 (2)	8.45 (2)	U: 4.59(2) [a] L: 8.43(3)	7.48 (2)	7.68 (2)	7.54 (2)	7.62 (2)	10.35 (3)
Surface Roughness [nm]	0.6 (1)	0.6 (1)	U: 1.4(2)[a] L: 0.8(1)	0.4 (1)	0.6 (1)	0.6 (1)	0.9 (1)	0.8 (1)
Neutrons								
Film Thickness [nm]	44.6 (3)	U: 9.9(2)[a] L: 33.4(3)	U: 9.0(2)[a] L: 26.7(3)	38.2 (3)	33.6 (2)	30.5 (2)	50.3 (4)	37.5 (3)
SLD [×10^6 Å^{-2}]	0.92 (3)	U: 0.89(3) L: 1.02(4)	U: 0.68(3) [a] L: 0.90(3)	0.93 (3)	1.48 (2)	1.65 (2)	0.94 (1)	1.98 (2)
Surface Roughness [nm]	0.7 (2)	U: 0.8(2) L: 5.8(3)	U: 2.3(2)[a] L: 3.6(3)	0.5 (1)	0.8 (2)	0.8 (1)	1.1 (1)	0.7 (2)

[a] "U" indicates the upper layer of the film, and "L" the lower layer.

3.3.6 Transmission Fourier transform infrared spectroscopy (FTIR)

Presented in Figure 3.8 are the transmission FTIR spectra for a 40 nm thick untreated PNVP film and for a PNVP film annealed at 200 °C for 3 hours. The assignment of the peaks from these spectra is summarised in

Table 3.3. Direct comparison between the two spectra is not quantitative, since the thickness (and therefore the path length) of the two films was slightly different, due to the shrinking of the film upon annealing. It is obvious though that the width of the amide carbonyl peak (1755-1590 cm^{-1}) increased after the heat treatment. This is indicative of an overlapping of contributions from amide groups lying in at least two different environments (see Figure 3.13 for the chemical structure of PNVP), suggesting the partial modification of bonds involving carbon atoms close to the amide group in the pyrrolidone ring. It may also indicate a partial oxidation of the amide group to form a carboxylic group that typically absorbs in the range 1780-1710 cm^{-1} in the solid state. The amide functionality (and hence intact pyrrolidone groups) remained abundant after annealing.

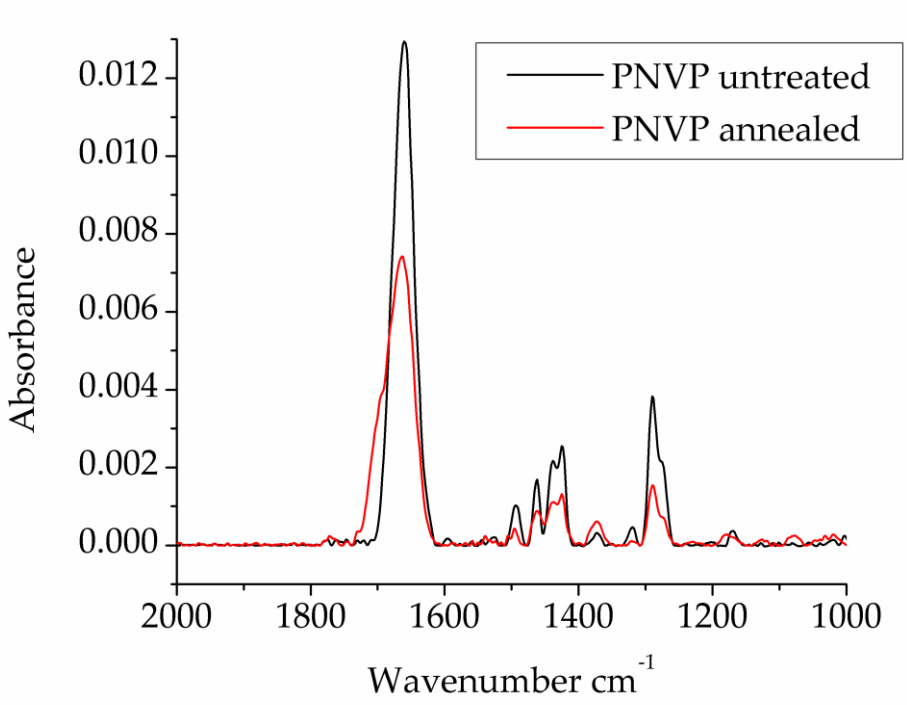

Figure 3.8 Fourier transform infrared (FTIR) spectra of an untreated PNVP film (black) and PNVP film annealed at 200 °C for 3 hours (red).

These spectra also indicate a change in the C-H composition before and after annealing. The areas of the C-H bending peaks in the ranges 1475-1410 cm^{-1} and 1305-1260 cm^{-1} were calculated. In order to have a measurement independent on the thickness of the film and to be able to compare data from the two different sets of samples, the areas of the peaks were normalized by the area of the amide carbonyl peak (1755-1590 cm^{-1}) within each spectrum. The values were then averaged over five different samples for each set. Assuming the amide carbonyl peak area to be constant, the normalized areas were different in the annealed film, with a 38% reduction in the C-H peak areas after annealing.

Table 3.3 FTIR data for untreated and annealed PNVP films. The selected C-H peak areas were normalized against the amide peak area in each spectrum.

		Normalized peak areas	
Mode	Range [cm^{-1}]	Untreated PNVP	Annealed PNVP
CH bending	1475-1410	0.185 ± 0.013	0.099 ± 0.009
CH bending	1305-1260	0.141 ± 0.007	0.061 ± 0.006
Amide C=O stretching	1755-1590	Used as reference	Used as reference

3.3.7 Cross-linking process: dependence on annealing time and temperature

The degree of PNVP cross-linking was investigated by spectroscopic ellipsometry in the temperature range between 160 °C and 200 °C for periods of annealing time between 30 minutes and 3 hours. This was done by measuring the percentage of the initial PNVP film that remained after thermal annealing at different annealing times and temperatures, and after rinsing the film in 150 mL of Milli-Q® water.

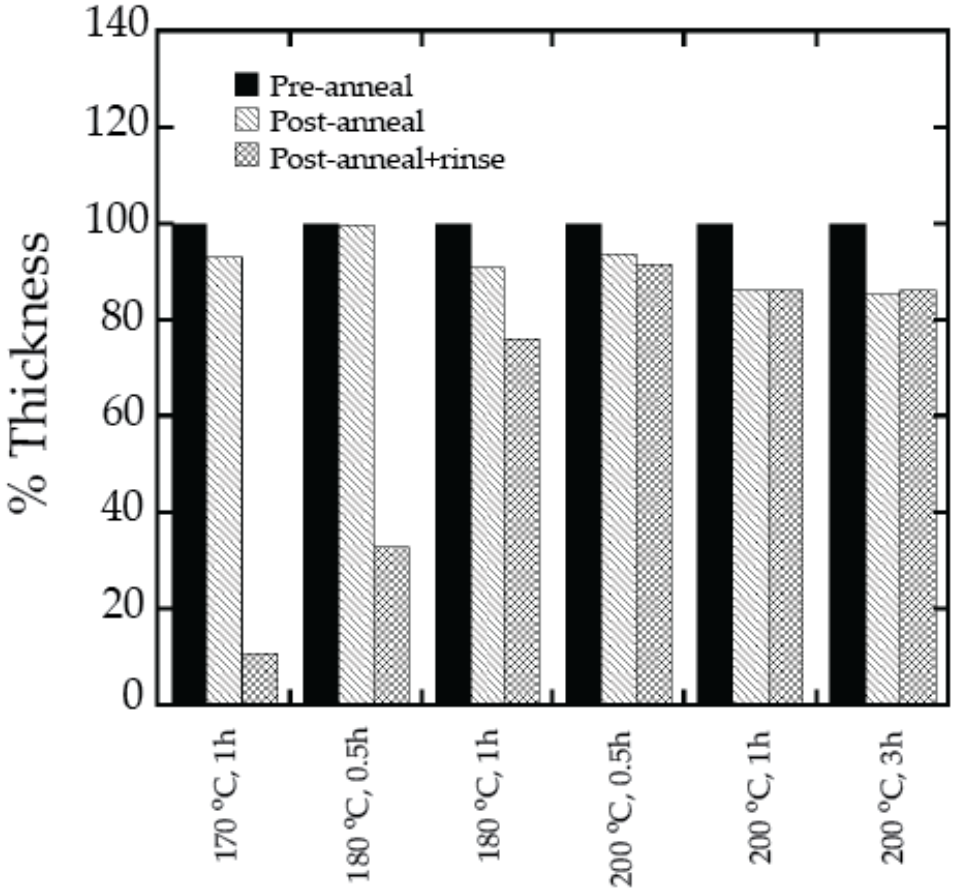

Figure 3.9 Percentage of PNVP film thickness change as a function of annealing time and temperature, and as a function of rinsing. The initial film thickness measured by spectroscopic ellipsometry is compared to the thickness after annealing at temperatures of 170 °C, 180 °C and 200 °C, and then again after rinsing with 150 mL Milli-Q® water. Each ellipsometric thickness measurement was taken two or three times. The error in the measurements is between 0.3 % and 2.4 %, except for the sample annealed at 170 °C for 1 hour, where the error is 11.6 %, and the sample annealed at 180 °C for 30 minutes, where the error is 10.4 %.

At the lower annealing temperature tested (160 °C) no cross-linking occurred for up to 3 hours annealing, evidenced by the fact that the PNVP films could be entirely washed away by 150 mL of Milli-Q® water. Similarly after annealing at 170 °C for 30 minutes the PNVP films were still entirely soluble in water. The data presented in Figure 3.9 demonstrate that the films underwent a gradual compaction as a consequence of cross-linking which

led to an initial slight decrease in film thickness (confirming X-ray and neutron reflectivity results). After this compaction, a film thickness decrease could be seen upon rinsing only if there was incomplete cross-linking, i.e. after annealing at the lower temperatures (170 °C and 180 °C), or after annealing at 200 °C for times shorter than one hour. After annealing for one to three hours at 200 °C the film was completely insoluble in water, so within experimental error, no thickness change was observed upon rinsing.

Reflectivity data showed clearly that the film density and composition changed continuously upon annealing at 200 °C between 30 minutes and 3 hours (Figure 3.6, Figure 3.7 and Table 3.2). This indicates that although the films became insoluble after just 60 minutes at 200 °C, complete cross-linking occurred after 3 hours. Partial cross-linking was only obtained for intermediate values of both annealing time and temperature. A trend was clearly visible on analysis of the data: increasing the annealing time and/or the annealing temperature increased the degree of cross-linking throughout the film.

3.3.8 Film stability in solvents

Annealed PNVP films were found to be highly resistant to a range of solvents, including water, ethanol and a solution of peroxide in concentrated sulphuric acid (see below). Changes in the solubility of the PNVP film in water as a result of cross-linking could be easily estimated by eye (Figure 3.10), as the fully annealed films could not be dissolved by immersion in water.

The difference in wettability of the clean silica-coated silicon substrates (water contact angle around 7°) and of annealed PNVP films (water contact angle around 20°) was used to evaluate the effect of different solvents on annealed PNVP films. From these wettability measurements, it

could be deduced that annealed PNVP films were stable in boiling water for up to 10 minutes, NoChromix® solution (Sigma-Aldrich, inorganic peroxide-based oxidizing agent in concentrated sulphuric acid, similar to the well known "piranha solution") for up to 10 minutes at room temperature, and after rinsing with ethanol. The only effective treatment found to completely remove the film from the wafer was treatment with an air plasma cleaner at a power of 29 W for more than 1 hour.

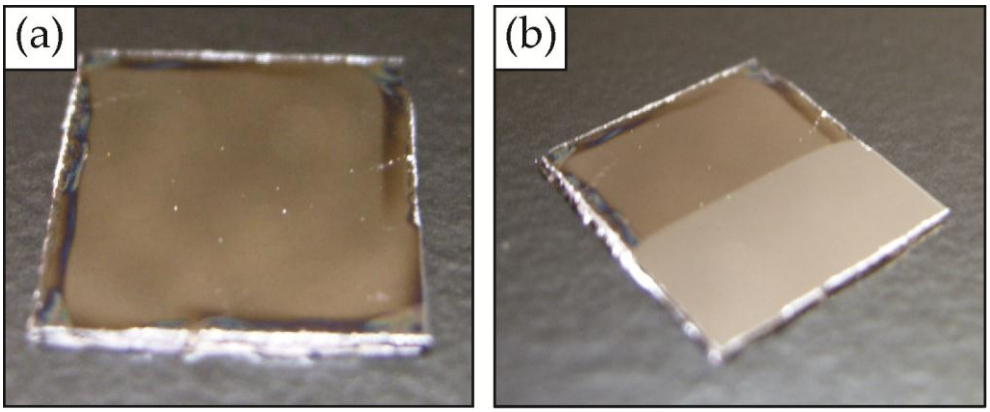

Figure 3.10 Pictures of (a) an untreated PNVP film and (b) a PNVP film annealed at 200 °C for 3 hours, both immersed in water for half their length for 10 seconds and then blown dry with pure nitrogen.

Shown in Figure 3.11 is the thickness, as measured by ellipsometry, of PNVP films annealed for 3 hours at 200 °C, following immersion in water at 37 °C for different periods of time. These measurements indicate that the film thickness was unchanged after immersion in water for up to three weeks. The slight variability in the normalized thickness was most likely due to residual adsorbed water on the hydrophilic surface of the polymer after drying.

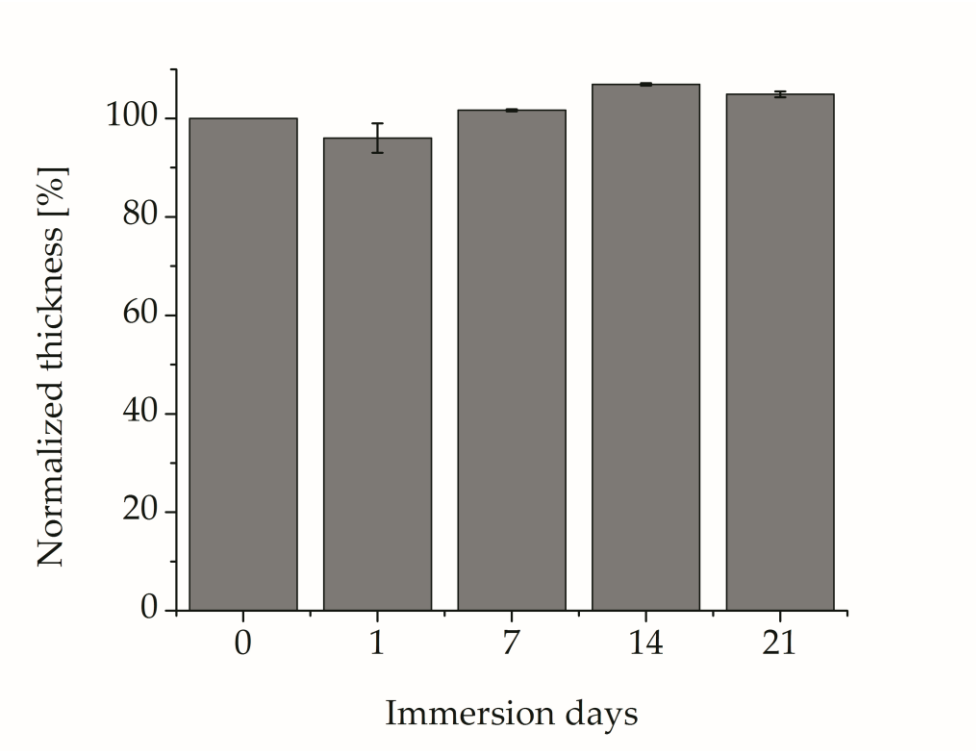

Figure 3.11 Stability of a PNVP film (annealed at 200 °C for 3 hours) after immersion in 37 °C Milli-Q® water for up to 3 weeks. The normalized thickness represents the measured thickness value after immersion, divided by the measured value before immersion, and averaged over three points on one sample for each immersion time. The error bars in the ellipsometric thickness measurements are typically 0.2 %, except for the measurement at 1 day immersion time where the error is ± 3%.

3.3.9 Protein adsorption on poly(N-vinylpyrrolidone) coatings

The quartz crystal microbalance (QCM) is a very sensitive technique for the detection of adsorbed mass on a surface. Shifts in the resonant frequency of a QCM crystal are proportional to the change in its mass, with a negative shift indicating an increase in mass (see Section 2.9). Shown in Figure 3.12 are QCM profiles obtained for the adsorption of FGN and IgG on completely cross-linked PNVP films, as well as on PS films and on bare gold surfaces (uncoated QCM crystal).

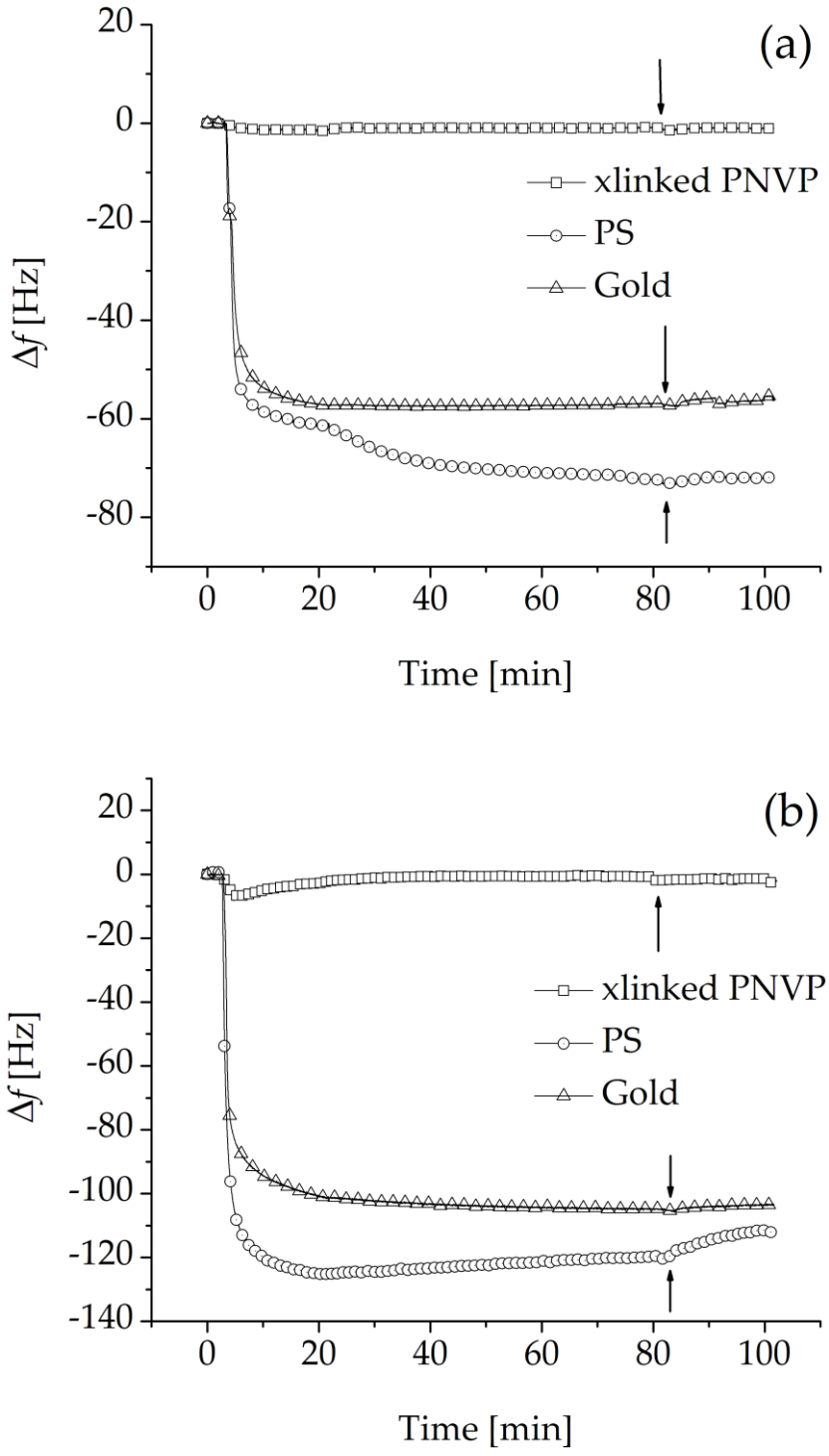

Figure 3.12 Quartz crystal microbalance analysis of (a) immunoglobulin G and (b) fibrinogen adsorption on PNVP films, PS films, and bare gold QCM crystal. The arrows indicate the flushing of the surface with fresh PBS to remove weakly adsorbed protein.

IgG and FGN were chosen because of their different structure and net charge at neutral pH values. IgG, as all antibodies, has a typical "Y" shape, and is more compact than FGN. IgG has an isoelectric point, i.e. the pH at which it has zero charge, between 6.4 and 9.95,[47] often in the basic part of the range, hence it is preferentially negatively charged in the buffer used. FGN is elongated, and has an isoelectric point of 5.5,[48] hence it has a net positive charge in the pH 7.4 buffer used. FGN was also chosen because it is one of the proteins that trigger an inflammatory response to foreign bodies in mammals.[49] The protein solution concentrations were both 1 mg mL^{-1}, a value close to that present in human plasma.[50] The analysis was performed at 37 °C to mimic protein adsorption under physiological conditions.

As shown in Figure 3.12, FGN and IgG adsorbed strongly on the two control surfaces (PS and gold) as evidenced by the strong negative frequency shift measured upon injection of the protein solution. The frequency shift increased rapidly in the first 10 minutes of exposure of the surfaces to the protein solution. With time, the number of available adsorption sites on the surface decreased and the adsorbed mass reached a plateau value. When the surfaces were rinsed with PBS (indicated in Figure 3.12 by the arrows) a small positive frequency shift was observed, indicating that a small amount of protein desorbed from the PS and gold surfaces. However, the bulk of the adsorbed protein remained on the surface, indicating a strong interaction between the proteins and the two substrates.

In the case of the annealed PNVP film, the frequency shift observed was minimal and barely detectable in comparison with the control surfaces. This indicates that almost no protein adsorbed onto the annealed PNVP surface. Using the Sauerbrey equation (Equation 2.9) the frequency shift can be converted into the adsorbed protein mass. The results were slightly overestimated because the adsorbed protein layer was not rigid and included water inside the adsorbed layer. The results are summarised in

Table 3.4: the adsorbed mass per unit area of IgG and FGN on the PNVP films was 21 ng cm^{-2} and 34 ng cm^{-2}, respectively, values close to those obtained on well known anti-fouling coatings such as PEG-based systems (cf. 10 - 30 ng cm^{-2} in reference 51).

Table 3.4 Frequency shifts and proteins adsorbed mass on different QCM sensors.

	Δf [Hz]	Δm [ng cm^{-2}]
IgG on PS	-73.1	1312
IgG on Gold	-57.2	1028
IgG on PVNP	-1.1	21
FGN on PS	-120.4	2162
FGN on Gold	-105.0	1876
FGN on PNVP	-1.9	34

3.4 Discussion

The above results illustrate the cross-linking behaviour of PNVP thin films following thermal treatment. The thermal and radiation treatments of PNVP have been investigated before, but a thermal cross-linking mechanism has never been investigated in detail before. It is known that the thermal treatment of PNVP in oxygen atmosphere gives rise to volatile degraded products at lower temperatures than in inert atmosphere,[42] but most degraded products occur at temperatures above those considered in this study (200 °C - 400 °C). At these higher temperatures the presence of an oxygen atmosphere gives rise to the formation of peroxide residues, which easily decompose, and give rise to the formation of active radicals.[42] The mechanism of photooxidation of PNVP films under UV light leads primarily to the formation of insoluble fractions.[41]

Our experimental observations indicate that the main chemical reaction occurring upon thermal annealing is a cross-linking process. This

process involves the CH groups on the pyrrolidone ring and on the backbone chain, without breaking the ring or involving the amide group (Figure 3.13). The thermal energy allows the formation of radicals by homolytic cleavage of some of the C-H bonds. Radicals from different chains can then react to form interchain C-C bonds and thus create a network that is insoluble in water. The hydrogen radicals formed can couple together or react with oxygen in the atmosphere. A similar mechanism has been suggested previously for chemically activated processes.[37] The coupling of radicals from different chains, which ultimately affects the cross-linking degree, is here facilitated by the fact that the polymer is liquid at 200 °C, since its T_g is about 160 °C. The chains are more mobile in the molten phase and the probability of two radicals reacting is higher than in the solid state.

Both the T_g and the liquid phase viscosity of a polymer increase with its molecular weight, so it could be postulated that the cross-linking process in the conditions used would be less efficient for much higher molecular weights. This would possibly lead to a network that retained some degree of solubility in water, making it a less desirable material to be used in a coating for biomedical applications because of leaching and deterioration issues.

The FTIR data support such a reaction scheme, showing that the amount of C-H groups in the PNVP film decreased significantly after annealing. Moreover, the amide peak showed an increase in width after annealing, suggesting the presence of amide groups with different environments (different neighbouring functional groups). Both results are in agreement with the cleavage of C-H bonds during the cross-linking process.

Reflectivity data also confirm the decrease in hydrogen content associated with the cleavage of C-H bonds during cross-linking. The combination of X-ray and neutron reflectometry measurements, in concert with the XPS data, could provide details of the composition and mass density of these annealed PNVP films. XPS measurements of the annealed

film (3 hours at 200 °C) suggested a C:N:O ratio of 73:11:16 (the hydrogen content for this film could not be determined using XPS).

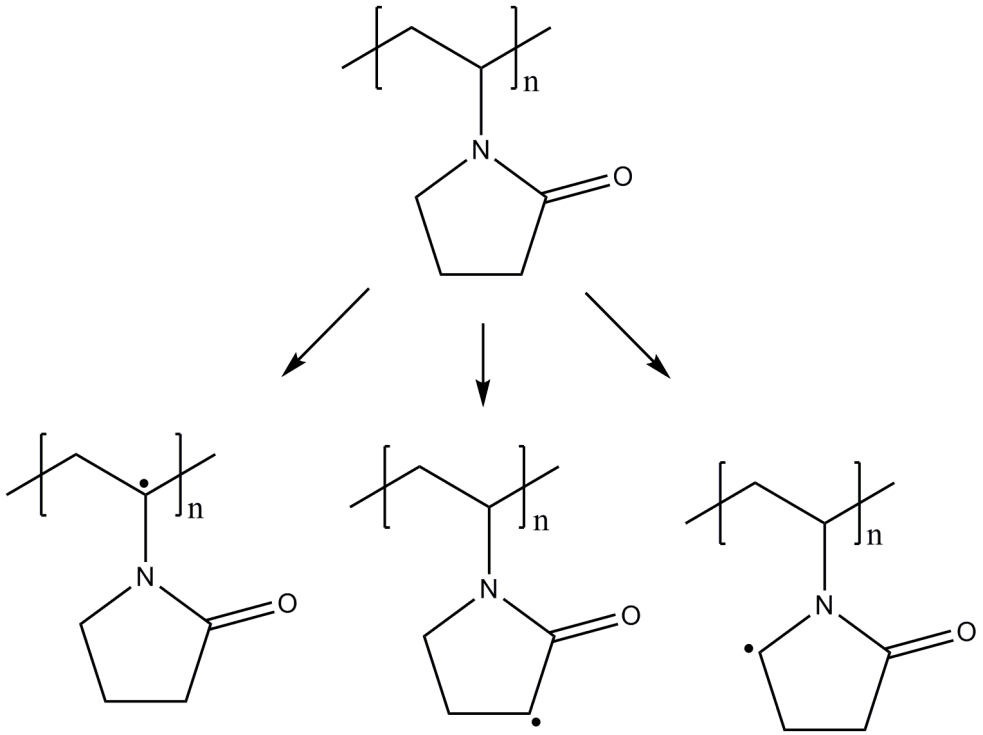

Figure 3.13 PNVP radical formation scheme proposed, similar to that for a chemically activated process.[37] The radicals that can be formed are shown.

The neutron and X-ray scattering length density values for the PNVP film both depend on the mass density and the composition of the modified polymer. These two unknowns (mass density and H content) could thus be extracted from the refined X-ray and neutron reflectivity data (Table 3.2), leading to a mass density of 1.15 g cm^{-3} (significantly denser than the as-prepared film) and a hydrogen content of 78 relative to the above C:N:O ratio. Thus, in comparison to the composition of the as-prepared film (C_6H_9NO, having a mass density of 0.79 g cm^{-3}), the film that was annealed for 3 hours has an approximate composition of $C_6H_{6.4}N_{0.9}O_{1.3}$. As mentioned

in the infrared spectroscopy results, the slight increase in the oxygen content was related to a mild degree of oxidation of the amide group.

The pyrrolidone ring, being neutral and hydrophilic, is mostly responsible for the low interaction between protein molecules and the polymer coating (see Section 1.4) and appeared not to be cleaved or altered during annealing to any significant degree, which explains conservation of the low protein adsorbing properties of the polymer film after annealing. The QCM data clearly demonstrates the low protein adsorbing properties of the cross-linked PNVP films compared to control surfaces such as gold and polystyrene. The calculated adsorbed mass can be compared to other types of antifouling coatings, such as those prepared by Zhang *et al*.[52] These authors prepared five thiol self-assembled monolayers on gold and three surface-initiated polymeric brushes; on the latter as little as 0.3 ng cm^{-2} of FGN adsorbed. The PNVP films prepared in this study did not perform quite as well as the grafted polymer brushes prepared by Zhang *et al.*,[52] but have the advantage that they do not require multistep processes often technically difficult to achieve and expensive to implement on a large scale or for large surface areas. Moreover, self-assembled monolayers on gold are unstable in the long term and are therefore likely only to be used in niche applications.[53] The thermally-annealed PNVP coatings prepared here are easily obtainable and have excellent repellent properties towards FGN and IgG, compared with similar PEG-based systems.[51, 54, 55] In fact, the cross-linked PNVP film studied here had better FGN repellent properties than grafted PNVP coatings obtained by surface initiated polymerization.[17]

The influence of annealing time and annealing temperature on the cross-linking process was also investigated. The cross-linking process did not occur at 160 °C within the annealing times investigated, while cross-linking was observed throughout the film after annealing at 200 °C for as little as 30 minutes. The degree of cross-linking increased gradually with

time, leading to densification of the film starting from the side closer to the heating source, and occurred rapidly at higher temperatures.

PNVP films prepared by the method proposed in this study are stable for long periods of time in contact with water at the average human body temperature, making them suitable applications where low protein adsorption is required. For example, these PNVP coatings could easily be adapted to the fabrication of microfluidic devices for biotechnological application, as the microfluidic channels could be made protein-repellent simply by flushing them with PNVP solutions, drying and annealing them. The simplicity of the coating technique allows access to highly protein-repellent surfaces in a cost effective and convenient manner.

3.5 Summary

In the work presented in this Chapter, a thermally-induced cross-linking mechanism for PNVP coatings was investigated for the first time. The cross-linking process was thoroughly characterized by neutron and X-ray reflectometry, which showed that the film density increased and the film thickness decreased with annealing temperature and time. The combination of neutron reflectivity data with XPS data produced information on the chemical composition of PNVP films before and after annealing, confirming that cross-linking was occurring. The process most likely takes place via radical reactions at C-H bonds, and does not require the breaking of the pyrrolidone ring. This was confirmed further by IR spectroscopy. The cross-linking rate could be controlled, as it increased with the annealing temperature, occurring within just a few hours at the highest temperature investigated (200 °C). Ellispometry data revealed that the cross-linking process was taking place from the bottom of the film upwards (i.e. from the

side closer to the heating source). The excellent protein-repellent properties of the PNVP were fully maintained after cross-linking, as shown by QCM data, and make these coatings valid alternatives to grafted PEG coatings, widely used for their antifouling properties but more complicated to prepare. The cross-linked films were insoluble in water and other harsh solvents, and were stable in water at body temperature (37 °C) for weeks, opening a wide range of applications for anti-fouling PNVP coatings for biomedical applications. Simple and cost-effective techniques such as dip-coating could be implemented to prepare the films, potentially allowing the coating of objects of large surface area and complex geometries. As mentioned in Chapter 1, the described bio-inert coatings could be suitable for reducing the inflammatory response to devices that are designed to be in contact with biological tissues for relatively short times, such as catheters and intravenous devices. Bio-inert coatings in such systems could avoid the formation of biofilms, which inevitably leads to dangerous infections, and the prevention of clogging from protein and cell aggregation.

3.6 References

1. Wilson, B. S.; Lawson, D. T.; Muller, J. M.; Tyler, R. S.; Kiefer, J., Cochlear implants: Some likely next steps. *Annual Review of Biomedical Engineering* **2003**, *5*, 207-249.
2. Thierry, B.; Tabrizian, M., Biocompatibility and biostability of metallic endovascular implants: State of the art and perspectives. *Journal of Endovascular Therapy* **2003**, *10* (4), 807-824.
3. Wilson, G. S.; Gifford, R., Biosensors for real-time in vivo measurements. *Biosensors and Bioelectronics* **2005**, *20* (12), 2388-2403.
4. Wisniewski, N.; Moussy, F.; Reichert, W. M., Characterization of implantable biosensor membrane biofouling. *Fresenius' Journal of Analytical Chemistry* **2000**, *366* (6), 611-621.
5. Wang, J., Glucose biosensors: 40 Years of advances and challenges. *Electroanalysis* **2001**, *13* (12), 983-988.

6. Andrade, J. D.; Hlady, V., Protein adsorption and materials compatibility - A tutorial review and suggested hypotheses. *Advances in Polymer Science* **1986**, *79*, 1-63.
7. Ratner, B. D.; Hoffman, A. S.; Schoen, F. J.; Lemons, J. E., *Biomaterials science: An introduction to materials in medicine*. Elsevier Academic Press: San Diego, CA, **1997**.
8. Vasilev, K.; Cook, J.; Griesser, H. J., Antibacterial surfaces for biomedical devices. *Expert Review of Medical Devices* **2009**, *6* (5), 553-567.
9. Bazaka, K.; Jacob, M. V.; Crawford, R. J.; Ivanova, E. P., Plasma-assisted surface modification of organic biopolymers to prevent bacterial attachment. *Acta Biomaterialia* **2011**, *7* (5), 2015-2028.
10. Zimmerli, W.; Sendi, P., Pathogenesis of implant-associated infection: the role of the host. *Seminars in Immunopathology* **2011**, *33* (3), 295-306.
11. Fang, C.; Zhang, M., Multifunctional magnetic nanoparticles for medical imaging applications. *Journal of Materials Chemistry* **2009**, *19* (35), 6258-6266.
12. Anderson, J. M.; Shive, M. S., Biodegradation and biocompatibility of PLA and PLGA microspheres. *Advanced Drug Delivery Reviews* **1997**, *28* (1), 5-24.
13. Anderson, J. M.; Rodriguez, A.; Chang, D. T., Foreign body reaction to biomaterials. *Seminars in Immunology* **2008**, *20* (2), 86-100.
14. McArthur, S. L.; McLean, K. M.; St John, H. A. W.; Griesser, H. J., XPS and surface-MALDI-MS characterisation of worn HEMA-based contact lenses. *Biomaterials* **2001**, *22* (24), 3295-3304.
15. Szleifer, I., Polymers and proteins: Interactions at interfaces. *Current Opinion in Solid State & Materials Science* **1997**, *2* (3), 337-344.
16. Kingshott, P.; Griesser, H. J., Surfaces that resist bioadhesion. *Current Opinion in Solid State & Materials Science* **1999**, *4* (4), 403-412.
17. Wu, Z.; Chen, H.; Liu, X.; Zhang, Y.; Li, D.; Huang, H., Protein adsorption on poly(N-vinylpyrrolidone)-modified silicon surfaces prepared by surface-initiated atom transfer radical polymerization. *Langmuir* **2009**, *25* (5), 2900-2906.
18. Feng, W.; Zhu, S. P.; Ishihara, K.; Brash, J. L., Protein resistant surfaces: Comparison of acrylate graft polymers bearing oligo-ethylene oxide and phosphorylcholine side chains. *Biointerphases* **2006**, *1* (1), 50-60.
19. Ma, Z. W.; Mao, Z. W.; Gao, C. Y., Surface modification and property analysis of biomedical polymers used for tissue engineering. *Colloids and Surfaces B: Biointerfaces* **2007**, *60*, 137-157.
20. Ostuni, E.; Chapman, R. G.; Holmlin, R. E.; Takayama, S.; Whitesides, G. M., A survey of structure-property relationships of surfaces that resist the adsorption of protein. *Langmuir* **2001**, *17* (18), 5605-5620.

21. Werner, C.; Maitz, M. F.; Sperling, C., Current strategies towards hemocompatible coatings. *Journal of Materials Chemistry* **2007**, *17* (32), 3376-3384.
22. Higuchi, A.; Shirano, K.; Harashima, M.; Yoon, B. O.; Hara, M.; Hattori, M.; Imamura, K., Chemically modified polysulfone hollow fibers with vinylpyrrolidone having improved blood compatibility. *Biomaterials* **2002**, *23* (13), 2659-2666.
23. Marchant, R. E.; Johnson, S. D.; Schneider, B. H.; Agger, M. P.; Anderson, J. M., A hydrophilic plasma polymerized film composite with potential application as an interface for biomaterials. *Journal of Biomedical Materials Research* **1990**, *24* (11), 1521-1537.
24. Wetzels, G. M. R.; Koole, L. H., Photoimmobilisation of poly(N-vinylpyrrolidinone) as a means to improve haemocompatibility of polyurethane biomaterials. *Biomaterials* **1999**, *20* (20), 1879-1887.
25. Robinson, S.; Williams, P. A., Inhibition of protein adsorption onto silica by polyvinylpyrrolidone. *Langmuir* **2002**, *18* (23), 8743-8748.
26. Robinson, B. V.; Sullivan, F. M.; Borzelleca, J. F.; Schwartz, S. L., *PVP, a critical review of the kinetics and toxicology of polyvinylpyrrolidone (povidone)*. Lewis Publisher: Chelsea, MI, **1990**.
27. Smith, L. E.; Rimmer, S.; MacNeil, S., Examination of the effects of poly(N-vinylpyrrolidinone) hydrogels in direct and indirect contact with cells. *Biomaterials* **2006**, *27* (14), 2806-2812.
28. Davies, W. L.; Gloor, W. T., Batch production of pharmaceutical granulations in a fluidized-bed. 2. Effects of various binders and their concentrations on granulations and compressed tablets. *Journal of Pharmaceutical Sciences* **1972**, *61* (4), 618-622.
29. Hoang, T.; Jorgensen, M. G.; Keim, R. G.; Pattison, A. M.; Slots, J., Povidone-iodine as a periodontal pocket disinfectant. *Journal of Periodontal Research* **2003**, *38* (3), 311-317.
30. Reimer, K.; Vogt, P. M.; Broegmann, B.; Hauser, J.; Rossbach, O.; Kramer, A.; Rudolph, P.; Bosse, B.; Schreier, H.; Fleischer, W., An innovative topical drug formulation for wound healing and infection treatment: In vitro and in vivo investigations of a povidone-iodine liposome hydrogel. *Dermatology* **2000**, *201* (3), 235-241.
31. Vogel, F. G. M., 50 years of PVP - Discovery of polyvinylpyrrolidone signaled the beginning of a half-century of progress in cosmetic polymers. *Soap Cosmetics Chemical Specialties* **1989**, *65* (4), 42.
32. Yañez, F.; Concheiro, A.; Alvarez-Lorenzo, C., Macromolecule release and smoothness of semi-interpenetrating PVP-pHEMA networks for comfortable soft contact lenses. *European Journal of Pharmaceutics and Biopharmaceutics* **2008**, *69* (3), 1094-1103.

33. Ravin, H. A.; Seligman, A. M.; Fine, J., Polyvinyl pyrrolidone as a plasma expander - studies on its excretion, distribution and metabolism. *New England Journal of Medicine* **1952**, *247* (24), 921-929.
34. Hamidi, M.; Azadi, A.; Rafiei, P., Hydrogel nanoparticles in drug delivery. *Advanced Drug Delivery Reviews* **2008**, *60* (15), 1638-1649.
35. Liu, Z.; Rimmer, S., Synthesis and release of 5-fluorouracil from poly(N-vinylpyrrolidinone) bearing 5-fluorouracil derivatives. *Journal of Controlled Release* **2002**, *81* (1-2), 91-99.
36. Meinhold, D.; Schweiss, R.; Zschoche, S.; Janke, A.; Baier, A.; Simon, F.; Dorschner, H.; Werner, C., Hydrogel characteristics of electron-beam-immobilized poly(vinylpyrrolidone) films on poly(ethylene terephthalate) supports. *Langmuir* **2004**, *20* (2), 396-401.
37. Barros, J. A. G.; Fechine, G. J. M.; Alcantara, M. R.; Catalani, L. H., Poly (N-vinyl-2-pyrrolidone) hydrogels produced by Fenton reaction. *Polymer* **2006**, *47* (26), 8414-8419.
38. Kuypers, M. H. Method of providing a substrate with a layer comprising a poly vinyl base hydrogel and a biochemically active material. Pat. Num. 0363504, **1990**.
39. Rosiak, J. M.; Olejniczak, J., Medical applications of radiation formed hydrogels. *Radiation Physics and Chemistry* **1993**, *42* (4-6), 903-906.
40. Rosiak, J. M.; Ulanski, P.; Pajewski, L. A.; Yoshii, F.; Makuuchi, K., Radiation formation of hydrogels for biomedical purposes - some remarks and comments. *Radiation Physics and Chemistry* **1995**, *46* (2), 161-168.
41. Hassouna, F.; Therias, S.; Mailhot, G.; Gardette, J. L., Photooxidation of poly(N-vinylpyrrolidone) (PVP) in the solid state and in aqueous solution. *Polymer Degradation and Stability* **2009**, *94* (12), 2257-2266.
42. Peniche, C.; Zaldivar, D.; Pazos, M.; Paz, S.; Bulay, A.; Roman, J. S., Study of the thermal degradation of poly(N-vinyl-2-pyrrolidone) by thermogravimetry-FTIR. *Journal of Applied Polymer Science* **1993**, *50* (3), 485-493.
43. Telford, A. M.; James, M.; Meagher, L.; Neto, C., Thermally cross-linked PNVP films as antifouling coatings for biomedical applications. *ACS Applied Materials & Interfaces* **2010**, *2* (8), 2399-2408.
44. Feldstein, M. M.; Shandryuk, G. A.; Kuptsov, S. A.; Platé, N. A., Coherence of thermal transitions in poly(N-vinyl pyrrolidone)–poly(ethylene glycol) compatible blends 1. Interrelations among the temperatures of melting, maximum cold crystallization rate and glass transition. *Polymer* **2000**, *41* (14), 5327-5338.
45. Moore, J. A.; Kaur, S., Blends of poly(amide-enaminonitrile) with poly(ethylene oxide), poly(4-vinylpyridine), and poly(N-vinylpyrrolidone). *Macromolecules* **1998**, *31* (2), 328-335.
46. Gengenbach, T., Monte Carlo simulation of the fitting quality of XPS analysis on polymer thin films. Personal communication. **2011**.

47. Prin, C.; Bene, M. C.; Gobert, B.; Montagne, P.; Faure, G. C., Isoelectric restriction of human-immunoglobulin isotypes. *Biochimica Et Biophysica Acta-General Subjects* **1995**, *1243* (2), 287-289.
48. Triantap.E; Triantap.Dc, Amino acid composition of human fibrinogen anticoagulant derivatives. *Biochemical Journal* **1967**, *105* (1), 393-400.
49. Tang, L.; Eaton, J. W., Fibrin(ogen) mediates acute inflammatory responses to biomaterials. *Journal of Experimental Medicine* **1993**, *178* (6), 2147-2156.
50. Lowe, G. D. O.; Rumley, A.; Mackie, I. J., Plasma fibrinogen. *Annals of Clinical Biochemistry* **2004**, *41*, 430-440.
51. Jo, S.; Park, K., Surface modification using silanated poly(ethylene glycol)s. *Biomaterials* **2000**, *21* (6), 605-616.
52. Zhang, Z.; Zhang, M.; Chen, S.; Horbett, T. A.; Ratner, B. D.; Jiang, S., Blood compatibility of surfaces with superlow protein adsorption. *Biomaterials* **2008**, *29* (32), 4285-4291.
53. Schlenoff, J. B.; Li, M.; Ly, H., Stability and self-exchange in alkanethiol monolayers. *Journal of the American Chemical Society* **1995**, *117* (50), 12528-12536.
54. Volden, S.; Zhu, K.; Nyström, B.; Glomm, W. R., Use of cellulose derivatives on gold surfaces for reduced nonspecific adsorption of immunoglobulin G. *Colloids and Surfaces B: Biointerfaces* **2009**, *72* (2), 266-271.
55. Rastogi, A.; Nad, S.; Tanaka, M.; Mota, N. D.; Tague, M.; Baird, B. A.; Abruña, H. D.; Ober, C. K., Preventing nonspecific adsorption on polymer brush covered gold electrodes using a modified ATRP initiator. *Biomacromolecules* **2009**, *10* (10), 2750-2758.

CHAPTER 4

Competition between dewetting and cross-linking in poly(*N*-vinylpyrrolidone)/polystyrene film bilayers

4.1 Introduction

In Section 1.7 of this Thesis, the dewetting phenomenon was described. It was seen that a liquid that does not wet a surface completely, due to unfavourable intermolecular forces at the solid-liquid interface, can be forced to form uniform films on the substrate by techniques such as spin-coating. In this case though, the films are generally not stable. Unstable or metastable thin films of low viscosity liquids, such as polymer films heated above the glass transition temperature, T_g, will transform, via dewetting, into their equilibrium state, i.e. a series of isolated droplets with a finite contact angle given by Young's equation. The dynamics of dewetting is dominated by the viscosity of the film, and by the profile of the interface potential that determines the instability.[1, 2] The dewetting process results in the formation of holes in the film that grow in time, with a rate that is inversely proportional to the film's viscosity. The material removed from the holes accumulates at the boundary of the holes, forming a rim. Both the rim and the diameter of the hole grow with time, until the hole impinges on adjacent holes, resulting in the formation of a network of liquid cylinders, which eventually break up into isolated droplets due to Rayleigh instability.[3]

The majority of the research on dewetting has been dedicated to single polymer films on smooth, solid substrates such as hydrophobised silicon. Less attention has been dedicated to investigating dewetting in bilayers of two immiscible polymers films, which is more complex (see reference 4 and references within). Whether the bottom film behaves as a rigid solid or as a highly viscous liquid depends on the relative viscosities of the two films.[5, 6] If the bottom film is not completely rigid (i.e. the viscosity of the top film is greater than the bottom film), it may deform at the liquid/liquid interface to minimize the total free energy of the system, and viscous dissipation may take place in both films.

In the work reported in this Chapter, the dewetting of poly(*N*-vinylpyrrolidone) (PNVP) films on polystyrene (PS) films was investigated. As described in Chapter 3, PNVP undergoes radical cross-linking upon thermal annealing. In this particular polymer film bilayer therefore, the viscosity of the top dewetting PNVP film increased (because of the increase in molecular weight) as the film dewetted on the bottom PS film. In Chapter 3, the significant potential for biological applications of cross-linked PNVP films was discussed; cross-linked PNVP films were found to have excellent protein-repellent properties, they were insoluble and stable in water for many weeks, as well as resistant to harsh solvents. Due to their ease of preparation, cross-linked PNVP films could potentially be used to coat objects of large surface area and complex geometries, and could be promising candidates as antifouling coatings for biomedical devices such as catheters. It is therefore of practical importance, as well as of fundamental interest, to fully understand the stability and dynamics of PNVP films as they undergo thermal cross-linking on different substrates, including substrates that they do not wet. The understanding of the dewetting dynamics of PNVP on PS may also be important for the development of micropatterned coatings for the localised immobilization of biomolecules and cells, as PS in moderately protein-adsorptive and PNVP in strongly protein-repellent (see Section 3.3.9). The patterning of proteins and cells on a surface was discussed in Section 1.6.

The competition between concurrent dewetting and cross-linking has not been previously investigated in any polymer bilayer system. Al-Akhrass *et al.*[7] studied the dewetting of photocross-linkable PS films, finding that the cross-linking of the polymer film restricted its ability to dewet. In their work, however, the UV irradiation used to achieve a desired cross-linking density was performed in a separate step to the dewetting process. In the study reported here, the dewetting and cross-linking of PNVP were both driven by

thermal annealing and were hence interdependent. Using time-lapse optical microscopy, the dewetting of PNVP films on PS films of two different molecular weights (and hence different melt viscosity) was investigated. Neutron reflectometry was used to study the inner bilayer structure in order to probe the importance of the relative viscosities of the two films, which change as a function of time due to the PNVP cross-linking mechanism. A model was developed in order to interpret the results. The model predicted the dynamics of dewetted hole growth in this system, whereby the cross-linking process impacted on the final dewetted morphology. Through this, reliable estimates of thermodynamic parameters for the cross-linking process, such as the apparent activation energy, were obtained.

4.2 Materials and methods

4.2.1 Preparation of thin film bilayers

The silicon wafers used as substrates and their cleaning procedure were described in Section 2.1.

In the following the samples are referred to as PNVP/PS6850K for the bilayer containing the high molecular weight PS (M_n 6850000 g mol^{-1}, *PDI* 1.04, PSS, Germany), and PNVP/PS96K for the bilayer containing the low molecular weight PS (M_n 96000 g mol^{-1}, *PDI* 1.04, PSS, Germany). The PS films were spin-cast at spin rate of 3000 rpm from a 8-15 mg ml^{-1} solution in anhydrous toluene (>99.9%, Sigma-Aldrich) on silicon wafers with a 2 nm native oxide film (MMRC Pty Ltd., Malvern VIC Australia). The average thickness of the PS films obtained was 58 ± 1 nm, as determined by spectroscopic ellipsometry (J.A. Woollam Co. Inc.), at an angle of incidence of 75°. The as-prepared films were smooth and featureless (RMS roughness =

220 ± 24 pm as measured by atomic force microscopy). The PNVP (M_n 29000 g mol^{-1}, 95%, *PDI* > 4, Sigma-Aldrich) was then spin-cast from a 10 mg ml^{-1} solution in ethanol on the PS film at a spin rate of 3000 rpm, to produce films of thickness 45 ± 1 nm. The as-prepared films were smooth and featureless (RMS roughness = 253 ± 8 pm as measured by atomic force microscopy).

The thickness of the PNVP/PS films was characterized by ellipsometry (see Section 2.4). The thickness of the SiO_2 layer (1 nm) on top of the silicon wafer was determined on the bare silicon wafer first, using the relevant model provided with the software. The system was treated as a monolayer. Then the PS film was spin-cast onto the silicon wafer. The system was modelled as a bilayer, where the SiO_2 thickness was fixed, and the polymer film was modelled using the Cauchy equation. The polymer thickness, and the constants A and B for the Cauchy equation, were measured. The constant A, which is by far the largest contribution to the refractive index, was approx. 1.56. The constant C for the Cauchy equation was fixed to zero. Finally, the PNVP film was spin-cast onto the PS film, and the polymer thickness, and the constants A and B for the Cauchy equation, were measured. The system was modelled as a multilayer (3 layers). The data collected for SiO_2 and PS were fixed, and the Cauchy parameters A and B, and film thickness for PNVP, were determined. The constant A was approx. 1.50.

The viscosity of the PS films was estimated using a combination of experimental data and a 3.5 scaling law with respect to molecular weight (MW). Melt state viscosity, η_0, values were calculated using the data presented in Kang *et al.*[8] and the temperature and MW dependence of the viscosity of polymers in the melt state (Equation 4.2).[9] The estimated values for the two different MW used, at the different temperatures investigated, are summarised in Table 4.1.

Table 4.1 Estimated values of viscosity for PS 96 Kg mol^{-1} and PS 6850 Kg mol^{-1} at the different temperatures employed in this investigation. The two PS films employed as substrates for the dewetting of PNVP films had very different viscosities, and this affected markedly the dewetting behaviour of PNVP.

	Viscosity [Pa s]	
Temperature [°C]	PS96K	PS6850K
160	3.50×10^{5}	1.07×10^{12}
170	1.10×10^{5}	3.38×10^{11}
175	6.30×10^{4}	1.93×10^{11}
177	5.05×10^{4}	1.55×10^{11}
180	3.65×10^{4}	1.12×10^{11}
182	2.94×10^{4}	9.03×10^{10}
185	2.14×10^{4}	6.56×10^{10}
187	1.73×10^{4}	5.31×10^{10}
190	1.27×10^{4}	3.89×10^{10}
200	4.60×10^{3}	1.41×10^{10}
210		5.35×10^{9}
220		2.11×10^{9}
230		8.62×10^{8}
240		3.65×10^{8}

4.2.2 Dewetting and cross-linking of PNVP films

Thermal annealing of the films was performed on a hot plate with fine temperature control (ATV Technologie GmbH, Muenchen, model TR-124) in air, under a reflection optical microscope (Nikon Instruments Inc, Melville NY). Microscope images of the dewetting films were collected for up to seven hours, with a variable capture interval, which was dependent on the speed of the process (typically between 15 and 60 seconds). The radius of the dewetted holes as a function of time was measured using the Nikon NIS Elements software.

4.2.3 Neutron reflectometry

PNVP films were characterized using X-ray and neutron reflectometry at the Australian Nuclear Scientific and Technology Organization (ANSTO) Lucas Heights facility in Sydney, under the direction of Prof. Michael James. Five films were characterized after different annealing procedures. Reflected beam spectra were collected at two different angles (0.5°, 2.0°) for 1 and 4 hours respectively. Direct beam measurements were collected under the same collimation conditions for 1 hour each.

Structural parameters associated with the investigated films were refined using the MOTOFIT package, with X-ray or neutron reflectivity data as a function of momentum transfer normal to the surface ($Q = 4\pi(\sin\theta)/\lambda$). Initial structural models were prepared based on a three film system on a silicon substrate: the top PNVP film, the bottom PS film, and a native silicon oxide (SiO_2) film adjacent to the silicon substrate. In refining this structural model, the thickness, scattering length density (*SLD*) and interfacial roughness of each polymer film were varied. The thickness of the SiO_2 film was refined, while the *SLD* was set at 3.47×10^{-6} Å^{-2}. The genetic optimisation method was used within MOTOFIT to minimize χ^2 values.

More details on neutron and X-ray reflectivity can be found in Section 2.5.

4.3 Results

4.3.1 Two competing processes: dewetting and cross-linking

The work in this Chapter focuses on the competition between two spontaneous processes in thin polymer bilayers consisting of a film of PNVP

on top of a film of PS. The first process observed in the experiments reported here was the dewetting of the top PNVP film. PNVP and PS are immiscible and strongly segregate, e.g. form micelles in block copolymers.[10] The Flory-Huggins interaction parameter χ for PS and PNVP was estimated by a group contribution using von Hildebrand solubility parameters,[11, 12] and was found to be 0.24 at room temperature and 0.16 at the lowest annealing temperature used (170 °C). The equilibrium contact angle θ of a droplet of PNVP on the PS film was measured by AFM to be approximately 75° ± 3°, and the equilibrium contact angle of PS on silicon oxide is 7.5°.[13] The argument here is in terms of Young's contact angle, even though if the PS film is a liquid, the PNVP/PS interface is not strictly constrained to be a plane; PNVP can form a lens to minimize the interfacial free energy, and the Neumann construction should be used.[3] However, in both cases the main conclusions are the same. In these experiments the spreading coefficient S for PNVP on PS was negative, ensuring that PNVP films were expected to dewet from PS films (Equation (4.1)):

$$S = \gamma_{PS} - \gamma_{PNVP} - \gamma_{PS/PNVP} = \gamma_{PNVP}(cos\,\theta - 1) = \\ = -3.86 \pm 0.18\, mN\, m^{-1} \tag{4.1}$$

where γ_{PS}, γ_{PNVP}, and $\gamma_{PS/PNVP}$ are the surface tension values of polystyrene and poly(*N*-vinylpyrrolidone) and the interfacial tension of polystyrene and poly(*N*-vinylpyrrolidone), respectively. The spreading parameter for PNVP on PS was calculated using γ_{PNVP}[14] = 49.36 mN m^{-1} and the contact angle determined experimentally. The spreading coefficient is also negative for PS on silicon (S ≈ -0.262 mN m^{-1}), so in principle PS films could dewet from the silicon substrate. However, the thermodynamic driving force for dewetting is much stronger in PNVP, and this was reflected in the experiments presented here, where complete dewetting of the bottom

PS film from the silicon substrate was not observed over the timeframes of the experiments.

The second process occurring was the thermally-induced cross-linking of PNVP. In the work reported in Chapter 3, this process was characterized by neutron reflectometry, infrared spectroscopy, X-ray photoelectron spectroscopy and ellipsometry in PNVP films prepared on silicon wafers, a substrate on which the PNVP films were stable and did not exhibit dewetting. PNVP films shrunk and became denser as a consequence of cross-linking. In the work presented in this Chapter, a range of temperatures were used, which achieved a controlled competition between the dewetting of the top PNVP film on the bottom PS film and the cross-linking of the PNVP chains within the top film. As will become clear, there was only a narrow range of temperatures where both processes proceeded at similar rates.

In principle, the additional process of layer inversion could affect PNVP/PS bilayers. Layer inversion is a phenomenon observed when a high surface energy polymer film is prepared on a low surface energy polymer film. When annealed above the T_g of both polymers, the two tend to rearrange to minimize the energy of the entire system, so the hydrophobic polymer migrates towards the air interface, and the hydrophilic polymer migrates towards the hydrophilic silica substrate. Layer inversion was recently investigated in poly(4-vinylpyridine)/polystyrene bilayers,[4] which are similar systems to the one investigated here, with the exception that poly(4-vinylpyridine) cannot undergo thermal cross-linking. The possible occurrence of layer inversion, as well as the internal structure of the bilayer before and after cross-linking, were investigated by neutron reflectometry.

4.3.2 Neutron reflectivity data

Neutron reflectometry (NR) was used to investigate the PNVP cross-linking process. The PNVP film was more likely to undergo layer inversion on low MW PS (PS96K) than on high MW PS, as long chain polymers are less mobile and have much slower reptation dynamics.[4] Because of this, the PNVP/PS96K system was chosen for investigation by NR, but the results can be extended to the PNVP/PS6850K system.

Shown in Figure 4.1 are neutron reflectivity curves for an as-prepared PNVP/PS96K bilayer (trace (a)) and for a bilayer annealed for 160 °C for 7 hours (*Sample 1*, trace (b)). The calculated reflectivity profiles in each case are given by the solid lines. A slight modulation in the Kiessig fringes is evident in the profile from the as-prepared film, indicating a significant difference in scattering length density (*SLD*) between the two polymer bilayer films. This modulation is less evident in the data from the annealed sample. Refined structural models from both of these films are given in Table 4.2. In both samples the *SLD* of the PS96K films was comparable to that observed for PS in the literature ($1.3\text{-}1.5\times10^{-6}$ Å^{-2}),[15, 16] and remained unchanged after annealing. This is a strong indication that the PS was not mixing with the PNVP, and the films maintained their integrity.

The *SLD* of the PNVP film spin-coated on the PS96K film in the as-prepared film (1.05×10^{-6} Å^{-2}) was slightly larger than that previously reported for a PNVP film prepared directly on silicon (0.93×10^{-6} Å^{-2}).[17] Upon annealing, the PNVP film shrunk in thickness, cross-linked and became denser. Annealing at 160 °C for 7 hours led to a decrease in thickness of 12% and an increase in *SLD* to 1.40×10^{-6} Å^{-2} (*Sample 1*, Table 4.2). Analysis of optical micrographs of the annealed sample showed that at this annealing temperature no dewetting was occurring, and the film remained smooth and continuous, as previously observed on the wettable silicon wafer (see Section

3.3.5).[17] An important implication of this is that by carefully selecting the annealing temperature it is possible, via thermally initiated cross-linking, to stabilize the PNVP film against dewetting on poorly wettable substrates such as PS.

Table 4.2 Refined structural parameters for as-prepared and annealed PNVP/PS96K bilayers, with errors on the last significant figure shown in parenthesis.

	Film as-prepared[a]	Sample 1 160 °C, 7 hours	Sample 2 175 °C, 30 min	Sample 3 175 °C, 1 hour	Sample 4 175 °C, 3 hours
PNVP film					
Thickness [Å]	411(2)	362(2)	392(3)	359(5)	375(9)
SLD [$\times 10^6$ Å^{-2}][b]	1.05(1)	1.40(1)	1.27(1)	1.32(1)	1.42(1)
Surface Roughness [Å]	9(1)	6(1)	6(1)	9(1)	7(1)
PS96K film					
Thickness [Å]	423(2)	426(3)	409(3)	397(6)	382(8)
SLD [$\times 10^6$ Å^{-2}]	1.47(1)	1.49(1)	1.51(1)	1.48(1)	1.49(1)
Interfacial Roughness [Å]	15(1)	12(1)	10(1)	8(1)	9(1)
SiO_2 film					
Thickness [Å]	11(1)	8(1)	7(1)	7(1)	6(1)
SLD [$\times 10^6$ Å^{-2}]	3.47	3.47	3.47	3.47	3.47
Roughness [Å]	4(1)	4(1)	4(1)	4(1)	4(1)
Si Roughness [Å]	4(1)	4(1)	4(1)	4(1)	4(1)

[a] The as-prepared sample information only directly relates to Sample 1 (annealed at 160 °C). Information on other as-prepared samples relating to Samples 2-4 is not reported in this table.

[b] The refined values of *SLD* for the PNVP film annealed at 175 °C have been corrected for the observed area of dewetted film.

Upon annealing at a higher temperature (175 °C, *Samples 2-4*, Table 4.2), the top PNVP film dewetted on the bottom PS96K film, while simultaneously undergoing cross-linking. The dewetted holes in the PNVP film increased in area with annealing time. Even at long annealing times, the maximum area occupied by the holes was relatively small (around 3 - 6% of

the total area of the film), indicating that at this temperature the dynamics of the cross-linking process dominated over that of dewetting. The reported value of area coverage by holes is an average over different areas of the sample, which had very different areas occupied by holes (between 0% - 15% of the total area of the film). The large samples used in NR (100 mm in diameter) presented regions with different density of dewetted holes throughout the film.

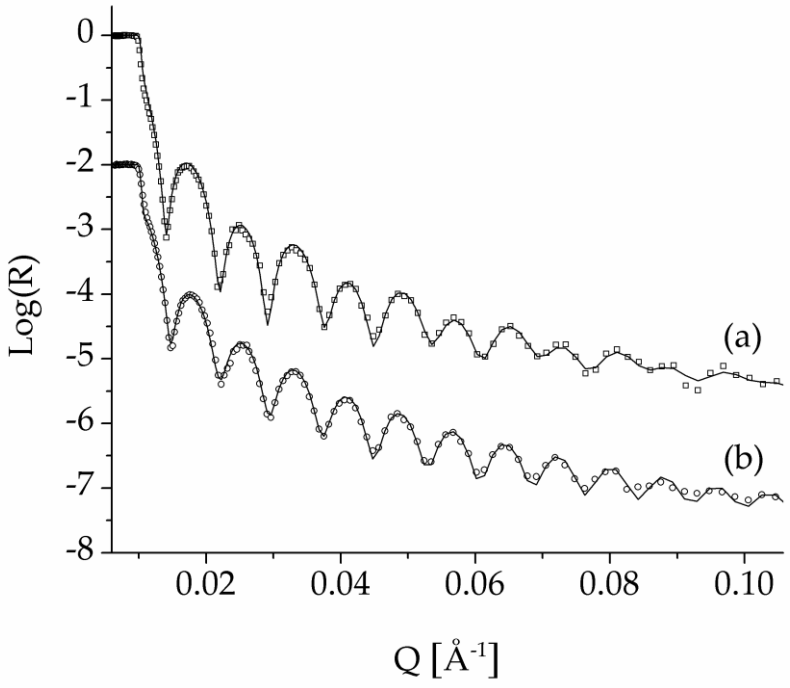

Figure 4.1 Neutron reflectivity data for (a) an as-prepared PNVP/PS96K bilayer, and (b) for a bilayer annealed for 160 °C for 7 hours. Observed data (points) and calculated data (solid lines) are reported.

Shown in Figure 4.2 is the evolution in neutron reflectivity with annealing time at 175 °C. After annealing for 30 minutes (*Sample 2*, trace (a)) the observed reflectivity showed similar features to the as-prepared films (Figure 4.1); however examination of the fitted structure showed a decrease

in the thickness of the PNVP film and an increase in *SLD* to 1.27×10^{-6} Å^{-2} (*Sample 2*, Table 4.2). Continued annealing for 1 hour (*Sample 3*, trace (b)) and 3 hours (*Sample 4*, trace (c)) gave rise to gradual increase in the degree of cross-linking, as revealed by larger *SLD* values (1.32×10^{-6} Å^{-2} and 1.42×10^{-6} Å^{-2} respectively; *Samples 3* and *4*, Table 4.2). Direct comparison between the as-prepared film (data not shown), and the bilayer film annealed at 175 °C for 3 hours, indicated a 10% shrinkage in the thickness of the upper PNVP film (from 417(3) Å to 375(9) Å). Although a small amount of dewetting took place while the PNVP film was cross-linking, the overall surface roughness of these bilayer films remained essentially the same and comparable with that of as-prepared films (Table 4.2).

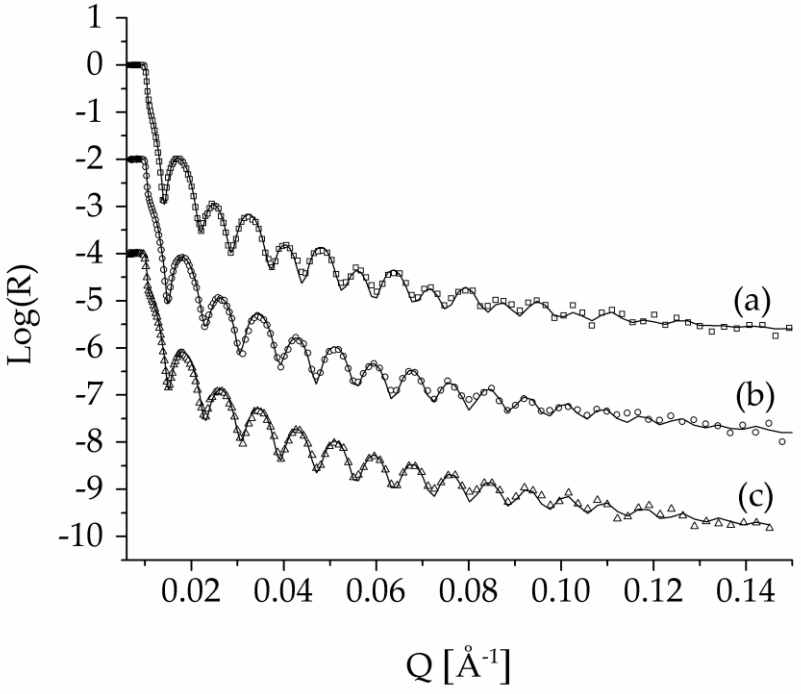

Figure 4.2 Neutron reflectivity data from PNVP/PS96K bilayers after annealing at (a) 175 °C for 30 minutes, (b) 1 hour, and (c) 3 hours. Observed data (points) and calculated data (solid lines) are reported.

Overall, the neutron reflectivity analysis showed that the *SLD* of PNVP films prepared on PS films increased with annealing time due to the gradual cross-linking of the PNVP, similarly to the behaviour observed for PNVP films on wettable silicon wafers (see Section 3.3.5).[17] The *SLD* of the PS films did not change throughout the annealing, as expected for a single and uniform film of an inert polymer, suggesting no interpenetration of the PNVP and PS films, hence no layer inversion.

4.3.3 Optical microscopy

Illustrated in Figure 4.3 row (a) is the dewetting of a PNVP film on a PS96K film at 200 °C. Dewetted holes formed in the top PNVP film via heterogeneous nucleation, and their diameter grew with annealing time until the holes begun to coalesce. Eventually the films reached a final dewetted state consisting of liquid cylinders of PNVP on top of the PS96K background phase, indicating that the initial rate of dewetting exceeded that of the cross-linking process, allowing the dewetting process to progress extensively. In all the experiments reported in this Section, the final breakup of the cylinders of PNVP into droplets was not observed, expected due to Rayleigh instability, possibly due to viscous friction at the liquid/liquid interface. The behaviour of PNVP dewetting on PS96K was significantly different at lower annealing temperatures. Shown in Figure 4.3 row (b) are time-lapsed optical images of PNVP/PS96K annealed at 182 °C: the PNVP film began to undergo dewetting, however the holes never became large enough to coalesce. Instead, the holes reached a maximum size, and then stopped growing. After this stage was reached, the size of the holes did not change significantly between 30 min and 6 hours of annealing.

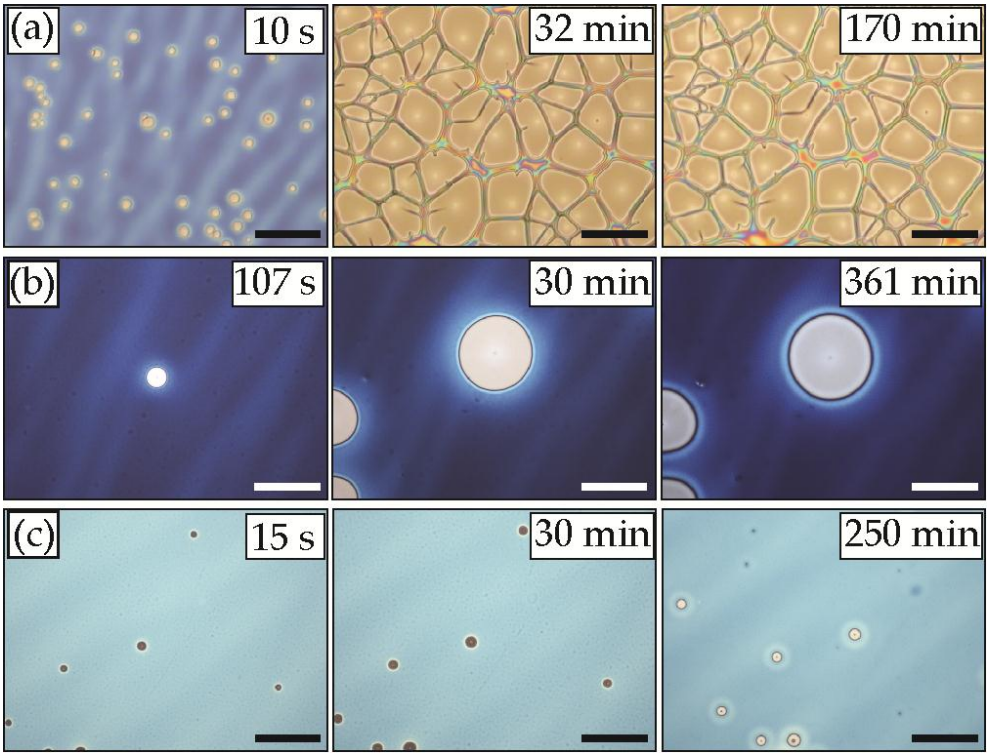

Figure 4.3 Time-lapse series of optical micrographs of a PNVP film of thickness 45 ± 1 nm dewetting on row (a) PS96K at 200 °C, row (b) PS96K at 182 °C, and row (c) PS6850K at 200 °C. The time from the start of annealing is shown in each micrograph. The scale bar in all the images equals 50 μm. The bright halos around the holes are rims of material collected on the dewetting front.

The dynamics of dewetting of PNVP films on PS6850K films were much slower. Shown in Figure 4.3 row (c) are time-lapse optical images of PNVP/PS6850K annealed at 200 °C, to be compared to the results for the dewetting of PNVP/PS96K at the same temperature (Figure 4.3 row (a)). While PNVP reached an advanced state of dewetting on low viscosity PS, it only formed small holes on the high viscosity substrate, after which hole growth ceased entirely. This behaviour was attributed to the fact that on the PS6850K substrate the viscous dissipation at the polymer/polymer interface is much higher, as reported previously.[4, 18] The lower mobility of the PS chains results in higher friction, hence loss of kinetic energy.

A large number of dewetting experiments were performed to investigate the dynamics of the growth of dewetted holes in the PNVP films by time-lapse optical microscopy. Shown in Figure 4.4 are the growth of dewetted holes (i.e. the hole radii as a function of time) in bilayer systems consisting of PNVP on top of PS96K (a) and PS6850K (b). In both cases the holes grew rapidly at the beginning of the annealing process, but later their growth slowed down and almost stopped; the hole radii reached a plateau value which stayed constant in the case of PNVP/PS6850K, and changed only slightly after many additional hours of annealing in the case of PNVP/PS96K. In both systems the plateau value, i.e. the maximum achievable hole size, increased strongly with increasing annealing temperature; the plateau value depended also on the nature of the bottom PS film used, as discussed in Section 4.4.

The dewetting dynamics for PS/PNVP bilayer systems presented here differ strongly from the well established dewetting behaviour for single polymer films on a non-wettable substrate. Typically, the growth of a dewetted hole is expected to be close to linear in liquid/solid systems[19] (i.e. the velocity of the dewetting front is constant) and non-linear in liquid/liquid systems.[20] The significant reduction in dewetting velocity observed here was attributed to a gradual increase in the viscosity of the PNVP melt, which is consistent with the simultaneous cross-linking of this film. The competitive effect of the PNVP cross-linking process prevented the PNVP film from achieving complete dewetting, even after many hours of annealing (typically 5 to 7 hours), due to this increase in melt viscosity.

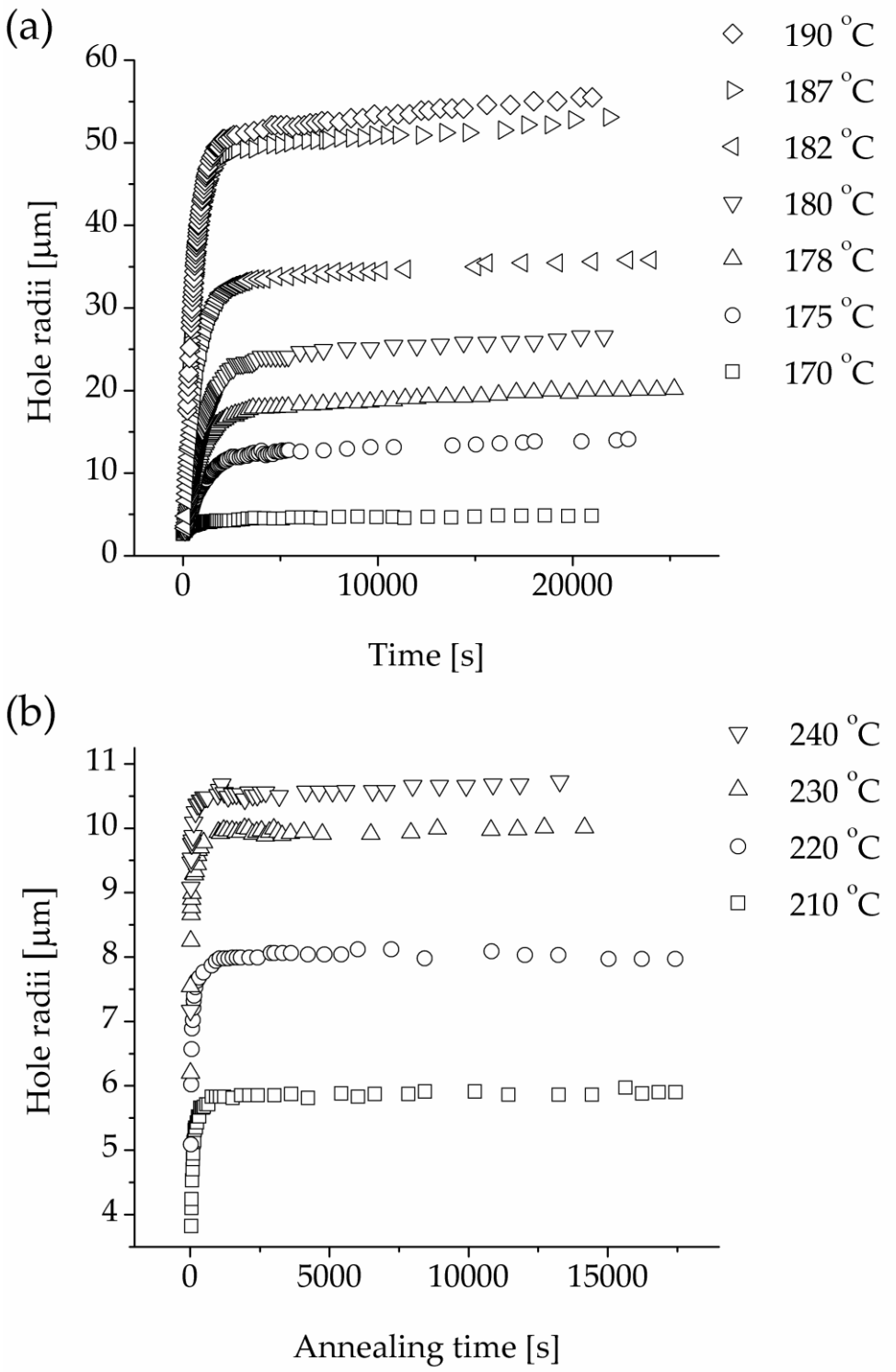

Figure 4.4 Hole radius as a function of annealing time at different temperatures for (a) PNVP/PS96K, and (b) PNVP/PS6850K. The hole radii initially grew rapidly, but after some time slowed down and reached a plateau value.

The two processes being considered here, namely dewetting and cross-linking, are both temperature dependent, therefore the relative rates of the two processes affect the final achievable morphology, and in particular the maximum achievable dewetted hole size. A model was developed that explains the dynamics of hole growth very well for the PNVP/PS6850K system, and for the PNVP/PS96K at short times (see Section 4.3.4).

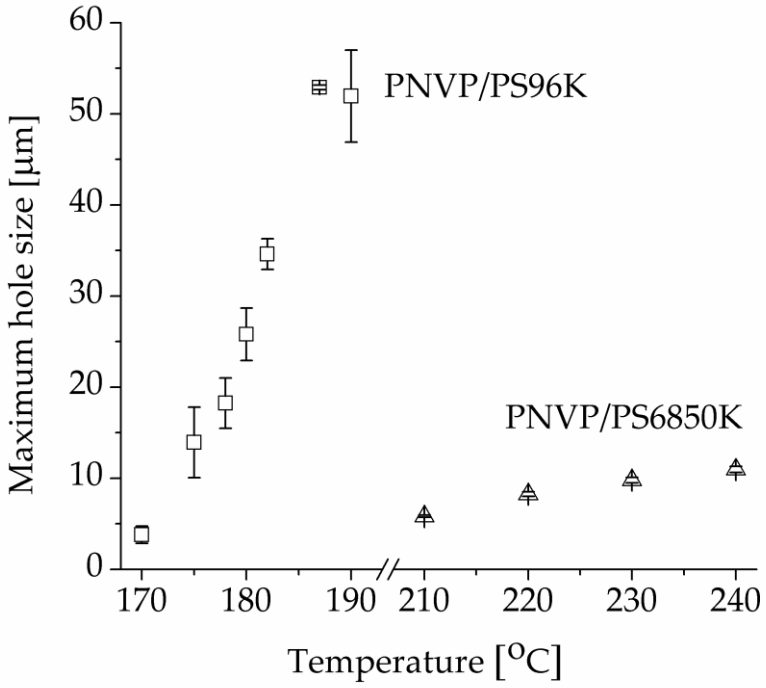

Figure 4.5 Maximum dewetted hole size as a function of temperature obtained in PNVP films on top of PS96K (squares) and PS6850K (triangles). Each data point is the average of 2-5 samples, and the error bars represent the 95% confidence interval.

Presented in Figure 4.5 is the maximum dewetted hole size as a function of temperature for the two systems investigated and two aspects of the hole growth are highlighted. Firstly, the maximum hole size achievable in the PNVP/PS bilayers strongly increased with annealing temperature. This observation is in agreement with the study of the dewetting of a

photocross-linkable polystyrene film by Al Akhrass *et al.*[7] The authors investigated hole growth dynamics in PS films containing azide groups that could be cross-linked with UV radiation, by inducing different degrees of cross-linking prior to dewetting. They observed that the higher the degree of cross-linking, the smaller was the maximum hole size achievable by dewetting. The PNVP/PS system behaved in a very similar way, but here the cross-linking was thermally initiated and was concurrent with the dewetting.

Secondly, the data in Figure 4.5 shows a marked difference in the maximum hole size achievable in the two systems under investigation. PNVP on PS96K could achieve a much higher degree of dewetting than on PS6850K before the cross-linking drastically slowed it down, despite the lower annealing temperatures employed.

Optical microscopy was also used to estimate the average density of the holes nucleated over time in the PNVP/PS96K system at different temperatures, as shown in Figure 4.6. There was a distinct break in the data at around 180 °C, with an average hole density around 400-500 holes mm^{-2} above 180 °C and an average hole density around 150-200 holes mm^{-2} below 180 °C. At temperatures below 180 °C, the holes grew slowly, and annealing times above 300 s were required to obtain holes big enough to be visible under the optical microscope with a 20x objective. The hole density was constant throughout the annealing process at each temperature, except at 177 °C and 180 °C, where the hole density increased moderately in time (by about 29 %). At temperatures above 180 °C, the average hole density values at different temperatures were similar to each other, and were constant in time. At high annealing temperatures, the holes all nucleated at very short annealing times, and were visible under the optical microscope after just 20 s.

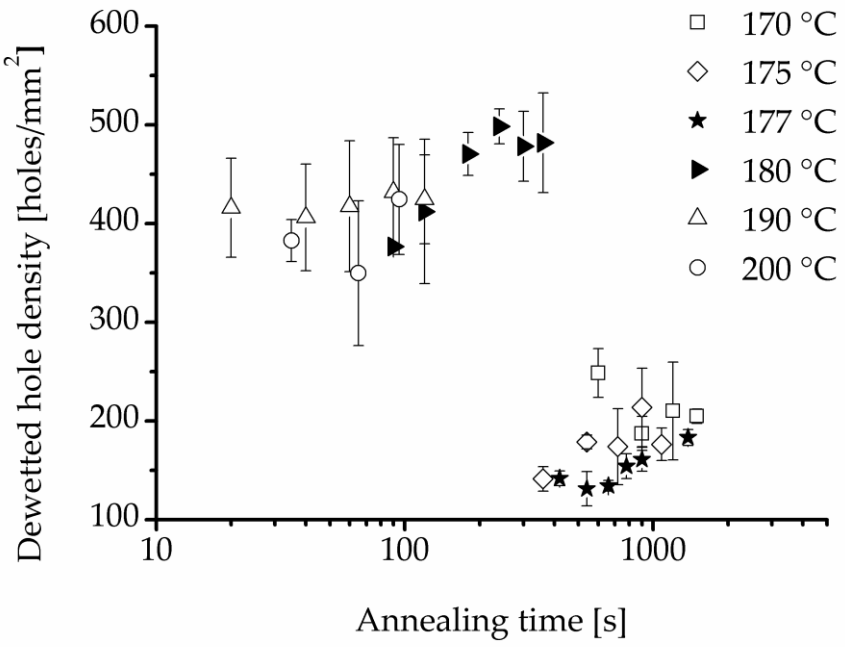

Figure 4.6 Average hole density formed on PNVP films of thickness 54 ±1 nm dewetting on PS96K films of thickness 74 ±1 nm at different annealing temperatures. The average hole density showed relatively no change for temperatures below 180 °C, and then drastically increased at 180 °C. For temperatures above 180 °C, the hole density showed again little change.

To reveal stress or deformation at the PS/PNVP interface, the PS film was selectively removed by washing the bilayers with toluene, which is a good solvent for the PS film, but a non-solvent for the cross-linked PNVP film. Firstly, a PNVP/PS96K bilayer was washed, which contained a PNVP film that was fully cross-linked before any dewetting occurred (annealed for 7 hours at 160 °C), and the result is shown in Figure 4.7. Upon washing with toluene the surface of the PNVP film, which initially appeared dark blue, uniform and featureless, showed many brown-black asterisk-shaped fractures on its surface, surrounded by light blue areas, were the film thickness had changed, as highlighted by the interference colour. It was believed that the toluene could penetrate through the cross-linked PNVP layer, through small pores or points of lower film density, and in doing so

dissolved circular sections of the bottom PS film, as shown by the change in colour from dark blue to light blue. Also, the washing process induced fractures and wrinkling of the top PNVP film, which probably highlighted regions of stress due to cross-linking in the film.

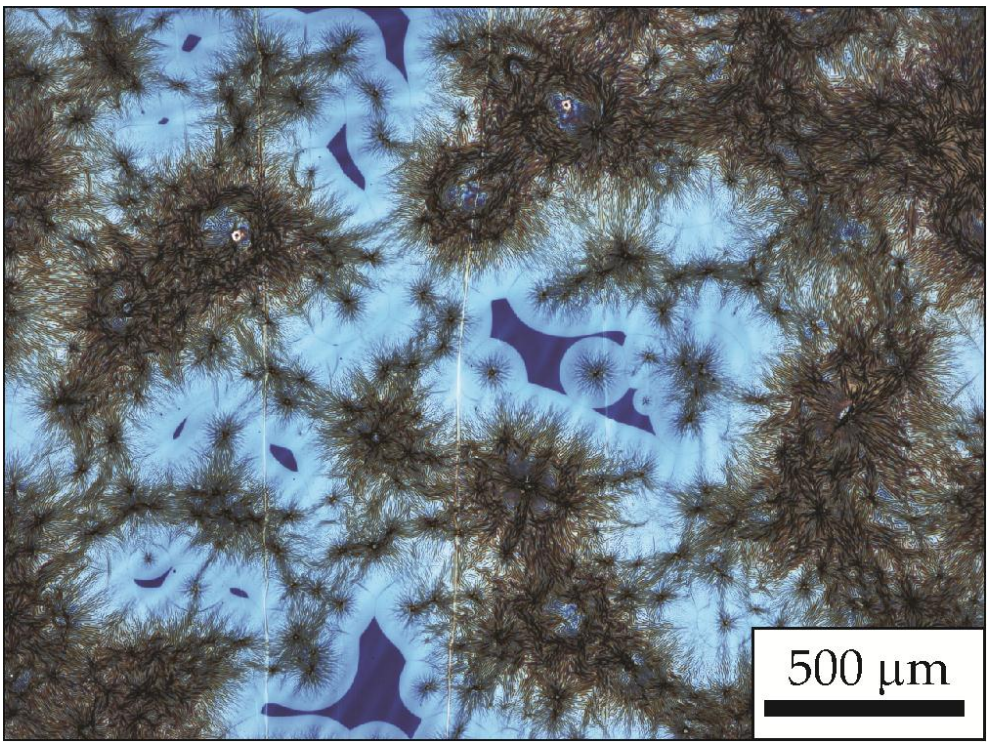

Figure 4.7 PNVP/PS96K bilayer annealed at 160 °C for about 7 hours and washed in toluene to selectively remove the PS film.

Shown in Figure 4.8(a) is a PNVP/PS96K sample annealed at 180 °C for about 7 hours, which contained several dewetted holes of approximately 23 micrometres in radius. In these conditions, as discussed in Section 4.4, the PNVP/PS96K bilayer had a chance to both dewet and cross-link during annealing, before being washed with toluene. The nucleation of holes in the dewetted PNVP exposed the underlying PS film, which was readily removed by the toluene, exposing the underlying silicon substrate (mirror-

like finish inside the holes). The cross-linked PNVP film developed extensive patterns of wrinkling, ridges and gullies, both radiating from the edges of the holes and zigzagging in the remainder of the film.

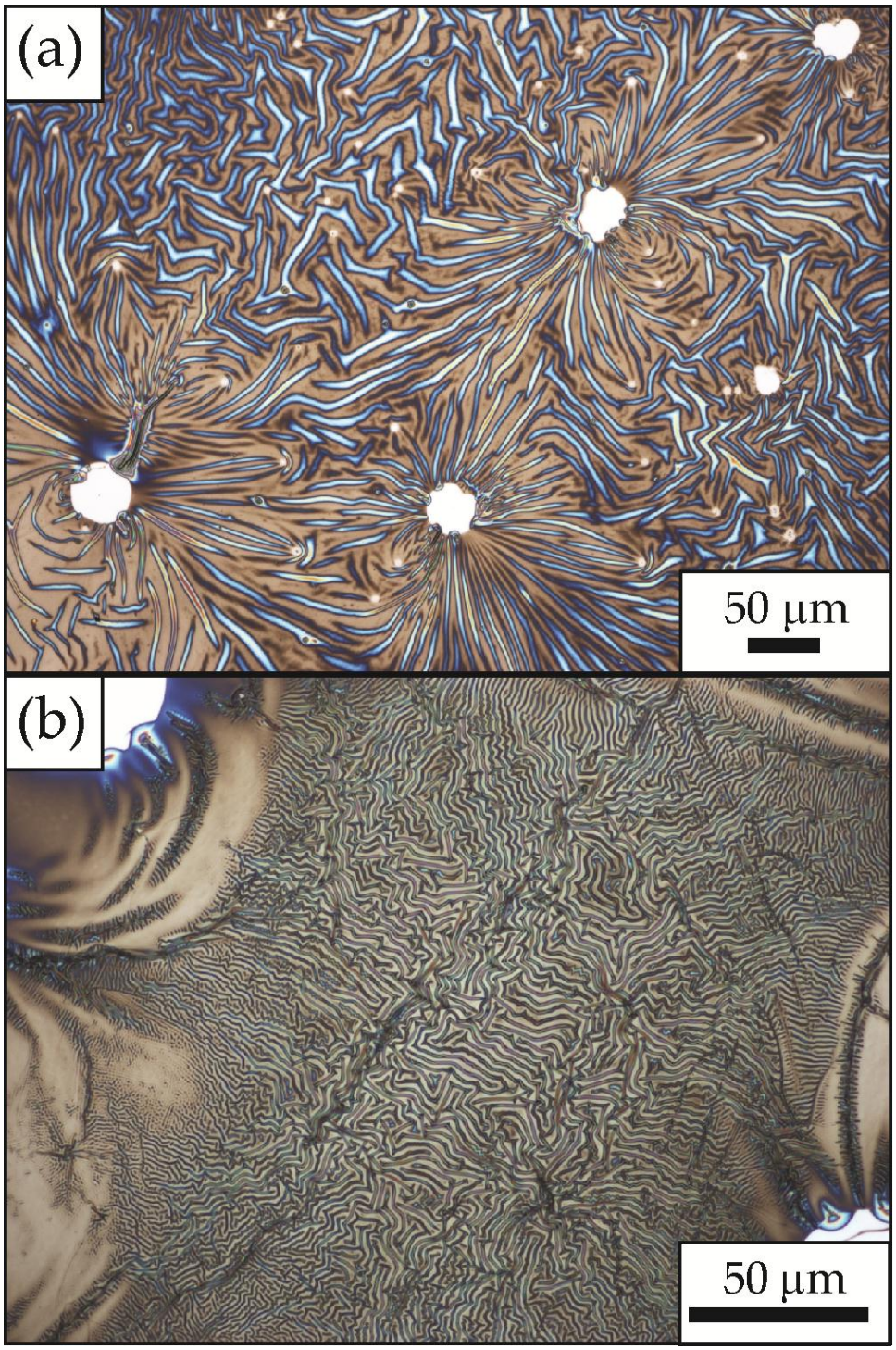

Figure 4.8 PNVP/PS96K bilayer annealed at (a) 180 °C and (b) 187 °C for about 7 hours and washed in toluene to selectively remove the PS film. The top cross-linked PNVP film collapsed on the silicon wafer forming a wrinkled structure.

Shown in Figure 4.8(b) is a different bilayer sample, annealed at 187 °C for about 7 hours, and then washed with toluene. This micrograph was taken in a portion of PNVP film between three holes, and showed extensive wrinkling as well. In both cases it is likely that the cross-linked PNVP films collapsed on the silicon substrate, after the complete removal of the PS, and wrinkled because of non-homogeneous stresses induced by the thermal cross-linking, which could relax into a pattern once the constraint of the underlying PS films was removed.

Similar observations were made in the work of Bonaccurso *et al.*,[21] where polystyrene sheets were cross-linked with plasma irradiation and developed with toluene vapours. The authors attributed the wrinkling effect to the presence of mechanical anisotropies in the extruded PS sheet, due to both the cross-linking with plasma, and a non-homogeneous material preparation.

4.3.4 Theoretical model

The behaviour was described of a polymer bilayer system where the top polymer film could undergo dewetting when heated above its T_g, while its ability to dewet was retarded by a thermal cross-linking process that occurred simultaneously. The cross-linking process was characterized by a first-order rate coefficient, denoted k_{XL}. The continual cross-linking of the polymer film increased the MW (and hence melt viscosity) of the polymer film, which altered the dewetting dynamics of the system. The model developed here is described as follows.

Based on the theory of the reptation of a polymer chain,[22-24] the viscosity of a polymer melt above the chain entanglement length follows an Arrhenius-type expression:

$$\eta_{melt} = \kappa e^{\frac{E_0}{k_B T}} \tag{4.2}$$

where E_0 is the energetic barrier to viscous flow, k_B is the Boltzmann constant, T is the temperature, and the coefficient k is the product:

$$\kappa = 0.34 N_A \rho \sqrt{\kappa_B T} (a_0 L_0 M_e^6)^{-2/3} M^{3.5} \tag{4.3}$$

where N_A is Avogadro's number, ρ the density of polymer in the melt, M_e the critical entanglement MW, L_0 the length of the polymer chain at the critical entanglement length and a_0 the diameter of the "reptation tube" at the critical entanglement length. The most significant term in Equation (4.3) is the dominant $M^{3.5}$ term, which indicates that at a given temperature, the viscosity of a polymer melt scales significantly with an increase in the polymer MW. For this purpose, the melt viscosity equation was re-written by collecting the constants into one parameter A:

$$\eta_{melt} = AM^{3.5} \tag{4.4}$$

While the cross-linking of a polymer film during thermal annealing is a chemical process with a chemically controlled rate coefficient (denoted k_{XL}), it was not mapped as a chemical change, but instead as the physical change that occurred when two chains in the melt cross-linked. It was assumed that when two chains cross-link, the MW of the resultant chain is the sum of the two MWs of the component chains. For these purposes, it was assumed that the MW (assuming the likelihood of cross-linking is uniform throughout the film) is an exponentially growing function in time:

$$M(t) = M_0 e^{\kappa_{XL} t} \tag{4.5}$$

where M_0 is the MW of the un-cross-linked film (i.e. time t = 0). This simple exponential function has been used before as a reasonable approximation to describe the rapid increase of the polymer MW upon random cross-linking.[25] In this work, the same PNVP used in the investigation reported in Chapter 3 was employed, which was polydisperse (PDI > 4); the polydispersity of this sample complicated the understanding of this system but, according to Tobita *et al.*,[25] the MW of randomly cross-linked polymers can be described by an exponential function regardless of their polydispersity. The only difference resides in the MW distribution of the resulting sol, which will be multimodal in the case of low polydispersity polymers and broad and smooth in the case of high polydispersity polymers. The combination of Equations (4.4) and (4.5) predicts that the melt viscosity is a function of time:

$$\eta_{melt}(t) = AM_0^{3.5}e^{3.5\kappa_{XL}t} \tag{4.6}$$

where the pre-coefficient A is given by $A = 0.34N_A\rho\sqrt{\kappa_B T}(a_0 L_0 M_e^6)^{-2/3}e^{\frac{E_0}{\kappa_B T}}$.

Equation (4.6) is a simple model that can be used to describe the melt viscosity of a PNVP film that undergoes cross-linking, based on the initial polymer average MW, the rate of cross-linking and a series of constants. Equation (4.6) suggests that the viscosity of the dewetting, cross-linking PNVP film significantly increases as a function of time. The implications are immediate for dewetting, as the velocity of a dewetting rim will be retarded by the significant increase in the viscosity of the polymer that is being displaced.

The expression for the time-dependent melt viscosity of a cross-linkable polymer film in Equation (4.6) was used to model the dewetting

behaviour (i.e. the growth of dewetted holes as a function of time) on liquid-like and solid-like substrates. There exists no literature on the melt viscosity of PNVP thin films. However, the assumption was that given the low average MW of the PNVP used (29K) relative to either of the PS films (PS96K and PS6850K), the initial melt viscosity of the top un-cross-linked PNVP film was lower than the melt viscosity of the bottom PS film, a situation known as "liquid/solid" dewetting.[6] The PNVP/PS96K system may well switch to a liquid/liquid dewetting regime as the melt viscosity of the top PNVP film continues to increase, potentially to values greater than the viscosity of the bottom PS film.[18] Based on the model of Brochard-Wyart *et al.*[26] (also described in detail in Wang *et al.*[27]), the dewetting velocity of a liquid film from a solid substrate can be described by the equation:

$$v(t) = \frac{1}{12\kappa\sqrt{2}} \frac{\gamma_{PNVP}}{\eta_{PNVP(t)}} \theta^3 \tag{4.7}$$

where γ_{PNVP} is the surface tension of PNVP, κ is a numerical dissipation factor (~ 10, see Brochard-Wyart *et al.*[28] and Wang *et al.*[27]) and θ is the contact angle of PNVP on PS. If the melt viscosity of the top PNVP film was constant, this model would predict a constant dewetting velocity in this regime, which has been demonstrated experimentally for holes with fully developed rims.[1, 29, 30] However, by combining Equations (4.6) and (4.7) the model developed here predicts an exponentially decaying dewetting velocity as a function of time:

$$v(t) = \frac{\gamma_{PNVP}}{12\kappa\sqrt{2}} \frac{\theta^3}{AM_0^{3.5}} e^{-3.5\kappa_{XL}t} \tag{4.8}$$

The integration of Equation (4.8) gives the expression for the radius of a dewetted hole as a function of time, which is given by:

$$R(t) = \frac{\gamma_{PNVP}}{42\kappa_{XL}\kappa\sqrt{2}} \frac{\theta^3}{AM_0^{3.5}}(1 - e^{-3.5\kappa_{XL}t}) \quad (4.9)$$

Equation (4.9) is therefore a simple description of the growth in time of a dewetted hole in a polymer film that can simultaneously undergo thermal cross-linking, such as PNVP. The hole growth was described by the parameter of interest (k_{XL}), known or experimentally measurable parameters (surface tension, contact angle and initial average MW) and coefficients or numerical factors such as A and κ. The majority of the terms that describe A can be estimated from theoretical values relating to the polymer. The fit of experimentally determined hole growth data for PNVP/PS systems at different temperatures with the model in Equation (4.9) provided thermodynamic information on the cross-linking process.

Equation (4.9) predicts that at long annealing times ($t \to \infty$) dewetting should cease and a maximum achievable hole size (denoted R_{max}) should be reached. This can be theoretically described as:

$$R_{max} = \frac{\gamma_{PNVP}}{42\kappa_{XL}\kappa\sqrt{2}} \frac{\theta^3}{AM_0^{3.5}} \quad (4.10)$$

It is important to notice that the model described by Brochard-Wyart et al.[26] assumes linear chains which are able to reptate, which allows for the flow of viscous polymer melts. In the system here investigated this assumption was only an approximation, because the development of a cross-linked network within the dewetting PNVP film not only increased dramatically the polymer viscosity, but introduced an elastic force which prevented the reptation of the chains and immobilised the polymer film, once the cross-linking density became greater than a critical value.

4.3.5 Data fitting with the developed model

Using the developed model (Equation (4.9)), the hole growth data previously displayed in Figure 4.4 was fitted. Due to the difficulty in obtaining experimental values or meaningful estimates of many of the parameters in the pre-exponential term within Equation (4.9), a simple two parameter fitting model was developed to describe the variation of dewetted hole radius as a function of time, namely:

$$R(t) = \frac{c}{3.5\ k_{XL}}(1 - \exp(-3.5k_{XL}t)) \qquad (4.11)$$

where c is the collection of parameters described above. Shown in Figure 4.9 is the comparison between experimental data and the developed model for PNVP/PS96K (a) and PNVP/PS6850K (b). The model provided an excellent fit to the experimental data in Figure 4.9(b) across the entire temperature range and time range studied (up to 5 hours of annealing, which were previously demonstrated to be sufficient to cross-link the whole PNVP film, see Chapter 3),[17] modelling the high initial dewetting velocity and cessation of hole growth. Mechanistically, these results could be interpreted as a confirmation that the PNVP melt flowed on the solid PS6850K film, until the cross-linked network was rigid enough to oppose the dewetting driving force. In the case of PNVP/PS96K (Figure 4.9(a)), the model described the growth profile of a dewetting hole at early and intermediate annealing times, and captured the concept that the dewetting velocity was greatly retarded as dewetting proceeded.

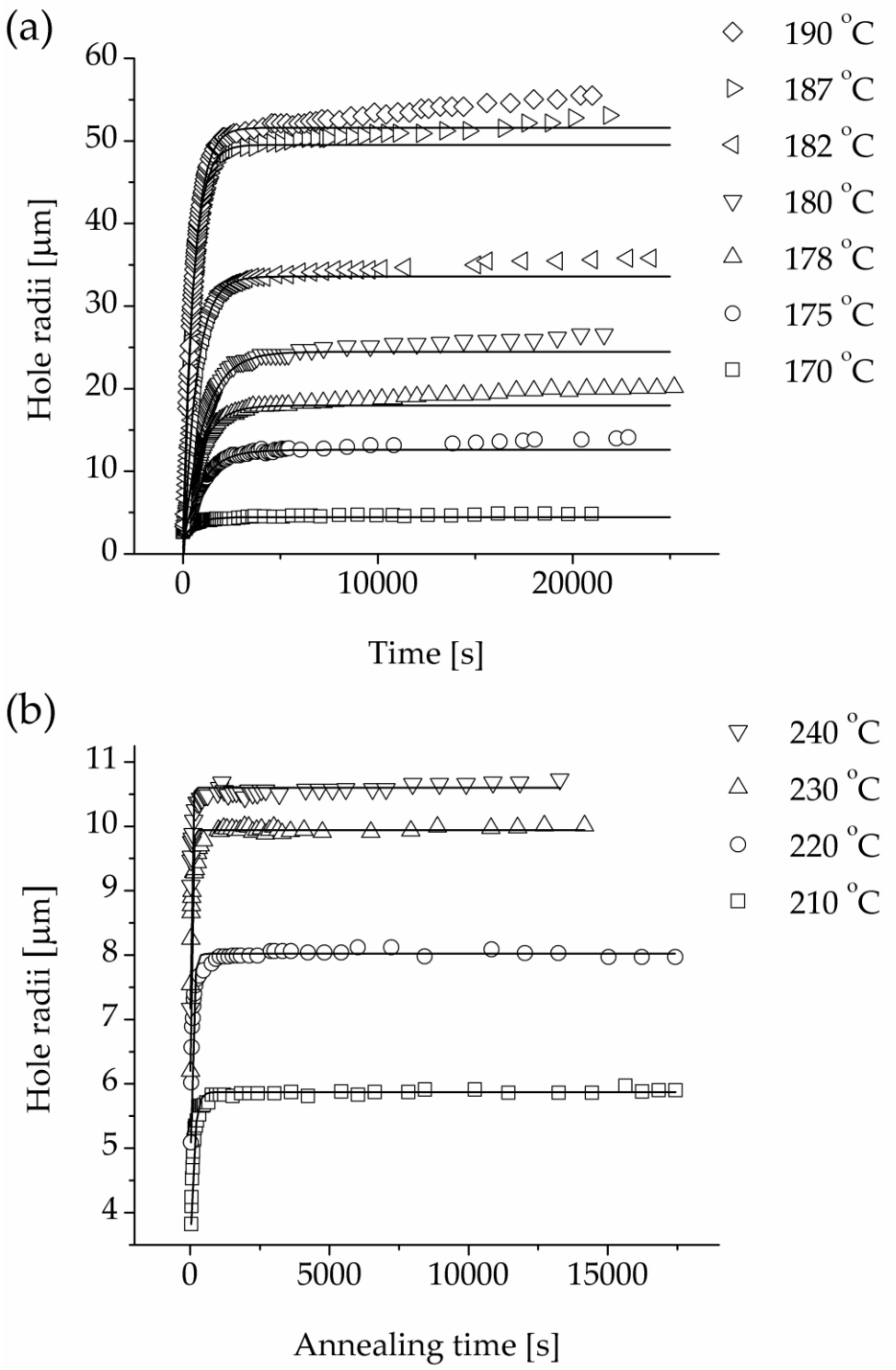

Figure 4.9 (a) Hole growth data (points) in a dewetting PNVP film on PS96K, fitted with the developed cross-linking model (lines), fitted for short annealing times (t < 5400 sec). The model was extrapolated for long annealing times. (b) Hole growth data (points) in a dewetting PNVP film on PS6850K system, fitted with the developed cross-linking model (lines).

The model however did not predict the very slow hole growth at long annealing times (above about 5400 seconds). It was observed that the hole radius slowly drifted towards higher values compared to the plateau that the model predicted, as shown in Figure 4.9(a). This deviation was likely due to the peculiar behaviour of the cross-linked PNVP film on liquid PS, and is discussed in Section 4.4.

To account for the competition between dewetting and cross-linking of PNVP, the model is dependent on the cross-linking rate coefficient k_{XL}, and as a result the modelling provided direct access to this rate coefficient via comparison to experiment. Values for k_{XL} were obtained for all the different temperatures studied in this work, enabling the temperature dependence of this rate coefficient to be mapped. The simplest model to describe a pseudo-first order chemical reaction like a radical cross-linking reaction is the Arrhenius model:

$$-ln\, k_{XL} = -ln\, A + \frac{E_a}{RT} \tag{4.12}$$

where k_{XL} is the cross-linking rate coefficient, A is a pre-exponential factor and E_a is the apparent activation energy.

An Arrhenius plot (Figure 4.10) was created to chart the variation of the cross-linking rate coefficient as a function of temperature. The linearity of the Arrhenius plot enabled the determination of the apparent activation energy, E_a, of the cross-linking process. The model predicted E_a to be 99 ± 6 kJ mol^{-1}, which is comparable with data for the radical thermal cross-linking of similar polymers. As an example, Madbouly *et al.* found an E_a of 60 - 74 kJ mol^{-1} for the cross-linking of poly(vinyl methyl ether).[31] Importantly, the rate coefficients determined for the cross-linking of PNVP obtained from the two

different systems investigated (PNVP/PS96K and PNVP/PS6850K) collapsed onto the same linear trend in Figure 4.10. This demonstrated that the cross-linking process, which is a chemically controlled reaction *via* hydrogen atom abstraction along the PNVP backbone to form radicals that can undergo cross-linking,[17, 32] was unrelated to the physical environment where the film was located, namely the nature of the PS substrate. The observed differences in the hole growth profiles of the two systems were solely related to the viscoelasticity of the PS substrate, which affected the hole growth and ultimately the competition between the two processes.

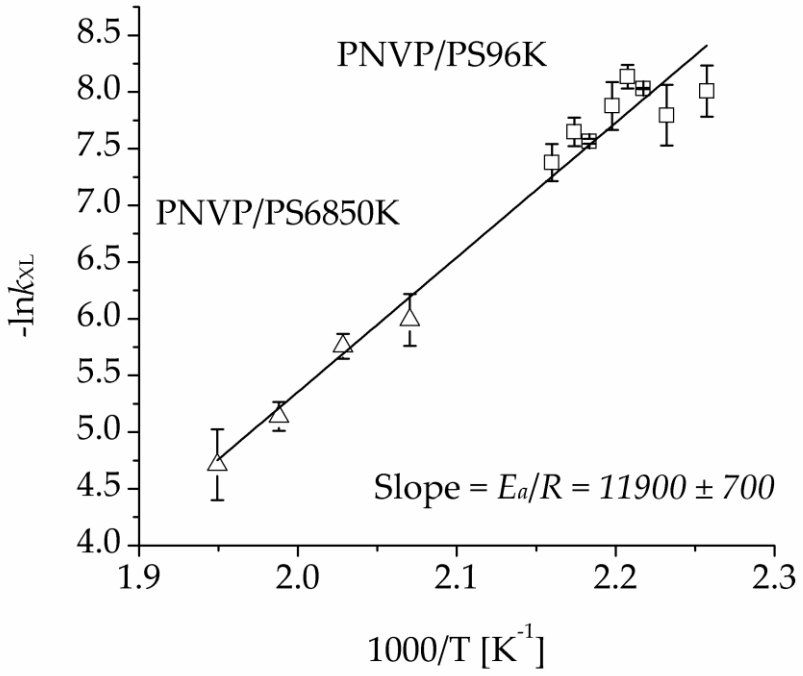

Figure 4.10 Arrhenius behaviour of the PNVP cross-linking rate coefficient. The cross-linking coefficients for both PNVP/PS96K and PNVP/PS6850K are displayed in different regions of the same graph as squares and triangles respectively, while a least squares linear fit is shown as a line.

4.4 Discussion

The competition between dewetting and cross-linking in PNVP/PS bilayer systems was investigated. It was anticipated that there would be two dominant regimes in these bilayer systems: one where dewetting was substantially influenced by cross-linking and one where it was not. The temperature at which the annealing was performed provided the key control parameter over the competition. In simple polymer bilayers, the higher the annealing temperature the faster the dewetting, and at any given temperature the rate of dewetting is inversely proportional to the viscosity of the top film and of the bottom film.[4, 18] In the experiments presented here, this general trend was counteracted by the fact that the rate of cross-linking in PNVP increased with increasing annealing temperature,[17] and the cross-linking slowed down the dewetting by both increasing the viscosity of PNVP, and by forming a network that locked-in stresses and prevented nucleation of the holes.

In these experiments, the cross-linking of PNVP affected especially the later part of the dynamics of the dewetting: an initial fast rate was followed by a very slow rate, and eventually a complete halt of hole growth occurred. For PNVP on PS96K, dewetting could only occur above approximately 165 - 170 °C, as below this temperature dewetting was completely prevented by cross-linking. Below 180 °C, dewetting occurred but with a significantly lower density of holes, due to the hampering of nucleation by cross-linking.

As the dewetting of the top film also depends on the viscosity of the bottom layer,[4, 18] it was anticipated that the two PNVP/PS systems would dewet to differing extents, with the PNVP/PS6850K case being slower and the closer to a true liquid/solid dewetting system. The observations reported confirmed the expectations.

The most interesting observations in this work derive from comparing the relative rates of the two competing processes, dewetting and cross-linking. The first significant observation was that the maximum achievable hole size depended on the system studied, being much smaller in the PNVP/PS6850K system than in the PNVP/PS96K system, across a wide temperature range. This was most likely due to two different viscous dissipation mechanisms. Using a simple scaling law relating the melt viscosity of a polymer to its MW,[22-24] the viscosity of the PS6850K film was estimated to be over 3×10^6 times greater than that of the PS96K film at a given temperature. This means that films of the low MW PS, PS96K, were more liquid and deformable at any given temperature than the high MW PS and as a result, during dewetting of the PNVP/PS96K bilayer, dissipation of energy could occur in both the dewetting film and in the PS substrate. This is equivalent to a lower friction at the PNVP/PS96K interface, so this phenomenon in turn results in a higher dewetting velocity, as reported previously.[4, 18, 33, 34]

While the dewetting of PNVP was much slower on PS6850K than on PS96K, the rate of the cross-linking process was independent of the MW of the PS film and was only dependent on the annealing temperature, being faster at higher temperatures. At the temperatures used for dewetting of the PNVP/PS6850K system, between 210 °C and 240 °C, cross-linking was much faster than dewetting, therefore dewetting was inhibited in its very early stages, leading to small holes. If temperatures below 200 °C were used for the PNVP/PS6850K system, no dewetting was observed at all as the friction at the PNVP/PS interface was too high, and the PNVP cross-linked as a uniform film.

On the other hand more advanced stages of dewetting could be obtained in the PNVP/PS96K system, which was annealed at temperatures between 170 °C and 190 °C, where cross-linking was relatively slower, and

dewetting was faster because of the low friction at the liquid/liquid interface.[35] If temperatures above 200 °C were used for the PNVP/PS96K system, dewetting proceeded to the highly advanced state of liquid cylinders before cross-linking was significant.

The second interesting observation was that the rate of growth of holes in PNVP films decreased sharply at long annealing times (approximately over 5400 s) (Figure 4.4). On PS6850K substrates, the size of dewetted holes in the PNVP film reached a plateau and then stopped entirely, a feature that was well captured by the simple molecular model reported in Section 4.3.4 (Figure 4.9(b)). On PS96K substrates, the hole growth slowed down drastically around 5400 s, but continued slowly over an extended period of time, with a small but constant increase in size from the plateau. The simple molecular model developed here fitted well the data for the PNVP/PS96K up to around 5400 s, but underestimated the subsequent very slow growth of holes (Figure 4.9(a)). It was believed that the difference was due again to the large difference in melt viscosity, as the PNVP/PS6850K system was likely to be similar to a liquid/solid system, and upon the complete cross-linking of the PNVP film, no movement of the hole rims could occur due to the rigidity of the underlying PS film. In the PNVP/PS96K bilayer, the PS96K was more similar to a liquid substrate: as the PNVP continued to cross-link, the film continued to shrink and became denser as the cross-linking process continued, which pulled on the hole rims, and the low viscosity of the liquid-like PS substrate allowed the holes to still grow very slowly. The rupture of a solid-like film induced by the motion of a liquid substrate was previously rationalized in simulations by Matar *et al.*[33] In their simulations the authors showed that if van der Waals forces were not explicitly included in the model of the solid top film, this would break up solely as a consequence of the forces governing the motion of the underlying liquid film. Similarly, the mobility in the liquid PS96K film may

have allowed the holes to slowly increase in size as the cross-linked PNVP film continued to shrink, even within a generally rigid network of PNVP.

A third and most interesting aspect of the competition between dewetting and cross-linking is highlighted by the hole density data for the PNVP/PS96K system (Figure 4.6). For annealing temperatures below 180 °C, when cross-linking was dominant with respect to dewetting, the probability of hole nucleation was low, since the stresses in the PNVP film that drove the nucleation process were locked in place by the cross-linking between polymer chains. Above the critical temperature of 180 °C, dewetting was the dominant process, and many more holes were nucleated before the cross-linking could lock the film stresses in place. It is very interesting to observe that the transition from a cross-linking-dominated regime to a dewetting-dominated regime was not gradual, but rather abrupt, with a three-fold increase in hole density within three degrees (177 °C to 180 °C). A careful analysis of the data though showed slight differences in the dewetting behaviour around the regime transition temperature of 180 °C. Both the data sets for 177 °C and 180 °C showed evidence of a thermally initiated nucleation, i.e. an increase in the number of nucleated holes over time at short annealing times, unlike the data sets for temperatures well above (> 190 °C) and well below (< 175 °C) the regime transition temperature, where all the holes nucleated roughly at the same time.[1] Thermal nucleation has been observed to occur in systems described by an interfacial potential intermediate between that of an unstable and that of a metastable film.[1] In the PNVP/PS system, the thermal nucleation process might have been observable only when dewetting and cross-linking balanced each other, at the transition between the cross-linking-dominated regime and the dewetting-dominated regime. At lower temperatures, the hole nucleation was heavily affected by the cross-linking, while at higher temperatures the holes nucleated without restriction.

The model developed here has limitations, which could affect the quality of the fit to the experimental data. This simple model ignores the effect of chain branching on viscosity, the potential difference between number and weight-average MW of the cross-linked polymer,[36] the effect of the initial polydispersity of PNVP on cross-linking, and the fact that cross-linking is initially more pronounced near the bottom surface of the film.[17] Despite these limitations, this model certainly captured the main features of the competition between dewetting and cross-linking, and allowed to make predictions on the dynamics of hole growth in PNVP films on both high and low MW PS. It also allowed to estimate a value for the activation energy for cross-linking, which was in good agreement with the literature on polymers similar to PNVP.

The cross-linking was further characterised quantitatively by NR and qualitatively by selective removal of the bottom film. NR on the bilayer systems confirmed earlier results in single layers (see Chapter 3),[17] indicating a decrease in film thickness and increase in density upon cross-linking of PNVP . The NR characterization also confirmed that no layer inversion took place in the PNVP/PS systems investigated, which might be expected in a bilayer where a high surface energy polymer is cast upon a low surface energy substrate. Layer inversion, however, would require the two layers to be able to flow freely in the melt state.[4] The increase in viscosity of the PNVP film with time, due to cross-linking, drastically reduced the mobility of the PNVP melt and hence prevented the layer inversion with the PS film.

The cross-linking process was highlighted qualitatively by selectively removing the PS film with toluene. The cross-linked PNVP remained insoluble in toluene, but allowed the toluene to penetrate through and dissolve the bottom PS film. This led to the lift-off and then resettling of the cross-linked film, a process which highlighted the presence of mechanical anisotropies in the film through extensive wrinkling patterns.

4.5 Summary

The dewetting of thin films of PNVP on top of PS films of two different molecular weights, 96000 g mol^{-1} and 6850000 g mol^{-1}, was investigated. Upon thermal annealing, the PNVP was capable of cross-linking as well as dewetting from the PS surface. Using a cross-linkable PNVP and bottom PS films of two different viscosities allowed us to gain a deeper understanding of the dewetting dynamics in polymer thin film bilayers with variable viscosity ratios. At the annealing temperature of 160 °C, the PNVP films cross-linked entirely before dewetting could occur. At higher annealing temperatures, but below the critical temperature of 180 °C, the rate of cross-linking was shown to be high enough to significantly hamper hole nucleation, reducing the final hole density. Above the critical temperature of 180 °C, the hole density was higher and approximately constant, and the competition between dewetting and cross-linking affected dynamics of hole growth, which was rapid in the early stages of the dewetting, but dramatically slowed down at long annealing times. At advanced stages of cross-linking, the PNVP stopped dewetting completely on the high viscosity PS, while it continued at a very low rate on the low viscosity PS. This was likely due the ability of the cross-linked PNVP film to slowly move on the liquid-like PS, while the high friction at the interface with the solid-like PS prevented any movement.

A model was developed to fit the hole growth in the dewetting PNVP film during cross-linking, based on the assumptions that the viscosity of PNVP increased exponentially as a result of the cross-linking process, and that the bilayer dewetted as a liquid/solid system. The model was excellent in fitting the data for PNVP dewetting on the high viscosity PS, and good in fitting the data for PNVP dewetting on low viscosity PS at short annealing times. At long annealing times, when the viscosity of the PNVP approached

that of the low MW PS films and the bilayer behaved more similarly to a liquid/liquid system, the model slightly underestimated the final hole size. The model allowed to derive the activation energy on the chemical process of cross-linking by mapping the physical process of hole growth.

As seen in Chapter 3, cross-linked PNVP films have excellent anti-fouling properties, and could be used as antifouling coatings in biomedical devices. The insight presented in this work will benefit the adaptation of such coatings to a number of materials used in medical devices which might be poorly wettable by PNVP. Moreover, the ability to produce patterns on protein-adsorptive PS holes in a cross-linked, protein-repellent PNVP film, with controllable hole size and density may be useful in the micropatterning of proteins and cells on a surface, as described in Section 1.6. Further work towards this end is presented in the following Chapters.

4.6 References

1. Seemann, R.; Herminghaus, S.; Neto, C.; Schlagowski, S.; Podzimek, D.; Konrad, R.; Mantz, H.; Jacobs, K., Dynamics and structure formation in thin polymer melt films. *Journal of Physics: Condensed Matter* **2005**, *17*, S267 - S290.
2. Seemann, R.; Herminghaus, S.; Jacobs, K., Dewetting patterns and molecular forces: A reconciliation. *Physical Review Letters* **2001**, *86* (24), 5534.
3. de Gennes, P.-G.; Brochard-Wyart, F.; Quere, D., *Capillarity and wetting phenomena*. Springer Science and Business Media Inc.: New York, **2004**.
4. Thickett, S. C.; Harris, A.; Neto, C., Interplay between dewetting and layer inversion in poly(4-vinylpyridine)/polystyrene bilayers. *Langmuir* **2010**, *26* (20), 15989-15999.
5. Brochard-Wyart, F. B.; Martin, P.; Redon, C., Liquid-liquid dewetting. *Langmuir* **1993**, *9* (12), 3682-3690.
6. Krausch, G., Dewetting at the interface between two immiscible polymers. *Journal of Physics-Condensed Matter* **1997**, *9* (37), 7741-7752.

7. Al Akhrass, S.; Ostaci, R. V.; Grohens, Y.; Drockenmuller, E.; Reiter, G., Influence of progressive cross-linking on dewetting of polystyrene thin films. *Langmuir* **2008**, *24* (5), 1884-1890.
8. Kang, H. M.; Lee, S. H.; Kim, S.; Char, K., Dewetting and layer inversion of inverted PVP/PS bilayer films. *Macromolecules* **2003**, *36* (23), 8579-8583.
9. Hao, T., Viscosities of liquids, colloidal suspensions and polymeric systems under zero or non-zero electric field. *Advances in Colloid and Interface Science* **2008**, *142*, 1-19.
10. Hussain, H.; Tan, B. H.; Gudipati, C. S.; Liu, Y.; He, C. B.; Davis, T. P., Synthesis and self-assembly of poly(styrene)-b-poly (N-vinylpyrrolidone) amphiphilic diblock copolymers made via a combined ATRP and MADIX approach. *Journal of Polymer Science, Part A: Polymer Chemistry* **2008**, *46* (16), 5604-5615.
11. Ahmad, H.; Yaseen, M., Application of a chemical group contribution technique for calculating solubility parameters of polymers. *Polymer Engineering and Science* **1979**, *19* (12), 858-863.
12. Fedors, R. F., Method for estimating both solubility parameters and molar volumes of liquids. *Polymer Engineering and Science* **1974**, *14* (2), 147-154.
13. Seemann, R.; Herminghaus, S.; Jacobs, K., Gaining control of pattern formation of dewetting liquid films. *Journal of Physics-Condensed Matter* **2001**, *13* (21), 4925-4938.
14. Caykara, T.; Yerlikaya, Z.; Kantoglu, O., Surface free-energy analysis of poly(N-vinyl-2-pyrrolidone-crotonic acid) copolymers prepared by gamma-ray-induced polymerization technique. *Journal of Applied Polymer Science* **2004**, *91* (3), 1893-1897.
15. Neto, C.; James, M.; Telford, A. M., On the Composition of the Top Layer of Microphase Separated Thin PS-PEO Films. *Macromolecules* **2009**, *42* (13), 4801-4808.
16. Gupta, R. R.; Lavery, K. A.; Francis, T. J.; Webster, J. R. P.; Smith, G. S.; Russell, T. P.; Watkins, J. J., Self-diffusion of polystyrene in a CO_2-swollen polystyrene matrix: A real time study using neutron reflectivity. *Macromolecules* **2002**, *36* (2), 346-352.
17. Telford, A. M.; James, M.; Meagher, L.; Neto, C., Thermally cross-linked PNVP films as antifouling coatings for biomedical applications. *ACS Applied Materials & Interfaces* **2010**, *2* (8), 2399-2408.
18. Lambooy, P.; Phelan, K. C.; Haugg, O.; Krausch, G., Dewetting at the liquid-liquid interface. *Physical Review Letters* **1996**, *76* (7), 1110-1113.
19. Jacobs, K.; Seemann, R.; Schatz, G.; Herminghaus, S., Growth of holes in liquid films with partial slippage. *Langmuir* **1998**, *14* (18), 4961-4963.

20. Wang, C.; Krausch, G.; Geoghegan, M., Dewetting at a polymer-polymer interface: Film thickness dependence. *Langmuir* **2001**, *17* (20), 6269-6274.
21. Bonaccurso, E.; Graf, K., Nanostructuring effect of plasma and solvent treatment on polystyrene. *Langmuir* **2004**, *20* (25), 11183-11190.
22. de Gennes, P. G., Reptation of a polymer chain in the presence of fixed obstacles. *The Journal of Chemical Physics* **1971**, *55* (2), 572-579.
23. Descloizeaux, J., Polymer melt - Reptation of a chain and viscosity. *Journal De Physique Lettres* **1984**, *45* (1), L17-L26.
24. Doi, M.; Edwards, S. F., Dynamics of concentrated polymer systems. 1. Brownian-motion in equilibrium state. *Journal of the Chemical Society-Faraday Transactions II* **1978**, *74*, 1789-1801.
25. Tobita, H.; Yamamoto, Y.; Ito, K., Molecular-weight distribution in random cross-linking of polymers - Modality of the molecular-weight distribution. *Macromolecular Theory and Simulations* **1994**, *3* (6), 1033-1049.
26. Brochard-Wyart, F.; Martin, P.; Redon, C., Liquid/liquid dewetting. *Langmuir* **1993**, *9* (12), 3682-3690.
27. Wang, C.; Krausch, G.; Geoghegan, M., Dewetting at a Polymer−Polymer Interface: Film Thickness Dependence. *Langmuir* **2001**, *17* (20), 6269-6274.
28. Brochard-Wyart, F.; Daillant, J., Drying of solids wetted by thin liquid films. *Canadian Journal of Physics* **1990**, *68*, 1084-1088.
29. Redon, C.; Brochard-Wyart, F.; Rondelez, F., Dinamics of dewetting. *Physical Review Letters* **1991**, *66* (6), 715-718.
30. Ghatak, A.; Khanna, R.; Sharma, A., Dynamics and morphology of holes in dewetting of thin films. *Journal of Colloid and Interface Science* **1999**, *212* (2), 483-494.
31. Madbouly, S. A.; Ougizawa, T., Thermal cross-linking of poly(vinyl methyl ether). III. Rheological kinetics of cross-linking reaction. *Journal of Macromolecular Science, Part B: Physics* **2005**, *43* (4), 819 - 832.
32. Barros, J. A. G.; Fechine, G. J. M.; Alcantara, M. R.; Catalani, L. H., Poly (N-vinyl-2-pyrrolidone) hydrogels produced by Fenton reaction. *Polymer* **2006**, *47* (26), 8414-8419.
33. Matar, O. K.; Gkanis, V.; Kumar, S., Nonlinear evolution of thin liquid films dewetting near soft elastomeric layers. *Journal of Colloid and Interface Science* **2005**, *286* (1), 319-332.
34. Xu, L.; Shi, T. F.; An, L. J., The competition between the liquid-liquid dewetting and the liquid-solid dewetting. *Journal of Chemical Physics* **2009**, *130* (18).
35. Kostourou, K.; Peschka, D.; Munch, A.; Wagner, B.; Herminghaus, S.; Seemann, R., Interface morphologies in liquid/liquid dewetting. *Chemical Engineering and Processing* **2011**, *50* (5-6), 531-536.

36. Macosko, C. W., Rheological changes during crosslinking. *British Polymer Journal* **1985**, *17* (2), 239-245.

CHAPTER 5

Patterned functional coatings for biomedical applications

5.1 Introduction

The development of cell biology has allowed deep insight into the behaviour of cells, how they interact with a surface and with neighbouring cells, and how they respond to environmental factors. Cell biology is at the foundation of the ability to engineer human tissues *in vitro* and to control the integration of artificial parts (e.g. prosthetics) with a biological host. Conventional cell studies are performed on flat substrates, typically Petri dishes or polystyrene flasks or plates comprising of a number of holes. The culture substrates are often coated with extra cellular matrix (ECM) proteins, to which cells easily adhere. This set up has proven to be efficient in the culturing of large numbers of cells, but suffers from a number of limitations, which are becoming obvious with the increasing knowledge of the important interactions, complexity and down-scaling of cell studies.

A flat culture substrate does not allow the performance of single cell studies, since the cells are not confined to a trackable area. Even if an isolated cell was seeded on such surface, it would be difficult to follow its development with an optical microscope, because of its mobility. Furthermore, the throughput of such system would be very poor.[1]

A second limitation of conventional cell culture substrates is that they do not allow studies on colonies of controlled size. The number of cells in a colony and the contact between them influences their behaviour, particularly in the case of embryonic stem cells (ESC). The smallest conventional culture substrate has an area of a few square millimetres (e.g. a 96-well plate), which is far too large to seed and observe aggregated colonies of tens of cells or less.[1]

A third limitation is the lack of control over cell localization on a surface. Cell proliferation may be influenced by the initial seeding cell density and separation, which cannot be controlled in a conventional cell

culture. Furthermore, accurate spatial control over cell immobilization is fundamental to the controlled growth of cell co-cultures. A flat surface coated with multiple types of cells does not allow for the ready manipulation of the degree of homotypic and heterotypic contact between cells. These conditions are fundamental in the study of the engineering of tissues *in vitro*.[2]

In the last decade, one of the most promising strategies to overcome these limitations and open a wide range of new possibilities has been the use of micropatterned surfaces.[1-3] These substrates are more or less ordered arrays of homogeneous domains surrounded by regions that are chemically different. They represent the ultimate miniaturization of conventional culture dishes in a device that allows for a much higher throughput. Patterned substrates can consist of two-dimensional or three-dimensional domains (wells or holes) on which the cells attach and spread. The bottom and (in the case of wells or holes) the walls of the domains can be coated with specific functionalities to influence the cells. Due to the micrometer scale of the pattern, single cells or small colonies can be immobilized in each domain. Furthermore, the area surrounding these domains may be modified to allow attachment of a second type of cell, to produce spatially controlled cell co-cultures.

Conventionally, microwells are produced by using microfabrication techniques such as photolithography, where a pattern is imprinted on a photoresist through a micro-engraved mask,[4] or soft lithography, where a micropatterned mould is used to stamp chemical functionalities on a surface.[5, 6] These techniques can achieve a wide range of geometries with a high lateral resolution and reproducibility. However, they suffer from high costs in equipment and in fabrication of highly detailed components (e.g. masks or moulds), and are able to pattern only flat surfaces.

In this work a novel method to obtain a micropattern on a surface for protein and cell immobilization is presented. This method is based on polymer thin film dewetting and polymer grafting, which are both cost effective techniques.

Dewetting was described extensively in Section 1.7. Briefly, dewetting is the process by which a liquid film, such as a polymer heated above its glass transition temperature (T_g), spontaneously breaks up, forming holes that grow with annealing time. The dewetting liquid retracts from the substrate exposing the underlying substrate, and accumulates in a raised rim around the holes. This effectively produces a chemically and topographically patterned surface. The size of the holes can be controlled by tuning the annealing time and temperature. The system here investigated consisted of a bilayer of polymer thin films: protein-adsorptive polystyrene (PS) on the bottom, and an engineered poly(methylmethacrylate) (PMMA)-like polymer, which bore ATRP initiators, as a second layer on top of the PS film. Once the pattern of holes was obtained by dewetting, the top "macroinitiator" layer was grafted with protein-repellent poly(poly(ethylene glycol) methyl ether methacrylate) (poly(PEGMA)) using surface-initiated activators generated by electron transfer atom transfer radical polymerization (AGET ATRP) (Section 1.5.5). The engineered surface obtained was an array of randomly distributed protein-adsorptive holes in a highly protein-repellent background. The pattern was characterized by optical microscopy, and investigated by X-ray photoelectron spectroscopic mapping to confirm the chemical contrast between the PS holes and the poly(PEGMA) brush.

In the work presented in Chapter 6, the pattern of polystyrene holes in the functional brush-coated background was used to control the localization of adsorbed ECM proteins. The pattern of protein-coated holes was then used to control cell attachment and spreading.

5.2 Materials and methods

5.2.1 Synthesis of the macroinitiator

A dry 4 mL glass tube was charged with 2-(2-bromopropanoyloxy)ethyl methacrylate (0.7 mL, 3.77 mmol) (kindly provided by Ms. Suzanne Pereira, CSIRO Clayton VIC), toluene (0.7 mL) (>99.9%, Sigma-Aldrich), doubly recrystallised azobis(isobutyronitrile) (AIBN; 0.6 mg, 3.6 μmol) (kindly provided by Sébastien Perrier's group, University of Sydney, NSW) and 2-cyanopropan-2-yl dithiobenzoate (CPDB; 8.0 mg, 36.3 μmol) (kindly provided by Dr. San Thang, CSIRO Clayton VIC). The tube was sealed with a rubber septum, and the mixture was deoxygenated by bubbling nitrogen for 5 minutes at 0 °C. The glass tube was then immersed in an oil bath at 65 °C and left to react with stirring for 22 hours. The reaction was stopped by cooling the vial to room temperature and exposing the contents to air. The viscous product was diluted in toluene and recrystallised from cold methanol. The polymer powder was dried under vacuum at room temperature. Size exclusion chromatography (SEC) calibrated with poly(methyl methacrylate) standards in THF was used to characterize the product. The conversion of the reaction was determined by NMR.

5.2.2 Preparation of thin film bilayers

The silicon wafers used as substrates and their cleaning procedure were described in Section 2.1.

PS (M_n 96000 g mol^{-1}, *PDI* 1.04; Polymer Standards Germany) was spin-cast in films on the clean silicon wafers from a 15 mg mL^{-1} filtered toluene solution (3000 rpm for 1 min). Macroinitiator films were then spin-

cast on top of the PS films from a 10 mg mL^{-1} acetonitrile (>99.9%, Merck) solution (4000 rpm for 1 min), acetonitrile being a non-solvent for PS. The average thickness of the films obtained was 58 ± 1 nm for PS and 28 ± 1 for the macroinitiator, as determined by spectroscopic ellipsometry (J. A. Woollam Co.).

The thickness of the PNVP/PS films was characterized by ellipsometry (see Section 2.4). The thickness of the SiO_2 layer (1 nm) on top of the silicon wafer was determined on the bare silicon wafer first, using the relevant model provided with the software. The system was treated as a monolayer. Then the PS film was spin-cast onto the silicon wafer. The system was modelled as a bilayer, where the SiO_2 thickness was fixed, and the polymer film was modelled using the Cauchy equation. The polymer thickness, and the constants A and B for the Cauchy equation, were measured. The constant C for the Cauchy equation was fixed to zero. The constant A, which is by far the largest contribution to the refractive index, was approx. 1.56. Then the macroinitiator film was spin-cast onto the PS film, and its thickness was determined using a PMMA model provided with the software. The system was modelled as a multilayer (3 layers), where the data for SiO_2 and PS were fixed. Finally, the poly(PEGMA) brush was grafted, and the polymer thickness, and the constants A and B for the Cauchy equation, were measured. The constant A was approx. 1.45. The system was modelled as a multilayer (4 layers), where the data for SiO_2, PS and macroinitiator were fixed.

Where required, the bilayers were dewetted by annealing on a hot plate with fine temperature control (ATV Technologie GmbH Muenchen) in air to obtain the desired pattern of holes. The annealing temperature used was 100 °C.

5.2.3 Surface-initiated polymerization of PEGMA from macroinitiator films

Flat bilayers (macroinitiator on PS), as well as patterned samples, were grafted with poly(ethylene glycol)methyl ether methacrylate (PEGMA; M_n about 475 g mol^{-1}) (Sigma-Aldrich), using AGET ATRP. PEGMA was passed over basic alumina prior to use to remove the inhibitors. In a typical run, PEGMA (1.425 g, 3 mmol), $CuCl_2 \cdot H_2O$ (3.4 mg, 0.02 mmol), tris-(pyridyl methyl) amine (TPMA; 5.8 mg, 0.02 mmol) (Sigma-Aldrich and in part kindly provided by Ms. Aeysha Hussein, University of Sydney, NSW), ethyl 2-bromopropanoate (3.6 mg, 0.02 mmol) and isopropyl alcohol/water 50% (12.7 mL) were thoroughly mixed in a 22 mL glass vial. Isopropyl alcohol (IPA; >99.5%), $CuCl_2 \cdot H_2O$ (>99%), and ethyl 2-bromopropanoate were purchased from Merck. A silicon wafer, pre-coated with a macroinitiator/PS bilayer, was immersed in the mixture, and the vial was sealed with a rubber septum. The solution was deoxygenated with nitrogen for 30 min in an ice bath, and then equilibrated at room temperature (ca 23 °C). A nitrogen purged ascorbic acid (Sigma-Aldrich) solution (60 mM, 50 μL, 3 μmol) was added to the reaction mixture with a micro-syringe, in order to start the polymerization by reducing part of the Cu(II) complex to the activator Cu(I) complex. The vessel was kept under gentle agitation for the time required. The reaction was stopped by exposing the catalyst to air, and samples of the reaction mixture were taken for SEC analysis. The substrate was rinsed in fresh IPA 50% for 30 min, and blown dry with nitrogen. The grafted film thickness was measured by ellipsometry.

In chain extension experiments, the grafted substrate was re-immersed in the same reaction mixture and after degassing, a fresh ascorbic acid solution was added to reinitiate the polymerization. The same procedure described above was then followed.

5.2.4 Characterization of synthesised polymers

In the synthesis of poly(PEGMA), SEC was used to determine the reaction conversion and the polymer MW and polydispersity. The SEC of poly(PEGMA) was performed on a Polymer Laboratories Ltd. GPC-50-Plus SEC system with a Polar-Gel 8μM guard column and two Polar-Gel columns (Polymer Laboratories Ltd.). The system was equipped with a PL-RI differential refractive index detector (DRI). The eluent was DMF + 0.1% LiBr at 50 ºC at a flow rate of 0.5 mL min^{-1}. The system was calibrated using poly(methylmethacrylate) standards in the range 690-790000 g mol^{-1}, using Mark-Houwink-Sakurada parameters or k = 14.1 and α = 0.697. All analysis was performed using the Cirrus® software.

To calculate the reaction conversion, the area of the peak corresponding to the unreacted monomer was divided by the sum of the areas of the monomer and polymer peaks. The method has been used previously in this system,[7] and its validity was checked by comparing selected data in preliminary experiments with data obtained by NMR analysis of the crude reaction mixture in deuterated DMSO. In the NMR method, the concentration of monomer *[m]* was calculated from the area of one of its vinyl proton peaks. The total concentration of polymer + monomer *[m+p]* was calculated from the area of the overlapping peaks relative to the ether protons in the ethylene glycol side chain of PEGMA. The conversion was then calculated as shown in Equation 5.1:

$$Conv = \frac{[m+p] - [m]}{[m+p]} \tag{5.1}$$

In the synthesis of the macroinitiator, NMR was used to determine the conversion and SEC to determine the polymer MW and polydispersity. The $^{1}_{1}H$ NMR analysis was performed on a Bruker® Avance 300 MHz

instrument, and analysed with the software MestRE-C® from Mestrelab research.

The SEC analysis of the macroinitiator was performed at 40 °C with a system equipped with a guard column and two PL-Gel Mixed-B columns (Polymer Laboratories Ltd.) with a Shimadzu RID-10A DRI detector. THF was used as the eluent with a flow rate of 1 mL min^{-1}, with toluene used as a flow rate marker. The system was calibrated with polystyrene standards ranging from 162 to 6035000 g mol^{-1} using Mark-Houwink-Sakurada parameters of $k = 14.1$ and $\alpha = 0.697$.

5.2.5 X-ray photoelectron spectroscopy (XPS)

XPS analysis and data fitting was performed by Dr. Thomas Gengenbach at the facilities in CSIRO Clayton VIC. XPS analysis was performed using an AXIS Ultra DLD spectrometer (Kratos Analytical Inc., Manchester, UK) with a monochromated Al K_α source at a power of 150 W (15 kV × 10 mA), a hemispherical analyser operating in the fixed analyser transmission mode and the standard aperture (analysis area: 0.3 mm × 0.7 mm). The total pressure in the main vacuum chamber during analysis was typically 10^{-8} mbar. Each specimen was analysed at an emission angle of 0° as measured from the surface normal. Assuming typical values for the electron attenuation length of relevant photoelectrons in organic compounds, the XPS analysis depth (from which 95 % of the detected signal originates) was between 5 and 10 nm.

Data processing was performed using CasaXPS processing software (Casa Software Ltd., Teignmouth, UK). All elements present were identified from survey spectra (acquired at a pass energy of 160 eV). To obtain more detailed information, such as chemical structure and oxidation states, high resolution spectra were recorded from individual peaks at 40 eV pass energy

(yielding a typical peak width for polymers of 1.0 – 1.1 eV). These data were quantified using a Simplex algorithm in order to calculate optimised curve fits and thus to determine the contributions from specific functional groups. The atomic concentrations of the detected elements were calculated using integral peak intensities and the sensitivity factors supplied by the manufacturer. Binding energies were referenced to the aliphatic hydrocarbon peak at 285.0 eV. The accuracy associated with quantitative XPS is about 10% - 15%. Reproducibility depends on the signal/noise ratio, but is usually < 5%. The latter is relevant when comparing similar samples.

XPS imaging was performed by Dr. Chris Easton at the facilities in CSIRO Clayton VIC. XPS images were acquired at a pass energy of 160 eV using the field of view (FOV) 2 lens (~400 μm x 400 μm) in high resolution mode. For each image recorded, a corresponding background image was collected at approximately 15 eV away from the peak under investigation and subsequently used for background correction within the Vision 2.0 acquisition software. Specifically, an image for O 1s was collected at 530 eV and the background image collected at 515 eV. The stitched image routine was employed to record an image over a larger area whilst maintaining the same high resolution scanning parameters as a single image.

5.3 Results

5.3.1 Synthesis of macroinitiator by RAFT

The macroinitiator was designed to have a structure similar to PMMA, for which the dewetting behaviour on PS is well understood.[8] The macroinitiator had a bromo-ester functionality capable of initiating ATRP (Figure 5.1).

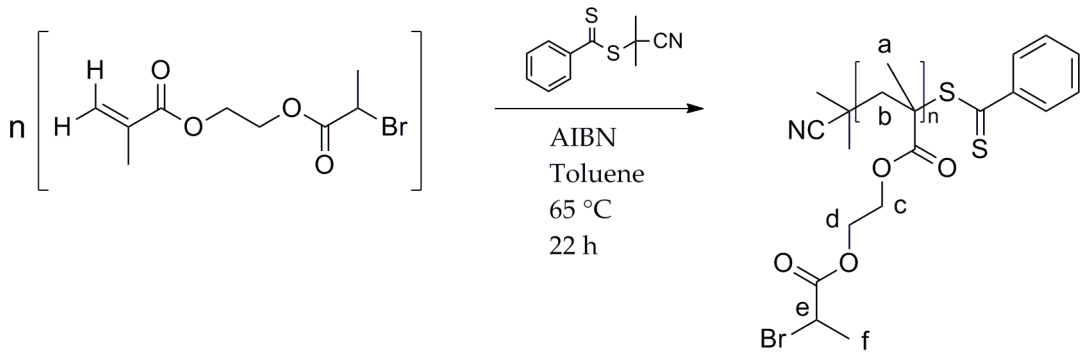

Figure 5.1 RAFT reaction scheme for the preparation of the macroinitiator. Each polymer chain contains the phenyl group from the RAFT agent, which was used in NMR analysis to evaluate the M_n.

The macroinitiator was synthesized by RAFT polymerization to obtain a well defined molecular weight (MW) as shown in Figure 5.1. The number average MW of the polymer (M_n) was 20700 g mol^{-1}, with a *PDI* of 1.28, as determined by SEC measurements. The polymer used was composed solely of 2-(2-bromopropanoyloxy)ethyl methacrylate, to maximize the grafting density of the poly(PEGMA) brush. In previous experiments, statistical copolymers of 2-(2-bromopropanoyloxy)ethyl methacrylate and methyl methacrylate were synthesized. The presence of methyl methacrylate (MMA) dilutes the initiator density in the copolymer film, likely decreasing the brush grafting density, and increases the glass transition temperature, T_g, of the copolymer. This synthetic strategy would most likely be useful for the tuning of the dewetting and polymerization initiation capabilities of the macroinitiator film, but it is beyond the scope of this work and the possibility was not investigated further.

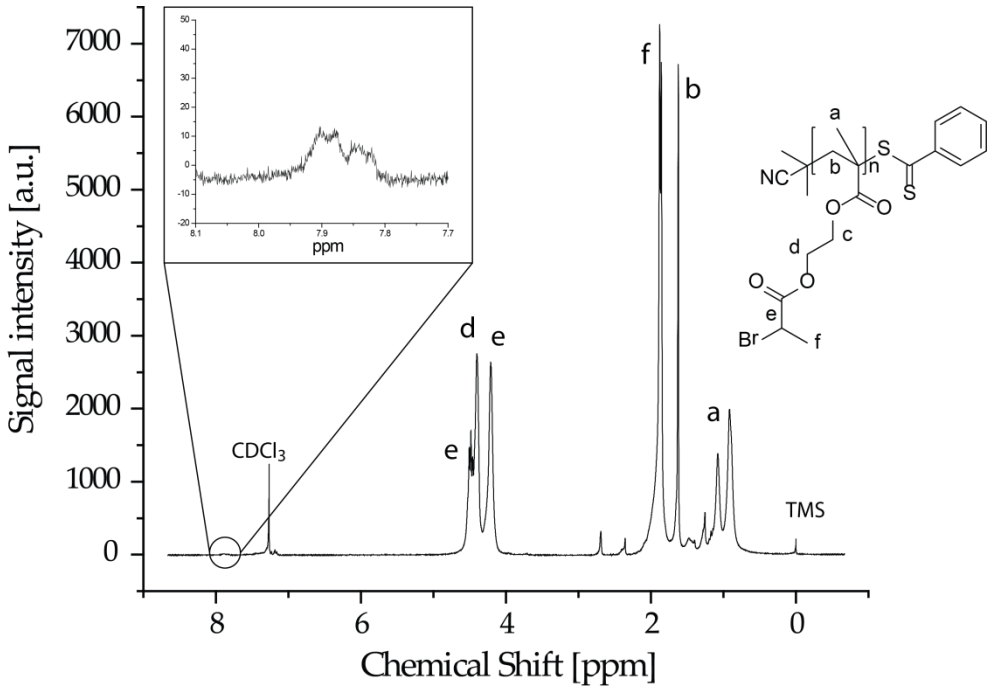

Figure 5.2 NMR spectrum of the macroinitiator, with peak assignment shown. An enlargement of the two downfield signals from the protons of the dithiobenzoate end-group is shown in the inset.

Presented in Figure 5.2 is a proton NMR spectrum of the purified macroinitiator. The analysis confirmed the identity of the polymer, as well as its average MW, determined by end-group functionality analysis. The distinct signals from the aromatic functionality in the RAFT agent were used to determine the degree of polymerization achieved in the reaction. The polymer was soluble in good solvents for PMMA, such as acetonitrile.

The macroinitiator was also characterized by differential scanning calorimetry (DSC) (Figure 5.3), to determine its T_g, which was needed for the subsequent dewetting experiments, as the polymer had to be a liquid in order to dewet. The DSC trace shows a glass transition at about 27 °C. Glass transitions appear as sudden changes in the trace slope. The slopes of the regions prior and after the transition are different (red lines). The T_g is the median point between these two regions. The DSC trace also shows a

melting at about 51 °C. In this setting, endothermic transitions are represented by negative heat flows. The finding suggests that the polymer is partly crystalline, and as such is not completely mobile for temperatures below the melting point, though it starts to soften above its T_g. The presence of both a melting point and a glass transition is discussed in Section 5.4, pg 215.

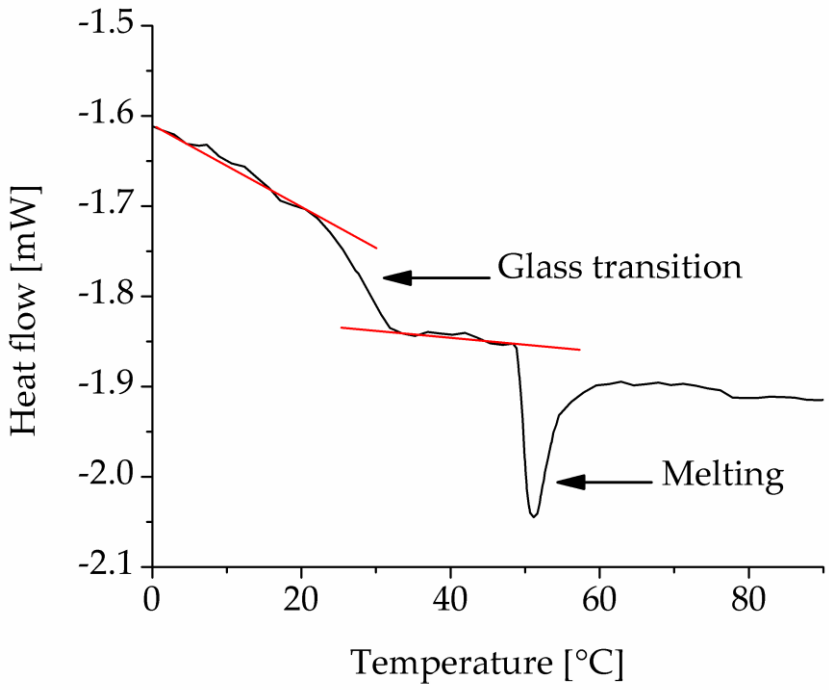

Figure 5.3 DSC trace of the macroinitiator collected between -50 °C and 100 °C, at the rate of 5 °C min^{-1}. The data collection was repeated for 3 cycles on the same sample, to check for sample degradation in the temperature range used. All the curves overlapped showing no degradation of the material with repeated cycles (data not shown). The DSC trace shows a glass transition at around 27 °C. The trace also shows a melting around 51 °C, which appears as a sharp endothermic peak (negative heat flow in this setting).

5.3.2 Optimization of the polymerization of poly(PEGMA) by activators regenerated by electron transfer atom transfer radical polymerization (ARGET ATRP)

The polymerization of PEGMA in water/alcohol mixture was first attempted by ARGET ATRP. This system was expected to be very robust because it is insensitive to the presence of small amounts of radical scavengers such as oxygen, which inhibit the radical polymerization, and uses stable copper species, so that the activator/deactivator ratio can be strictly controlled. A more detailed explanation of the advantages of ARGET ATRP over conventional ATRP was reported in Section 1.5.5. The qualities of ARGET ATRP match well one of the fundamental principles of this work, which was to design simple fabrication processes to meet the requirements of low cost and manufacturing ease for the biological and medical communities.

The optimization of the reaction followed different stages. In the first stage, poly(PEGMA) was polymerized from a macroinitiator film *via* ARGET ATRP, following basic principles of the technique: use low catalyst concentration and large excess of reducing agent. The macroinitiator initially used was not the one described in Section 5.3.1, but a statistical copolymer of MMA (85% mol) and 2-(2-chloropropanoyloxy)ethyl methacrylate (Cl-MMA, 15% mol), with M_n = 23800 g mol^{-1}. The MW distribution was narrow but bimodal, yet this was not considered to be an issue for the grafting optimization. The bimodal MW distribution would only affect the dewetting, which was not studied in this first part of the investigation. This copolymer was chosen as it is structurally similar to PMMA, the dewetting of which has been well studied on PS.[8] The investigation reported in Sections 5.3.2 and 5.3.3 indicated that a bromo-initiator, rather than a choro- one, was to be preferred in order to improve the control over the polymerization of

PEGMA. Also, a homopolymer was advantageous in order to maximize the initiator sites density on the surface, whilst being able to dewet from PS. By the end of the optimization of the grafting reaction, the macroinitiator described in Section 5.3.1 was selected. In the optimized grafting of poly(PEGMA), the term "macroinitiator" always refers to the bromine methacrylate homopolymer described in Section 5.3.1. In this first stage, degassing of the reaction mixture was performed in order to work in standardized conditions, i.e. same oxygen concentration, and no sacrificial initiator was used. The reducing agent employed was ascorbic acid, which is inexpensive and non-toxic. The change in pH caused by the addition of ascorbic acid to the solution can affect amine-containing ligands. Ligands which have high base dissociation constants, such as the commonly used PMDETA and Me_6TREN, are quite sensitive to protonation, which leads to catalyst complex instability.

Table 5.1 Stage one of the optimization. Reaction conditions for the grafting of poly(PEGMA) from a Cl-MMA/MMA copolymer macroinitiator film by ARGET ATRP. No sacrificial initiator was used at this stage. Note that the molar ratios are relative to the catalyst concentration, as it was not possible to easily estimate the true amount of initiator groups on the surface.

Reagent	Name	MW [g mol^{-1}]	mmol	conc [%w]	Molar ratio
Monomer	PEGMA475	475	4.155	30	6000
Catalyst	$CuCl_2 \cdot H_2O$	170.48	0.000693		1
Ligand	TPMA	290.36	0.002078		3
Reducing agent	Ascorbic Acid	176.12	0.020775		30
Solvent	MeOH 70%				
Temperature	30 °C				
Reaction time	60 min				

Here, TPMA was chosen because it is a weak base and is hence less susceptible to protonation. This ligand combines high activity and stability, which make it the optimal choice for this system.[9] The reaction conditions,

summarised in Table 5.1, were chosen based on conditions reported in the literature by other groups with various ATRP systems.[7, 10, 11]

The reaction progressed at a very fast rate, and after just 30 minutes the poly(PEGMA) chains had grown to a sufficiently high MW to delaminate the macroinitiator film from the underlying PS, because of the high solubility of the poly(PEGMA) in the reaction media.

To better control the brush growth, the monomer concentration was reduced from 30% w/v to 20% w/v and finally to 10% w/v, keeping the other conditions unchanged. For the higher monomer concentrations, the reaction was too fast to control the poly(PEGMA) brush growth. Only at the lower concentration was no delamination of the macroinitiator film observed. The poly(PEGMA) brush film thickness could be measured by ellipsometry, and showed a steady increase with time (Figure 5.4).

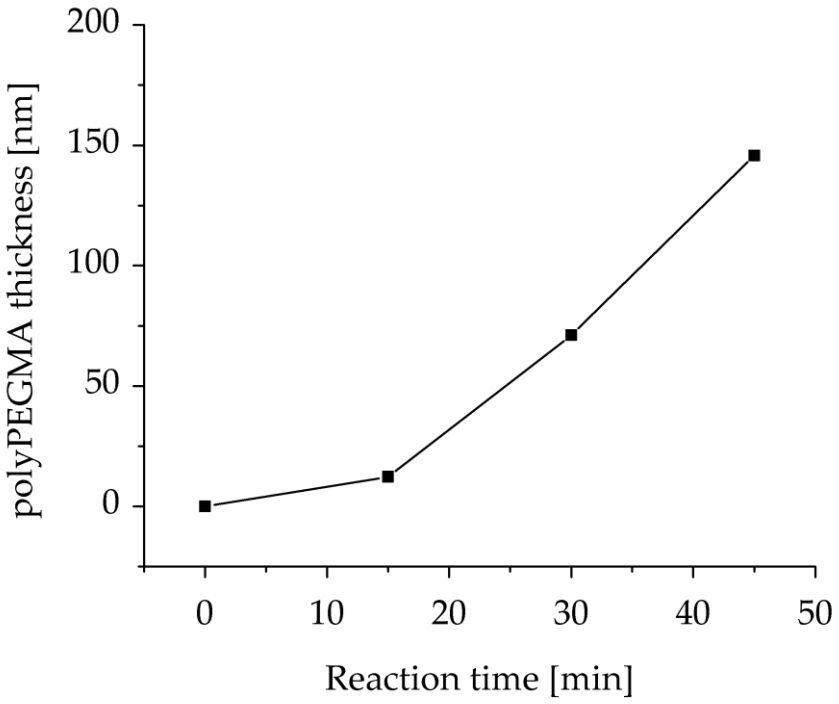

Figure 5.4 Ellipsometric data of poly(PEGMA) layer thickness as a function of the reaction time obtained by surface-initiated ARGET ATRP from a Cl-MMA/MMA copolymer macroinitiator film. The reaction conditions are summarised in Table 5.1. The errors on the measurements were in the range 0.14%-2.2%.

The shape of the curve seems to suggest that there was a small induction time at the beginning of the reaction, and that the brush thickness increased linearly thereafter. In addition, the curve does not plateau in the timeframe studied, as expected from a reaction reaching completion, indicating that unconsumed monomer was still present after 45 min. This result was consistent with the theoretical behaviour of this system, as the ATRP reaction rate is governed by the monomer concentration.[12]

Table 5.2 Stage two of the optimization. Reaction conditions for grafting of poly(PEGMA) from a Cl-MMA/MMA copolymer macroinitiator film by ARGET ATRP. A sacrificial initiator was used to better control the polymerization. The molar ratios are relative to the sacrificial initiator concentration. The x for the initiator quantities indicates that the concentration of this species on the surface was unknown.

Reagent	Name	MW [g mol^{-1}]	mmol	conc [%w]	Molar ratio
Monomer	PEGMA475	475	3	10	150
Initiator	Cl-MMA copolymer film	x	x	x	x
Sacrificial initiator	ethyl 2-chloropropanoate	136.58	0.02		1
Catalyst	$CuCl_2 \cdot H_2O$	170.48	0.001		0.05
Ligand	TPMA	290.36	0.003		0.15
Reducing agent	Ascorbic Acid	176.12	0.03		1.5
Solvent	MeOH 70%				
Temperature	30 °C				
Reaction time	45 min				

In the second stage of the optimization process, once the poly(PEGMA) brush thickness could be controlled (i.e. the polymerization rate was slow enough obtain a defined brush thickness without delamination), the focus moved to the control of the polymer MW and polydispersity. Ethyl 2-chloropropanoate was introduced as a sacrificial initiator; this molecule is analogous to the ATRP initiator side chain in the macroinitiator. The hypothesis was that identical polymers would be grown from the surface and in solution. This hypothesis was discussed in Section

1.5.6. This means that the analysis of the free chains in solution could give indirect information on the MW and polydispersity of the grafted chains. Furthermore, the presence of the sacrificial initiator improved the control of the chain growth on the surface, because of a higher concentration of deactivator formed in solution. The use of sacrificial initiators in surface grafting reactions was discussed in detail in Section 1.5.6. The reaction conditions used are summarised in Table 5.2.

These conditions however, produced a highly polydisperse brush, as revealed by analysis of the SEC data obtained from the free chains grown in solution, which showed broad, multimodal peaks after only 15 minutes of polymerization (Figure 5.5).

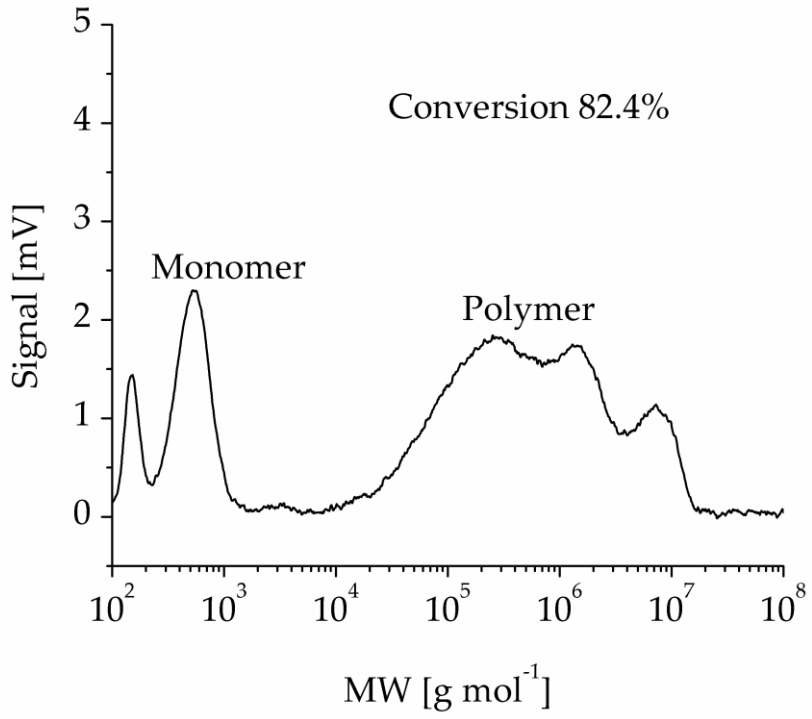

Figure 5.5 SEC trace of the products of ARGET ATRP of PEGMA in solution, initiated by ethyl 2-chloropropanoate. The trace shows the narrow peak of the unreacted monomer and a very broad peak for the polymer, with multiple contributions from populations of different MWs. The conversion was very high after only 15 minutes of reaction, and the reaction was clearly uncontrolled.

In the third stage of the optimization process, the polymerization dynamics were then investigated in solution, in order to gain control on the chain growth. The main issue when using a copper catalyst in aqueous solvent is the occurrence of side reactions such as ligand substitution of the halogen or the chelating ligand with water.[13] In low catalyst concentration systems, these side reactions reduce the already limited concentration of the deactivator species, which is the more labile of the catalyst forms. Assuming that this was the main issue causing lack of control in the polymerization in the system under study, the first strategy to improve the control over the reaction was to increase the TPMA ligand concentration. Summarised in Table 5.3 are the reaction conditions for these tests. The higher TPMA concentration improved the MW polydispersity of the product. The SEC data showed monomodal peaks after 7, 15, 30, 45 and 75 minutes, with *PDI*s steadily growing from 1.45 to 2.90. This was still considered to be relatively poor control over the polymer growth, as good control is indicated by *PDI*s < 1.2. Yet, the increase of ligand concentration seemed to have a positive effect on the control over the polymerization reaction.

Table 5.3 Stage three of the optimization. Reaction conditions for polymerization of PEGMA in solution by ARGET ATRP. The TPMA ligand concentration was increased to 10 times the catalyst concentration. Note that the molar ratios are relative to the sacrificial initiator concentration.

Reagent	Name	MW [g mol^{-1}]	mmol	conc [%w]	Molar ratio
Monomer	PEGMA475	475	3	10	150
Sacrificial initiator	ethyl 2-chloropropanoate	136.58	0.02		1
Catalyst	$CuCl_2 \cdot H_2O$	170.48	0.001		0.05
Ligand	TPMA	290.36	0.01		0.5
Reducing agent	Ascorbic Acid	176.12	0.03		1.5
Solvent	MeOH 70%				
Temperature	30 °C				
Reaction time	75 min				

In the fourth stage of the optimization process, increasing the concentration of the reducing agent was employed as second strategy to control the polymerization and obtain narrowly distributed polymer MW. As explained in Section 1.5.4, termination can occur in ATRP when two growing radicals meet, and this produces an excess of deactivator species, which can eventually alter the ATRP equilibrium and stop the reaction by reducing the concentration of active radicals. The increased concentration of deactivator also increases the likelihood of side reactions with the solvent occurring. The increase of ascorbic acid in this experiment was aimed at readily reducing the oxidized copper in order to withdraw it from undesired equilibria and maintain the activator/deactivator ratio. Such a large excess of ascorbic acid was used in these experiments that deoxygenation of the reaction mixture was considered unnecessary. The limited amount of oxygen in the sealed vessel would be scavenged by the reducing agent, which would still be present in high concentration compared to that of the catalyst.

Table 5.4 Stage four of the optimization. Reaction conditions for polymerization of PEGMA in solution by ARGET ATRP. The ascorbic acid concentration was increased to 300 times the catalyst concentration, to reduce side reactions at the metal centre, which reduce its ability to control the reaction. The molar ratios are relative to the sacrificial initiator concentration.

Reagent	Name	MW [g mol^{-1}]	mmol	conc [%w]	Molar ratio
Monomer	PEGMA475	475	3	10	150
Sacrificial initiator	ethyl 2-chloropropanoate	136.58	0.02		1
Catalyst	$CuCl_2 \cdot H_2O$	170.48	0.001		0.05
Ligand	TPMA	290.36	0.003		0.15
Reducing agent	Ascorbic Acid	176.12	0.3		15
Solvent	MeOH 70%				
Temperature	30 °C				
Reaction time	90 min				

The result of increasing the ascorbic acid concentration, while leaving all other quantities unchanged (compare Table 5.4 with Table 5.3), was to slightly improve the polydispersity of the final product, giving a monomodal peak with *PDI* of 2.1 (from the SEC data) after 90 minutes.

An attempt was eventually made to reduce side reactions of the copper catalyst with water by using pure alcohol as the solvent. Ethanol was used instead of methanol to reduce the amount of toxic chemicals used. The reaction led to no conversion after 6 hours and only a few percent after 23 hours. The product after this time had a very broad MW distribution.

The fifth and last stage of the optimization process dedicated to improving the control over the product MW, was to increase the catalyst concentration. Although this partly defeats the purpose of using ARGET ATRP, which allows the use of extremely small quantities of catalyst, it is a straightforward solution. When the catalyst concentration is high enough, the side reactions that occur have little effect on the activator/deactivator ratio, which controls the broadening of the MW polydispersity. The conditions employed are summarised in Table 5.5. In these experiments a moderate excess of ligand was used to ensure catalyst stability, and the reaction mixture was degassed for consistency in oxygen concentration through the different experiments.

Presented in Figure 5.6 is the polydispersity of poly(PEGMA) synthesized using different concentrations of copper catalyst. The *PDI* of the final product after 45 minutes reaction, extracted from the SEC data, dramatically decreased with increasing catalyst concentration, confirming the hypothesis described above. The conversion after 45 minutes for the lower polydispersity was 29.3%.

Table 5.5 Stage five of the optimization. Reaction conditions for polymerization of PEGMA in solution by ARGET ATRP. The catalyst concentration was increased to 0.15, 0.2, 0.5 and 1 compared to the sacrificial initiator, to render negligible the side reactions that affect the activator/deactivator ratio. The TPMA to copper ratio was kept at 10:1 for all the experiments.

Reagent	Name	MW [g mol^{-1}]	mmol	conc [%w]	Molar ratio
Monomer	PEGMA475	475	3	10	150
Sacrificial initiator	ethyl 2-chloro propanoate	136.58	0.02		1
Catalyst	$CuCl_2 \cdot H_2O$	170.48	0.003, 0.004, 0.01, 0.02		0.15, 0.2, 0.5, 1
Ligand	TPMA	290.36	0.03, 0.04, 0.1, 0.2		1.5, 2, 5, 10
Reducing agent	Ascorbic Acid	176.12	0.09, 0.12, 0.3, 0.6		4.5, 6, 15, 30
Solvent	MeOH 70%				
Temp.	30 °C				
Reaction time	45 min				

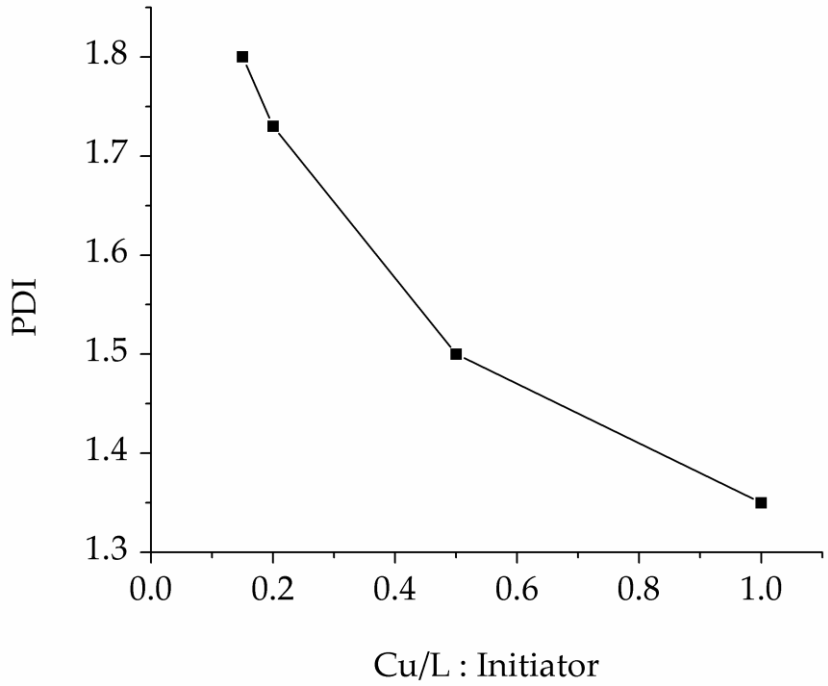

Figure 5.6 MW polydispersity of poly(PEGMA) synthesised by ARGET ATRP, using different concentrations of catalyst. The PDI decreased with increasing catalyst concentration, indicating improved control. A reasonable estimation for the error on the PDI values is 0.03%.

The optimization conditions obtained from the tests described above are summarised below, and were combined to perfect the ARGET ATRP of PEGMA:

High ligand concentration

High reducing agent concentration

High catalyst concentration

No deoxygenation was used, so as to fully employ the ease of use of ARGET ATRP. The final optimized set of reaction conditions are summarised in Table 5.6.

Table 5.6 Final optimized reaction conditions for polymerization of PEGMA in solution by ARGET ATRP. The catalyst, ligand and reducing agent concentrations investigated independently in the various stages were combined to obtain a set of optimal conditions to produce a polymer with low MW polydispersity.

Reagent	Name	MW [g mol^{-1}]	mmol	conc [%w]	Molar ratio
Monomer	PEGMA475	475	2	10	100
Sacrificial initiator	ethyl 2-chloropropanoate	136.58	0.02		1
Catalyst	$CuCl_2 \cdot H_2O$	170.48	0.02		1
Ligand	TPMA	290.36	0.2		10
Reducing agent	Ascorbic Acid	176.12	2		100
Solvent	MeOH 70%				
Temperature	30 °C				
Reaction time	45 min				

The targeted degree of polymerization was decreased to obtain shorter chains, which would be expected to have a weaker delamination effect on the macroinitiator film when used in grafting experiments. The reaction gave poly(PEGMA) with comparably lower polydispersity (*PDI* = 1.34 from SEC in Figure 5.7). The maximum conversion obtainable though was poor, being 39.1% after 90 minutes, suggesting that the catalyst must

still participate in side reactions resulting in poisoning. A possible explanation for the low conversion could be that a very high concentration of ascorbic acid can begin to affect even the weakly basic TPMA ligand, destabilizing the catalyst complex.

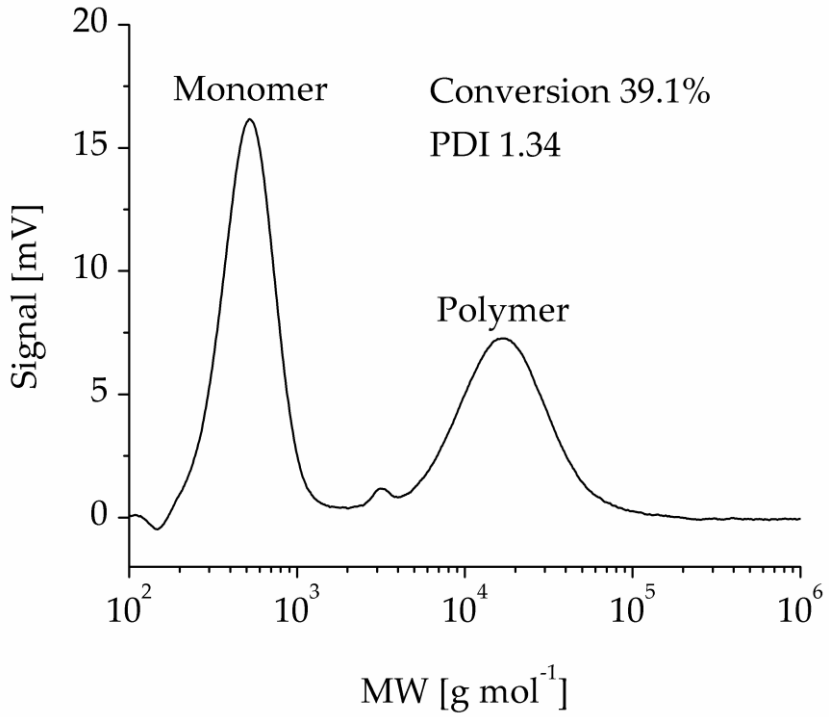

Figure 5.7 SEC trace of the products of ARGET ATRP of PEGMA in solution, initiated by ethyl 2-chloropropanoate. The trace shows the narrow peak of the unreacted monomer and a narrow peak for the polymer. The calculated PDI was 1.34, which indicated that the reaction had a moderate degree of control. The conversion reached a maximum of 39.1% after 45 minutes, after which the reaction stopped.

5.3.3 Optimization of the polymerization of poly(PEGMA) by activators generated by electron transfer atom transfer radical polymerization (AGET ATRP)

The controlled polymerization of PEGMA in water/alcohol using ARGET ATRP was overall only partly successful. The system under study

was very susceptible to side reactions involving the copper catalyst. Possible side reactions included the ligand exchange of the halogen or the TPMA with water or PEGMA on the more susceptible deactivator form of the catalyst; this effectively resulted in the reduction of the concentration of deactivator in the system, and hence of the control over the ATRP process. This is consistent with the observation that when an excess of TPMA ligand, an excess of ascorbic acid, or a high catalyst concentration were used, the polydispersity of the synthesized polymer was reduced, implying more control over the polymerization.

The investigation moved then to a similar system: AGET ATRP, described in Section 1.5.5. This system is still quite robust because, like ARGET ATRP, it is insensitive to the presence of small amounts of oxygen. Initially, the system was not degassed, and a sufficient amount of reducing agent was added to consume all the oxygen present in the sealed vessel and partly reduce the copper(II) to initiate the polymerization.

The reaction control was firstly improved by using a bromo-ester rather than a chloro-ester as both free initiator and macroinitiator (film for surface-initiated polymerization). Upon the ATRP uncapping and recapping process (Section 1.5.4), the halogen exchange between the initiator and the catalyst allows for a higher degree of control over the poly(PEGMA) MW. The more labile carbon-bromine bond cleaves easily in the initiation step, giving high initiation efficiency. The bromine is then replaced by chlorine in the recapping step, which forms a stronger halogen-carbon bond, reducing the reaction rate and allowing all the chains to grow together.[14]

Showed in Figure 5.8 is the comparison of PEGMA polymerizations carried out in two experiments under the same reaction conditions (Table 5.7), except that in one case the initiator was ethyl 2-bromopropanoate and in the other it was ethyl 2-chloropropanoate. The bromo-initiator (curve (a)) gave better control over the polymer MW at low conversions (Figure 5.8(A)),

and showed a bimodal distribution at higher conversions (Figure 5.8(B)), suggesting that termination by disproportionation was occurring. In such process, two propagating tertiary carbon radicals disproportionate by exchanging a proton, to form a vinyl-capped chain and a saturated methyl-capped chain. The chloro-initiator instead (curve (b)), gave a broader MW distribution, which hindered the expected bimodal MW distribution at high conversions. In both cases, the MW increased with conversion, which was an additional indication that the reaction was controlled. The SEC data is summarised in Table 5.8.

Table 5.7 Reaction conditions for polymerization of PEGMA in solution by AGET ATRP. The reaction was initiated in one case by ethyl 2-chloropropanoate, and in the other by ethyl 2-bromopropanoate.

Reagent	Name	MW [g mol^{-1}]	mmol	conc [%w]	Molar ratio
Monomer	PEGMA475	475	2	10	150
Sacrificial initiator	ethyl 2-chloropropanoate OR ethyl 2-bromopropanoate	136.58	0.02		1
Catalyst	$CuCl_2 \cdot H_2O$	170.48	0.02		1
Ligand	TPMA	290.36	0.02		1
Reducing agent	Ascorbic Acid	176.12	0.08		4
Solvent	MeOH 70%				
Temperature	30 °C				
Reaction time	120 min				

Table 5.8 SEC data for AGET ATRP of PEGMA in solution. The bromo-initiator gave better control over the MW, as showed by the lower values of PDI compared to the chloro-initiator.

Halogen in initiator	Reaction time [min]	Conversion [%]	M_n [g mol^{-1}]	*PDI*
Cl	30	24.0	26700	1.25
	120	48.5	37600	1.59
Br	30	35.1	21800	1.12
	120	51.8	32900	1.43

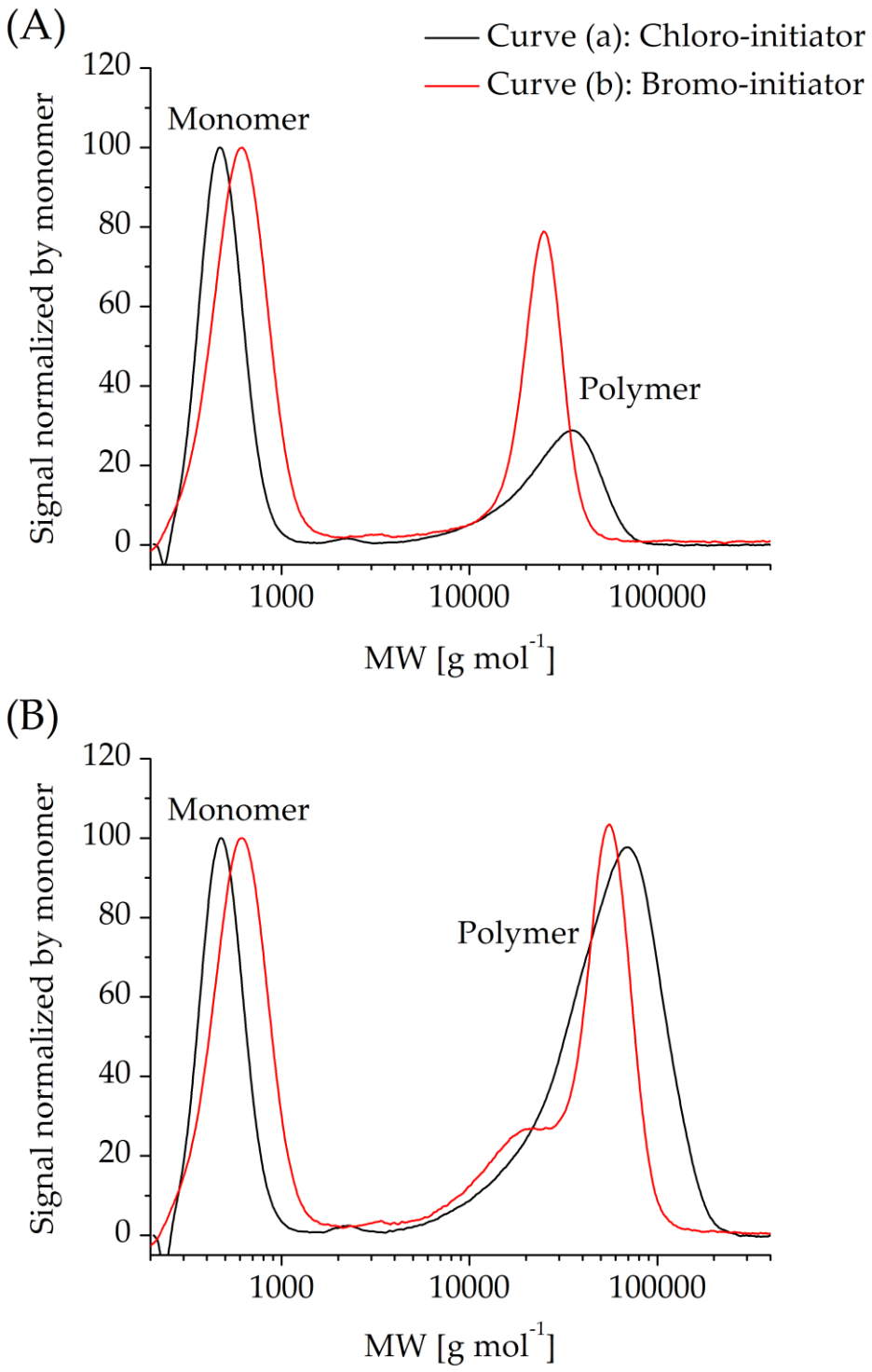

Figure 5.8 Comparison of SEC traces for AGET ATRP of PEGMA carried out under the same reaction conditions, but with different types of initiator, which was ethyl 2-bromopropanoate in curve (a) and ethyl 2-chloropropanoate in curve (b), after (A) 30 min and (B) 120 min. Conversions and PDIs are reported in Table 5.8.The monomer peaks in the curves present a slight misalignment due to the fact that their MWs were at the very limit of the SEC calibration range in these experiments. Such difference is negligible at higher MWs.

The ratio of sacrificial initiator to monomer to catalyst to ligand was retained from the previous studies on ARGET ATRP. Instead the amount of reducing agent was varied to experimentally establish the ideal concentration to obtain good control over the polymerization. Because of variability in the polymer MW versus reaction time obtained in different experiments, the deoxygenation step was reintroduced. The hypothesis was that the oxygen concentration in different samples was variable, because it depended on temperature, pressure and vigorous solvent mixing; this resulted in different induction times during which the oxygen was consumed, and changed the reaction time required to obtain a targeted conversion.

In the absence of radical scavengers such as oxygen, theoretically the amount of reducing agent to be added could be calculated based on the targeted activator/deactivator ratio, though practically the reaction mixture is difficult to completely deoxygenate. Moreover, the ascorbic acid used as reducing agent, though it has the advantages of being inexpensive and non-toxic, is fairly unstable towards UV photodegradation once in solution. This process can slightly reduce the effective concentration of reducing species. Degassing the mixture did improve the reproducibility of the synthetic method, but the amount of ascorbic acid to be added had to be determined empirically, through a systematic study. Because of the high concentration of catalyst, there was no need here to use an excess of ligand.

The solvent used was changed from 30/70 methanol/water to 50/50 isopropanol/water, to improve the macroinitiator film stability and reduce its swelling during the surface-initiated reaction. More detail on this topic is reported in the following Section, where various conditions were employed in the surface-initiated AGET ATRP of PEGMA from a macroinitiator film.

Table 5.9 Reaction conditions for grafting of poly(PEGMA) from a bromo-macroinitiator film (described in Section 5.3.1) by AGET ATRP. The concentration of reducing agent was varied to determine the optimal value for good MW control.

Reagent	Name	MW [g mol^{-1}]	mmol	conc [%w]	Molar ratio
Monomer	PEGMA475	475	2	10	150
Sacrificial initiator	ethyl 2-bromo propanoate	136.58	0.02		1
Catalyst	$CuCl_2 \cdot H_2O$	170.48	0.02		1
Ligand	TPMA	290.36	0.02		1
Reducing agent	Ascorbic Acid	176.12	0.003, 0.006, 0.009, 0.04		*0.15*, 0.3, 0.45, 2
Solvent	IpOH 50%				
Temperature	RT (about 23°C)				
Reaction time	30 min				

Table 5.10 SEC data for the free chains grown in solution during the grafting of poly(PEGMA) from a bromo-macroinitiator film (described in Section 5.3.1) by AGET ATRP. For the reducing agent to catalyst ratio of 2, the reaction was very poorly controlled. The highlighted ratio (underlined) was chosen because it was the minimum value for which polymerization occurred whilst making sure that the deactivator concentration remained high.

Reducing agent : catalyst	**Conversion**	***M*$_n$ [g mol^{-1}]**	***PDI***
0.15	*37%*	*20469*	*1.16*
0.3	41%	22287	1.14
0.45	35%	19927	1.15
2	--	--	1.7

Summarised in Table 5.9 are the reaction conditions tested, and in Table 5.10 the conversions, polymer MWs and *PDIs* obtained. From this systematic series of experiments, the optimal reaction conditions were selected (highlighted in Table 5.9). Among the ascorbic acid concentration conditions, the lowest was selected to account for some variability in the reaction mixture oxygen content, so to be sure to avoid the formation of high

concentrations of activator. In Section 5.3.4 the surface-initiated AGET ATRP of PEGMA from flat macroinitiator films is described.

Table 5.11 General summary of the different approaches employed to attain control over the polymerization of PEGMA by ARGET and AGET ATRP.

	Reagents molar ratio [PEGMA]:[Initiator]: [CuCl2]:[TPMA]:[AscA]	[PEGMA] [%w/v]	Solvent	Observations
ARGET Stage 1	6000:x:1:3:30	30	MeOH 70%	Film detachment
	4000:x:1:3:30	20	MeOH 70%	Film detachment
	4000:x:1:3:30	10	MeOH 70%	Good film growth in time. Improved film formation by reducing [PEGMA]
ARGET Stage 2	150:1:0.05:0.15:1.5	10	MeOH 70%	First attempt to grow free chains in solution. Multimodal MW distribution with high dispersity
ARGET Stage 3	150:1:0.05:0.5:1.5	10	MeOH 70%	*PDI* = 1.45-2.90. Improved control with TPMA excess
ARGET Stage 4	150:1:0.05:0.15:15	10	MeOH 70%	*PDI* = 2.1 Improved control with AscA excess
ARGET Stage 5	150:1:0.15-1:1.5-10:4.5-30	10	MeOH 70%	*PDI* = 1.8-1.35. Improved control with CuCl2 excess
ARGET Stage 6	100:1:1:10:100	10	MeOH 70%	*PDI* = 1.34. Combined findings. CuCl2, AscA and TPMA excess
AGET Stage 1	150:1:1:1:4	10	MeOH 70%	Br initiator gave betetr *PDI* than Cl initiator (1.12-1.43 compared to 1.25-1.59)
AGET Stage 2	150:1:1:1:0.15-2	10	IpOH 50%	*PDI* = 1.16-1.7. Lowest [AscA] gave better control

Finally, Table 5.11 summarises in one glance the different approaches used to gain control over the polymerization of PEGMA by ARGET and AGET ATRP, and the related outcomes.

5.3.4 Grafting of protein-repellent poly(poly(ethylene glycol) methyl ether methacrylate) brushes from macroinitiator films

Homogeneous and flat macroinitiator films on PS were grafted with PEGMA brushes, and the kinetics of the process were characterized using ellipsometry. In the following sections, the term "macroinitiator" refers to the bromine methacrylate homopolymer described in Section 5.3.1. The grafting was carried out using AGET ATRP. The grafting of a brush on a polymer film composed of physically entangled chains is not an easy task. As the bilayer was required to dewet prior to the grafting reaction, the top film (i.e. the macroinitiator film) could not be modified (e.g. by cross-linking) to stabilize it towards solubilisation in good solvents or swelling. The macroinitiator was soluble in the monomer PEGMA, and it swelled in low MW alcohols (particularly methanol and ethanol). Therefore, the grafting conditions had to be finely tailored to avoid film damage or delamination. As discussed later, some swelling of the macroinitiator film was unavoidable in this particular system, though it did not affect the final functional properties of the grafted bilayer. Nevertheless, the grafting reaction was designed to have the highest degree of control possible. The best reaction conditions were found to be a low monomer concentration (10% w/v) and a 50% mixture of isopropyl alcohol and water as a solvent. The low monomer concentration prevented the dissolution of the macroinitiator film. Water is a non-solvent for the macroinitiator, and stabilized it. Pure water could not be used here because it did not completely dissolve PEGMA at room temperature, giving a faintly turbid solution. When PEGMA was not

completely dissolved, the attack of the macroinitiator film and formation of microscopic holes was observed. An alcohol was the best choice as a co-solvent, because it could solubilise all the components of the reaction mixture without dissolving the macroinitiator film. To reduce the film swelling to a minimum, isopropanol was chosen, because its larger molecular volume was likely to limit its penetration in the film.

Summarised in Figure 5.9 are the kinetics of the grafting process. Presented in Figure 5.9(a) are the SEC traces obtained for the free polymer grown in solution, at increasing conversions. Each chromatogram contains a peak from the unreacted PEGMA monomer at low MW (converted from elution time), and a peak for the poly(PEGMA) at higher MW.

The curves were all normalized by the monomer peak intensity, for ease of comparison. Analysis of the data suggests that as the polymerization proceeded, the polymer concentration increased, as well as its MW. It is important to emphasize that the polymer peak width remained narrow throughout the reaction, indicating control over the MW distribution of the product.

Presented in Figure 5.9(b) are the average MWs of the free polymer estimated by SEC, plotted against conversion. The data shows a slight deviation from theory (which assumes 100% initiation and chains growing all at the same rate),[12] though this might have been due to the difference in hydrodynamic volume of poly(PEGMA) and PMMA, with which the SEC was calibrated. Nonetheless, the average MW increased with conversion in a linear fashion, confirming that the system was in fact a controlled radical polymerization. In Figure 5.9(b) are also the PDI values against conversion for the poly(PEGMA) chains in solution, and indicated that the MW polydispersity remained very low throughout the reaction. The SEC data are summarised in Table 5.12.

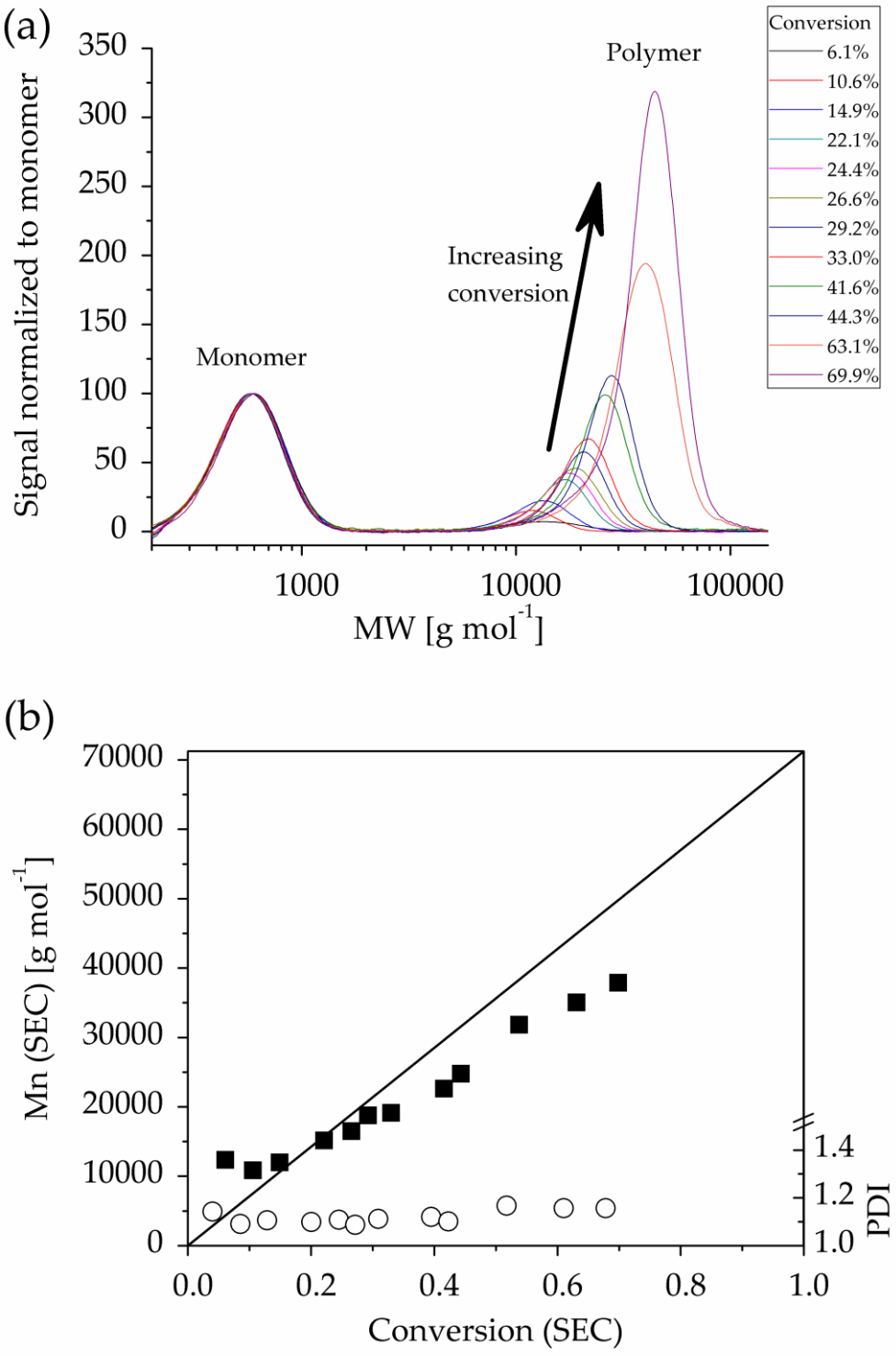

Figure 5.9 (a) SEC traces at different conversions, for the free poly(PEGMA) grown in solution from the sacrificial initiator during surface-initiated AGET ATRP from a macroinitiator film. (b) First order kinetics of the polymerization. The estimated M_n (SEC) of the free polymer is plotted against conversion (filled squares). The theoretical trend is shown as a straight line. The PDI values measured as a function of conversion are shown as empty circles, and use the right vertical axis.

Table 5.12 Experimental data extracted from the SEC analysis of the free poly(PEGMA) grown in solution from the sacrificial initiator during surface-initiated AGET ATRP from a macroinitiator film.

Conversion [%]	M_n [g mol^{-1}]	*PDI*
0	0	
6.1	12400	1.14
10.6	10800	1.09
14.9	12000	1.11
22.1	15100	1.10
26.6	16500	1.11
29.2	18800	1.09
33.0	19100	1.11
41.6	22600	1.12
44.3	24800	1.10
53.8	31800	1.17
63.1	35000	1.16
69.9	37900	1.16

Presented in Figure 5.10 is the variation of grafted poly(PEGMA) film thickness against the estimated M_n obtained by SEC (red symbols and line). A theoretical trend for the thickness was also reported, calculated from the experimental M_n, assuming fully stretched configuration of the poly(PEGMA) chains (black symbols and line). The repeating unit length in such a configuration is roughly 0.25 nm.[15] The theoretical thickness L_{th} was hence given by Equation 5.2:

$$L_{th} = DP \times conv \times 0.25\ nm \tag{5.2}$$

where DP is the maximum degree of polymerization and $conv$ is the conversion. The observed thickness trend deviated significantly from the expected one, and the reason for this difference is discussed in Section 5.4.

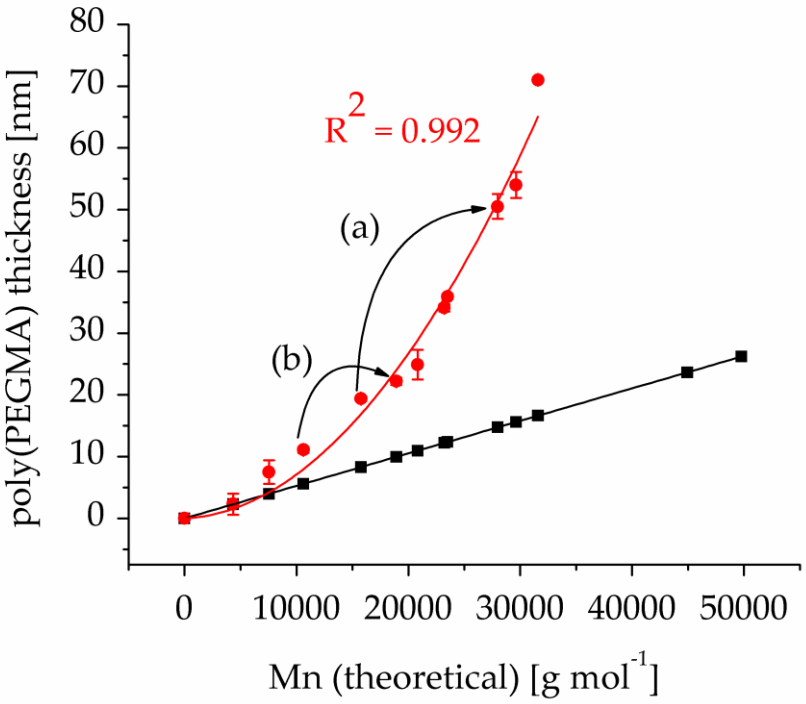

Figure 5.10 Thickness of grafted poly(PEGMA) film against MW of free polymer estimated by SEC (red circles). The data was fitted with a second order polynomial function, which allowed prediction of the thickness for a given conversion (i.e. theoretical MW) (red line). The least square error (R^2) is reported. The theoretical thickness against conversion (i.e. theoretical MW) is shown (black squares and line). The graph includes the results of two independent chain extension experiments. The first reaction (a) was stopped at 22.1% conversion, which gave a poly(PEGMA) layer thickness of 19.4 nm, and then reinitiated and allowed to proceed to 39.3%% conversion, which gave a thickness of 50.5 nm. The second reaction (b) was stopped at 14.9% conversion, which gave a poly(PEGMA) layer thickness of 11.1 nm, and then reinitiated and allowed to proceed to 26.8% conversion, which gave a thickness of 22.2 nm.

The "living" nature of the brush was investigated by chain extension tests. The polymerization was allowed to proceed to a given conversion, and then the sample was exposed to oxygen to stop the chain growth. The substrate was washed and characterized by ellipsometry to determine the poly(PEGMA) layer thickness, and the free polymer was analysed by SEC to

determine its MW. The substrate was then immersed again in the reaction media, which was deoxygenated again. The polymerization was restarted by adding more ascorbic acid, and it was found that the free polymer had a higher MW, and the substrate showed an increased poly(PEGMA) thickness, confirming the chain extension of the brush. These chain extension tests are indicated by the arrows in Figure 5.10.

5.3.5 Characterization of the grafted poly(PEGMA) layer

The topography of the grafted poly(PEGMA) brush on the macroinitiator film was characterized by Tapping Mode™ AFM imaging in air. Presented in Figure 5.11 are AFM images of the ungrafted macroinitiator film, along with images of the grafted poly(PEGMA) layer for different thickness values. All of the poly(PEGMA) brush surfaces appeared smooth, with root mean square (RMS) roughness values below 1 nm (table in Figure 5.11), which was comparable to that of the bare macroinitiator film.

The values of the RMS roughness were obtained as an average over one sample in 3 different positions on the surface. The few topographical features visible in Figure 5.11were low in vertical scale, with a maximum tip-to-valley height of 4 nm. By comparison, the average expected length of isolated poly(PEGMA) chains was much larger in all cases. The smooth surfaces were a strong indication that the brush had a high grafting density, and the chains were compressed together.

The multilayer containing the grafted poly(PEGMA) brush was also characterized by XPS analysis. XPS analysis and data fitting were performed by Dr. Thomas Gengenbach at the facilities in CSIRO Clayton VIC. Shown in Figure 5.12 are reference survey spectra obtained from the surface of the three main components of the analysed multilayers: PS, macroinitiator and poly(PEGMA).

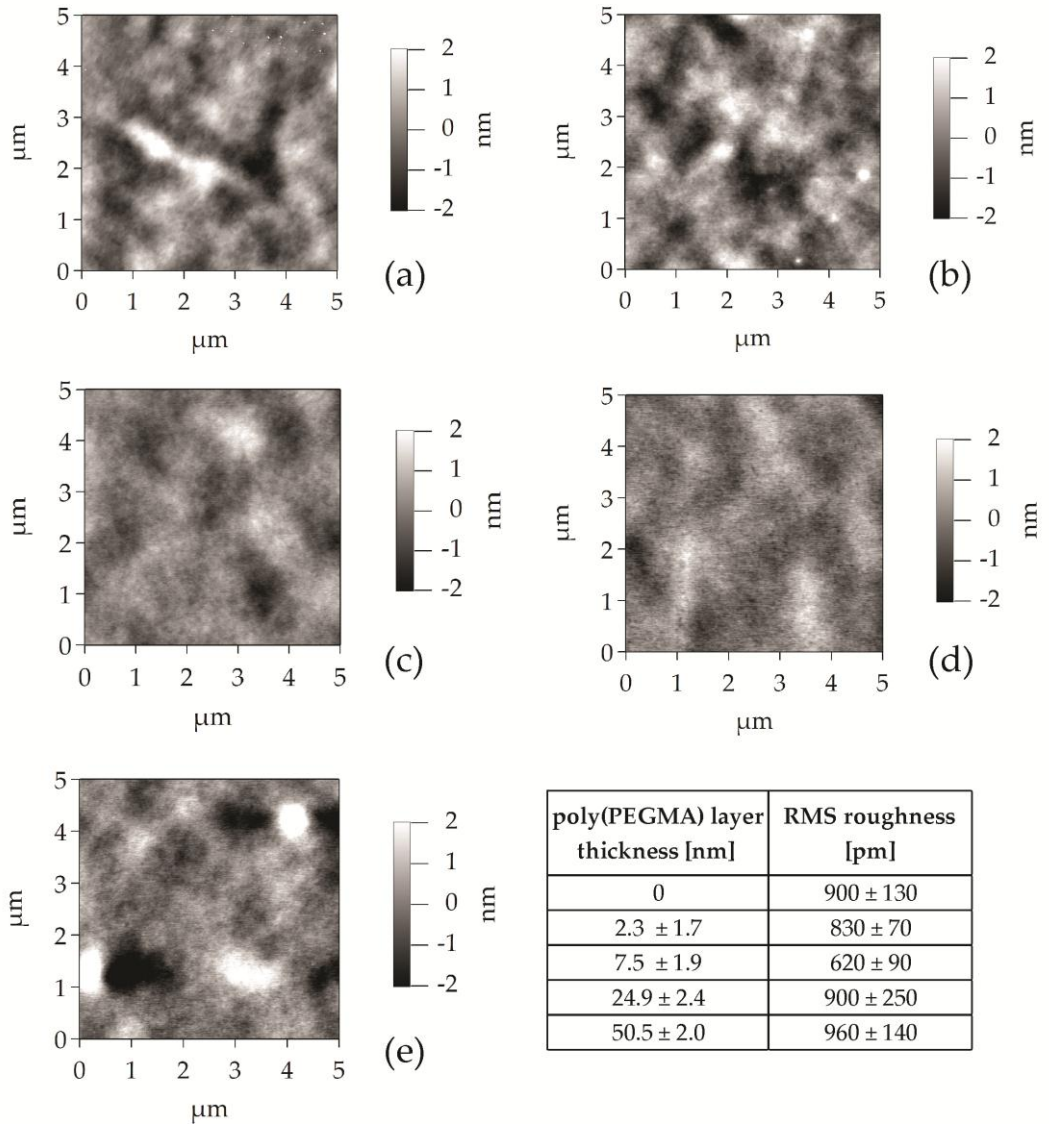

poly(PEGMA) layer thickness [nm]	RMS roughness [pm]
0	900 ± 130
2.3 ± 1.7	830 ± 70
7.5 ± 1.9	620 ± 90
24.9 ± 2.4	900 ± 250
50.5 ± 2.0	960 ± 140

Figure 5.11 Tapping Mode™ AFM topography images in air of (a) the bare macroinitiator film, and poly(PEGMA) brushes of different thicknesses grafted on the macroinitiator: (b) 2.3 nm, (c) 7.5 nm, (d) 25 nm, (e) 50 nm. The RMS roughness values for the different samples are reported in the table.

The PS spectrum (curve (a)) showed a very small signal for oxygen, and contained a strong C 1s signal, while oxygen was a main component of poly(PEGMA), from its ester and ether groups (curve (c)). In the macroinitiator film (curve (b)) oxygen was present as well, from its ester

groups, together with bromine, from the ATRP initiator moiety, and sulphur, from the RAFT agent used to synthesise the macroinitiator.

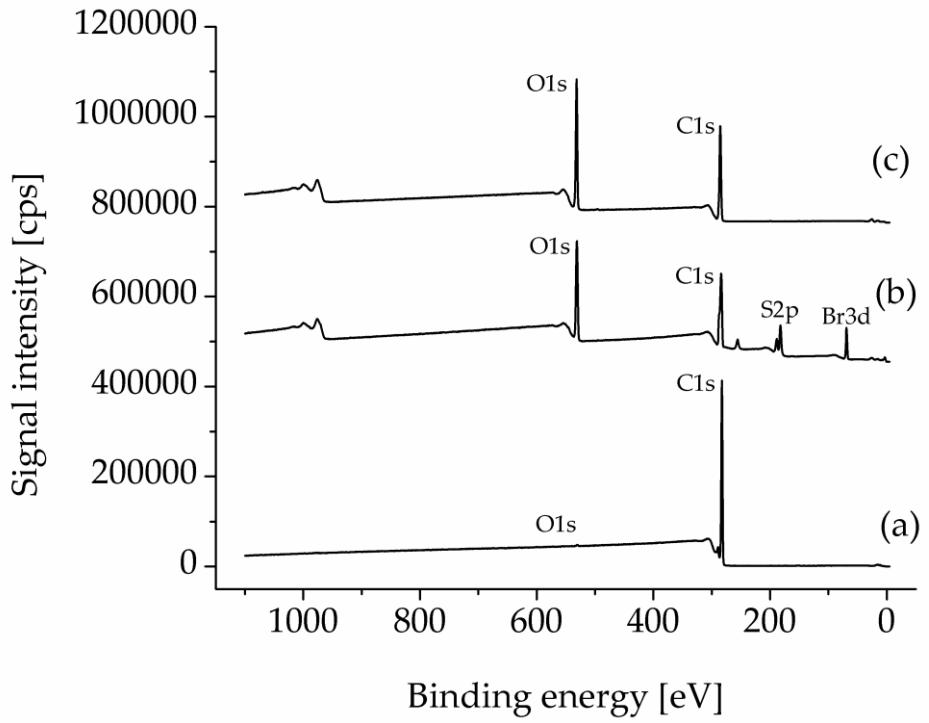

Figure 5.12 Survey XPS spectra obtained for single layers of (a) PS, (b) macroinitiator and (c) poly(PEGMA), spin-coated on silicon wafers. The spectra were offset by 45000 cps (trace (b)) and 75000 cps (trace (c)) for clarity.

Presented in Figure 5.13 are high resolution C 1s XPS spectra obtained from the same films. In Figure 5.13(a) the spectrum of the PS film showed contributions from aliphatic carbons C-C and C-H (C1) and aromatic carbons C=C (C6, or "shake up" peaks). As-received PS is often slightly oxidised, and this is the reason for the presence of ether and alcohol carbons C-O (C3) and secondary shifted aliphatic carbons C*-C-O connected to those (C2). In Figure 5.13(b), the spectrum of the macroinitiator film showed contributions from aliphatic carbons (C1), ether and alcohol carbons (C3) and second shifted aliphatic carbons connected to those (C2), carbonyl carbons C=O (C4)

and ester carbons C*-O-C=O (C5). Finally, in Figure 5.13(c) the spectrum of the poly(PEGMA) brush showed similar contributions to those obtained for the macroinitiator film, i.e. C1-C5, however, with a much more pronounced peak corresponding to the ether carbon from the PEG side-chains (C3).

XPS analysis was also used to characterise the composition of the poly(PEGMA) brush at different stages of grafting. The first sample of the series was a macroinitiator/PS bilayer, while the rest of the samples were poly(PEGMA) brushes grafted from such bilayers, at different conversions (i.e. brush thickness).

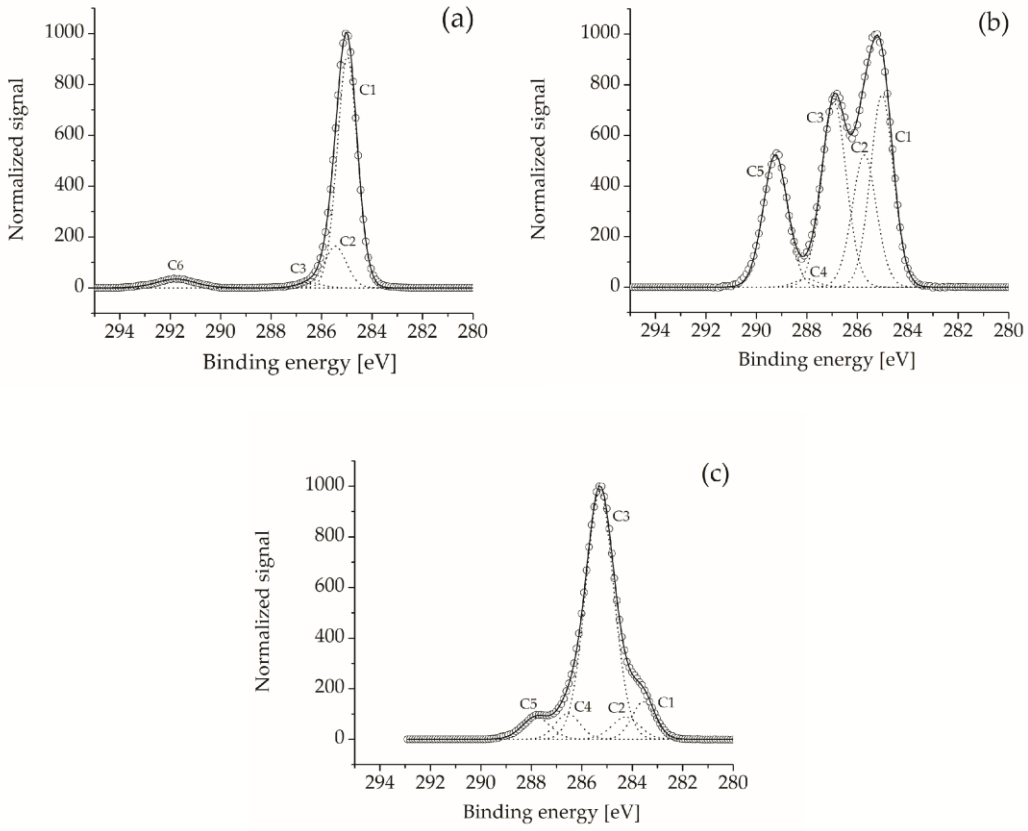

Figure 5.13 High resolution XPS C 1s spectra of (a) PS, (b) macroinitiator and (c) poly(PEGMA). The graphs show the experimental data (open circles), and the envelope fit (solid line) given by the combination of the individual carbon contributions (dotted lines). The numbering system is described in the text.

Presented in Figure 5.14 is a collection of high resolution XPS C 1s spectra for the sample series at increasing thickness of the brush. The spectra were normalized to the component peak with the highest intensity in each spectrum, which was component C1 when the brush thickness was low, and component C3 when the brush thickness was high (above 7.5 nm), and the poly(PEGMA) contribution was dominant over the macroinitiator one.

With increasing brush thickness, component C3 (red) became increasingly intense, and quickly dominated the XPS profile. Component C5 (green) in turn became less intense the more PEGMA was grafted on the macroinitiator, because of the smaller number of ester groups in poly(PEGMA) compared to the macroinitiator. Such XPS profiles are typical for PEG-containing films.[16, 17]

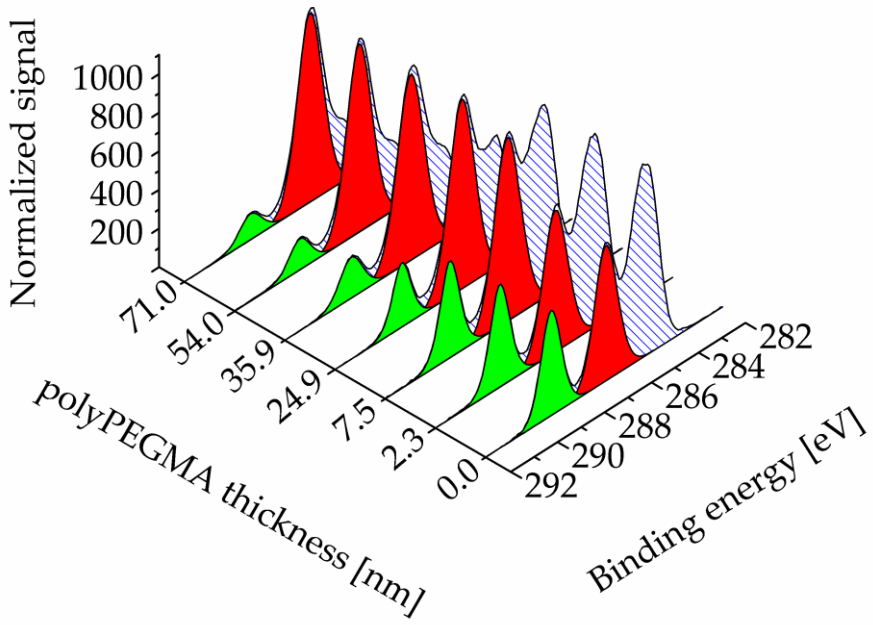

Figure 5.14 High resolution XPS C 1s spectra of poly(PEGMA) brushes grafted on macroinitiator films, at different brush thickness. Component C3, mainly from poly(PEGMA) (green), and component C5, mainly from the macroinitiator (red), are highlighted in each spectrum.

The changes in the contribution of components C3 and C5 over the total carbon concentration in each sample were plotted against the brush thickness in Figure 5.15.

This figure shows clearly the increasing intensity of component C3 from the poly(PEGMA) and the decreasing intensity of component C5 arising mainly from the macroinitiator, with increasing brush thickness. An important feature of this plot is that even when the poly(PEGMA) brush was much thicker than the XPS sampling depth (typically 10 nm), component C5/C was much higher than what would be expected from the brush alone (around 4.55%), and remained higher than the expected value up to the thickest brush analysed. This is a strong indication of a thick intermixed interface between the macroinitiator film and the poly(PEGMA) brush.

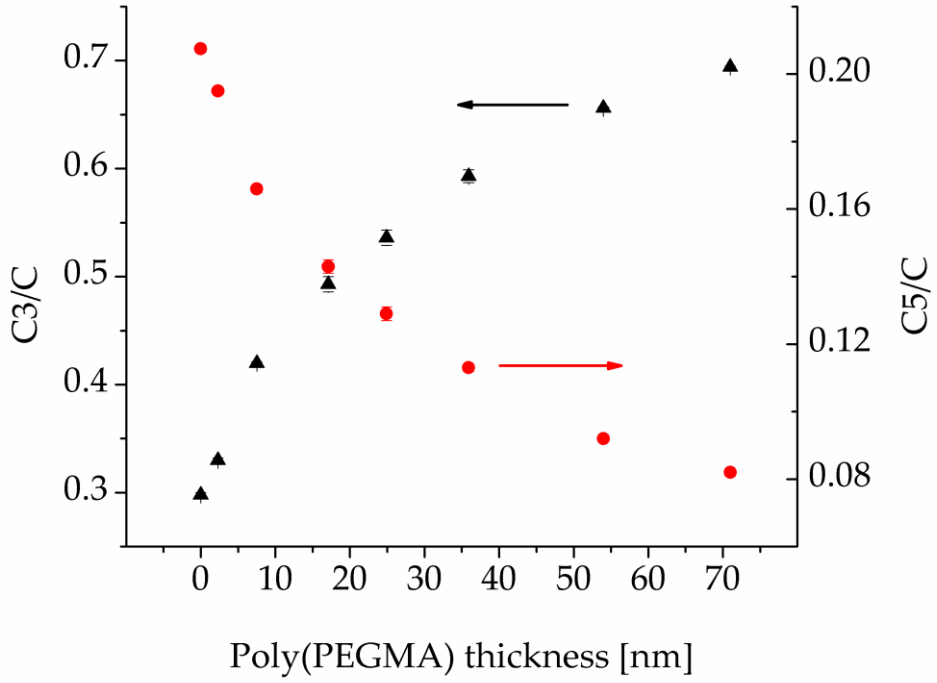

Figure 5.15 C1s high resolution XPS C3 and C5 contributions over the total concentration of carbon in poly(PEGMA) brushes grafted from macroinitiator/PS bilayers at different brush thickness.

Collected in Table 5.13 are the total carbon, oxygen and bromine atomic compositions of the different samples in the series, including the theoretical values expected for the macroinitiator alone and for the thickest poly(PEGMA) brush, assuming initiation efficiency of 100% and no living groups buried deeper than the detection depth of the instrument (about 10 nm). The thickest brush had a lower bromine concentration than the theoretical value. The errors on the measurements represent the standard deviations from the average on 3 different positions on each surface.

Table 5.13 XPS elemental composition data obtained via XPS analysis for poly(PEGMA) brushes grafted from the macroinitiator surface to different conversions (i.e. with different thickness values), compared to the compositions obtained for the macroinitiator surface (both experimental and theoretical) and that obtained for a theoretical brush of thickness 71 nm. The errors on the theoretical values for this poly(PEGMA) brush are calculated based on the polydispersity of the PEG side-chains.

poly(PEGMA) brush thickness [nm]	C 1s [%]	O 1s [%]	Br 3d [%]
0	67.0 ± 0.2	28.5 ± 0.5	4.4 ± 0.3
0 (theor.)	68.24	28.57	7.14
2.3 ± 1.7	67.2 ± 0.1	29.6 ± 0.1	3.1 ± 0.1
7.5 ± 1.5	67.92 ± 0.06	30.13 ± 0.01	1.96 ± 0.05
17.1 ± 0.5	67.28 ± 0.03	30.31 ± 0.06	2.29 ± 0.02
24.9 ± 2.4	68.11 ± 0.01	31.0 ± 0.3	0.9 ± 0.3
35.9 ± 0.4	67.7 ± 0.1	30.80 ± 0.05	1.41 ± 0.03
54.0 ± 2.1	67.37 ± 0.08	31.6 ± 0.1	0.77 ± 0.01
71.00 ± 0.16	67.5 ± 0.1	31.8 ± 0.1	0.53 ± 0.02
71.00 (theor.)	65.67 ± 0.05	31.34 ± 0.09	3.0 ± 0.1

It is important to notice that because of the dynamic rearrangement of the chains in a brush, the end-groups were likely to be distributed

throughout the brush film, and not all present at the outer extremities of the blush layer.

Table 5.14 XPS C1s elemental composition data for the poly(PEGMA) brushes at different thicknesses on top of the macroinitiator film, compared to the compositions obtained for a reference sample of pure poly(PEGMA).

poly(PEGMA) brush thickness [nm]	C1 [%]	C2 [%]	C3 [%]	C4 [%]	C5 [%]
0	26.8 ± 0.9	21.7 ± 0.9	30.0 ± 0.6	0.75 ± 0.7	20.8 ± 0.2
2.3 ± 1.7	25.9 ± 0.1	21.2 ± 0.1	33.0 ± 0.2	0.45 ± 0.08	19.51 ± 0.09
7.5 ± 1.5	22.93 ± 0.06	17.61 ± 0.08	42.0 ± 0.1	0.93 ± 0.05	16.58 ± 0.06
17.1 ± 0.5	20.6 ± 0.8	14.2 ± 0.2	49.3 ± 0.7	1.6 ± 0.3	14.3 ± 0.2
24.9 ± 2.4	20.3 ± 0.3	11.0 ± 0.2	53.7 ± 0.7	2.16 ± 0.08	12.9 ± 0.2
35.9 ± 0.4	16.2 ± 0.5	11.25 ± 0.07	59.3 ± 0.6	1.9 ± 0.2	11.28 ± 0.07
54.0 ± 2.1	13.66 ± 0.08	9.18 ± 0.08	65.56 ± 0.05	2.41 ± 0.03	9.20 ± 0.08
71.00 ± 0.16	11.9 ± 0.2	8.18 ± 0.08	69.42 ± 0.09	2.28 ± 0.01	8.20 ± 0.08
Pure poly(PEGMA) ref.	9.6 ± 0.9	8.0 ± 0.6	66.1 ± 1.2	8.4 ± 0.8	8.0 ± 0.6

Collected in Table 5.14 are the atomic compositions of the different carbon components for the same samples. The different ratios between the carbon components give accurate information on the composition and growth of the brush. The errors on the data represent the standard deviation from the average over 3 positions on each surface. These are generally good estimates of the deviation between the experimental data and the fitting, as well as other sources of errors such as variability on the surface of the sample. The fitting quality on a typical XPS measurement can vary greatly,

depending on the number of components included in the fitting of a spectrum. For the measurements reported here for the C 1s spectra, the error arising from the fitting was estimated by Monte Carlo simulations, which suggested that although the error on the major components was low (1% - 4%), the error on the very small component C4 was quite high (61%).[18] The precision of the measurements reported in Table 5.13 and Table 5.14 hence, have to be considered with caution.

5.3.6 Patterning by dewetting

The roughness of the substrate can influence the patterns obtained by dewetting, as asperities may nucleate a large hole density in addition to that caused by stresses within the polymer film. The substrate chosen as a support for the films was a flat silicon wafer, coated with about 1 nm of silicon oxide with a low roughness (RMS roughness typically below 0.3 nm). The silicon wafer was spin coated with a thick polystyrene (PS) film, which provided the hydrophobic substrate on which the macroinitiator film could dewet. Molten PS did not dewet from the silica coated silicon surface in the timescale of these experiments, because of the weak dewetting driving force.[19] Moreover, the macroinitiator film was liquid at temperatures above about 50 °C, which is much lower than the T_g of PS (about 110 °C), so the bottom PS film remained unchanged upon annealing. The macroinitiator film quickly dewetted when the system was annealed at 100 °C. Presented in Figure 5.16 are optical micrographs of a macroinitiator film (28 ± 1 nm) dewetting on a PS film (58 ± 1 nm), at different annealing times. As observed in simple polymer bilayer systems,[8] the top layer rapidly formed holes (Figure 5.16(a)) that grew in time (Figure 5.16(b-e)) and eventually coalesced, forming a pattern of dewetted droplets (Figure 5.16(f)). The desired pattern could be easily fixed by cooling down the film to room temperature.

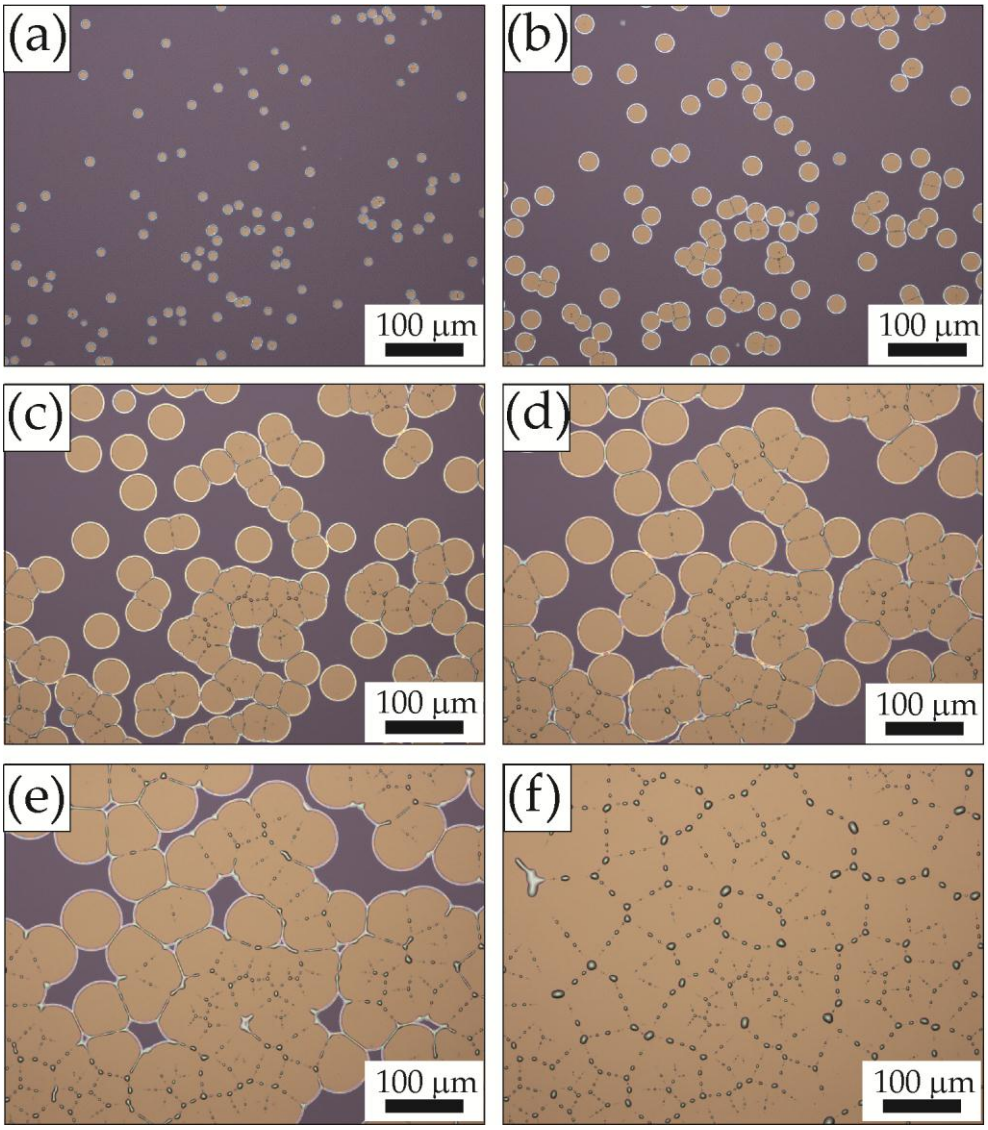

Figure 5.16 Optical micrographs of a macroinitiator film dewetting from a PS substrate, upon annealing at 100 °C. The annealing times were (a) 1 min 50 s, (b) 4 min 5 s, (c) 8 min 40 s, (d) 11 min 50 s, (e) 16 min 45 s, (f) 46 min 25 s.

The dewetted polymer film was then grafted with protein-repellent poly(PEGMA) using AGET ATRP, as described in Section 5.3.4. Shown in Figure 5.17(a, b) is a dewetted pattern before and after grafting about 60 nm of poly(PEGMA) brush. The pattern retained its appearance, since poly(PEGMA) was selectively grafted on the macroinitiator alone, and not inside the holes. The presence of the brush gave the rims on the top

dewetted layer a birefringence that could not be observed in the macroinitiator alone, and made the colour of the film change from purple to blue, because of the increased thickness.

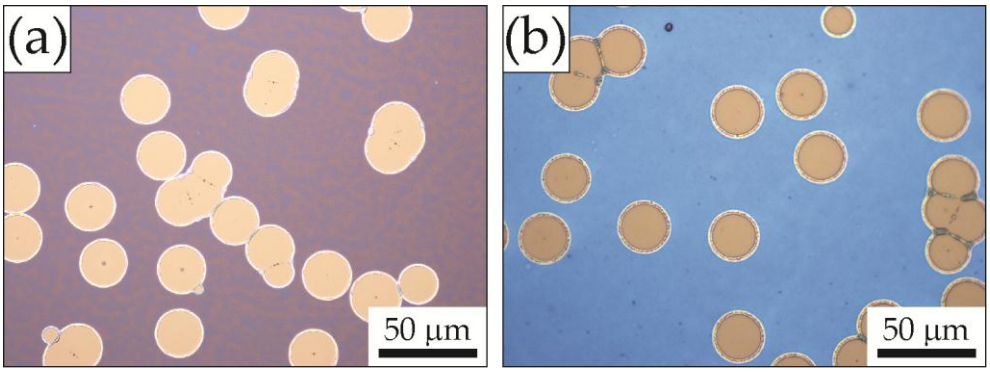

Figure 5.17 Optical micrographs of (a) a dewetted, ungrafted macroinitiator film and (b) a dewetted macroinitiator film after grafting approximately 60 nm of poly(PEGMA). Picture (b) shows a different colour of the film and a birefringent effect on the rims of the dewetted holes.

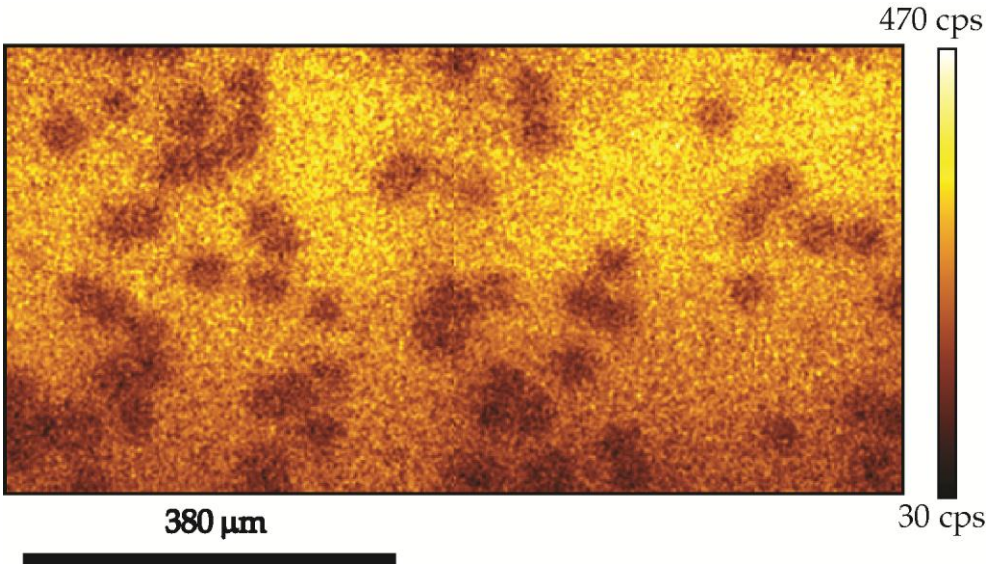

Figure 5.18 XPS map of a dewetted macroinitiator film on a PS film, grafted with about 60 nm of poly(PEGMA). The O1s signal of poly(PEGMA) was targeted, and the surface was scanned in a raster.

The grafted patterns were imaged using XPS, to confirm the chemical contrast between the holes and the background. XPS mapping was performed by Dr. Chris Easton at the facilities in CSIRO Clayton VIC. The detector was fixed on the O1s signal of poly(PEGMA), and the surface of the sample was scanned in a raster. The XPS map (Figure 5.18) showed bright areas where the poly(PEGMA) signal was strong, and dark round areas in correspondence of the dewetted holes.

5.4 Discussion

This work describes a novel functional coating for protein and cell patterning on a surface. The study combines polymer brush grafting and polymer thin film bilayer dewetting to produce a pattern of protein-adsorptive holes in a protein-repellent background. Patterning of proteins is important to control cell attachment on a surface, for applications such as single-cell studies and geometrically controlled cell co-cultures for tissue engineering. Photolithography,[20-22] electron beam lithography,[23] or soft lithography[24] have been used to either directly etch a pattern in a flat brush or to pattern an initiator from which the brush was eventually grafted. A detailed review on the patterning of brushes was published by Ducker *et al.*[25] The process presented here does not suffer from high cost and/or requirement for advanced fabrication skills, since the pattern is obtained by a self-assembled process that simply requires heating. This approach has the advantage of being able to produce patterns on non-flat surfaces, because substrates with different shapes may be dip-coated with polymer thin films, giving it wide applicability. Finally, this approach is flexible because different types of patterns and patterns of different sizes, between a few tens

of nanometres and a few tens of micrometers, can be easily produced by tailoring film thickness and MW of the macroinitiator, and dewetting time.

The use of polymer films as anchoring layers for brush grafting is not common in the literature, and the combination of this approach with patterning by dewetting has not been reported before. In their recent work, Rodriguez-Emmenegger *et al.*[26] coated a variety of substrates with an amino-rich nylon 6,6 polymer film by means of radio frequency magnetron sputtering, reacted the amine groups with bromo-isobutyrate and finally grafted antifouling oligo(ethylene glycol) methacrylate and carboxybetaine acrylamide *via* surface-initiated ATRP. The method reported in this work is simpler, because the film may be applied by spin-coating or dip-coating, which require inexpensive and easy to use equipment, and the ATRP initiating moiety is already present in the polymer used to cast the film, hence does not need to be added in a separate step. A similar approach can be found in the work of Edmondson and co-workers, where the macroinitiator film is produced either by layer-by-layer deposition of polyelectrolyte polymers containing ATRP initiators,[27, 28] or by deposition of bio-inspired polydopamine films containing ATRP initiators.[29] Polydopamine was also very recently employed by Tsai *et al.*[30] as an anchoring film incorporating PEG and other antifouling macromolecules for biomedical applications. Ohno *et al.* published work on a system very similar to the one presented here.[11] They prepared a macroinitiator film by uncontrolled random copolymerization, which contained cross-linkable azide groups. The polymer was cast in a film on different substrates, and a pattern of cross-linked initiator film was prepared by exposure to UV through a mask. The pattern was then grafted with protein-repellent poly(PEGMA). The work presented here differs mainly in the patterning approach, which here was by spontaneous thin film dewetting.

The macroinitiator in this work was designed not only as an anchoring substrate for the brush, but as a layer capable of dewetting from the base PS film, in order to form the desired pattern. A methacrylate backbone was chosen because of the known ability of PMMA to dewet on PS. The PMMA/PS system was previously investigated by Neto,[8] and represents the basis on which this work was built. The macroinitiator has a lower T_g than PMMA, and has a melting point which PMMA lacks, as evident from the DSC characterization in Figure 5.3. This behaviour is likely to be related to the long bulky side chains of the polymer, which can form a mesophase with different characteristics from the methacrylate backbone.[31] Nevertheless, the macroinitiator was capable of dewetting from PS, and was in a glassy state at room temperature, so that the pattern formed was stable.

The macroinitiator was here synthesised by RAFT polymerization, to obtain a product with controlled MW. This is important because the polymer's MW affects the hole density in a dewetting pattern, as discussed in Section 1.7.6. Highly disperse or multimodal MWs are likely to still produce patterns of holes with low size distribution (e.g. see work in Chapter 4), but the hole density would be poorly controlled. RAFT polymerization was also chosen because it relies on different chemistry from ATRP, hence it was not affected by the presence of ATRP-initiating moiety in the monomer. The macroinitiator was able to dewet on PS by heterogeneous nucleation, achieving patterns of randomly distributed holes which grew with annealing time, as shown in Figure 5.16. The dewetted pattern was retained after grafting of the poly(PEGMA) brush (Figure 5.17), as the brush is attached selectively to the macroinitiator and does not affect the PS holes. The marked chemical contrast between the patterned brush and the PS present in the dewetted holes was obvious from the XPS mapping, where the presence of oxygen, characteristic of the poly(PEGMA) brush, was highlighted (Figure 5.18).

The brush grafting from the macroinitiator films was performed by surface-initiated AGET ATRP. Once optimized, this system is more user-friendly than conventional ATRP, because only the stable oxidized form of the copper catalyst is used, and the presence of a reducing agent makes it less susceptible to the presence of small amounts of oxygen. As a result, the equipment necessary is reduced to simple glassware and a nitrogen line, instead of a Schlenk line and rigorous deoxygenating procedures. AGET ATRP, as conventional ATRP, is a very fast process when water is used as solvent or co-solvent, because the copper catalyst forms more active complexes in polar media.[32] In our system, 50% conversion was obtained after only 45 minutes at room temperature. The initial attempt to use ARGET ATRP was unsuccessful, because side reactions on the catalyst, such as ligand exchange with water and monomer, are important when the catalyst concentration is very low. The investigation of ARGET ATRP to polymerise PEGMA was nonetheless fruitful to guide the following optimization of AGET ATRP. The results indicated that the control over the polymer MW could be improved by using small excesses of TPMA and/or catalyst.

The use of a reversible-deactivation polymerisation method such as AGET ATRP allowed control over the thickness of the growing brush, which was proportional to the reaction conversion in solution. The brush growth (i.e. the thickness of the macroinitiator plus graft layer, minus the thickness of the macroinitiator layer determined before the grafting reaction) did not show the expected linear evolution with conversion, but followed a defined second order polynomial trend (Figure 5.10). This was likely due to swelling of the macroinitiator film and growth of poly(PEGMA) chains from deep within the film, as well as on its surface. The ability of monomer to penetrate the macroinitiator film and polymerise from within it has been observed in the case of polyelectrolyte multilayers containing ATRP initiators.[27] Unlike other systems,[11] the macroinitiator film could not be cross-linked to prevent

swelling, because it had to retain its ability to dewet. During grafting, the very polar poly(PEGMA) brush stretches into the polar solution, due to the combination of steric hindrance and swelling with water to reduce the enthalpy. The increase in entropy of such a configuration though, exerts a pulling force on the macroinitiator chains, which relax, loosen up and release from entanglement. This allows buried units of the macroinitiator chains to come in contact with the monomer and catalyst, initiating new poly(PEGMA) chains. The bromo-ester initiation sites in the macroinitiator react more readily than the chloro-capped propagating poly(PEGMA) chains. The process resulted in an intermixed layer of macroinitiator and poly(PEGMA) that grew faster and faster with conversion. Once the poly(PEGMA) chains had grown to over about 40000 g mol^{-1}, the macroinitiator film plus graft layer detached altogether from the PS substrate. The delamination effect of grafted PEG chains grafted on entangled polymers has been recently employed by Ruhs *et al.*[33] to disassemble amyloid fibrils. A similar delamination effect was observed by Tugulu *et al.*[34] for poly(PEGMA) brushes grafted from silane-anchored ATRP initiators on silica.

The XPS data for poly(PEGMA) brushes of different thicknesses, i.e. different stages of growth, show clearly that macroinitiator chains were always present very close to the brush surface, supporting the hypothesis of the formation of a thick intermixed layer of macroinitiator and poly(PEGMA). The theoretical atomic concentration for the ester (C5) component for pure poly(PEGMA) is 4.55% ± 0.21%, taking into account the monomer polydispersity (equal likelihood of having 8 or 9 ethylene oxide units in the side chain). The experimental atomic concentration was far greater than this when the brush was theoretically thicker than the XPS maximum probing depth (10 nm), and no macroinitiator should have been observed. For the thickest brush grown (71 nm) the C5/C component was

still about double the theoretical value, indicating the presence of macroinitiator chains, which bore more ester functionalities than poly(PEGMA).

A minor contribution to the thickness deviation from the theory could be due to a lower initiation efficiency on the surface compared to that in solution, possibly due to high radical density on the surface in the initiation step, which could lead to higher degree of polymerization than expected, as well as a higher polydispersity. As discussed in Section 1.5.6, the assumption that the free chains are identical to the grafted chains is still debated, and may not be valid for any substrate geometry. The XPS data summarised in Table 5.13, which shows that the bromine concentration detected in the thickest poly(PEGMA) brush was much lower than expected from the polymer formula, must be considered with caution. The data may indicate that many living ends were buried inside the brush because of chain collapse and spatial rearrangement, which is more likely when the grafted chains are long and loosely grafted. This is the type of brush obtainable when low initiation occurs. This though is not a conclusive proof of low initiation efficiency, since the dynamics of chains within a brush allow for the burial of chain ends also in densely grafted brushes grown with initiation efficiency of 100%. Moreover, the X-rays employed in XPS could potentially cleave some of the labile C-Br bonds, ultimately affecting the reliability of quantitative analysis, although this is unlikely over the timeframe that the analysis was carried out. Finally, some bromine may be lost by termination events during the polymerization of PEGMA. In our work, the main goal was to design a system that could be used to pattern proteins and cells, hence obtaining perfectly monodisperse brushes was not a major concern.

As each of the repeating units in the macroinitiator contained a halo-ester functionality, and the grafting was not limited to the surface, but involved initiators from deep within the film, the effective ATRP initiator

density was very high in this approach. Estimates of the grafting density (data not shown), in combination with the estimated degrees of polymerisation and comparisons between the distance between molecules and the radii of gyration of the grafted molecules suggest that the graft layer was in a highly stretched brush conformation. Further evidence that this was the case is provided in Chapter 6, where the protein-repellent properties of the grafted surfaces were explored through adsorption experiments with fluorescently tagged proteins, as well as atomic force microscopy analysis. Wang *et al.*[35] characterised poly(*N*-isopropylacrylamide) brushes grafted from self assembled monolayers of thiol-terminated initiators on gold, at different grafting densities. In their AFM images, collected on the same scale as the present work (5x5 μm^2), low and high grafting densities could be distinguished. At low grafting densities, the dry brush appeared as isolated domes corresponding to single collapsed chains. At higher grafting densities, the chains were compressed together, so they retained some degree of stretching even when dry, and showed a flat, featureless surface. A similar qualitative approach was taken here, assuming a similar behaviour of the poly(PEGMA) brush. The surface of the brushes here prepared appeared smooth (Figure 5.11), and no isolated mushroom-like chains could be found. This is consistent with a high grafting density of the brush.

The use of AGET ATRP, besides allowing control on the brush thickness, produced brushes with post-functionalisable "living" ends, as shown by the ability of the brushes to reinitiate the polymerisation in chain extension experiments (Figure 5.10). This gives the system high versatility in biomedical applications: the brush surface may be easily functionalised to meet different specific needs, for example it could be reacted with a peptide able to immobilise a specific type of cell, or with a bactericidal moiety to prevent bacterial biofilm formation.

5.5 Summary

A novel method to obtain a chemical and topographical pattern on a surface was presented. The pattern was obtained by the combination of dewetting, to produce a pattern of PS holes, and surface grafting with a poly(PEGMA) brush, to impart strong antifouling properties around the holes.

The macroinitiator film used as the anchoring substrate for the growth of the poly(PEGMA) brush was designed so to have a high concentration of ATRP initiators, as well as to be able to dewet on the underlying PS film, to produce a pattern of holes that exposed the protein-adsorptive PS. The macroinitiator was proven to quickly dewet on PS by annealing at 100 °C, forming the expected pattern of holes.

The poly(PEGMA) brush was produced using reversible-deactivation radical polymerization techniques. The first attempt was ARGET ATRP, which was only partially successful because of the strong influence of side reactions involving the catalyst, which reduced the control over the reaction. Nevertheless, the investigation on the ARGET ATRP system was useful in determining a set of optimal conditions for the grafting of poly(PEGMA) using AGET ATRP, a similarly robust technique. The employment of AGET ATRP led to high control over the MW and polydispersity of poly(PEGMA) in solution, using a simple experimental set up.

The brush growth was predictable for any given conversion, though not linear as expected by theoretical assumptions. In this system, the brush was likely to grow on top as well as within the macroinitiator layer. The result of the grafting was a pure poly(PEGMA) brush on top of a heavily intermixed layer of macroinitiator and poly(PEGMA). The brush produced satisfied all the requirements for the applications it was designed for: its thickness was predictable and controllable, its grafting density was high

enough for protein-repellence applications, as seen by AFM and by theoretical calculations, and its surface presented "living" ends that were able to re-initiate the polymerization reaction in chain extension experiments. The poly(PEGMA) brush was grafted on macroinitiator films patterned by dewetting, and XPS mapping confirmed that the grafting was selective to the top dewetted film, and did not affect the PS holes.

The patterned functional coatings here developed are suitable for protein and cell patterning, in applications where control over attachment and spreading of cells is required. This work presents an inexpensive, easy and versatile way to produce microwells on a surface for biomedical applications, as an alternative to other established patterning techniques.

5.6 References

1. Charnley, M.; Textor, M.; Khademhosseini, A.; Lutolf, M. P., Integration column: microwell arrays for mammalian cell culture. *Integrative Biology* **2009**, *1* (11-12), 625-634.
2. Kaji, H.; Camci-Unal, G.; Langer, R.; Khademhosseini, A., Engineering systems for the generation of patterned co-cultures for controlling cell-cell interactions. *Biochimica et Biophysica Acta (BBA) - General Subjects* **2011**, *1810* (3), 239-250.
3. Khademhosseini, A.; Langer, R.; Borenstein, J.; Vacanti, J. P., Microscale technologies for tissue engineering and biology. *Proceedings of the National Academy of Sciences of the United States of America* **2006**, *103* (8), 2480-2487.
4. Gates, B. D.; Xu, Q. B.; Stewart, M.; Ryan, D.; Willson, C. G.; Whitesides, G. M., New approaches to nanofabrication: Molding, printing, and other techniques. *Chemical Reviews* **2005**, *105* (4), 1171-1196.
5. Xia, Y. N.; Whitesides, G. M., Soft lithography. *Annual Review of Materials Science* **1998**, *28*, 153-184.
6. Love, J. C.; Estroff, L. A.; Kriebel, J. K.; Nuzzo, R. G.; Whitesides, G. M., Self-assembled monolayers of thiolates on metals as a form of nanotechnology. *Chemical Reviews* **2005**, *105* (4), 1103-1169.

7. Oh, J. K.; Min, K.; Matyjaszewski, K., Preparation of poly(oligo(ethylene glycol) monomethyl ether methacrylate) by homogeneous aqueous AGET ATRP. *Macromolecules* **2006**, *39* (9), 3161-3167.
8. Neto, C., A novel approach to the micropatterning of proteins using dewetting of polymer bilayers. *Physical Chemistry Chemical Physics* **2007**, *9* (1), 149-155.
9. Matyjaszewski, K.; Jakubowski, W.; Min, K.; Tang, W.; Huang, J. Y.; Braunecker, W. A.; Tsarevsky, N. V., Diminishing catalyst concentration in atom transfer radical polymerization with reducing agents. *Proceedings of the National Academy of Sciences of the United States of America* **2006**, *103* (42), 15309-15314.
10. Matyjaszewski, K.; Dong, H. C.; Jakubowski, W.; Pietrasik, J.; Kusumo, A., Grafting from surfaces for "Everyone": ARGET ATRP in the presence of air. *Langmuir* **2007**, *23* (8), 4528-4531.
11. Ohno, K.; Kayama, Y.; Ladmiral, V.; Fukuda, T.; Tsujii, Y., A Versatile method of Initiator fixation for surface-initiated living radical polymerization on polymeric substrates. *Macromolecules* **2010**, *43* (13), 5569-5574.
12. Matyjaszewski, K.; Xia, J. H., Atom transfer radical polymerization. *Chemical Reviews* **2001**, *101* (9), 2921-2990.
13. Tsarevsky, N. V.; Pintauer, T.; Matyjaszewski, K., Deactivation efficiency and degree of control over polymerization in ATRP in protic solvents. *Macromolecules* **2004**, *37* (26), 9768-9778.
14. Matyjaszewski, K.; Shipp, D. A.; Wang, J. L.; Grimaud, T.; Patten, T. E., Utilizing halide exchange to improve control of atom transfer radical polymerization. *Macromolecules* **1998**, *31* (20), 6836-6840.
15. Yamamoto, S.; Ejaz, M.; Tsujii, Y.; Fukuda, T., Surface interaction forces of well-defined, high-density polymer brushes studied by atomic force microscopy. 2. Effect of graft density. *Macromolecules* **2000**, *33* (15), 5608-5612.
16. Hamilton-Brown, P.; Gengebach, T.; Griesser, H. J.; Meagher, L., End terminal, poly(ethylene oxide) graft layers: Surface forces and protein adsorption. *Langmuir* **2009**, *25* (16), 9149-9156.
17. Thissen, H.; Gengenbach, T.; du Toit, R.; Sweeney, D. F.; Kingshott, P.; Griesser, H. J.; Meagher, L., Clinical observations of biofouling on PEO coated silicone hydrogel contact lenses. *Biomaterials* **2010**, *31* (21), 5510-5519.
18. Gengenbach, T., Monte Carlo simulation of the fitting quality of XPS analysis on polymer thin films. Personal communication. **2011**.
19. Seemann, R.; Herminghaus, S.; Jacobs, K., Gaining control of pattern formation of dewetting liquid films. *Journal of Physics-Condensed Matter* **2001**, *13* (21), 4925-4938.
20. Jia, X. Y.; Jiang, X. S.; Liu, R.; Yin, J. E., Facile approach to patterned binary polymer brush through photolithography and surface-initiated

photopolymerization. *ACS Applied Materials & Interfaces* **2010**, *2* (4), 1200-1205.
21. Cho, W. K.; Kong, B.; Park, H. J.; Kim, J.; Chegal, W.; Choi, J. S.; Choi, I. S., Long-term stability of cell micropatterns on poly((3-(methacryloylamino)propyl)-dimethyl(3-sulfopropyl)ammonium hydroxide)-patterned silicon oxide surfaces. *Biomaterials* **2010**, *31* (36), 9565-9574.
22. Andruzzi, L.; Senaratne, W.; Hexemer, A.; Sheets, E. D.; Ilic, B.; Kramer, E. J.; Baird, B.; Ober, C. K., Oligo(ethylene glycol) containing polymer brushes as bioselective surfaces. *Langmuir* **2005**, *21* (6), 2495-2504.
23. Rastogi, A.; Paik, M. Y.; Tanaka, M.; Ober, C. K., Direct patterning of intrinsically electron beam sensitive polymer brushes. *ACS Nano* **2010**, *4* (2), 771-780.
24. Tu, H.; Heitzman, C. E.; Braun, P. V., Patterned poly(N-isopropylacrylamide) brushes on silica surfaces by microcontact printing followed by surface-initiated polymerization. *Langmuir* **2004**, *20* (19), 8313-8320.
25. Ducker, R.; Garcia, A.; Zhang, J. M.; Chen, T.; Zauscher, S., Polymeric and biomacromolecular brush nanostructures: progress in synthesis, patterning and characterization. *Soft Matter* **2008**, *4* (9), 1774-1786.
26. Rodriguez-Emmenegger, C.; Kylian, O.; Houska, M.; Brynda, E.; Artemenko, A.; Kousal, J.; Alles, A. B.; Biederman, H., Substrate-independent approach for the generation of functional protein resistant surfaces. *Biomacromolecules* **2011**, *12* (4), 1058-1066.
27. Edmondson, S.; Vo, C. D.; Armes, S. P.; Unali, G. F.; Weir, M. P., Layer-by-layer deposition of polyelectrolyte macroinitiators for enhanced initiator density in surface-initiated ATRP. *Langmuir* **2008**, *24* (14), 7208-7215.
28. Edmondson, S.; Armes, S. P., Synthesis of surface-initiated polymer brushes using macro-initiators. *Polymer International* **2009**, *58* (3), 307-316.
29. Zhu, B. C.; Edmondson, S., Polydopamine-melanin initiators for surface-initiated ATRP. *Polymer* **2011**, *52* (10), 2141-2149.
30. Tsai, W. B.; Chien, C. Y.; Thissen, H.; Lai, J. Y., Dopamine-assisted immobilization of poly(ethylene imine) based polymers for control of cell-surface interactions. *Acta Biomaterialia* **2011**, *7* (6), 2518-2525.
31. Bershtein, V. A.; Egorov, V. M., *Differential scanning calorimetry of polymers*. Ellis Horwood Ltd: Chichester, **1994**.
32. Nanda, A. K.; Matyjaszewski, K., Effect of [bpy]/[Cu(I)] ratio, solvent, counterion, and alkyl bromides on the activation rate constants in atom transfer radical polymerization. *Macromolecules* **2003**, *36* (3), 599-604.
33. Ruhs, P. A.; Adamcik, J.; Bolisetty, S.; Sanchez-Ferrer, A.; Mezzenga, R., A supramolecular bottle-brush approach to disassemble amyloid fibrils. *Soft Matter* **2011**, *7* (7), 3571-3579.

34. Tugulu, S.; Klok, H. A., Stability and nonfouling properties of poly(poly(ethylene glycol) methacrylate) brushes-under cell culture conditions. *Biomacromolecules* **2008**, *9* (3), 906-912.
35. Wang, X.; Tu, H.; Braun, P. V.; Bohn, P. W., Length scale heterogeneity in lateral gradients of poly(N-isopropylacrylamide) polymer brushes prepared by surface-initiated atom transfer radical polymerization coupled with in-plane electrochemical potential Gradients. *Langmuir* **2006**, *22* (2), 817-823.

CHAPTER 6

Control of cell adhesion and growth on patterned functional surfaces

6.1 Introduction

The ultimate aim of this work was to achieve control over cell patterning on a surface. The first step towards this aim was to achieve patterning of cell-attachment-mediating proteins, after which cells could attach onto the protein-coated domains. In the work reported in this Chapter, these two steps were investigated.

The cell is an elaborate unit designed to perform its functions in concert with other cells. This strict dependency is at the base of cell organisation in the human body. Cells can only grow and differentiate when in the correct environment, i.e. they form a tissue when surrounded by appropriate neighbouring cells, and conversely they remove themselves from an unsuitable environment. Cell death occurs *via* a process called apoptosis.

In vivo, cells are surrounded by neighbouring cells as well as a complex matrix of proteins, which are specific for each tissue, and soluble signalling molecules (cytokines) that cells use to communicate. Most types of cells are programmed to undergo apoptosis unless they can attach to and receive signalling cues from the interaction with appropriate extra cellular matrix (ECM) molecules and other biological molecules (e.g. growth factors) adsorbed onto the ECM. This specific type of apoptosis is termed anoikis (from the Greek "homelessness").[1-3] Blood cells are an exception to this generalisation, since they are part of a special connective tissue (i.e. the blood).

Cells attach to ECM molecules *via* cell-surface-expressed proteins called integrins. Humans have a collection of 24 different integrins, which bind to specific regions, or epitopes, on ECM proteins. Attachment *via* these receptors not only provides a physical attachment to the home tissue, but also establishes a mechanical stress-dependent signalling framework

involving numerous proteins and kinases (enzymes which regulate signal transduction in cell processes). The stress exerted on the cell skeleton as a result of the anchoring through the integrins may activate certain downstream pathways which are the base of cell death and proliferation. This mechanotransduction mechanism is described in detail in Section 1.6. Integrins independently activate many of the same chemical pathways as growth factor receptors (GFRs) do; these receptors are responsible for the activation of downstream pathways which lead to cell proliferation. Integrins can even directly cross-talk with GFRs, to the extent that the cell can interact efficiently with the soluble growth factors (signalling molecules) in the biological medium only when they are attached to the correct ECM molecules.[4-6]

Anoikis malfunction *in vivo* has been reported to enhance tumour metastasis.[7] Cells normally undergo anoikis in order to prevent uncontrolled growth of cell masses in foreign locations. Instead, cells with malignant potential are capable of developing mechanisms to resist anoikis, and thereby survive after detachment from the home ECM and become migratory.[8] Furthermore, malignant tumour cells can re-design their chemical pathways to express the integrins they require to attach to a hostile ECM, thereby becoming invasive and proliferating in foreign tissues.[2] A typical example of anoikis resistance in tumour cells can be found in melanomas. Melanocytes are cells designed to produce melanin, the natural pigment in our skin, eyes and hair. Melanocytes located in the epidermis, the outer layer of the skin, cannot normally penetrate the underlying dermis and migrate because they do not express integrins capable of binding to collagen, which is the main component of the ECM of the dermis. Malignant melanocytes are capable of expressing collagen-binding integrins to survive in the dermis and migrate to the blood stream, becoming metastatic.[9]

Anoikis may be controlled *in vitro* by seeding a cell on a surface patterned with appropriate ECM proteins (i.e. the cells express integrins which can interact with specific epitopes on the ECM molecules), where cell attachment and spreading are guided, as described in detail in Section 1.6. The cells can attach only onto the domains which contain adsorbed ECM proteins. Hence, in order to achieve controlled patterned cell attachment using this approach, cell attachment proteins must adsorb only in the desired domains. The cell-attachment domains in the adsorbed proteins must also be presented to the cell in a bioactive conformation, in order to exhibit the appropriate integrin-binding sites on the surface. If the scale and geometry of the pattern is appropriate to generate the correct signalling and concordant mechanical stresses within the cell, anoikis can be avoided. Furthermore, the set of chemical and mechanical stimuli provided by a patterned surface can induce cell proliferation. A viable adherent cell on a surface exhibits a flattened shape, often with appendices extending away from the centre. A non-viable cell generally exhibits a rounded shape and no spreading.[10-12] As described in Section 1.6, state of the art cell patterning might allow for the control of the behaviour of multiple cell lines within an organised co-culture, to produce tissue-like materials.

In this Chapter, a variety of patterns obtained by polymer thin film dewetting were used for localised protein adsorption on surfaces. A primitive PMMA/PS dewetted pattern was first investigated, and the results compared to that obtained for the more effective brush-grafted patterns described in Chapter 5. Such patterns present protein-adsorbtive polystyrene holes in a background of highly densely packed, protein-repellent poly(poly(ethylene glycol) methyl ether methacrylate) (poly(PEGMA)) grafted chains. In this study, fibroblasts were seeded on the patterns to investigate their ability to provide controlled cell attachment. Two sets of patterns of holes with different diameters were studied. The presence or lack

of cell attachment and spreading was monitored, and the viability of the adhered cells was investigated by selective staining of an attached cell population.

6.2 Materials and methods

6.2.1 Protein tagging with fluorescent dye for visualisation

Fluorescein isothiocyanate (FITC, Sigma Aldrich) was used to tag bovine serum albumin (BSA, Sigma-Aldrich) and human fibrinogen (FGN, Sigma-Aldrich) as per the procedure recommended by Invitrogen Molecular Probes™. The isothiocyanate reacts readily with amine-containing amino acid sidechains within the protein molecules. Briefly, 10 mg of protein were dissolved in 1 mL of 0.1 M sodium bicarbonate buffer. Separately, 5 mg of FITC were dissolved in 0.5 mL of DMSO. 20 μL of the dye solution were slowly added to the protein solution with stirring at room temperature, which was then incubated at the same temperature for 1 hour. Finally, the conjugate was separated from the unreacted dye using a column packed with Sephadex® G-25 gel filtration media and 10 mM phosphate buffer saline (PBS; 140 mM NaCl, 3 mM KCl, pH 7.4) as eluent. The resulting protein solutions were estimated to be 1-2 mg mL^{-1} in concentration, depending on the volume of eluent used for each batch. The solutions were divided into 500 μL aliquots, wrapped in aluminium foil and frozen.

6.2.2 Protein adsorption experiments

The adsorption of protein molecules (collagen-I) and poly(amino acid) molecules (poly-L-lysine) on the dewetted PMMA/PS samples was

established by atomic force microscopy (AFM). The surfaces were incubated with either a 15 μg mL^{-1} solution of poly-L-lysine (Sigma-Aldrich) in PBS for 1 minute, or a 50 μg mL^{-1} solution of collagen-I (from rat tail, Sigma-Aldrich) in 0.02 M acetic acid for 1 h. They were then rinsed with 2 mL PBS and 2 mL Milli-Q® water and blown dry with nitrogen.

In the case of the patterns grafted with poly(PEGMA) brushes, fluorescently tagged BSA and FGN were used to observe qualitative differences between protein adsorption on different domains of the dewetted, grafted samples. In all protein adsorption experiments the protein solutions were thawed and used immediately, taking care not to expose the product to light, which may cause photobleaching. Any remaining solution was frozen again, but discarded after the second thawing if not used completely. Repeated freezing and thawing cycles can denature proteins. A drop (about 100 μL) of the 1-2 mg mL^{-1} solution was deposited on each patterned surface, and left to incubate for 3-4 hours at room temperature in the dark. The surfaces were then rinsed by immersing them a few times in fresh PBS buffer to remove the non-adsorbed protein, and then in Milli-Q® water to remove excess salts from the buffer used. Finally, the samples were gently blown dry with nitrogen. The presence of adsorbed protein was then established by optical fluorescence microscopy within 24 hours, and then *via* imaging of the surface using Tapping Mode™ AFM in air.

Characterisation *via* optical microscopy was performed using an Olympus BX61 optical microscope in differential interference contrast (DIC) mode. Visualisation of the patterns was carried out using both visible light, and in fluorescence mode (excitation wavelength 494 nm, emission wavelength 518 nm) in order to identify the areas where the fluorescently-tagged proteins had adsorbed.

6.2.3 Cell attachment experiments

Cell attachment onto the micropatterned surfaces was performed by Ms. Veronica Glattauer in the CSIRO laboratories in Clayton VIC. L929 mouse fibroblasts (cell line ATCC-CCL-1, Rockville, MD) were used to investigate attachment and spreading on samples. Cells were cultured in minimum essential medium (MEM) containing 10% foetal bovine serum and 1% non-essential amino acids. The samples were analysed with and without pre-adsorption of bovine vitronectin (kindly supplied by Ms Penny Bean, CSIRO North Ryde, VIC). Where pre-coating was required, the samples were covered with 50 μL of bovine vitronectin solution in PBS (600 μg mL^{-1}) and incubated at 37 °C for 4 hours. Subsequently the samples were washed three times with fresh PBS. Pre-coated and non pre-coated samples were then soaked in phosphate buffer saline (PBS) containing double strength antibiotic-antimycotic reagent (Invitrogen) for 2 hours at room temperature prior to cell culture.

Where pre-staining of cells was performed, a suspension of cells at a density of $1x10^5$ cells mL^{-1} was reacted with a fluorescent DiLC12 membrane stain (Molecular Probes) at 1μg mL^{-1} for 1 hour at 37 °C. Cells were then seeded at $2.8x10^4$ cells cm^{-2} in a non-treated tissue culture plate (Nunc, Denmark) containing the sample, which was then incubated at 37 °C, 5% CO_2 in air for 24 hours.

For the live/dead assay (Molecular Probes), cells were seeded at $2.8x10^4$ cells cm^{-2} for 24 hours as above, and the assay carried out using staining with calcein (live cells, green) and ethidium homodimer (dead cells, red) at concentrations of 2 μM and 4 μM, respectively.

Samples were imaged using a fluorescent Nikon inverted microscope (Eclipse T2000-U). Cell counts were performed on four different areas of

each image, and the resulting value reported as the average within a 95% confidence interval.

6.3 Results

6.3.1 Protein attachment on patterned surfaces

The first and most basic pattern investigated was a dewetted poly(methylmethacrylate) (PMMA) on polystyrene (PS). This basic model was expected to exhibit some protein adsorption contrast at low protein concentration.[13] Presented in Figure 6.1 is an AFM image of a dewetted hole in a PMMA/PS bilayer after incubation with a 15 μg mL^{-1} solution of poly-L-lysine for 1 min. The poly(amino acid) adsorbed only on the PS domain (white dots), and was not observed on the smooth PMMA surface.

This result indicated the presence of a difference in the relative poly(amino acid) adsorption onto the PMMA surface (lower) and the PS surface (higher) in the dewetted films at relatively low poly(amino acid) solution concentrations.

After the promising test with poly-L-lysine, the dewetted PMMA/PS model system was tested for collagen-I adsorption. Collagen-I is an ECM protein commonly found in connective tissue, adsorbed layers of which have been shown to mediate cell attachment *in vitro*.[14] Shown in Figure 6.2 are the inside of a dewetted hole (a), where the PS was exposed, and the area outside the hole (b), where the PMMA was present, after incubation with a 50 μg mL^{-1} solution of collagen-I for 1 hour. The conditions used for collagen-I were suggested by Prof. Jenny Gamble at the Centenary Institute (Sydney) as being optimal for the formation of a thick collagen layer on tissue culture PS, which is ideal for cell attachment. In Figure 6.2(a) it can be

seen that collagen-I adsorbed strongly on the untreated PS, in a similar way to tissue culture PS, resulting in a thick layer of microfibrils. Under these conditions, there was not a large observable difference between collagen-I adsorption on PMMA and PS, although collagen-I was clearly present on the PMMA layer at a reduced surface concentration, i.e. at a lower fibril density (Figure 6.2(b)). Interestingly, the microfibrils formed by the collagen-I on PMMA were thicker than those formed on the PS surface. This simple test highlighted that although PMMA and PS did show differences in their protein adsorption properties, the contrast was not strong enough to create clear protein patterning under realistic biological working conditions, i.e. protein concentration of 50 μg mL^{-1} to a few mg mL^{-1}.

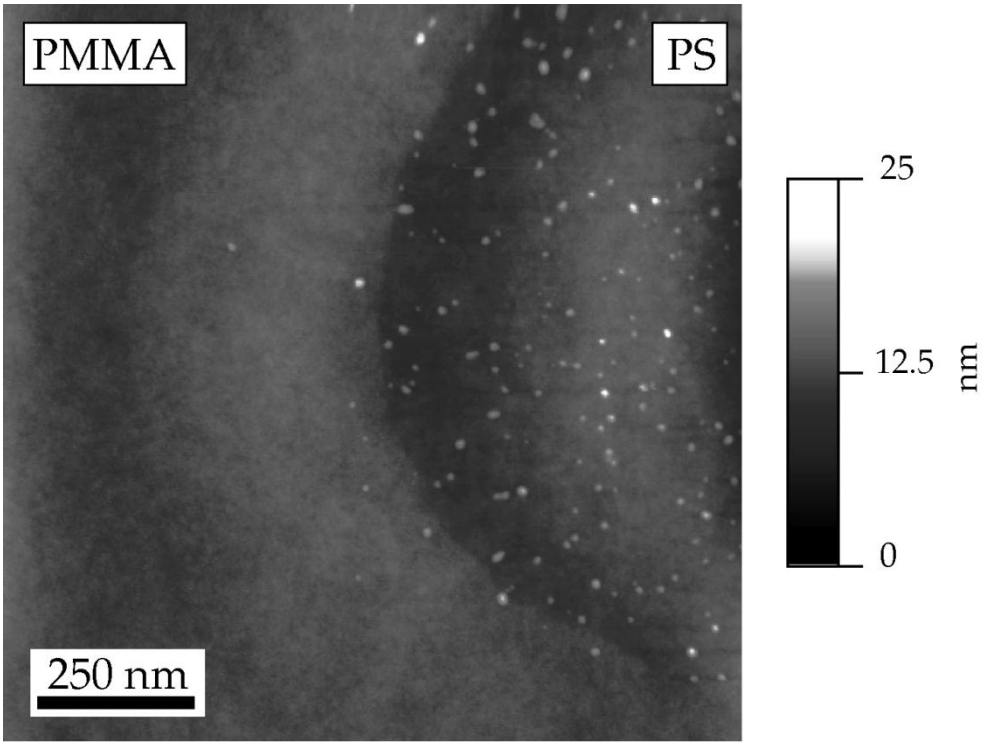

Figure 6.1 AFM topography image of the edge of a dewetted hole in a PMMA/PS bilayer incubated with a 15 μg mL^{-1} solution of poly-L-lysine in PBS. The poly(amino acid) adsorbed only on the PS domain (white dots), and not on the PMMA (smooth surface).

The investigation was then focused on the poly(PEGMA) grafted patterns, which were expected to have enhanced protein adsorption contrast compared to PMMA/PS. The samples were incubated with fluorescein tagged protein solutions. As in Section 3.3.9, two different proteins (BSA and FGN) were chosen because of their different structure, in order to evaluate the adsorption behaviour of a range of proteins. FGN is elongated and may form fibrils, while BSA has a more compact globular shape. Both proteins have a net positive charge in the pH 7.4 buffer used, since their isoelectric points are 4.5[15] and 5.5[16] respectively. The protein solution concentrations used were 1-2 mg mL^{-1} and the incubation periods were 3-4 hours.

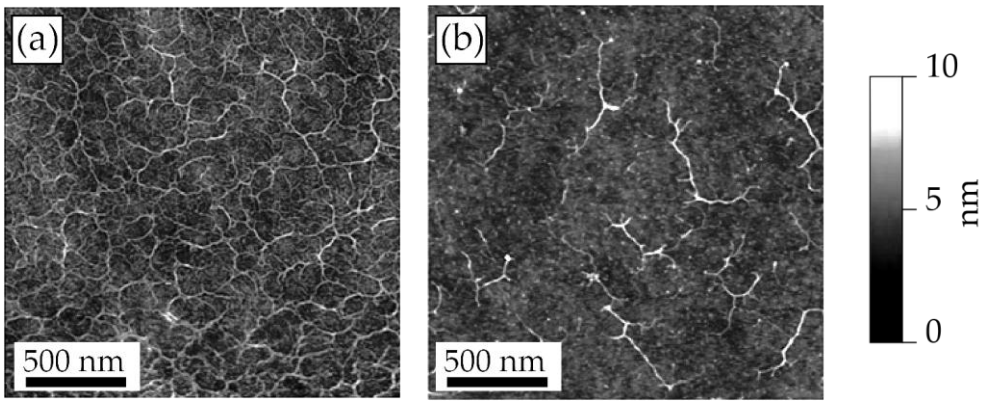

Figure 6.2 AFM topography images of (a) the PS domain inside a dewetted hole and (b) the PMMA background outside the dewetted holes, after incubation of the surface with a 50 μg mL^{-1} solution of collagen-I. The protein collected in microfibrils, and densely coated the PS surface. The adsorption on the PMMA surface was much lower, as indicated by the lower number of microfibrils present on the surface.

Presented in Figure 6.3(a,b) and Figure 6.4 are optical micrographs of macroinitiator films at different stages of dewetting, grafted with a 60 nm thick poly(PEGMA) layer, along with fluorescence micrographs of the samples incubated with the fluorescent protein solutions. The strong

contrast in the green fluorescent signal demonstrated that FGN (Figure 6.3) and BSA (Figure 6.4) were only adsorbed where the underlying PS was exposed, and that the adsorption was undetectable in the areas where poly(PEGMA) graft layers were present.

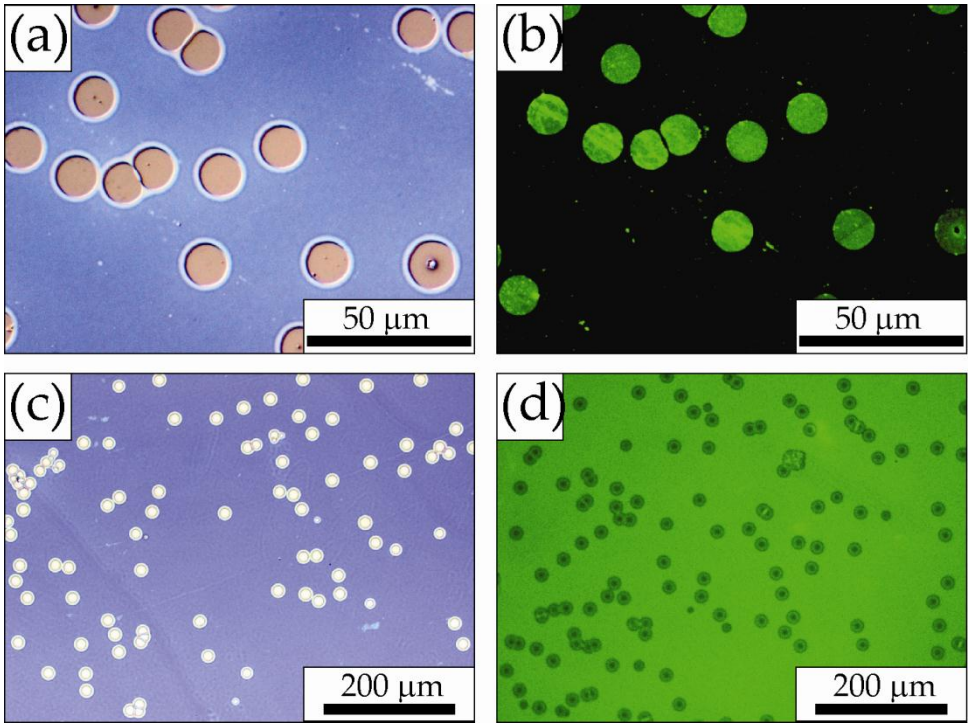

Figure 6.3 (a) Optical micrographs and (b) fluorescence micrographs of a dewetted pattern grafted with a 60 nm thick poly(PEGMA) brush, incubated with a 2 mg mL^{-1} solution of FITC tagged human fibrinogen. The protein adsorbed only where the underlying polystyrene was exposed. The exposure time in fluorescence mode was 10 s. Micrographs (c) and (d) show, respectively, an optical and a fluorescence micrograph of a control sample of patterned macroinitiator on PS without grafted poly(PEGMA), incubated with a 200 µg mL^{-1} solution of FITC-fibrinogen for 10 min and rinsed with PBS and water. No fluorescence contrast was apparent on the pattern. The exposure time in fluorescence mode was 600 ms.

Analysis of the data showed that the grafting was successful on all of the different dewetted patterns, and clearly demonstrated that the presence

of a graft layer allowed for the localisation of different types of proteins in the dewetted domains.

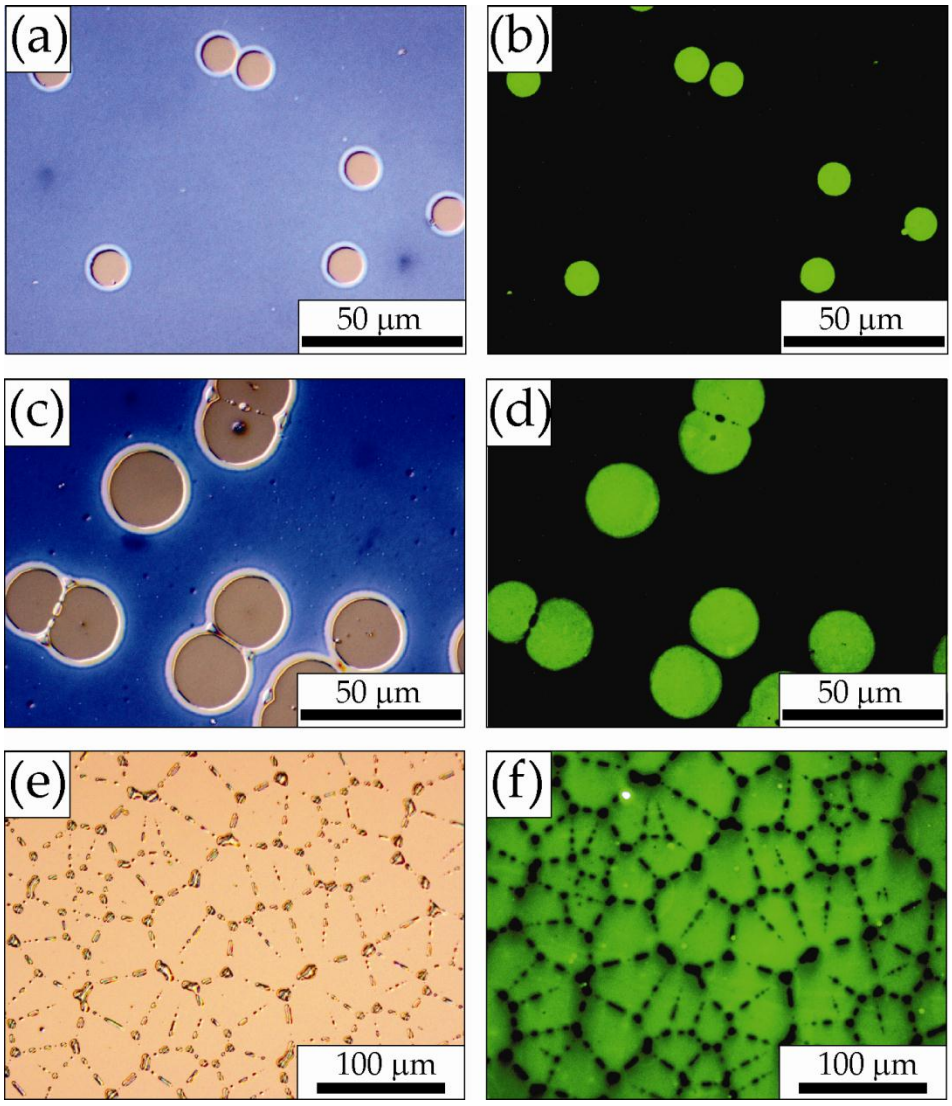

Figure 6.4 (a, c, e) Optical micrographs and (b, d, f) fluorescence micrographs of dewetted patterns grafted with a 60 nm thick poly(PEGMA) brush, incubated with a 1 mg mL^{-1} solution of FITC tagged bovine serum albumin in PBS, for increasing dewetting times. The protein (green fluorescent) adsorbed only where the underlying polystyrene was exposed. The exposure time in fluorescence mode was 10 s.

Further support for this is demonstrated in Figure 6.3(c,d) in which micrographs are presented from a control experiment carried out with a

non-grafted macroinitiator dewetted on PS, incubated with a 200 μg mL^{-1} solution of FITC-fibrinogen for 10 min. It is clear from the fluorescence micrograph (Figure 6.3(d)) that without the presence of the poly(PEGMA) graft layer, the protein molecules adsorbed all over the surface. This control experiment confirmed that the poly(PEGMA) brush was effective in significantly reducing the adsorption of protein molecules.

The localised protein adsorption in the holes was characterised further using AFM imaging. Presented in Figure 6.5 is a three-dimensional AFM image of a dewetted hole in a pattern grafted with a poly(PEGMA) brush with a dry thickness of approximately 60 nm.

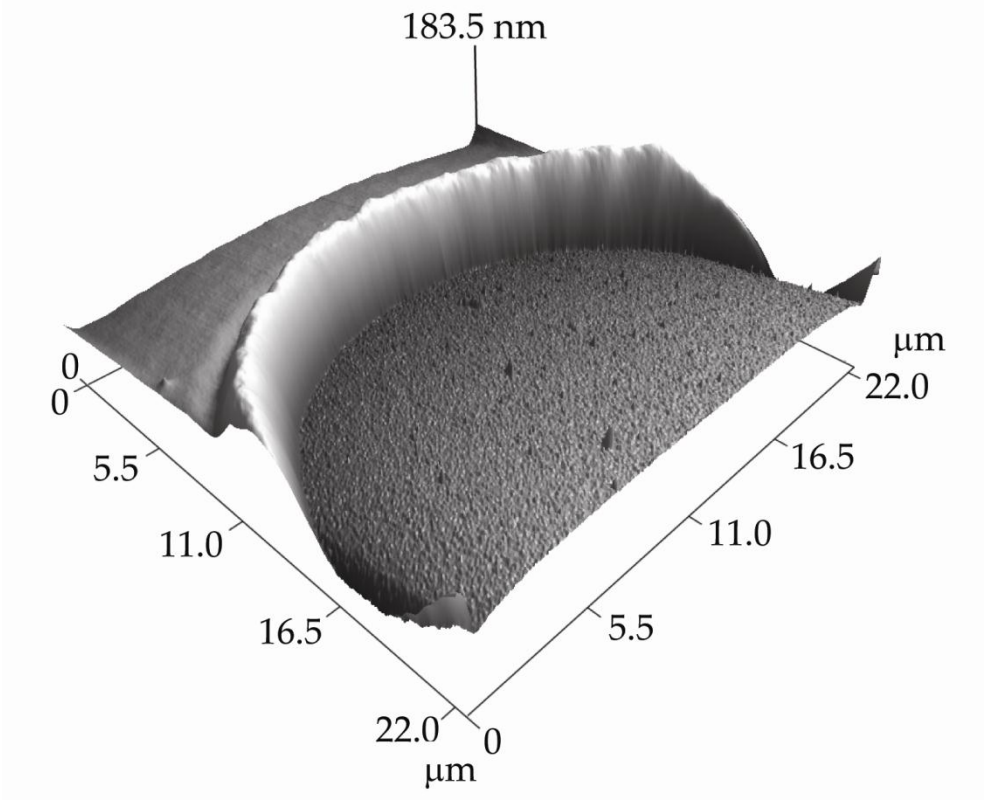

Figure 6.5 AFM three-dimensional topography image of a dewetted hole in a pattern grafted with a 60 nm thick poly(PEGMA) brush. The image shows the difference between the very smooth brush and the polystyrene surface, which contained an adsorbed albumin layer and was therefore significantly rougher. The hole is surrounded by the characteristic rim of accumulated polymer on the dewetting front.

The sample was imaged after the fluorescence microscopy characterisation (see above). The surface was smooth outside the hole, where the brush was present. However, inside the hole, where the underlying polystyrene was exposed to the protein solution (BSA), the surface roughness was much greater. The topography of this surface was very different from that of a clean PS film, which is featureless. The difference in topographies indicated that indeed protein molecules were adsorbed inside the holes on the dewetted poly(PEGMA) grafted samples. The RMS roughness for a flat PS film, estimated by analysis of the AFM images, was 220 ± 24 pm. The value obtained for the poly(PEGMA) grafted surface was 960 ± 140 pm, whilst for the protein-coated PS surface, a value of 1700 ± 50 pm was obtained. This quantitative measurement showed that the roughness of the protein-coated PS was much higher than both the flat PS and the protein-repellent poly(PEGMA) brush.

6.3.2 Cell attachment on patterned surfaces

Cell attachment experiments on the micropatterned surfaces were performed by Ms. Veronica Glattauer in the CSIRO laboratories in Clayton VIC. The first experiments using L929 fibroblasts were performed on the three separate components of the poly(PEGMA) grafted patterned multilayer, in order to confirm the expected behaviour. Presented in Figure 6.6 are fluorescence micrographs of fibroblasts attached onto PS (a-b), macroinitiator (c-d) and poly(PEGMA) 60 nm thick brush (e-f) films, respectively with and without vitronectin pre-adsorption. In both cases, the poly(PEGMA) brush was very effective in reducing the attachment of fibroblasts. In Figure 6.6(a), some loosely adhering cell aggregates were visible. The presence of aggregates of this type is typical for surfaces for which cell attachment is very low, such as commercial Thermofisher

Hydrocell™ and Corning® Ultralow Cell Attachment surfaces. On these surfaces, cells tend to aggregate in colonies that easily detach from the surface.

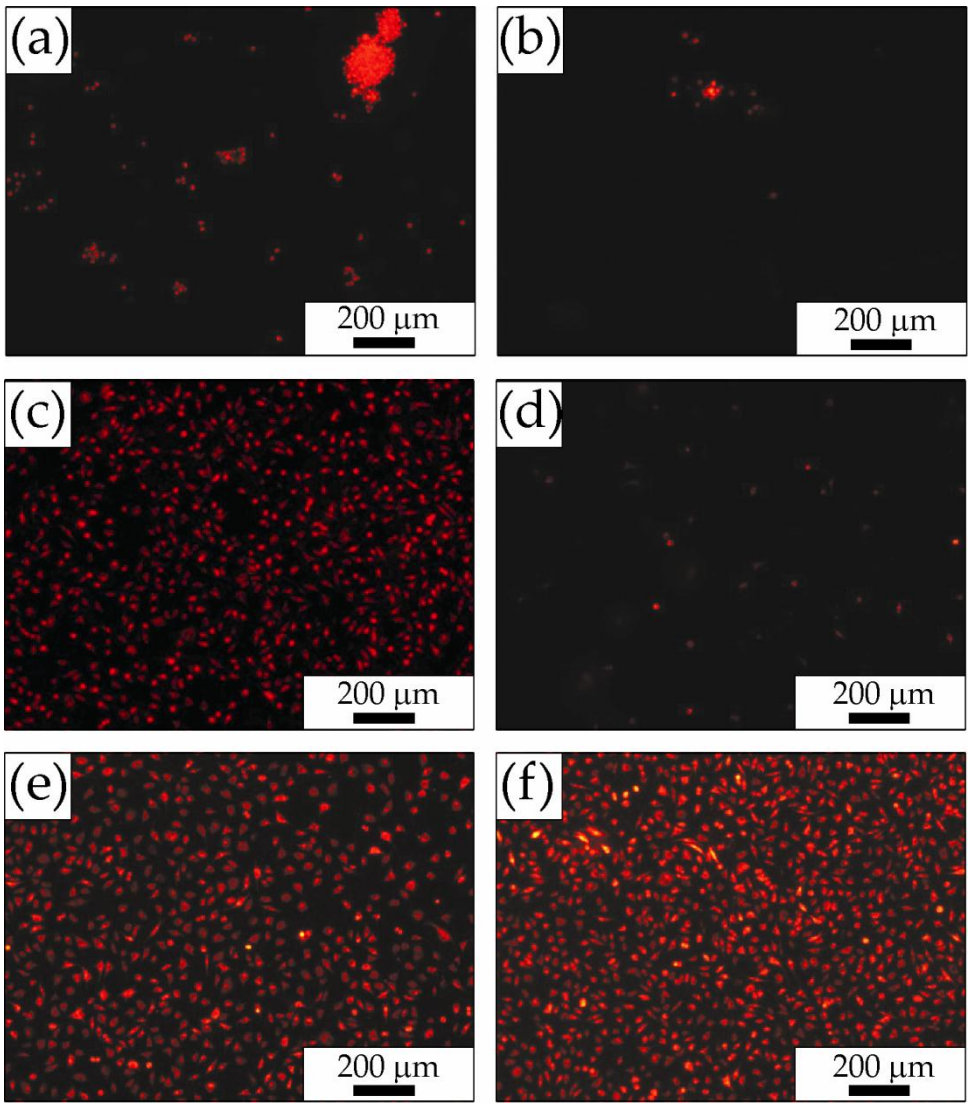

Figure 6.6 Images obtained for L929 fibroblast attachment on the different components of the patterned multilayer. Cell attachment was carried out on (a) a flat poly(PEGMA) brush with vitronectin pre-coating, (b) a flat poly(PEGMA) brush without vitronectin pre-coating, (c) a PS film with vitronectin pre-coating, (d) a PS film without vitronectin pre-coating, (e) a macroinitiator film with vitronectin pre-coating and (f) a macroinitiator film without vitronectin pre-coating. The cell membranes appear in red as a result of DiLC12 staining. Cell attachment was carried out over 24 hours.

The few single cells visible on the poly(PEGMA) brush had a rounded shape, indicating no functional adhesion onto the surface. The low cell attachment properties of the poly(PEGMA) brush becomes even more obvious when Figure 6.6(a) and Figure 6.6(c) are compared. Under the same conditions, strong cell attachment and spreading was observed on the PS film with a pre-adsorbed vitronectin coating, while little attachment was observed where no pre-adsorption was employed. The average number of attached fibroblasts on vitronectin-coated PS, 470 ± 80 cells mm^{-2}, far exceeded that on uncoated PS, 26 ± 5 cells mm^{-2}.

The cell attachment on the macroinitiator film was also greater than on poly(PEGMA), particularly when no vitronectin pre-coating was employed. The average number of attached cells was 360 ± 80 cells mm^{-2} with vitronectin pre-coating and 590 ± 40 cells mm^{-2} without pre-coating. From these observations, the best cell attachment contrast on the patterned coating was expected for vitronectin pre-coating. This procedure was expected to dramatically improve the cell attachment on the underlying PS surface in the holes whilst having little impact on the low cell attachment properties of the poly(PEGMA) grafted regions of the pattern.

The fibroblast attachment experiments were performed on two different patterned substrates, both grafted with a poly(PEGMA) brush of approximately 60 nm thickness (dry), but with different hole sizes: 20 μm diameter and 40 μm diameter. Presented in Figure 6.7 is a fluorescence micrograph of fibroblasts seeded onto a dewetted pattern with 20 μm holes. After 24 hours, no selective cell attachment was observed, i.e. rounded cells could be found all over the surface, both on the poly(PEGMA) brush and on the vitronectin-coated PS domains. A rounded cell shape indicates non-functional adhesion. Fibroblasts were able to spread only when they could bridge over adjacent 20 μm holes (red arrows).

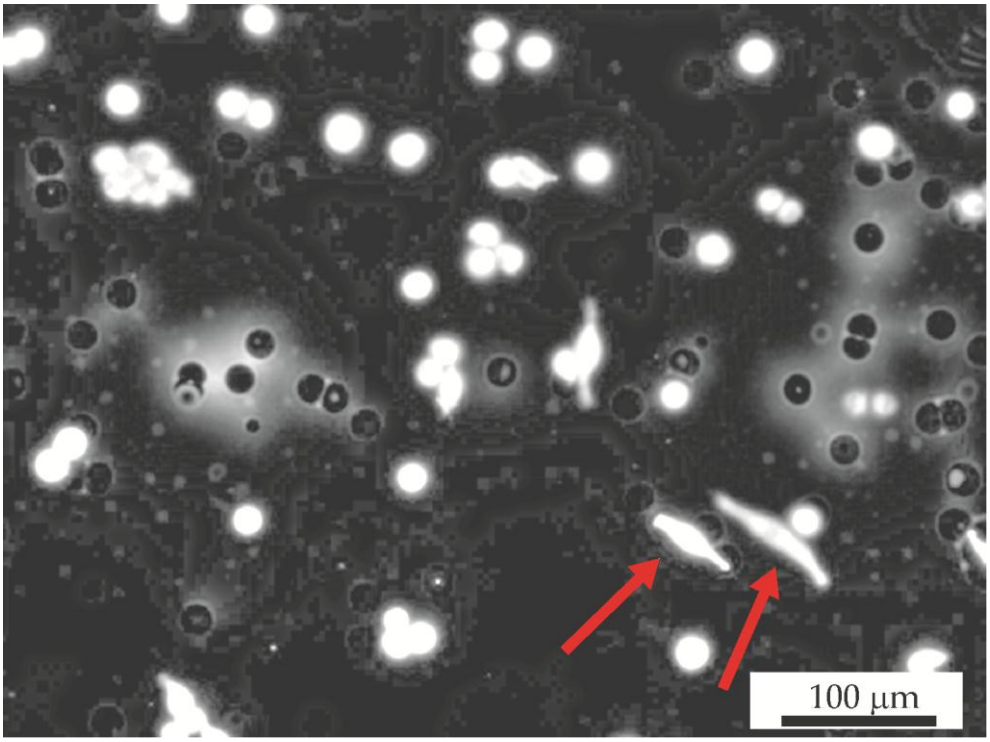

Figure 6.7 Fluorescence micrograph showing fibroblasts adhesion on a brush-grafted pattern with 20 µm diameter holes, pre-coated with vitronectin. The image was converted to grey scale to better visualise both the hole rims and the fluorescent cells. The red arrows indicate cells spreading over multiple holes.

The situation was very different on the patterns with larger holes. Presented in Figure 6.8 is a fluorescence micrograph of fibroblasts attached onto a dewetted pattern with 40 µm holes. The fibroblasts were not only localised almost exclusively inside the PS holes, but also showed obvious signs of spreading (red arrows) within the holes to cover the vitronectin coating: most cells showed a bright centre and darker regions which stretched over the bottom of the holes. The darker regions were likely podia, appendices used for spreading and moving through the establishment of focal adhesion points. Cell spreading is a strong indication of interaction with the surface, and of good viability. Only a small number of cells were

present on the poly(PEGMA) brush area surrounding the holes and showed a rounded morphology, consistent with non-functional adhesion.

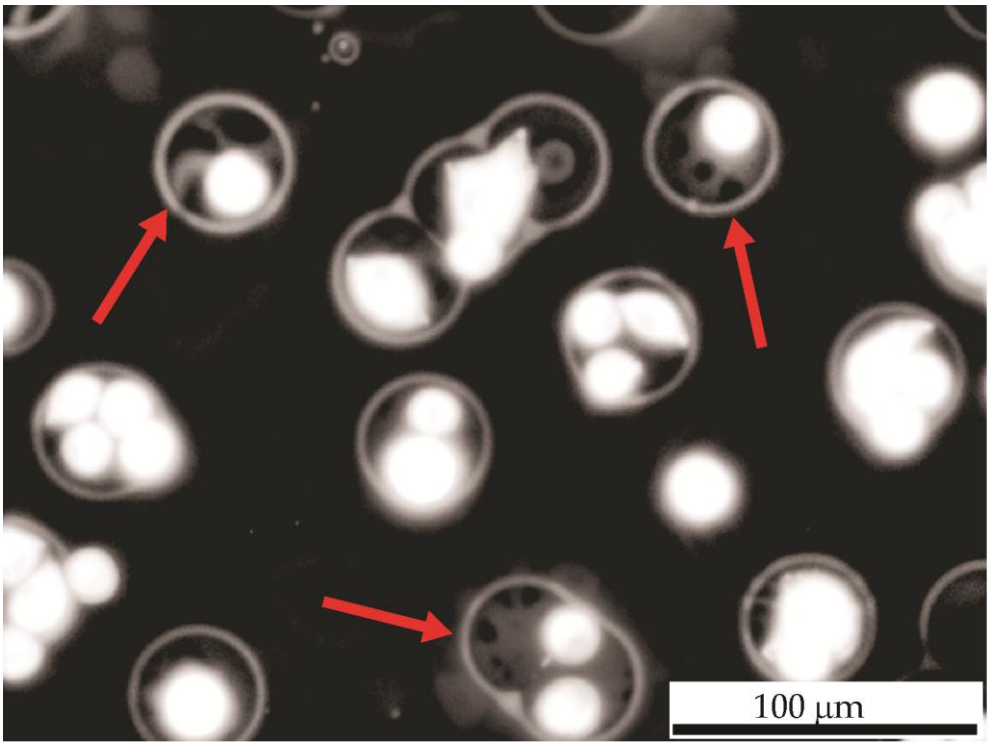

Figure 6.8 Fluorescence micrograph showing fibroblast adhering onto a brush-grafted pattern with 40 μm diameter holes, pre-coated with vitronectin. The image was converted to grey scale to better visualise both the hole rims and the fluorescent cells. The red arrows indicate the spreading cells.

To further investigate the viability of the patterned fibroblasts, a live/dead staining procedure was employed. In this technique, two different dyes were used, a green one which stains viable cells (calcein) and a red one which stains dead cells (ethidium homodimer). Presented in Figure 6.9 are bright field and fluorescence micrographs obtained for this staining protocol on fibroblasts adhered on a pattern with a grafted poly(PEGMA) layer with a thickness (dry) of approximately 60 nm, surrounding 40 μm diameter holes. The fibroblasts adhered only inside the PS holes, seen from the comparison of micrographs (a) and (b), which were obtained from the same

sample area. All the adherent cells fluoresced green, indicating that they were viable. As observed in Figure 6.8(c), the cells had spread morphology when they were not densely packed in the vitronectin-coated PS domains. Only very few cells were stained with the red fluorescent dye, indicating that they were non-viable (Figure 6.9(c)).

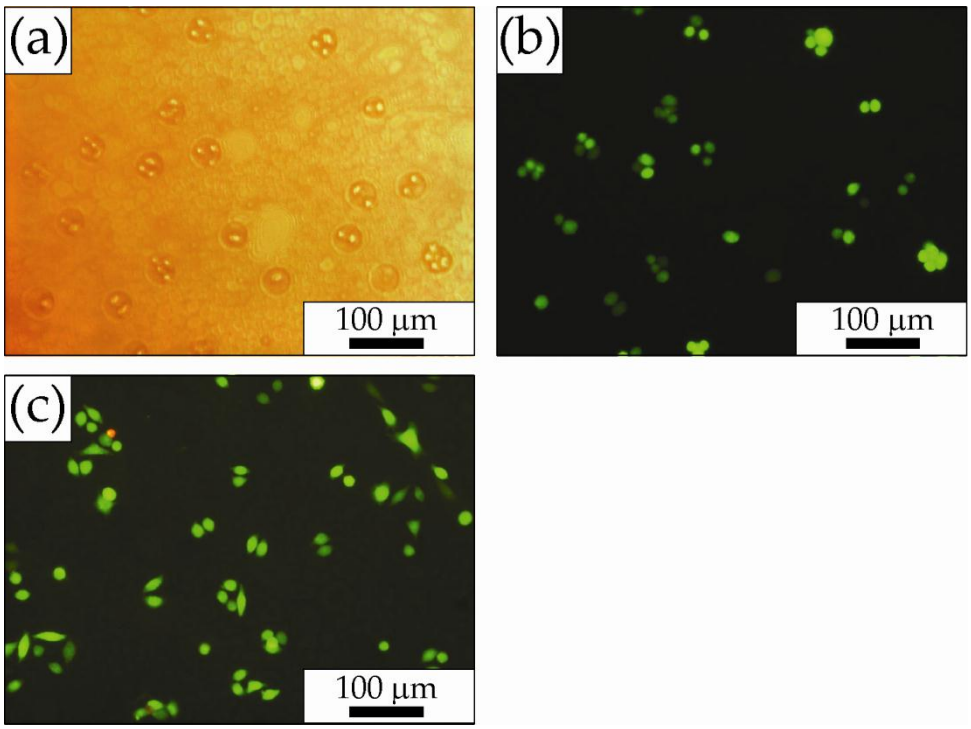

Figure 6.9 (a) Optical micrograph and (b,c) fluorescence micrographs of fibroblasts adhered on a poly(PEGMA)-grafted pattern of 40 µm diameter holes. The cells adhered only inside the PS holes which were pre-coated with vitronectin, as shown in images (a) and (b), taken in the same area of the sample. The live/dead staining revealed live cells in green and dead cells in red. All cells, except for a few exceptions, were alive, and were well spread when not clustered too densely within the vitronectin-coated PS domains.

6.4 Discussion

The first system investigated was a basic pattern obtained by dewetting a PMMA film on a PS film, which was first investigated by Neto.[13]

In Neto's study, differential adsorption between the dewetted PMMA film and the underlying PS layer was demonstrated for the patterning of immunoglobulin G from a low concentration solution (15 μg mL^{-1}). In this study, selective adsorption of poly-L-lysine on the PS domains, inside the dewetted holes, from a low concentration solution (1 μg mL^{-1}, 1 minute) (Figure 6.1) was observed for the same PMMA/PS system. Selective protein adsorption on a patterned surface is known to be dependent on the protein concentration and the incubation time.[17] Low protein concentrations favour greater differences in protein adsorption on the different surface domains, but the adsorbed amount of protein deposited on the adsorptive domains can be limited. This was clear when analysing the results of collagen-I adsorption on the PMMA/PS pattern (Figure 6.2). Here, higher protein solution concentration and longer incubation time (50 μg mL^{-1}, 1 hour) were used. The protein was visible in AFM images on both domains (PMMA and PS), though with a higher surface concentration on the PS domains.

The results for the simple PMMA/PS system were compared with the novel poly(PEGMA) grafted system described in Chapter 5. The poly(PEGMA)-grafted, patterned coating was extremely efficient in controlling the adsorption of BSA and FGN into localised domains. The fluorescence microscopy characterisation of fluorescently tagged proteins on the prepared surfaces, as well as the AFM imaging, showed a very sharp contrast between adsorption on the PS domains and the areas where a poly(PEGMA) brush was grafted. The brush swelled in the aqueous buffer used to prepare the protein solutions, and became highly resistant to compression and penetration by proteins, as a result of the high grafting density of the poly(PEGMA) molecules. The hydrophobic PS on the other hand promoted the physisorption of proteins, which often contain extensive hydrophobic domains. The adsorption of a protein on PS is also driven by the entropy gain that results from the liberation of the solvation water highly

organised on both the PS and the protein surfaces.[18] A detailed description of the interaction between proteins and polymer surfaces can be found in Section 1.4. The protein solution concentrations used were 1-2 mg mL^{-1}, and the incubation periods were 3-4 hours, conditions that should strongly facilitate the adsorption of proteins in comparison to the ones used for PMMA/PS, indicating the efficacy of the coatings developed in this work in patterning different proteins.

As the patterns were shown to be able to control the localised adsorption of proteins, they were expected to also be good candidates for controlling the adhesion of cells. Fibroblasts are cells from the connective tissue, and like all solid tissue cells they need to adhere and spread to be fully functional. Cells can adhere on a surface when the appropriate anchoring points are presented, i.e. the correct ECM proteins exposing cell binding epitopes. Surfaces with very high protein affinity may be coated in adhesive ECM from the culture medium used during cell culture. Minimum essential media (MEM) conventionally contain a certain concentration of blood serum, where adhesive ECM proteins such as vitronectin and fibronectin are abundant. Surfaces that have lower capacity for protein adsorption may not be optimally coated with adhesive ECM proteins from the serum. In this case, the surface can be pre-coated with a pure solution of the desired ECM protein, prior to cell seeding. To cover both possible scenarios in this investigation, fibroblast adhesion was tested on the three separate components of the patterned multilayers developed in Chapter 5, i.e. PS, macroinitiator and poly(PEGMA) brush, with and without pre-coating with vitronectin. Vitronectin was chosen because it is one of the proteins essential to cell adhesion, it is abundant in blood serum and many other tissues, and it adsorbs readily on many surfaces.[19-21]

The poly(PEGMA) brush was capable of reducing cell attachment to very low levels in both cases, based on its very low affinity for protein

adsorption and therefore cell attachment.[22, 23] Cell attachment was prevalent on the macroinitiator surface, particularly on the sample that was not pre-coated with vitronectin. This suggested that proteins could readily adsorb on this polymer surface, so that even the small concentration of ECM proteins present in the serum in the MEM alone facilitated cell adhesion. The enhanced cell adhesion when no vitronectin pre-coating was employed may be explained with different activity of vitronectin and the other ECM proteins after adsorption. In the pre-coated sample, the large amount of vitronectin present on the surface would have governed the cell adhesion, while in the non pre-coated sample, more active ECM proteins could have intervened in the cell adhesion. Interestingly, on the PS film, which was shown to strongly adsorb protein molecules (see Section 3.3.9), very poor cell attachment was observed when no vitronectin was pre-adsorbed. Polystyrene conventionally used in culture dishes is treated with plasma discharge to significantly improve cell adhesion.[24, 25] The plasma discharge treatment was found to partially oxidise the polymer surface and make it more hydrophilic.[26] Our experiments showed that untreated PS was less efficient in adhering cells from growth media.[27] As shown in Figure 6.6, the PS surface became highly suitable for cell adhesion once it was pre-coated with vitronectin. Many factors have to be taken into consideration to explain this result. Steele *et al.*[28] demonstrated that the adsorption of vitronectin on tissue culture PS facilitated greater cell attachment than on untreated PS. Vitronectin adsorption on untreated PS can also be reduced by competing adsorption of other proteins present in blood serum and conventional growth media, such as fibrinogen, fibronectin and albumin, while this effect is of little importance on tissue culture PS.[28, 29] Therefore, when vitronectin was present in low concentrations and in a complex mixture of components, such as in standard cell culture MEM, it could not adequately cover untreated PS films, and hence cells were less able to attach. On the other

hand, when the untreated PS surface was incubated with a high concentration solution of pure vitronectin (in this work 600 μg mL^{-1} for 4 h), the higher adsorbed amount or optimal adsorbed conformation of the protein allowed for cell attachment.

The high protein adsorption achievable by pre-adsorbing vitronectin on PS was also likely to control the preservation of protein conformation and full function after adsorption on a surface. The integrin-binding epitopes in the adsorbed ECM proteins must be exposed to the cells, and not buried in the protein supramolecular assembly. Depending on the protein-surface interactions, this may not always be true. Proteins adsorbed on a surface may radically change their tertiary and quaternary structures,[30-34] and may even undergo more severe conformational changes such as the disruption of their stable secondary structures (α-helixes and β-sheets).[35, 36] An example of such behaviour can be observed when comparing Figure 6.2 (a) and (b). The structure of collagen-I microfibrils in the dry state differed when the protein was adsorbed on PMMA or PS. The microfibrils were thicker on PMMA, and bead-like structures were apparent, which are characteristic of another type of collagen (collagen VI).[32] These morphologic differences were indications that the collagen had a different structure depending on whether it was adsorbed on PS or PMMA.

The lack of exposed integrin-binding sites may cause cell anoikis even when the appropriate ECM proteins are present on the surface. Pre-incubating a surface with a high concentration of ECM proteins, such as vitronectin, for sufficient time to achieve maximum surface coverage, enhances protein-protein interaction and ensures the formation of protein clusters. Clustered proteins are more likely to retain their functional configuration and expose integrin-binding sites. The formation of protein clusters on a surface has been observed for vitronectin,[37, 38] as well as other ECM proteins such as fibronectin.[39, 40] Toromanov *et al.*[37] investigated cell

adhesion on surfaces pre-incubated with different concentrations of vitronectin. Using AFM, they showed that when moderately hydrophobic poly(ethylacrylate) films were incubated with low concentration vitronectin solutions, the proteins adsorbed as isolated molecules, while when the films were incubated with high concentration solutions, the proteins formed clusters of 3-5 molecules. They also showed that fibroblast adhesion and spreading was greater on the surfaces that were covered in vitronectin clusters rather than isolated molecules, indicating a higher abundance of integrin-binding sites on the clusters. Hull *et al.*[40] observed a similar behaviour when investigating the adsorption of fibronectin on mica surfaces. Using AFM, they showed that fibronectin adhered as isolated molecules from low concentration solutions and as extended clusters (islands) from high concentration solutions. Using time of flight secondary ion mass spectroscopy and AFM force measurements using probes modified with integrin peptides, they then evaluated the abundance of integrin-binding sites exposed to the solution after protein adsorption. They showed that clustered fibronectin was more likely to retain its functional structure and ability to adhere cells by presenting the appropriate integrin-binding sites.

Once the best cell adhesion conditions for the system were established, the influence of the patterns in localising cell attachment could be thoroughly investigated. The first important observation that must be discussed is the influence of the hole size on cell adhesion. No selective cell adhesion was observed on the patterns with smaller holes (20 μm diameter), and cells could be found all over the surface, regardless of the different pattern domains. All cells had a rounded shape, indicating poor attachment and most likely poor longer term viability. Good control over the adhesion of fibroblasts was observed on the patterns with larger holes (40 μm diameter). The cells adhered almost exclusively on the vitronectin-coated domains, and showed good spreading. This was a clear indication of control

over the cell behaviour. When not spread, mouse fibroblasts had an average size of 20 μm, and hence in the 20 μm pattern there was insufficient surface area available to allow spreading of the cells. The only exceptions were those areas where the protein-coated domains were close enough for the cells to bridge between them (see Figure 6.7). In such cases, the fibroblasts would elongate greatly to increase their contact area. Instead, when the domains were large enough, as in the 40 μm patterns, the fibroblasts could spread within each domain and strongly attach to the surface. The ability to control cell spreading on protein domains of different sizes has been well documented, and was thoroughly described in Section 1.6.

The coatings developed here were not only useful for the patterning of cells, but they allowed for good cell viability, which is crucial for biomedical applications. The spreading of the cells in the pattern holes (Figure 6.8) was a strong clue for good cell viability. Dead or dying cells tend to assume a rounded shape, while healthy cells actively interact with their ECM and extend their appendices in order to reach distant anchoring points. The formation of focal adhesion points is of the utmost importance for survival, because it allows the rise of mechanical stresses in the cell framework, which are transduced in chemical signals that can suppress the programmed death (anoikis). Section 1.6 collects a large number of references on the subject. The viability of cells adhered on the 40 μm patterns was further confirmed by live/dead staining. The cells all showed green fluorescence, apart from a few exceptions, indicating that they were all alive. From Figure 6.9(c) it is clear that cells could spread on the vitronectin coated domains only if the site was not overly crowded. This allows a deeper understanding of the cells' behaviour on the surfaces investigated. It appears that fibroblasts could have a low degree of spreading yet maintain good viability, but only if they had a high number of neighbouring cells to physically interact with. It is known that cells gather chemical and

mechanical cues not only from their ECM, but also from their neighbouring cells, so they might be able to suppress anoikis by having either or both stimuli.[1, 41] In the results reported in Figure 6.8 andFigure 6.9, both these scenarios were observed.

6.5 Summary

The present Chapter reports the investigation of protein adsorption and cell adhesion on polymer bilayers patterned by dewetting, to form surfaces with randomly distributed, protein-adsorptive holes. The main investigation focused on the patterned coatings described in detail in Chapter 5. The first pattern investigated was a dewetted PMMA/PS, which showed good protein adsorption contrast between the PS domains and the PMMA background for poly-L-lysine at low solution concentration. The system was not as effective in patterning collagen-I under conditions routinely used to prepare cell-adhesive coatings. Instead, the patterns grafted with poly(PEGMA) described in Chapter 5 showed selective protein adsorption in the PS holes from high protein solution concentrations, as seen in the AFM and fluorescence microscope investigations with albumin and fibrinogen. The results were consistent for all the different pattern scales (i.e. different PS holes size) investigated. For cell studies, cell-adhesive vitronectin was pre-patterned in the PS holes, ensuring good coverage and likely forming protein clusters able to expose the integrin binding epitopes. Two different pattern scales were tested: one with 20 μm diameter holes, the size of which was comparable to the one of the fibroblasts, and one with 40 μm diameter holes, much bigger than the size of the fibroblasts. Effective cell patterning of fibroblasts was obtained only when the dewetted holes were larger than the cells and provided space for cell spreading. The cells adhered

selectively in the large PS domains, and showed good viability, as ascertained by optical microscopy observation of cell spreading, as well as by selective live/dead staining.

The coatings developed here could be used as random arrays of microwells for single-cell studies or growth of cell colonies with well defined size. As described in Chapter 5, the grafted brush contains end groups which may be modified chemically in order to selectively attach a peptide for the localisation of a second type of cell around the holes, in order to create a geometrically controlled cell co-culture for tissue engineering.

6.6 References

1. Chiarugi, P.; Giannoni, E., Anoikis: A necessary death program for anchorage-dependent cells. *Biochemical Pharmacology* **2008**, *76* (11), 1352-1364.
2. Gilmore, A. P., Anoikis. *Cell Death and Differentiation* **2005**, *12*, 1473-1477.
3. Nagaprashantha, L. D.; Vatsyayan, R.; Lelsani, P. C. R.; Awasthi, S.; Singhal, S. S., The sensors and regulators of cell-matrix surveillance in anoikis resistance of tumors. *International Journal of Cancer* **2011**, *128* (4), 743-752.
4. Comoglio, P. M.; Boccaccio, C.; Trusolino, L., Interactions between growth factor receptors and adhesion molecules: breaking the rules. *Current Opinion in Cell Biology* **2003**, *15* (5), 565-571.
5. Danen, E. H. J.; Yamada, K. M., Fibronectin, integrins, and growth control. *Journal of Cellular Physiology* **2001**, *189* (1), 1-13.
6. Margadant, C.; Sonnenberg, A., Integrin-TGF-beta crosstalk in fibrosis, cancer and wound healing. *EMBO Reports* **2010**, *11* (2), 97-105.
7. Douma, S.; van Laar, T.; Zevenhoven, J.; Meuwissen, R.; van Garderen, E.; Peeper, D. S., Suppression of anoikis and induction of metastasis by the neurotrophic receptor TrkB. *Nature* **2004**, *430* (7003), 1034-1040.
8. Simpson, C. D.; Anyiwe, K.; Schimmer, A. D., Anoikis resistance and tumor metastasis. *Cancer Letters* **2008**, *272* (2), 177-185.
9. Montgomery, A. M. P.; Reisfeld, R. A.; Cheresh, D. A., Integrin $\alpha v\beta 3$ rescues melanoma cells from apoptosis in three-dimensional dermal

collagen. *Proceedings of the National Academy of Sciences of the United States of America* **1994**, *91* (19), 8856-8860.
10. Doonan, F.; Cotter, T. G., Morphological assessment of apoptosis. *Methods* **2008**, *44* (3), 200-204.
11. Kerr, J. F. R.; Wyllie, A. H.; Currie, A. R., Apoptosis - Basic biological phenomenon with wide-ranging implications in tissue kinetics. *British Journal of Cancer* **1972**, *26* (4), 239-257.
12. Re, F.; Zanetti, A.; Sironi, M.; Polentarutti, N.; Lanfrancone, L.; Dejana, E.; Colotta, F., Inhibition of anchorage-dependent cell spreading triggers apoptosis in cultured human endothelial cells. *Journal of Cell Biology* **1994**, *127* (2), 537-546.
13. Neto, C., A novel approach to the micropatterning of proteins using dewetting of polymer bilayers. *Physical Chemistry Chemical Physics* **2007**, *9* (1), 149-155.
14. Behring, J.; Junker, R.; Walboomers, X. F.; Chessnut, B.; Jansen, J. A., Toward guided tissue and bone regeneration: morphology, attachment, proliferation, and migration of cells cultured on collagen barrier membranes. A systematic review. *Odontology* **2008**, *96* (1), 1-11.
15. Kubota, Y.; Ueki, H., Determination of isoelectric point of bovine plasma albumin by cellulose acetate paper electrophoresis. *Journal of Biochemistry* **1968**, *64* (3), 405-&.
16. Triantap.E; Triantap.Dc, Amino acid composition of human fibrinogen anticoagulant derivatives. *Biochemical Journal* **1967**, *105* (1), 393-400.
17. Lau, K. H. A.; Bang, J.; Kim, D. H.; Knoll, W., Self-assembly of protein nanoarrays on block copolymer templates. *Advanced Functional Materials* **2008**, *18* (20), 3148-3157.
18. Browne, M. M.; Lubarsky, G. V.; Davidson, M. R.; Bradley, R. H., Protein adsorption onto polystyrene surfaces studied by XPS and AFM. *Surface Science* **2004**, *553* (1-3), 155-167.
19. Bale, M. D.; Wohlfahrt, L. A.; Mosher, D. F.; Tomasini, B.; Sutton, R. C., Identification of vitronectin as a major plasma-protein adsorbed on polymer surfaces of different copolymer composition. *Blood* **1989**, *74* (8), 2698-2706.
20. Wilson, C. J.; Clegg, R. E.; Leavesley, D. I.; Pearcy, M. J., Mediation of biomaterial-cell interactions by adsorbed proteins: A review. *Tissue Engineering* **2005**, *11* (1-2), 1-18.
21. McFarland, C. D.; Thomas, C. H.; DeFilippis, C.; Steele, J. G.; Healy, K. E., Protein adsorption and cell attachment to patterned surfaces. *Journal of Biomedical Materials Research* **2000**, *49* (2), 200-210.
22. Xu, F. J.; Zhong, S. P.; Yung, L. Y. L.; Kang, E. T.; Neoh, K. G., Surface-active and stimuli-responsive polymer-Si(100) hybrids from surface-initiated

atom transfer radical polymerization for control of cell adhesion. *Biomacromolecules* **2004**, *5* (6), 2392-2403.
23. Singh, N.; Cui, X.; Boland, T.; Husson, S. M., The role of independently variable grafting density and layer thickness of polymer nanolayers on peptide adsorption and cell adhesion. *Biomaterials* **2007**, *28* (5), 763-771.
24. Pratt, K. J.; Williams, S. K.; Jarrell, B. E., Enhanced adherence of human adult endothelial-cells to plasma discharge modified polyethylene terephthalate. *Journal of Biomedical Materials Research* **1989**, *23* (10), 1131-1147.
25. Tamada, Y.; Ikada, Y., Cell-adhesion to plasma-treated polymer surfaces. *Polymer* **1993**, *34* (10), 2208-2212.
26. Pitt, W. G., Fabrication of a continuous wettability gradient by radio-frequency plasma discharge. *Journal of Colloid and Interface Science* **1989**, *133* (1), 223-227.
27. Maroudas, N. G., Chemical and mechanical requirements for fibroblast adhesion. *Nature* **1973**, *244* (5415), 353-354.
28. Steele, J. G.; Dalton, B. A.; Johnson, G.; Underwood, P. A., Polystyrene chemistry affects vitronectin activity - An explanation for cell attachment to tissue-culture polystyrene but not to unmodified polystyrene. *Journal of Biomedical Materials Research* **1993**, *27* (7), 927-940.
29. Fabrizius-Homan, D. J.; Cooper, S. L., Competitive adsorption of vitronectin with albumin, fibrinogen and fibronectin on polymeric biomaterials. *Journal of Biomedical Materials Research* **1991**, *25* (8), 953-971.
30. Llopis-Hernandez, V.; Rico, P.; Ballester-Beltran, J.; Moratal, D.; Salmeron-Sanchez, M., Role of surface chemistry in protein remodeling at the cell-material interface. *PLoS One* **2011**, *6* (5), e19610-1.
31. Bergkvist, M.; Carlsson, J.; Oscarsson, S., Surface-dependent conformations of human plasma fibronectin adsorbed to silica, mica, and hydrophobic surfaces, studied with use of atomic force microscopy. *Journal of Biomedical Materials Research Part A* **2003**, *64A* (2), 349-356.
32. Sherratt, M. J.; Holmes, D. F.; Shuttleworth, C. A.; Kielty, C. M., Substrate-dependent morphology of supramolecular assemblies: Fibrillin and type-VI collagen microfibrils. *Biophysical Journal* **2004**, *86* (5), 3211-3222.
33. Sherratt, M. J.; Bax, D. V.; Chaudhry, S. S.; Hodson, N.; Lu, J. R.; Saravanapavan, P.; Kielty, C. M., Substrate chemistry influences the morphology and biological function of adsorbed extracellular matrix assemblies. *Biomaterials* **2005**, *26* (34), 7192-7206.
34. Raghavachari, M.; Tsai, H. M.; Kottke-Marchant, K.; Marchant, R. E., Surface dependent structures of von Willebrand factor observed by AFM under aqueous conditions. *Colloids and Surfaces B-Biointerfaces* **2000**, *19* (4), 315-324.
35. Norde, W.; Favier, J. P., Structure of adsorbed and desorbed proteins. *Colloids and Surfaces* **1992**, *64* (1), 87-93.

36. Sang, L. C.; Coppens, M. O., Effects of surface curvature and surface chemistry on the structure and activity of proteins adsorbed in nanopores. *Physical Chemistry Chemical Physics* **2011**, *13* (14), 6689-6698.
37. Toromanov, G.; Gonzalez-Garcia, C.; Altankov, G.; Salmeron-Sanchez, M., Vitronectin activity on polymer substrates with controlled -OH density. *Polymer* **2010**, *51* (11), 2329-2336.
38. Zhang, H. L.; Bremmell, K.; Kumar, S.; Smart, R. S. C., Vitronectin adsorption on surfaces visualized by tapping mode atomic force microscopy. *Journal of Biomedical Materials Research Part A* **2003**, *68A* (3), 479-488.
39. Meadows, P. Y.; Bemis, J. E.; Walker, G. C., Single-molecule force spectroscopy of isolated and aggregated fibronectin proteins on negatively charged surfaces in aqueous liquids. *Langmuir* **2003**, *19* (23), 9566-9572.
40. Hull, J. R.; Tamura, G. S.; Castner, D. G., Structure and reactivity of adsorbed fibronectin films on mica. *Biophysical Journal* **2007**, *93* (8), 2852-2860.
41. Shekaran, A.; Garcia, A. J., Nanoscale engineering of extracellular matrix-mimetic bioadhesive surfaces and implants for tissue engineering. *Biochimica et Biophysica Acta (BBA) - General Subjects* **2011**, *1810* (3), 350-360.

CHAPTER 7

Conclusions and outlook

7.1 Conclusions and outlook

This Thesis describes novel strategies to address the needs for coatings for the modification of devices in selected fields in biology and medicine by using polymer thin films. Polymer coatings are widely used in biomedical applications, and present many advantages compared to other materials. The chemical and mechanical properties of polymers can be finely tailored for the desired performance. For homopolymers such as poly(*N*-vinylpyrrolidone) (PNVP), investigated in Chapters 3 and 4, the main chemical properties are defined by the monomer functionality (neutral charge, hydrophilic), while the physical properties are defined by the average molecular weight and molecular weight polydispersity. The advent of reversible-deactivation radical polymerization methods such as atom transfer radical polymerization (ATRP) and radical addition-fragmentation chain transfer (RAFT) polymerization has provided the tools for building well-defined copolymers with multiple combinations of chemical functionalities and multiple architectures (e.g. block copolymers, dendritic structures and star-shaped polymers) as well as providing end-groups for conjugation purposes. In Chapter 5 and 6, the comb-like copolymer poly(poly(ethylene glycol)methyl ether methacrylate) (poly(PEGMA)) was employed, due to its ease of polymerization and highly hydrophilic, neutrally charged poly(ethylene glycol) side chains. The resulting architecture has remarkable low protein adsorbing properties.

The use of polymers for biomedical applications is also advantageous because of the ease and variety of coating preparation methods available. Polymer thin films can be easily deposited on a surface by a variety of methods, including spin-coating or dip-coating. Both techniques form a thin film by removal of volatile solvent from a polymer solution on the desired substrate. Dip-coating can be used to apply polymer films on non-flat and

large surfaces, such as might be required for biomedical devices. Unlike spin-coating though, dip-coating cannot force a polymer to form a film on a non-wettable surface, because it does not take advantage of the centrifugal forces available in spin-coating. In dip-coating, while the surface is being extracted from the polymer solution, and once the polymer solution has almost completely dried out, the concentrated polymer is likely to dewet from a non-wettable substrate in the absence of an external force. The employment of dip-coating may require the use of polymer film interlayers to reduce the driving force for dewetting and stabilise the functional coating on the substrate. The variety of polymers and functional groups available through advanced polymerisation techniques again can be of great benefit here.

The designer of coatings for biomedical applications must be conscious of the variety of different needs in the field, and tailor the approach used accordingly. In this Thesis, two types of coatings suitable for different biomedical applications were developed. The first coating was described in Chapter 3: PNVP was used to develop a bio-inert coating designed to strongly reduce protein adsorption. For many surfaces, protein molecules will generally begin to adsorb in the first few seconds after being placed in contact with a biological medium. In the absence of a low protein-adsorbing coating, a protein layer forms on the substrate and acts as an anchoring surface for macrophages and host cells, which can initiate an inflammatory reaction and form scar tissue, and for bacteria, which are many times more likely to start an infection if they can form an impenetrable biofilm on the substrate. All these issues are often found when interfacing a medical implant with the human body. Protein-repellent coatings, such as the PNVP one developed here, may assist in preventing these issues.

In this work, for the first time a thermally-induced cross-linking mechanism for PNVP coatings was investigated. The cross-linking process

most likely takes place *via* radical reactions at C-H bonds, and does not require the breaking of the pyrrolidone ring. The cross-linking rate increased with the annealing temperature, reaching completion throughout the depth of the film within a few hours at 200 °C. The excellent protein-repellent properties of the PNVP were fully maintained after cross-linking, and make the developed coatings valid alternatives to grafted PEG coatings, widely used for their antifouling properties but more complicated to prepare. The cross-linked films were stable in water for weeks, opening a wide range of applications for antifouling PNVP coatings. Medical devices such as urinary catheters and intravenous devices, often clogged by cells and primary sites for infections, could be lined with a PNVP film from an ethanol solution, and baked at temperatures as low as 160 °C for about 7 hours to be rendered protein-repellent. This simple procedure may increase the safety of use of such medical devices, and reduce the health and monetary costs associated with device replacement and device-related complications. Because of the annealing step required to cross-link and stabilise the PNVP coatings, the medical devices have to be able to withstand moderately high temperatures for several hours; this is the case for urinary and intravenous catheters, commonly made of moderately thermoresistant silicon rubber or polyurethanes.

As described in Chapter 4, PNVP films are capable of cross-linking as well as dewetting upon annealing on common plastics such as PS, forming holes that grow with annealing time. The results of the investigation showed that the competition of dewetting and cross-linking affected the final hole growth, which was rapid in the early stages of the dewetting, but dramatically slowed down at long annealing times. The behaviour was different when the PNVP was supported by low viscosity PS (liquid-like) or high viscosity PS (solid-like). At advanced stages of cross-linking the PNVP dewetting stopped completely when the substrate was a high viscosity PS,

while it continued at a very low rate if the substrate was a low viscosity PS. This was likely due to the ability of the cross-linked PNVP film to slowly move on the liquid-like PS, while the friction at the interface with the solid-like PS prevented any movement.

A model was developed to fit the hole growth in the dewetting PNVP film during cross-linking, based on the assumption that the molecular weight, and hence the viscosity, of PNVP increased exponentially as a result of the cross-linking process. The model was based on the assumption of a liquid/solid system, and was shown to be very powerful, resulting in excellent fitting of the data obtained for PNVP dewetting on solid-like PS. The fits of the data obtained for PNVP dewetting on low viscosity PS were also good, albeit not at long annealing times, when the viscosity ratio between the PNVP and the PS films changed to such an extent that the bilayer was better described by a liquid/liquid system. From the model, we were also able to produce information on the activation energy of the cross-linking process.

One of the main results of the study of dewetting of PNVP on PS was that by tuning the annealing temperature, the ratio of the rates of PNVP film dewetting and cross-linking could be tuned to achieve the desired hole size, or no holes at all. These findings open up the possibility of preparing antifouling and micropatterned PNVP coatings on non-wettable substrates, widening the variety of devices that could potentially be modified with these types of coatings.

Future work on cross-linked PNVP coatings would include the investigation of their influence on inflammatory responses and of their cytotoxicity, as well as of microbial film formation. These are significant unmet clinical needs. Ideally, *in vivo* studies with model surfaces and practical devices would demonstrate whether the PNVP coatings developed in this work would be useful in real-world applications.

The second coating developed in the work reported in this Thesis is presented in Chapters 4, 5 and 6. Here, micropatterned polymer thin films were developed for the control of protein adsorption and cell adhesion. There are many reasons why this is important. The control of cell density and spreading on a surface can help to direct their fate towards death, proliferation and even differentiation, which is the basis of tissue engineering *in vitro*. In different applications, the isolation of single cells or small colonies of cells in arrays of separated micro-bioreactors can allow fundamental studies on the interaction of a cell with its microenvironment and with its neighbouring cells. This is particularly important for growing stem cells in populations that maintain their pluripotency, i.e. their ability to differentiate in many kinds of cells, which is still a challenging objective, as the field's understanding of the mechanisms that govern their natural tendency to specialise is still poor. Other applications may include high-throughput screening of libraries of chemical compounds or particle capture in microfluidic devices.

Dewetting of polymer thin films to produce micropatterned surfaces with adequate chemical contrast can be used to pattern cells onto controlled domains to obtain arrays of micro-bioreactors. Thin film dewetting is a technique for the formation of patterns that is inexpensive, simple and flexible, and relies on polymer thin films, which can be prepared on flat as well as non-flat surfaces. These advantages make dewetting a valid alternative to other patterning techniques available, such as photolithography and micro-contact printing. The formation of ordered patterns cannot be readily achieved, though for the biomedical applications described here, order is not a pre-requisite for function.

An example of micropatterned surface for biomedical applications is the patterned PNVP/PS coating studied in Chapter 4. This coating presented protein-adsorptive PS holes in protein-repellent PNVP background. In

future work, extra cellular matrix proteins such as vitronectin could be selectively deposited in the PS holes, with no adsorption on the antifouling PNVP background. Cells could then adhere on the protein-coated domains in the desired pattern. The hole size was readily controlled by the annealing temperature and time, and the hole density could be controlled by tuning the PNVP film stress, by selecting the appropriate annealing temperature, molecular weight of the polymer, and employing pre-annealing treatments.

A more complex patterned coating achieved by dewetting was investigated in Chapters 5 and 6. Here, thin film dewetting was again used to obtain a pattern of holes, but the dewetted upper film was made protein-repellent in a separate step by grafting a comb-like PEG methacrylate brush, using controlled, surface-initiated atom transfer radical polymerization (ATRP). The surface-initiated polymerization from a polymer film was investigated. The poly(PEGMA) brush grew from the surface of the films as well as within it, inducing a marked swelling and forming an intermixed layer. The formation of a dense brush was confirmed by AFM, which showed a smooth and featureless surface. A dense brush is required to reduce protein adsorption to low levels. The chemical difference, and hence the ability to adhere proteins, between the holes and their background was established by XPS imaging techniques.

The use of a protein adsorbing lower layer and a low protein adsorbing upper layer allowed for the localisation of extra cellular matrix proteins, which resulted in the localised attachment of fibroblasts. Patterns of dewetted holes with different length scales all showed selective protein adsorption in the PS holes, as seen in the AFM and fluorescence microscope investigations with albumin and fibrinogen. For cell studies, cell-adhesive vitronectin was pre-patterned in the holes, ensuring good coverage and likely forming protein clusters able to expose the integrin-binding domains. Effective cell patterning of fibroblasts was obtained only when the dewetted

holes were larger than the cells and provided space for cell spreading. The adhered cells showed good viability.

This coating combined the advantages of dewetting, i.e. ease of use and low cost, with the advantages of surface-initiated ATRP, i.e. grafted chains with tuneable properties and with functionalisable end groups. In future work, the living ends of the grafted chains could be selectively tagged with a peptide that promoted selective cell adhesion. For example, cell type 1 could be selectively adhered on the PS domains, and cell type 2 could be attached to the selective peptide in the regions around cell type 1. The result would be a geometrically controlled cell co-culture, where homotypic and heterotypic interactions could be tuned.

An additional future perspective could take advantage of the thermoresponsive behaviour of PEG methacrylate bottle brushes: these polymers have been shown to have lower critical solution concentrations compatible with biological environments, in the case of short PEG side-chains (2-3 units).[1] This implies that they can be made to collapse on the substrate or extend away from it by tuning the temperature. Collapsed brushes promote cell adhesion, while they become repellent once they are swollen. This property was proven to be effective in patterning cells into geometrically controlled cell co-cultures, as reviewed by Hannachi *et al.*[2] for the case of thermoresponsive poly(*N*-isopropyl acrylamide). In the coating developed in this work, one type of cell could be selectively adhered into the polystyrene domains when the PEG methacrylate brush is swollen, and a second type of cell could be adhered onto the background once the brush has been forced to collapse. If the PS was also modified to be selectively grafted with a different thermoresponsive brush, for example polymerised by RAFT, the pattern of thermoresponsive brushes could be employed to grow fully detachable cell co-culture sheets for tissue grafting.[2]

7.2 References

1. Bebis, K.; Jones, M. W.; Haddleton, D. M.; Gibson, M. I., Thermoresponsive behaviour of poly (oligo(ethyleneglycol methacrylate) s and their protein conjugates: importance of concentration and solvent system. *Polymer Chemistry* **2011**, *2* (4), 975-982.
2. Hannachi, I. E.; Yamato, M.; Okano, T., Cell sheet technology and cell patterning for biofabrication. *Biofabrication* **2009**, *1* (2), 022002.

Amendments to the submitted version of this Thesis: Publications arising from this work, including copyright credits

Chapter 3 contains data reproduced in part with permission from "Telford, A. M.; James, M.; Meagher, L.; et al.; Thermally Cross-Linked PNVP Films as Antifouling Coatings for Biomedical Applications, ACS Applied Materials & Interfaces 2010, 2 (8), 2399-2408". Copyright 2010 American Chemical Society.

Chapter 4 contains data reproduced in part with permission from "Telford, A. M.; Thickett, S. C.; James, M.; et al; Competition between Dewetting and Cross-Linking in Poly(N-vinylpyrrolidone)/Polystyrene Bilayer Films, Langmuir 2011, 27 (23), 14207-14217". Copyright 2011 American Chemical Society.

Chapter 5 contains data reproduced in part with permission from "Telford, A. M.; Neto, C.; Meagher, L.; Robust Grafting of PEG-methacrylate Brushes from Polymeric Coatings, Polymer 2013, 54 (21), 5490–5498". Copyright 2013 Elsevier.

Chapters 5 and 6 contain data reproduced in part with permission from "Telford, A. M.; Meagher, L.; Glattauer, V.; et al.; Micro-patterning of Polymer Brushes: Grafting from Dewetting Polymer Films for Biological Applications, Biomacromolecules 2012, 13 (9), 2989-2996". Copyright 2012 American Chemical Society.